Structural cell biology of mammalian sperm

Miguel Ricardo Rilloraza Leung

Pembroke College
University of Oxford

A thesis submitted in partial fulfillment
of the requirements for the degree of
Doctor of Philosophy

Michaelmas 2020

Abstract

Reflecting the sheer diversity of reproductive modes and fertilization arenas, sperm are among the most structurally specialized and structurally diverse eukaryotic cell types. In this thesis, I apply recent developments in cellular cryo-electron tomography and image processing to explore the molecular landscape of mammalian sperm in a near-native state, free of artefacts from chemical fixation and heavy metal staining. I show that the major organelle-cytoskeleton interfaces in sperm, the head-tail junction and the mitochondrial sheath, are characterized by ordered supramolecular assemblies that are conserved across species. I also detail the structural elaborations that enable mammalian sperm flagella to swim through viscous fluids, from protofilament-bracing structures that reinforce microtubules at the nano-scale to large accessory structures that impose micron-scale asymmetries and anisotropies on the entire assembly. I report the native subcellular organization of the flagellar base, which is crucial for generating and shaping the flagellar beat, revealing that the connecting piece is an elastic scaffold that is remodelled during the beat cycle. I then trace membrane remodelling events during capacitation and the acrosome reaction, which are functional maturation events necessary for sperm to become fertilization-competent. I find that the unique geometry of the sperm head supports an atypical membrane fission-fusion process that maintains cell integrity while facilitating massive membrane protein relocalization, thus transforming the molecular landscape of the sperm surface and creating a platform for interaction and fusion with the egg. This thesis unveils new aspects of sperm biology at unprecedented levels of detail, thus providing vital foundations for linking molecular structure to sperm motility and energetics, sperm-egg fusion, and gamete evolution.

Structural cell biology of mammalian sperm



Miguel Ricardo Rilloraza Leung

Pembroke College

University of Oxford

A thesis submitted in partial fulfillment
of the requirements for the degree of

Doctor of Philosophy

Michaelmas 2020

DON'T PANIC

— Douglas Adams, *The Hitchhiker's Guide to the Galaxy*

Abstract

Reflecting the sheer diversity of reproductive modes and fertilization arenas, sperm are among the most structurally specialized and structurally diverse eukaryotic cell types. In this thesis, I apply recent developments in cellular cryo-electron tomography and image processing to explore the molecular landscape of mammalian sperm in a near-native state, free of artefacts from chemical fixation and heavy metal staining. I show that the major organelle-cytoskeleton interfaces in sperm, the head-tail junction and the mitochondrial sheath, are characterized by ordered supramolecular assemblies that are conserved across species. I also detail the structural elaborations that enable mammalian sperm flagella to swim through viscous fluids, from protofilament-bracing structures that reinforce microtubules at the nano-scale to large accessory structures that impose micron-scale asymmetries and anisotropies on the entire assembly. I report the native subcellular organization of the flagellar base, which is crucial for generating and shaping the flagellar beat, revealing that the connecting piece is an elastic scaffold that is remodelled during the beat cycle. I then trace membrane remodelling events during capacitation and the acrosome reaction, which are functional maturation events necessary for sperm to become fertilization-competent. I find that the unique geometry of the sperm head supports an atypical membrane fission-fusion process that maintains cell integrity while facilitating massive membrane protein relocalization, thus transforming the molecular landscape of the sperm surface and creating a platform for interaction and fusion with the egg. This thesis unveils new aspects of sperm biology at unprecedented levels of detail, thus providing vital foundations for linking molecular structure to sperm motility and energetics, sperm-egg fusion, and gamete evolution.

Acknowledgements

The Clarendon Fund and the Nuffield Department of Medicine Prize Studentships

My supervisors: Dr. Tzviya-Zeev-Ben-Mordehai and Prof. E. Yvonne Jones

My colleagues in STRUBI: Agata Krupta, Margaret Jones, Weixian Lu, Ollie Hayward, Dr. Arianna Marini, Dr. Daven Vasishtan, Dr. Lindsay Baker, Dr. Ben Vollmer, Dr. Vojta Pražák

My colleagues in the Cryo-EM Group at UU: Dr. Mihajlo Vanevic, Dr. Stuart Howes, Bianca Rhemrev, Ravi Teja Ravi, Marc Roelofs, Dr. Eka Kartvelishvili, Dr. Hannah Wapenaar, Dr. Juliette Fedry, Dr. Gonzalo Obal-Caballero, Lennart Pagani, Jo Judernatz, Loes Teeuwen, Suzan Leemans, Dr. Laura van Bezouwen, Ingr. Chris Schneijdenberg, Hans Meeldijk

My colleagues in the Veterinary Faculty at UU: Dr. Liz Bromfield, Dr. Heiko Henning, Dr. Paula Maitan, Min Zhang, Dr. Bart Gadella

My colleagues in the Mass Spectrometry Group at UU: Dr. Riccardo Zenezini-Chiozzi, Johannes Hevler, Prof. Albert Heck

The Netherlands Centre for Electron Nanoscopy (NeCEN), and operators Dr. Rebecca Dillard and Dr. Chris Diebolder

The Oxford Philippines Society

Peter, Evan

Kyra, Martin, Isaiah, Jelo

Sir Neil, Ma'am Denise

Meg, Nikki, YL, '12 friends

Ate Agnes, Mico, Kuya Mel, Kuya Pablo, Nanay Conching, Ms Lita, Nanang

Ate Car, Kuya Alan, Bryan

Ate Lhen, Kuya Bong, Jaz, Jill

Dad, Mom, Gabbie, Toby, Tommy, Lola Nita, Lolo Nelson, Lola Tami, Kuya Marc

and Kim - *to infinity and beyond*

Declaration

All of the work in this thesis is my own, except the following:

Horse sperm was generously provided by Paula Maitan and Dr. Heiko Henning.

Mouse sperm was generously provided by Dr. Elizabeth Bromfield.

Bovine sperm was generously provided by Dr. Heiko Henning.

Mass spectrometry was done by Dr Riccardo Zenezini-Chiozzi & Johannes Hevler.

Contents

List of Figures **x**

List of Tables **xiii**

List of Abbreviations **xiv**

1 Introduction **1**

1.1 Thesis overview and objectives 4
1.2 Structural cell biology: the whole is more than the sum of its parts . . 4
1.3 Electron microscopy is the core method for visualizing cell structure . . 6
1.4 Cryo-electron tomography enables nanometer resolution imaging of cells in a fully-hydrated, near-native state 7
1.5 Enter the muse: the deceptively simple sperm cell 13
1.5.1 The head 15
1.5.2 The neck 16
1.5.3 The midpiece 19
1.5.4 The tail 21
1.5.5 Accessory structures of the mammalian sperm flagellum 25
1.5.6 The endpiece 28
1.5.7 Functional maturation of mammalian sperm 29

2 Materials and Methods **33**

2.1 Sperm preparation 34
2.1.1 Pig sperm 34
2.1.2 Horse sperm 35
2.1.3 Mouse sperm 35
2.1.4 Bovine sperm 36
2.2 Cryo-ET grid preparation 36
2.3 Cryo-focused ion beam milling 38
2.4 Tilt series acquisition 38
2.5 Tomogram reconstruction 39
2.6 Tomogram segmentation 39
2.7 Subtomogram averaging 39
2.7.1 Proximal centriole triplets, axonemal doublets, central pair apparatus 40
2.7.2 Endpiece singlets 40

2.7.3 Nuclear envelope densities, outer mitochondrial membrane (omm) densities, ATP synthase, microtubule plugs 41
2.7.4 Particles in nuclear clearing zones 41
2.7.5 Acrosome crystalloids 42
2.7.6 Plotbacks 42
2.8 Measurements and quantification 42
2.8.1 Mitochondrial dimensions 42
2.8.2 Internal mitochondrial ultrastructure 43
2.8.3 Membrane distances 43
2.9 Cryo-scanning transmission electron microscopy (cryo-STEM) 43
2.10 Mass spectrometry 44
2.10.1 Sperm preparation 44
2.10.2 Whole cell proteomics 45
2.10.3 Whole cell cross-linking mass spectrometry 45

3 The molecular architecture of the sperm head-tail junction, a specialized nucleus-cytoskeleton contact site 47
3.1 Introduction 47
3.2 Results and Discussion 49
3.2.1 The sperm head is compact. 49
3.2.2 A conserved supramolecular array of proteins in the nuclear envelope forms the base of the head-tail junction. 52
3.3 Concluding Remarks 59

4 A conserved supramolecular array anchors mitochondria to the cytoskeleton in the sperm mitochondrial sheath 60
4.1 Introduction 60
4.2 Results and Discussion 62
4.2.1 Mitochondrial dimensions vary across species and spatially along the midpiece. 62
4.2.2 Cristae architecture varies across species. 66
4.2.3 Inter-mitochondrial junctions are associated with novel linker complexes. 67
4.2.4 Mitochondria are anchored to the cytoskeleton through a conserved ladder-like array in the outer mitochondrial membrane. 69
4.2.5 Glycerol kinase-like proteins and voltage dependent anion channels are probable constituents of the ladder-like array. 72
4.2.6 Amorphous calcium granules form in mitochondria of sperm incubated in capacitating conditions. 76
4.3 Concluding Remarks 78

5 The multi-scale architecture of mammalian sperm flagella 80
5.1 Introduction 80
5.2 Results and Discussion 83
5.2.1 The conserved ciliary microtubule core is accessorized in a diverse manner across lineages and across cell types. 83
5.2.2 Accessory structures are integral parts of mammalian sperm flagella and impose large mechanical asymmetries on the core axoneme. 98
5.3 Concluding Remarks 109

6 Acrosome destabilization transforms the molecular landscape of the mammalian sperm surface 110
6.1 Introduction 110
6.2 Results and Discussion 112
6.2.1 The plasma membrane and outer acrosomal membrane are closely apposed even in non-capacitated sperm. 112
6.2.2 Acrosome swelling and membrane destabilization already occur during capacitation. 114
6.2.3 Acrosome destabilization results in release of morphologically heterogeneous, protein-decorated vesicles along with patches of crystalloid material. 121
6.2.4 An atypical fission-fusion pathway maintains cell integrity after acrosome destabilization. 124
6.2.5 The acrosome reaction leads to topographical and molecular remodelling of the sperm surface. 126
6.2.6 An updated model of how capacitation-associated membrane destabilization restructures the sperm surface. 130
6.3 Concluding Remarks 134

7 Summarizing Discussion 135
7.1 Major findings, implications, and future directions 136
7.1.1 Organelle-cytoskeleton interaction sites are characterized by conserved and highly ordered supramolecular assemblies. . . . 136
7.1.2 Asymmetry and anisotropy in mammalian sperm flagella. 139
7.1.3 Sperm centrioles present an opportunity to study the remodeling of an otherwise conserved structure. 140
7.1.4 Microtubule inner proteins are diverse both within the flagellum and across cell types and lineages. 141
7.1.5 The acrosome reaction is a unique membrane fission-fusion event that reflects the structural organization of the mammalian sperm head. 145

7.2 Challenges and opportunities in structural cell biology 147
7.2.1 “What’s that blob?” 147
7.2.2 All samples great and small 148
7.2.3 Out of the lab and into the field 149

References **151**

List of Figures

1.1 An overview of the cryo-electron tomography (cryo-ET) workflow. . . . 8
1.2 The Volta phase plate enhances contrast in cellular tomograms. 10
1.3 Three-dimensional segmentation and subtomogram averaging can aid analysis and interpretation of cryo-tomograms. 12
1.4 The structural organization of a mammalian sperm cell. 14
1.5 Structural organization of the neck region. 17
1.6 Sperm centrioles represent a unique opportunity to study the structural plasticity of a conserved assembly. 18
1.7 Morphogenesis of the mitochondrial sheath in mouse spermatids. . . . 20
1.8 The molecular architecture of the axoneme. 22
1.9 Mammalian sperm flagella are characterized by large accessory structures. 26
1.10 The acrosome reaction is a dramatic membrane remodeling event that prepares the sperm for fusion with the egg. 31

2.1 The cryo-electron tomography (cryo-ET) workflow for imaging mammalian sperm. 37

3.1 The sperm head is compact. 49
3.2 The sperm nuclear envelope consists of discrete domains characterized by distinct protein signatures. 51
3.3 Nuclear pockets contain particles that resemble 20S proteasomes. . . . 53
3.4 Subunits of the 20S proteasome are enriched in sperm heads relative to sperm tails. 55
3.5 A hexagonal array of trimeric protein densities in the nuclear envelope forms the base of the head-tail junction. 56
3.6 Nuclear envelope densities have molecular dimensions consistent with SUN proteins. 58

4.1 Cryo-focused ion beam milling and use of the Volta phase plate (VPP) improve cryo-ET imaging of the midpiece. 63
4.2 Mitochondrial dimensions vary across species and spatially along the midpiece. 64
4.3 Cristae organization varies across species. 67
4.4 Ladder-like arrays on the axoneme-facing surface of the outer mitochondrial membrane (OMM) are conserved. 69
4.5 Structural details of ladder-like arrays on sperm mitochondria. 70
4.6 Ladder-like arrays anchor sperm mitochondria to the cytoskeleton. . . 71

4.7 Glycerol kinase-like proteins and voltage dependent anion channels are probable constituents of the ladder-like array. 73
4.8 Amorphous calcium granules form in mitochondria of pig sperm incubated in capacitating conditions. 77

5.1 The proximal centriole (PC) in mammalian sperm contains novel microtubule inner proteins. 85
5.2 Structural features of the pig sperm proximal centriole (PC). 86
5.3 The distal centriole (DC) in mammalian sperm is composed of doublet microtubules arrayed asymmetrically around a pair of singlet microtubules. 88
5.4 Structural details of the central pair apparatus projection network in mammalian sperm. 90
5.5 The mammalian sperm central pair apparatus (CPA) has a conserved projection network but species-specific microtubule inner proteins. . . 91
5.6 The mammalian sperm axoneme anchors unique accessory structures and species-specific microtubule inner proteins. 92
5.7 Comparing the mammalian sperm axoneme with other structures. . . . 94
5.8 Singlet microtubules in the endpiece are capped by a conserved plug but contain species-specific microtubule inner proteins. 96
5.9 Structural organization of the fibrous sheath in relation to the axoneme. 99
5.10 The attachment of outer dense fibers to axonemal doublets varies along the length of the sperm flagellum. 101
5.11 Outer dense fibers impose mechanical asymmetry on the mammalian sperm flagellum. 102
5.12 The connecting piece forms a large, asymmetric chamber around the sperm centrioles. 103
5.13 The connecting piece is an elastic scaffold that is remodelled during the beat cycle. 106
5.14 Quantifying structural deformations in the sperm neck. 108

6.1 Representative micrographs of intact and disrupted non-capacitated sperm. 113
6.2 The plasma membrane and the outer acrosomal membrane are closely apposed even in non-capacitated sperm. 114
6.3 Assessment of capacitation and acrosome status by flow cytometry and fluorescence microscopy. 115
6.4 Changes in sperm head dimensions with capacitation and ionophore-stimulated acrosome reaction. 116

6.5 Capacitation is associated with acrosome swelling and membrane destabilization. 117
6.6 Long contact zones are visible in capacitated and acrosome-reacting sperm. 118
6.7 Additional examples of membrane fission-fusion intermediates in late-stage capacitated sperm. 119
6.8 Membrane destabilization, fusion, and vesiculation of the plasma membrane and the outer acrosomal membrane. 120
6.9 Representative micrographs of fully acrosome-reacted sperm. 121
6.10 The acrosomal shroud consists of morphologically heterogeneous protein-decorated vesicles. 123
6.11 The acrosomal shroud in acrosome-reacted sperm after progesterone stimulation. 124
6.12 Membrane destabilization leads to acrosome vesiculation and to the dispersal of acrosome contents. 125
6.13 Subtomogram averaging of crystalloid patches from acrosomes of capacitated sperm. 126
6.14 An atypical fission-fusion pathway maintains cell integrity after acrosome destabilization. 127
6.15 The acrosome reaction transforms the topography of the sperm surface. 128
6.16 Additional examples of the new topography of acrosome-reacted sperm. 129
6.17 The acrosome reaction transforms the molecular landscape of the sperm surface. 131
6.18 Membrane protein decoration on the post-acrosomal plasma membrane of acrosome-reacted sperm after progesterone stimulation. 132
6.19 A revised model of how capacitation-related membrane destabilization leads to the acrosome reaction. 133

7.1 Cryo-electron tomography of mammalian sperm across scales. 137
7.2 The diversity of microtubule-based assemblies within a single motile cilium. 143

List of Tables

3.1 Image acquisition and processing metrics for subtomogram averaging of protein complexes in the mammalian sperm nucleus and nuclear envelope 52
3.2 Proteasome subunits in pig sperm identified through label-free mass spectrometry 54

4.1 Measurements of mitochondrial width in different regions of the mid-piece in sperm from three mammalian species 65
4.2 Image acquisition and processing metrics for subtomogram averaging of mitochondrial protein complexes in mammalian sperm 68
4.3 Outer mitochondrial membrane proteins in pig sperm identified through label-free mass spectrometry 75

5.1 Image acquisition and processing metrics for subtomogram averaging of microtubule-based assemblies in mammalian sperm 84

6.1 Number of tomograms in the dataset representing each membrane remodelling intermediate. 118

List of Abbreviations

AMP . . . . . adenosine monophosphate

AR . . . . . acrosome reaction

ART . . . . . assisted reproductive technology

ATP . . . . . adenosine triphosphate

BP . . . . . baseplate

BSA . . . . . bovine serum albumin

cAMP . . . . . cyclic adenosine monophosphate

CP . . . . . connecting piece

CPA . . . . . central pair apparatus

cryo-EM . . . . . cryo-electron microscopy

cryo-ET . . . . . cryo-electron tomography

cryo-FIB . . . . . cryo-focused ion beam

CSM . . . . . cross-link spectrum match

DC . . . . . distal centriole

DSSO . . . . . disuccinimidyl sulfoxide

EDX . . . . . energy dispersive X-ray spectroscopy

EM . . . . . electron microscopy

FITC . . . . . fluorescein isothiocyanate

FS . . . . . fibrous sheath

GK . . . . . glycerol kinase

HAADF . . . . . high-angle annular dark field

IAM . . . . . inner acrosomal membrane

IDA . . . . . inner dynein arm

iBAQ . . . . . intensity-based absolute quantification

IMM . . . . . inner mitochondrial membrane

INM . . . . . inner nuclear membrane

IVF . . . . . in vitro fertilization

KASH . . . . . Klarsicht, ANC-1, and Syne homology

LFQ . . . . . label-free quantification

LINC . . . . . linker of nucleoskeleton and cytoskeleton

MF . . . . . microfilament

MIP . . . . . microtubule inner protein

N-DRC . . . . . nexin-dynein regulatory complex

NE . . . . . nuclear envelope

NPC . . . . . nuclear pore complex

OAM . . . . . outer acrosomal membrane

ODA . . . . . outer dynein arm

ODF . . . . . outer dense fiber

OMM . . . . . outer mitochondrial membrane

ONM . . . . . outer nuclear membrane

PAS . . . . . post-acrosomal sheath

PC . . . . . proximal centriole

PM . . . . . plasma membrane

PNA . . . . . peanut agglutinin

POC . . . . . proteome of centriole

PT . . . . . perinuclear theca

RS . . . . . radial spoke

SC . . . . . striated column

SEM . . . . . scanning electron microscopy

SNARE . . . . . soluble N-ethylmaleimide sensitive factor attachment protein receptor

SPATA . . . . . spermatogenesis-associated protein

STEM . . . . . scanning transmission electron microscopy

SUN . . . . . Sad1 and UNC84 domain containing

TALP . . . . . Tyrode's medium supplemented with albumin, lactate, and pyruvate

TEM . . . . . transmission electron microscopy

VDAC . . . . . voltage-dependent anion channel

VPP . . . . . Volta phase plate

WDR . . . . . WD40 repeat

XL-MS . . . . . cross-linking mass spectrometry

1 Introduction

Contents

1.1 Thesis overview and objectives 4
1.2 Structural cell biology: the whole is more than the sum of its parts 4
1.3 Electron microscopy is the core method for visualizing cell structure 6
1.4 Cryo-electron tomography enables nanometer resolution imaging of cells in a fully-hydrated, near-native state 7
1.5 Enter the muse: the deceptively simple sperm cell 13
1.5.1 The head 15
1.5.2 The neck 16
1.5.3 The midpiece 19
1.5.4 The tail 21
1.5.5 Accessory structures of the mammalian sperm flagellum . . 25
1.5.6 The endpiece 28
1.5.7 Functional maturation of mammalian sperm 29

Biological systems are organized across different scales: atoms assemble into biomolecules, which polymerize into macromolecules, which interact to form complexes, ultimately building the smallest living unit of matter – the cell. Cells are the fundamental unit of life, yet they are enormously, almost unfathomably, complex. There are over 400 differentiated cell types in the human body (Vickaryous and Hall, 2006), and each cell type is specialized for a defined set of functions; for example, muscle cells for movement, red blood cells for oxygen transport, and gametes for reproduction. The diversity of cell types is reflected in the equally-staggering diversity of cellular form.

Until recently, however, our understanding of cellular structure was limited to the scale of organelles and large substructures (on the order of tens of nanometers to microns), so cell biology has typically remained separate from structural biology, which deals with the scale of atoms and molecules (on the order of Ångstroms). The in-between, sometimes called the cellular mesoscale (Goodsell et al., 2020), remains largely uncharted territory. This dearth of information represents a major conceptual gap in our understanding of how cellular function emerges from interactions among subcellular components. Modern electron microscopy methods, led by advancements in cryo-electron microscopy and cryo-electron tomography, now enable explorations of this regime, uniting previously disparate fields into the discipline of structural cell biology. This thesis applies recent advancements in cellular cryo-electron tomography to study the mesoscale landscape of a highly specialized mammalian cell type – the sperm cell.

But of all the metazoan cell types, *why choose to study sperm*? From an academic perspective, the answer is simple: mammalian gametes represent extremes of cellular organization. The male gamete – the sperm – loses most of its cytoplasm and many of the organelles present in its somatic counterparts, thus becoming a small, streamlined cell. The female gamete – the egg – accumulates cytoplasm in preparation for embryonic development, thus becoming one of the largest cell types. Sperm also face unique challenges in that they are produced in one organism and function entirely in another, resulting in an arduous journey towards the egg. The sperm and the egg must then fuse, merging both their genetic information and their cellular cargo, to initiate new life.

Beyond the necessarily epistemological reasons outlined above, studying gamete biology is important for another key reason: reproductive health is a public health issue. Yet approximately 218 million women of reproductive age in low- to middle-income countries have an unmet need for contraception, and nearly half of all pregnancies in these countries are unintended (Sully et al., 2020). There have been no major new non-hormonal contraceptives in the past twenty years (Hemmerling et al., 2020), even though reducing unwanted pregnancies would significantly reduce maternal and

childhood deaths (Cleland et al., 2006). Furthermore, because male contraceptive options are limited, the burdens of contraception – financial, emotional, and physical – fall primarily on women (Thirumalai and Page, 2020). On the other side of the same coin, the World Health Organization (WHO) estimates that infertility afflicts a silent population of nearly 180 million couples in developing countries (Ombelet, 2011). In these regions, many cases of infertility are secondary effects of sexually-transmitted diseases (Nachtigall, 2006). Despite this, couples in developing countries have very limited access to expensive assisted reproductive technologies (only 48 of the 191 WHO member states even offer *in vitro* fertilization, IVF). Although it is estimated that male factors contribute to up to half of all infertility cases (Brugh and Lipshultz, 2004), the social burdens of infertility in these regions, which are tied to expectations of motherhood, also fall disproportionately on women (Cui, 2010; Nachtigall, 2006). Knowledge of gamete ultrastructure is vital for understanding how these cells function and interact, and for developing strategies to either encourage or prevent their union.

Looking beyond our own species, reproductive biology is also a crucial component of efforts to conserve and protect biodiversity in a changing world (Comizzoli and Holt, 2019; Holt et al., 2003). The International Union for the Conservation of Nature (IUCN) reports that more than 32,000 species are at risk of extinction, including 41% of all amphibians, 34% of reptiles, 33% of reef-building corals, 26% of mammals, and 14% of birds (https://www.iucnredlist.org/). Disconcertingly, the geographic regions with the highest concentrations of unique and endemic species are also those under the most human pressure (Gumbs et al., 2020). The ongoing biodiversity crisis – the sixth mass extinction – is sometimes cited as the most serious environmental threat we face because it is *irreversible*, and because every species lost represents a loss in the planet's ability to maintain ecosystem services (Ceballos et al., 2015, 2020). Improving assisted reproductive technologies for biodiversity conservation hinges on intensifying research efforts into basic reproductive biology, which is remarkably poorly understood for many species (Comizzoli and Holt, 2019; Wildt et al., 2010).

1.1 Thesis overview and objectives

This thesis aims to contribute to our understanding of how mammalian sperm are organized across scales, from subcellular compartments to organelles to individual macromolecular complexes. It is fundamentally a curiosity-driven expedition into the unfamiliar landscape of a seemingly familiar cell. When possible, I compare sperm from several mammalian species in conjunction with what is reported in the literature for other lineages and cell types. Cellular cryo-electron tomography is the core of my experimental armory, but I draw from complementary experiments, including proteomics and cross-linking mass spectrometry, as well as from results reported in the literature, in order to propose molecular identities and functions for the structures I resolve. The long-term goal of such comparative structural studies (which is necessarily beyond the scope of any individual thesis) is to work towards an understanding of how subcellular structure relates to cellular physiology.

This thesis is organized into an introductory chapter **(Chapter 1)**, a methods chapter **(Chapter 2)**, four results chapters **(Chapters 3 to 6)**, and a summarizing discussion chapter **(Chapter 7)**. Chapters 3 to 5 deal primarily with *structure*, specifically the molecular architecture of the sperm head, midpiece, and tail, respectively. The last section of Chapter 5 and Chapter 6 both deal with *how structure changes in relation to function*, covering sperm movement and preparation for gamete fusion, respectively. Each results chapter begins with a short introduction that aims to relate specific aspects of sperm structure to broader themes in cell biology. This thesis ends with a summarizing discussion that covers general themes arising from the results, addresses limitations of the current study, and suggests avenues for future endeavors.

1.2 Structural cell biology: the whole is more than the sum of its parts

Structural biology contributes significantly to our understanding of cellular systems by allowing us to relate chemical properties of macromolecules with their biological functions. Traditionally, structural biology was dominated by a divide-and-conquer

approach where individual macromolecules are purified from the cellular environment and either coaxed into ordered arrays to study by X-ray crystallography, studied in solution by nuclear magnetic resonance (NMR) spectroscopy, or trapped in a thin film of vitreous ice to image by single particle cryo-electron microscopy (cryo-EM). All of these methods require relatively large amounts of highly pure, highly stable material, which often requires engineering proteins to enhance their expression or thermostability. The limitation of traditional structural biology approaches is that many macromolecular complexes are either intrinsically hard to purify or simply *cannot* be divorced from the cellular milieu. These challenging targets may either be transient assemblies or may require very specific subcellular environments in order to function. In such cases, the only way to obtain structural information is to study the target within its native environment – the cell.

However, there is a more fundamental motivation for structural cell biology beyond simply solving structures of proteins that cannot be purified – cells are so much more than just bags of macromolecules floating around in solution. Every level of biological organization possesses emergent properties that cannot be recapitulated simply by combining constituent parts of the scale below (Anderson, 1972; Novikoff, 1945; Woese, 2004). A comprehensive understanding of living systems can only be achieved by integrating information across biological scales. Beyond asking questions of how individual proteins function, it is important to consider *where* in the cell they act, and how they act *in relation* to other cellular components such as membranes or cytoskeletal assemblies. There are likely to be interactions between macromolecular complexes in cells that we cannot anticipate solely from studying them in isolation. Structural cell biology as a discipline aims to study macromolecular complexes within the native cellular environment, seamlessly bridging the resolution gap between structural biology and cell biology.

1.3 Electron microscopy is the core method for visualizing cell structure

The cellular mesoscale remains largely uncharted. This is in no small part because techniques to visualize intact cells at sufficiently high resolution were not widely available until recently. Transmission electron microscopy (TEM) is well-suited to the task because it is able to image samples over a wide range of scales, from individual atoms to whole cells or tissues, but cellular TEM does not come without its challenges. Because electrons scatter strongly in air, the electron microscope needs to be operated under vacuum – a particularly hostile environment for cells, which are composed mostly of water. Furthermore, electrons used for imaging are accelerated to very high energies that are damaging to biological samples, which are inherently radiation-sensitive.

Preparing cellular samples for conventional TEM thus involves "protecting" them through chemical fixation and dehydration. Because electrons need to penetrate the sample in order to generate an image, TEM has a strict thickness limit. Consequently, samples thicker than ~1 μm (for an electron at an accelerating voltage of 300 kV) (Grange et al., 2017) are not suitable for high-resolution TEM. Because most cells are thicker than this, they are often embedded in a block of resin, which is then cut with a diamond knife to obtain thin sections. These sections are then mounted on EM grids and are stained with heavy metals like uranium or lead salts to enhance contrast.

Our modern understanding of cell biology is built on foundations laid by conventional TEM-based structural work (Fawcett and Porter, 1954; Palade, 1953, 1955a,b; Porter et al., 1945). However, the harsh sample preparation methods required can both limit the achievable resolution and introduce artefacts (Dubochet et al., 2007; Pilhofer et al., 2010). For instance, chemical fixation and dehydration can distort fine structure by promoting macromolecular aggregation (Dubochet et al., 2007; Kellenberger and Kistler, 1979). When using heavy metal stains, the signal observed comes from the stain and not from the sample itself; thus, apparent differences in density are caused by differences in the propensity of different biological materials to be stained rather

than by genuine differences in density. Furthermore, achievable resolution is limited to the grain size of the stain, which is why membranes and large assemblies are readily visible in conventional TEM images but most small- or medium-sized proteins are not.

1.4 Cryo-electron tomography enables nanometer resolution imaging of cells in a fully-hydrated, near-native state

The ultimate goal of any imaging method is to capture its subject in a state as close as possible to reality. For cell biology, this translates to imaging cells in a fully-hydrated state, free of chemical fixatives or stains. This is precisely the essence of cryo-EM. Cryo-EM is based on rapid vitrification and subsequent imaging of frozen-hydrated specimens at a temperature so low that water does not evaporate significantly in the microscope vacuum. To prepare samples for cryo-EM, cells are cooled so rapidly that they are frozen before water can rearrange to form crystals, thus trapping them in a glass-like or vitreous state (Dubochet et al., 1982; Lepault and Dubochet, 1986). Small cells can be vitreously frozen simply by rapidly plunging them into liquid ethane or ethane/propane (Tivol et al., 2008) cooled to liquid nitrogen temperatures. However, larger cells need to be frozen under high pressure (Dubochet, 1995) to be uniformly vitrified throughout. Applying high pressure inhibits ice crystal formation by suppressing volume expansion, effectively decreasing the cooling rate required for vitrification and making it practical to vitrify samples up to a few hundred microns thick (Moor, 1987).

Cryo-EM has gained traction in structural biology because of advancements in electron detectors, microscope hardware, and image processing (Glaeser, 2019). In so-called single particle analysis, high-resolution structures of purified proteins can be obtained by averaging many different projection images of individual particles (ideally) randomly oriented in thin, vitreous ice. With parallel advancements in automated data collection and biochemistry, single particle cryo-EM has become a go-to method for biomolecular structure determination.

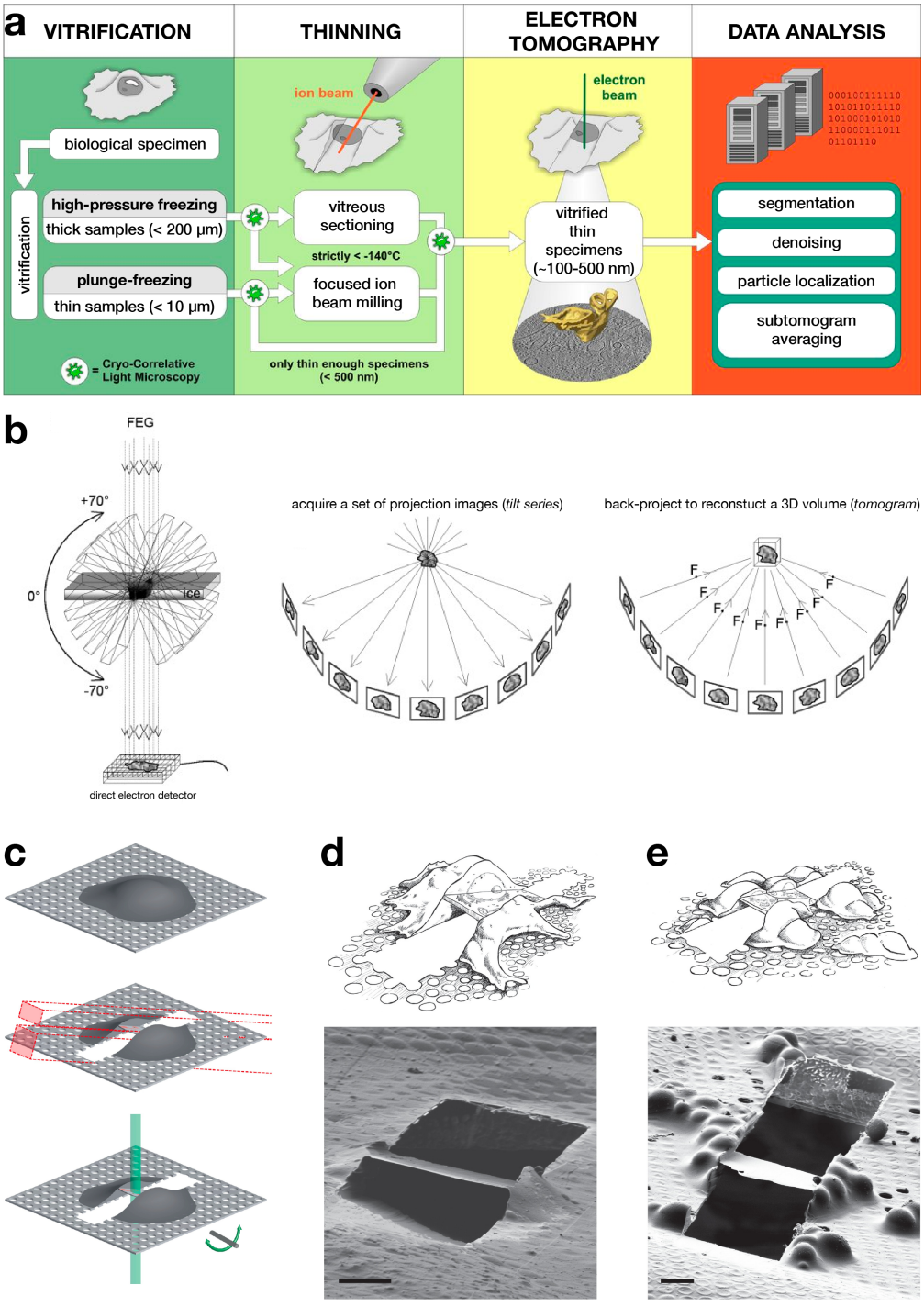


Figure 1.1 | An overview of the cryo-electron tomography (cryo-ET) workflow. (a) The cryo-ET workflow involves sample vitrification, thinning, imaging, and data processing. Figure modified from Lučić et al., 2005. **(b)** Data acquisition involves collecting projection images of a sample as it is gradually tilted relative to the electron beam. The resulting set of projection images is called a tilt series, which can then be computationally aligned and back-projected to yield a three-dimensional volume or tomogram. Figure modified from Grünewald et al., 2003. **(c)** Cryo-FIB milling is an on-grid thinning method that uses a beam of ions to remove material, leaving a thin lamella that can be used for high-resolution imaging. **(d,e)** Sample geometries for milling lamellae through large cells (d) or through clusters of small cells (e). Figures adapted from Villa et al., 2013.

Cellular samples pose distinct challenges that necessitate specialized image acquisition and processing strategies. Cells are extremely complex, and the amount of data needed to characterize an entire cell is immense. Cells are also extremely variable – no two cells look alike under the EM, which precludes direct averaging procedures. As such, the preferred method for cellular EM is cryo-electron tomography (cryo-ET) **(Fig. 1.1)**. In cryo-ET, the sample is gradually tilted in the electron beam and a series of projection images is acquired **(Fig. 1.1b)**. Images in the resulting tilt series are then aligned and back-projected to yield a tomogram **(Fig. 1.1d)**. Because the sample is tilted in discrete angular steps and to a limited overall angular range, such a tomogram is an incomplete three-dimensional reconstruction of the original object. Despite these limitations, cryo-ET can provide high-resolution three-dimensional information on pleiomorphic objects or rare events, all within the context of a fully-hydrated cell. Cryo-ET also provides a uniquely multi-scale capability in that it can resolve membranes and organelles as well as individual protein complexes **(Fig. 1.2)**.

As mentioned above, sample thickness is one of the major challenges for TEM. Since most mammalian cells are thicker than a few microns, direct imaging by cryo-ET is limited to small cells or to the thin peripheries of larger cells. In recent years, cryo-focused ion beam (FIB) milling (Marko et al., 2007; Rigort et al., 2012) has emerged as the method of choice for fine thinning of cellular material without compression artefacts **(Fig. 1.1c)**. Cryo-FIB milling is performed in a dual-beam instrument equipped with both a focused ion beam and a scanning electron microscope (SEM, the hybrid instrument is called a FIB/SEM). In these instruments, ions (typically gallium) are accelerated towards the sample, where they sputter material off of the surface, leaving a thin lamella usually ~150-250 nm thick **(Fig. 1.1d,e)**. SEM is used for overview imaging, targeting, and monitoring the milling process.

Unstained biological material consists mainly of elements with low atomic number, which results in very low contrast in the electron microscope. More recently, however, the Volta phase plate (VPP) has emerged as a method of enhancing contrast (Danev et al., 2014) **(Fig. 1.2a,b)**. The VPP is a heated thin film of amorphous carbon placed in the back-focal plane of the objective lens. When the VPP is irradiated by

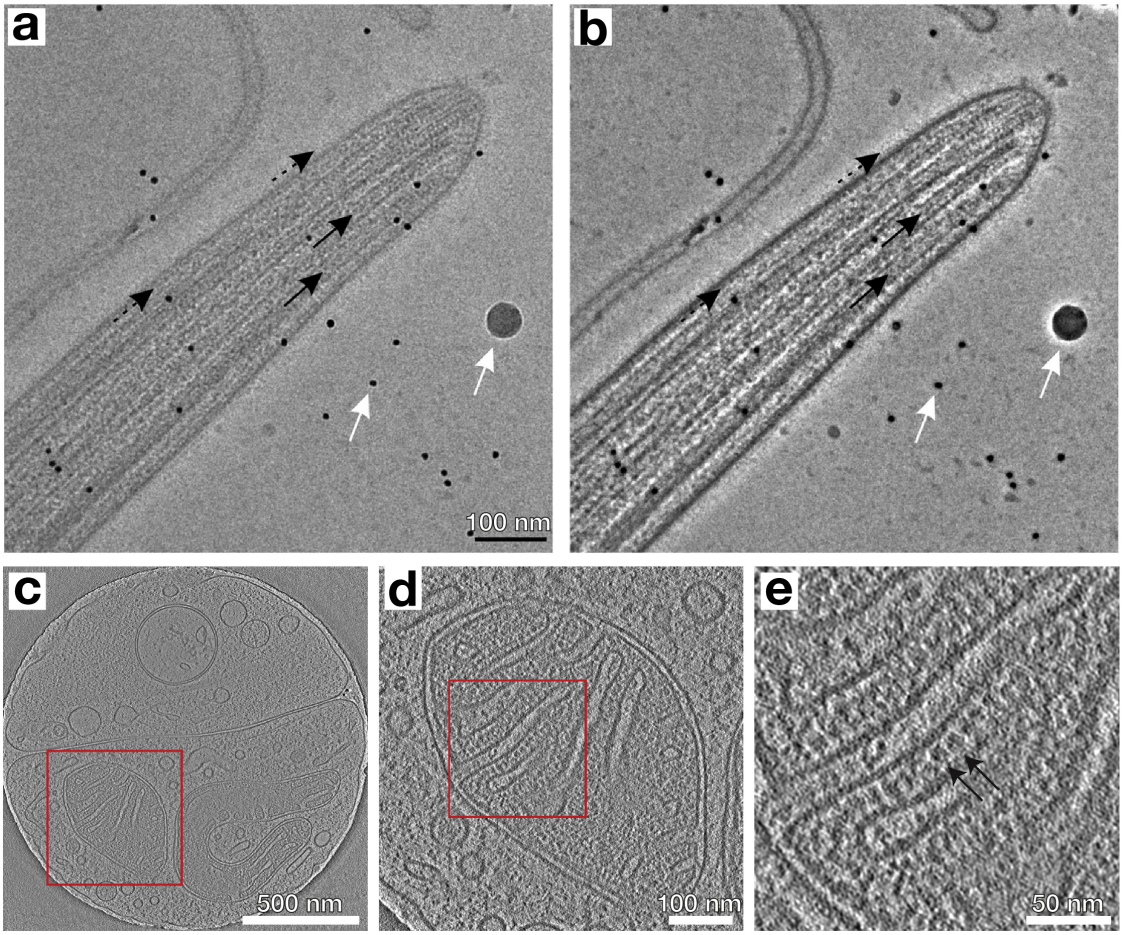


Figure 1.2 | The Volta phase plate (VPP) enhances contrast in cellular tomograms. (a,b) Cryo-EM projection images of the endpiece of an *Ascaris* sperm flagellum collected (a) without the VPP at a defocus of -5 μm and (b) with the VPP close to focus. Panels adapted from Danev et al., 2014. **(c-e)** Slices through VPP cryo-tomograms of a neuronal process, showing how cryo-ET can visualize cellular organization across scales, from subcellular compartments (c) to organelles (d) to macromolecular complexes like ATP synthase (e, arrows). Panels adapted from Fukuda et al., 2015.

the electron beam, its surface potential changes, ultimately resulting in a phase shift between the unscattered and scattered electron beams. This additional phase shift allows high-contrast imaging close to focus, which facilitates the interpretation of cellular tomograms; for instance, using the VPP can make it easier to find target particles in dense compartments such as the mitochondrial matrix (Fukuda et al., 2015) **(Fig. 1.2c-e)**.

Because of the sheer complexity of cellular tomograms, they often need to be annotated or segmented in order to aid interpretation. Segmentation can be performed by

expert annotator manually tracing the structures of interest throughout the tomogram, but as data acquisition becomes faster and more reliable, more efficient ways of segmenting tomograms are also necessary. Deep learning and neural network-based approaches have been developed that greatly facilitate the segmentation process (Chen et al., 2017a; Zeng et al., 2018) **(Fig. 1.3a)**.

When a tomogram contains multiple copies of a given structure, these copies can be aligned and averaged, enhancing signal-to-noise and improving resolution **(Fig. 1.3b)**. This process is known as subtomogram averaging, and has the potential to reach subnanometer resolutions in ideal cases (O'Reilly et al., 2020; Sutton et al., 2020; Tegunov et al., 2020). Although most applications do not reach near-atomic resolutions that are now almost synonymous with single-particle cryo-EM, subtomogram averaging nonetheless yields molecular-resolution maps of proteins or protein complexes that often simply cannot be purified. These maps can then be integrated with information from X-ray crystallography, single-particle cryo-EM, structural mass spectrometry, and molecular dynamics to build multi-scale models of large protein complexes within the cellular environment (O'Reilly et al., 2020; von Kügelgen et al., 2020; Watanabe et al., 2020).

More importantly, however, cryo-ET combines molecular-resolution information with cellular context, which means that different proteins, protein complexes, or even conformational states or assembly intermediates, can be traced back to their positions in the original tomograms. Among others, this has revealed spatial relationships between the nuclear pore complex and the cytoskeleton (Mahamid et al., 2016); between the nuclear pore complex and nuclear-resident proteasomes (Albert et al., 2017); and between proteasomes and the endoplasmic reticulum (Albert et al., 2020). The ability to plot molecular structures back into their cellular locations also revealed relationships between dynein activity states and flagellar bending in sea urchin sperm axonemes (Lin and Nicastro, 2018).

Because cryo-tomograms represent reasonably complete snapshots of cells, the most interesting features of cellular tomograms are often the structures that one does not initially seek out, which are often completely unknown. For instance, a number of

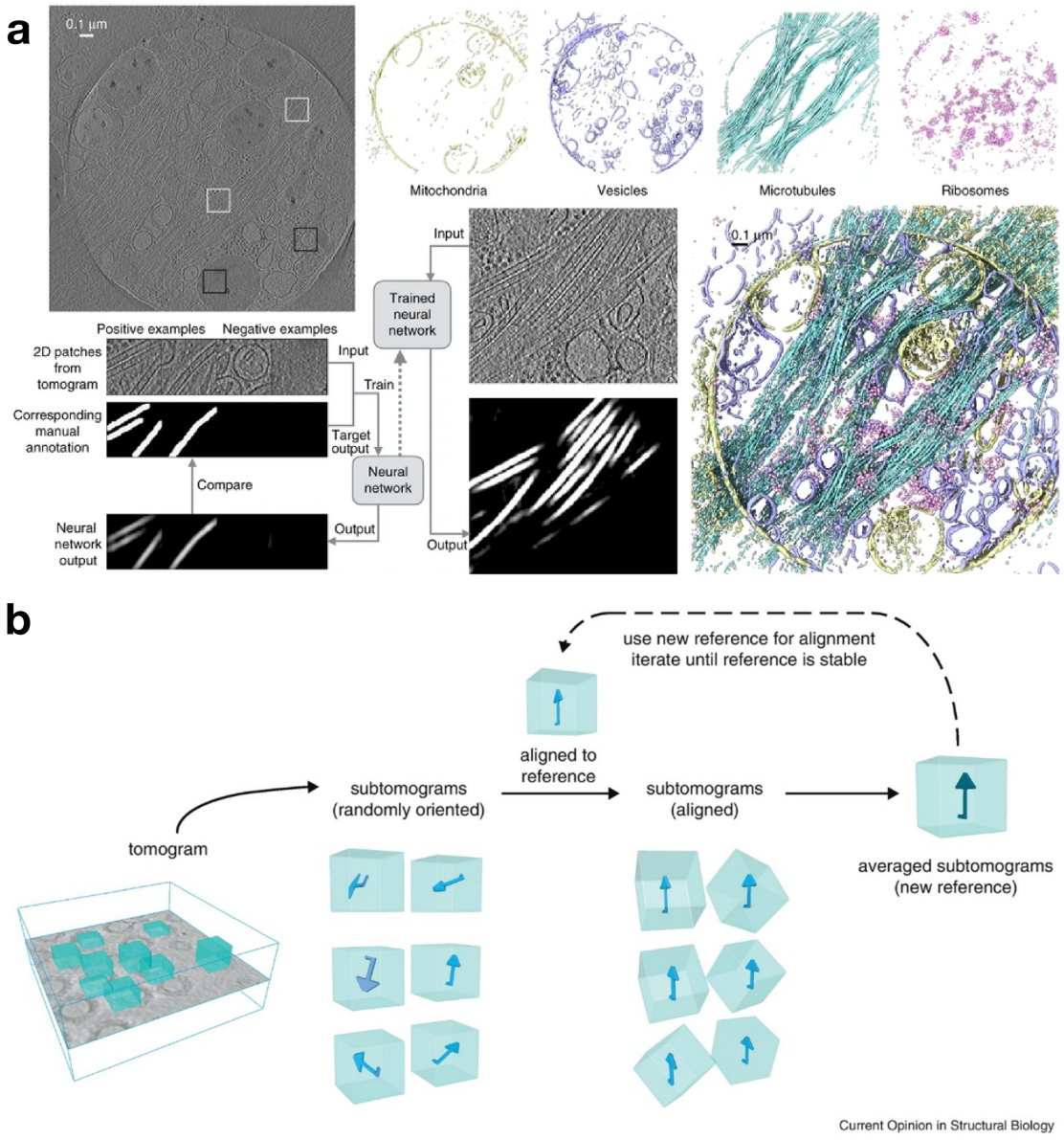


Figure 1.3 | Three-dimensional segmentation and subtomogram averaging can aid analysis and interpretation of cryo-tomograms. **(a)** Because cellular tomograms are complex and crowded, they often need to be annotated or segmented to aid interpretation. Semi-automated neural network-based methods, such as those implemented in the EMAN2 software package, improve throughput and reduce subjectivity. Figure adapted from Chen et al., 2017a. **(b)** When multiple copies of a particular protein or protein complex are present in a tomogram, these can be computationally extracted, aligned, and averaged to enhance signal-to-noise and improve resolution. Figure adapted from Wan and Briggs, 2016.

large structures that are fairly prominent in cryo-tomograms of bacterial cells remain uncharacterized (Dobro et al., 2017). Recently, cellular tomography of coronavirus-infected cells uncovered a large molecular pore spanning the double bilayer of the coronavirus replication organelle; although the precise molecular composition of the pore remains unclear, it provides a structural mechanism by which viral genomes and RNA can be transported into the cytoplasm (Wolff et al., 2020). It was cryo-ET that first revealed that axonemal doublet microtubules contain a novel class of luminal microtubule-binding proteins called microtubule inner proteins (Nicastro et al., 2011, 2006) whose molecular identities are only starting to be defined a decade later (Ichikawa et al., 2019; Ma et al., 2019; Owa et al., 2019). Cellular cryo-ET thus has immense discovery potential, and careful descriptions of novel structures can trigger an avalanche of follow-up research aiming to define their molecular identities.

1.5 Enter the muse: the deceptively simple sperm cell

With these tools in hand, we now focus our microscopes on the sperm cell. Despite its diminutive appearance, the sperm is a highly specialized cell type. Reflecting its singular, defined function – to find and fuse with the egg – a mature sperm cell generally consists of a head, which contains the genetic payload, and a tail, which propels the payload towards its target. Sperm have fascinated biologists since their discovery by none other than van Leeuwenhoek himself (van Leeuwenhoek, 1677), and in the intervening 350 years, both gross morphology and detailed ultrastructure have been described for sperm from hundreds of species. Conventional TEM revealed that sperm are intricately structured **(Fig. 1.4)**, with organelles that adopt specialized sperm-specific configurations, with immense variation across species (Fawcett, 1970, 1975; Mortimer, 2018).

However, despite decades of study, sperm biology remains poorly understood and new structures are constantly being discovered (Chung et al., 2014; Fishman et al., 2018; Zabeo et al., 2018). In this section, I provide an overview of sperm structure with an emphasis on mammalian systems. I summarize the relevant literature, but I also highlight outstanding questions that are ripe for exploration.

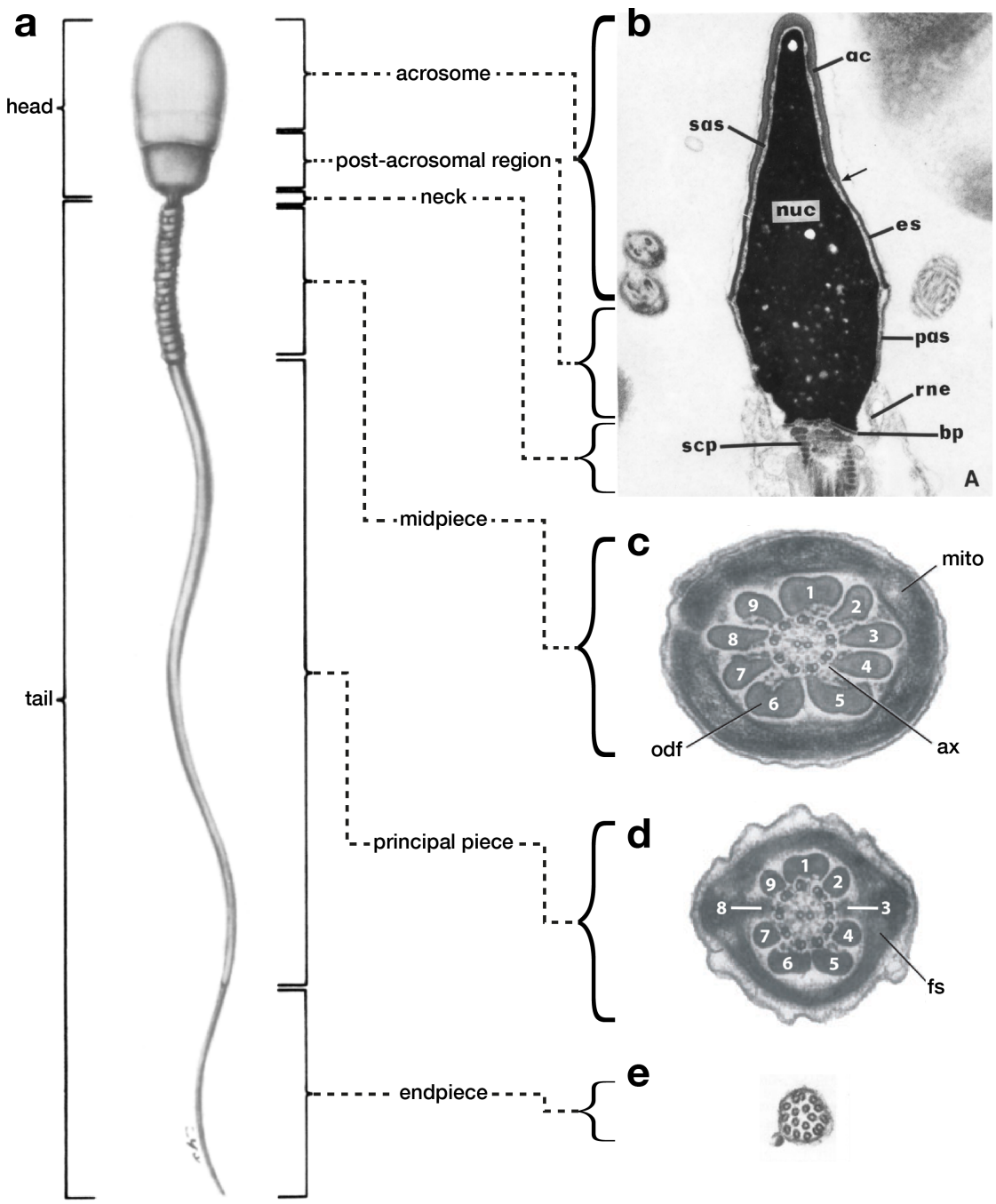


Figure 1.4 | The structural organization of a mammalian sperm cell. (a) A bovine sperm cell drawn as it would be seen under the light microscope. Figure adapted from Fawcett, 1975. **(b-e)** Transmission electron micrographs from conventional heavy metal-stained thin sections of fixed mammalian sperm. **(b)** A sagittal section through the head and neck, adapted from Mortimer, 1994. Labels: ac - acrosome, sas - subacrosomal space (also known as the perinuclear theca), nuc - nucleus, es - equatorial segment, pas - post-acrosomal sheath, rne - redundant nuclear envelope, bp - baseplate, scp - striated columns of the connecting piece. **(c)** A transverse section through the midpiece, adapted from Olson and Linck, 1977. Labels: mito - mitochondria, odf - outer dense fibers (numbered), ax - axoneme. **(d)** A transverse section through the principal piece, adapted from Olson and Linck, 1977. Labels: fs - fibrous sheath. **(e)** A transverse section through the endpiece, adapted from Serres et al., 1984

1.5.1 The head

The sperm head is streamlined and compact. It consists primarily of the nucleus **(Fig. 1.4b)**, which occupies as little as a tenth of the volume of a somatic nucleus. During spermiogenesis, chromatin is compacted through the replacement of histones with highly basic protamines (Johnson et al., 2010; Rathke et al., 2014). No substructure has yet been visualized in intact sperm nuclei, although *in vitro* reconstitution experiments suggest that protamine-packaged chromatin adopts a toroidal structure (Allen et al., 1997; Hud et al., 1993). Sperm chromatin is often punctuated by electron-lucent areas that have been called "nuclear vacuoles" **(Fig. 1.4b)**, which vary greatly in size and shape both across cells within an ejaculate and across sperm from different species (Mortimer, 2018). The precise nature of these "vacuoles" is unclear. In **Chapter 3**, I report novel findings on a macromolecular complex I observe within these regions.

The sperm nucleus is also atypical in that nuclear pore complexes are expunged from most of the nuclear envelope during spermiogenesis. Instead, they are relegated to a specialized domain called the redundant nuclear envelope, which is found in the sperm neck (Ho, 2010). Given that a number of organelles are lost during spermiogenesis, there is much speculation about why the redundant nuclear envelope is retained in mature sperm and what its functions could be. There is growing evidence that it acts as a calcium store (Ho and Suarez, 2003), though it has also been proposed to be a degradation microcompartment for nuclear proteins (Haraguchi et al., 2007).

Overlying the anterior two-thirds of the nucleus is a large vesicle called the acrosome **(Fig. 1.4a,b)**. The acrosome is limited by a single bilayer, but by convention the region facing the nucleus is called the inner acrosomal membrane and the region underlying the plasma membrane is called the outer acrosomal membrane. Most textbooks portray the acrosome as a bag of enzymes that aid sperm penetration through the egg vestments, but the real situation is much more complex. Firstly, the contents of the acrosome appear to be organized into soluble and particulate components (Kim et al., 2005). There are reports of both amyloid-like (Guyonnet et al., 2014) and crystalloid-like (Olson and Winfrey, 1994) properties in the acrosome, but neither of these have been structurally characterized. Secondly, the role of acrosomal

contents in penetrating the zona pellucida is controversial. Mice carrying a targeted disruption that abolishes the activity of acrosin, the major acrosomal protease, are still fertile (Baba et al., 1994). Meanwhile, acrosin-disrupted rat sperm show delayed penetration of the cumulus layer, but still penetrate the zona and go on to fertilize eggs (Isotani et al., 2017). On the other hand, acrosin-knockout hamsters are infertile because they are unable to penetrate the zona (Hirose et al., 2020). In **Chapter 6**, I report the structure of crystalloid components of the acrosomal matrix.

1.5.2 The neck

The sperm neck is the region between the head and the tail **(Fig. 1.5)**. The base of the head, where it anchors to the tail, is called the implantation fossa. Here, the nuclear envelope overlies an electron-dense structure called the baseplate. The baseplate in turn couples to a large cytoskeletal scaffold called the connecting piece, which surrounds the base of the flagellum. Several proteins have been implicated in head-tail coupling, including SPATA6, a pericentriolar matrix protein; SUN5, a nuclear envelope protein; and PMFBP1, a testis-specific protein that localizes to the connecting piece (Shang et al., 2017; Yuan et al., 2015; Zhu et al., 2018). However, the precise nature of sperm-head tail attachment is unclear, owing in part to a lack of three-dimensional structural information on this region. In **Chapter 3**, I shed light on this by reporting a novel supramolecular assembly in the nuclear envelope at the base of the head-tail junction.

Embedded within the connecting piece are the centrioles, which are typically composed of triplet microtubules arranged in a ninefold-symmetric barrel (Loncarek and Bettencourt-Dias, 2018; Winey et al., 2014) **(Fig. 1.6)**. Triplet microtubules consist of a complete 13-protofilament A-tubule, a 10-protofilament B-tubule that shares four additional protofilaments with the wall of the A-tubule, and a 10-protofilament C-tubule that shares four protofilaments with the wall of the B-tubule. Centrioles are found in a wide range of eukaryotic cell types, where they serve dual functions, namely to nucleate a cilium either for motility or sensory functions and to orchestrate cell division (Ross and Normark, 2015) **(Fig. 1.6a)**. Centriole number is tightly

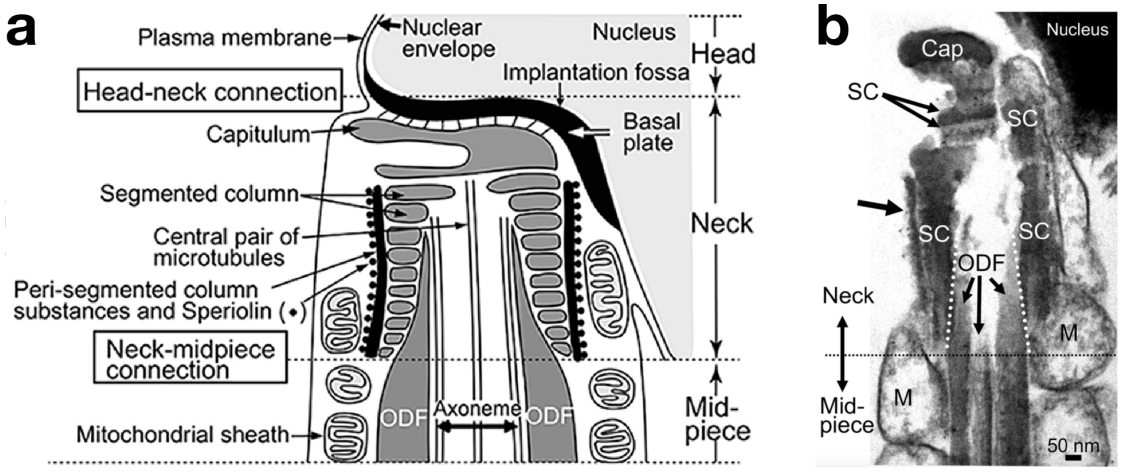


Figure 1.5 | Structural organization of the neck region. (a) Schematic and **(b)** conventional transmission electron micrograph of the neck region of a mouse sperm cell. In (b), labels are: Cap - capitulum, SC - segmented columns, ODF - outer dense fibers, M - mitochondria. Images adapted from Ito et al., 2019.

regulated in dividing cells (Avidor-Reiss et al., 2019); most cells have exactly two centrioles during G1 phase. During S phase, a new centriole is assembled in the immediate vicinity of each centriole, resulting in two pairs of centrioles that are each recruited to and organize one of the mitotic spindle poles. Thus, after mitosis, each daughter cell inherits precisely two centrioles.

Mammalian fertilization involves the fusion of two cells, which raises the problem of how proper centriole number is achieved during early development. In most cases, nature's solution is to eliminate centrioles from the oocyte (Avidor-Reiss and Leroux, 2015; Avidor-Reiss et al., 2019; Manandhar et al., 2005; Schatten, 1994). Centrioles were likely retained in sperm because the evolutionarily ancient role of the centriole is the formation of a cilium, which is critical for the motile gamete (Ross and Normark, 2015). Thus, centrioles are paternally inherited in most lineages (Avidor-Reiss et al., 2019).

However, classical EM revealed that most mammalian sperm possess only a single, structurally typical centriole – called the proximal centriole – and a second, highly degenerated centriole – called the distal centriole (Fawcett and Phillips, 1969) **(Fig. 1.6b-d)**. It was thus thought that mammalian sperm contribute one centriole during fertilization, leaving the origin and the nature of the second centriole a mystery

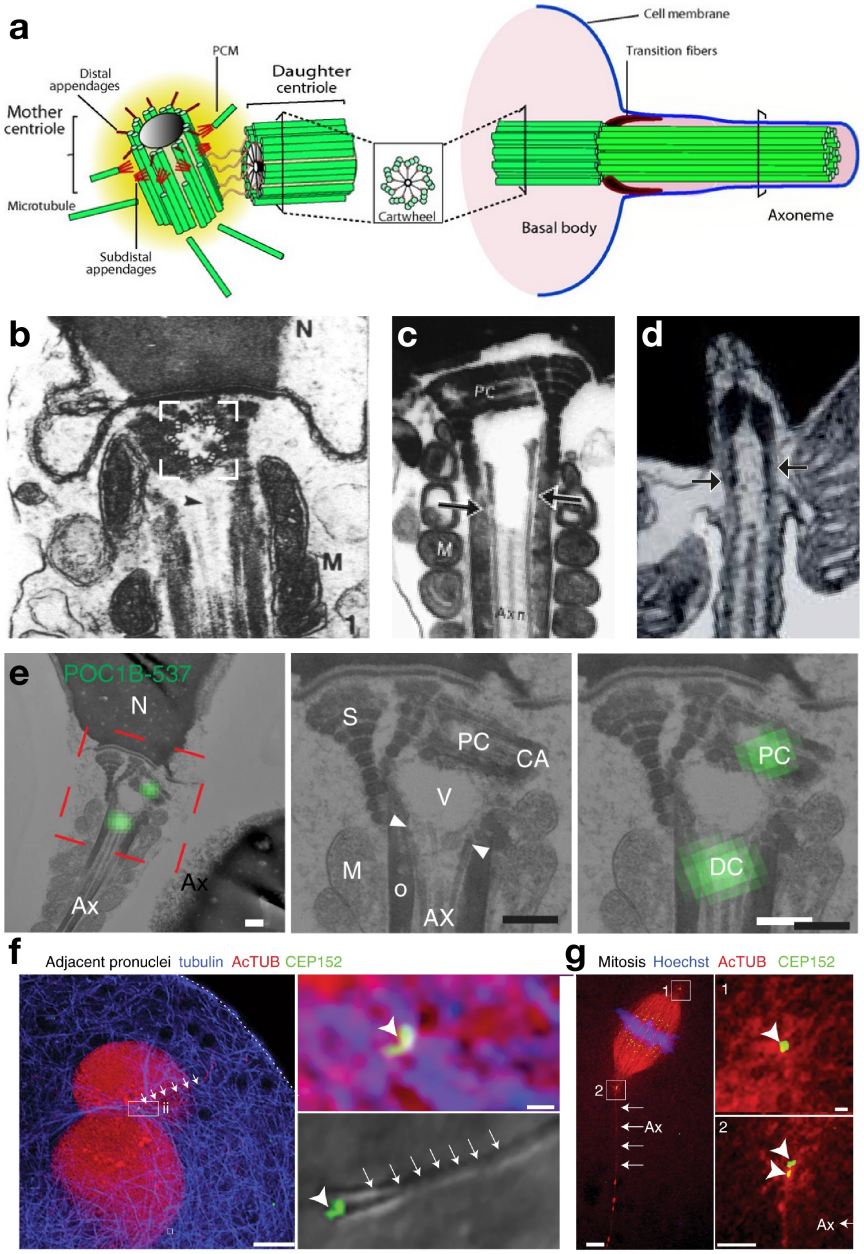


Figure 1.6 | Sperm centrioles represent a unique opportunity to study the structural plasticity of a conserved assembly. (a) Centrioles are comprised of triplet microtubules arranged into a ninefold-symmetric barrel, often around a scaffold called the cartwheel. Centrioles have two major functions in cycling cells, namely to orchestrate cell division (left) and to nucleate the formation of a cilium (right). Figure adapted from Ross and Normark, 2015. **(b, c)** Non-rodent mammalian sperm have one structurally typical centriole (the proximal centriole, PC in panel c) and one atypical centriole (the distal centriole, DC, arrowhead in panel b and arrows in panel c). Panel (b) shows a human spermatozoon and is adapted from Sathananthan et al., 1996 while panel (c) shows a rhesus monkey spermatozoon and is adapted from Manandhar et al., 2000. **(d)** In contrast, the DC does not degenerate in marine invertebrate sperm (arrows). Figure shows an *Arbacia* sperm cell and is adapted from Fawcett, 1970. **(e)** Correlative light and EM shows that the centrosomal protein POC1B labels both the PC and the DC in human sperm. **(f, g)** Fluorescence microscopy shows that the DC is functional during the first mitotic division in bovine zygotes. Panels (e-g) are from Fishman et al., 2018. **Scale bars:** (e) 200 nm, (f, g) left panels - 10 μm, right panels - 1 μm.

(Manandhar et al., 2005; Ross and Normark, 2015; Woolley and Fawcett, 1973). Recent efforts have shown that the distal centriole at the base of the flagellum, once thought to be degenerated based on its atypical structure, is in fact a functional centriole (Fishman et al., 2018) **(Fig. 1.6e-g)**. Structural information on the atypical sperm centriole would yield valuable insight into the architectural plasticity of this organelle. This is particularly important as centriole defects contribute to ciliopathies, to cancer, and potentially to unexplained male-factor infertility (Avidor-Reiss et al., 2019; Schatten, 2011). In **Chapter 5**, I present the molecular organization of sperm centrioles in their native subcellular milieu.

1.5.3 The midpiece

The part of the tail immediately distal to the neck region is called the midpiece **(Fig. 1.4c)**. In mammals, the midpiece is defined by a sheath of mitochondria wrapped into a tight spiral around the flagellum. In contrast, marine invertebrate sperm have only one or a few mitochondria. The overall length of the midpiece, the total number of mitochondria in the sheath, and the arrangement of mitochondria within the sheath all seem to vary across species, but are remarkably consistent within species (Fawcett, 1970, 1975). Furthermore, midpiece length is heritable (Woolley and Beatty, 1967) and appears to correlate positively with sperm swimming ability (Fisher et al., 2016).

Although the first instinct is to associate mitochondria with energy generation, the extent to which sperm motility is powered by ATP from mitochondrial respiration is controversial. The controversy arises because mammalian sperm flagella are extremely long, which represents a significant hurdle for efficient ATP distribution along the tail (Takao and Kamimura, 2008). An energy-buffering creatine kinase shuttle akin to that in vertebrate muscle is present in sea urchin sperm (Tombes and Shapiro, 1987; Yeung et al., 1996), but creatine kinase is absent from boar and bull sperm (Kamp et al., 1996), has very low activity in human sperm (Yeung et al., 1996), and is dispensable for fertility in mouse sperm (Steeghs et al., 1995). While mitochondrial respiration is the only pathway for ATP production in sea urchin sperm, the glycolytic pathway is also active in mammalian sperm. Energy for mammalian sperm motility is

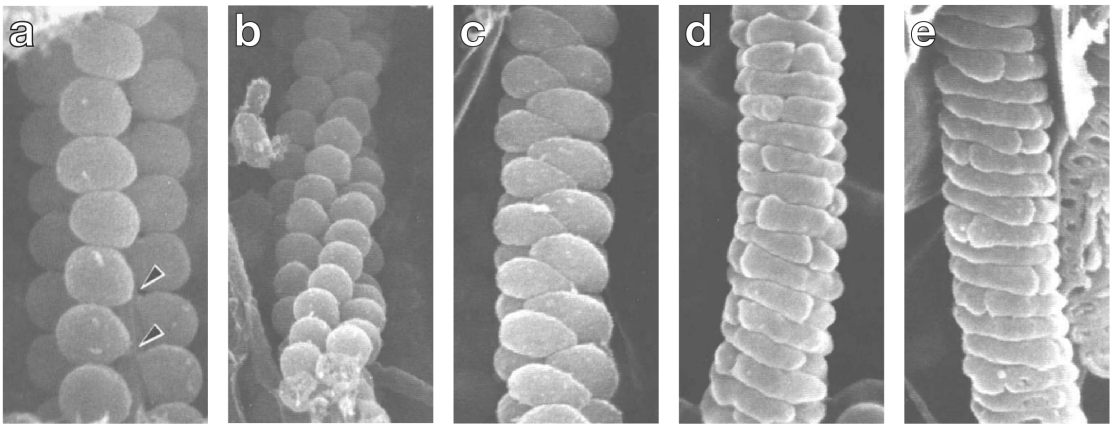


Figure 1.7 | Morphogenesis of the mitochondrial sheath in mouse spermatids. (a-e) Scanning electron micrographs of mitochondrial sheath morphogenesis in mouse testes. **(a)** First, spherical mitochondria are recruited from the cytoplasm to the flagellum, where they form orderly rows. **(b)** These rows then twist around the axoneme, **(c)** then individual mitochondria elongate and **(d)** wrap around each other. **(e)** As a result, sperm mitochondria form a tight helix around the axoneme. Images adapted from Otani et al., 1988.

likely derived both glycolysis and mitochondrial respiration (Balbach et al., 2020), but the relative contributions from each vary across taxa (Cardullo and Baltz, 1991; Davila et al., 2016; Marin et al., 2003; Mukai and Okuno, 2004). However, there is very little information about the internal organization of sperm mitochondria and how this might relate to differences in sperm metabolism.

Our knowledge of how the mitochondrial sheath assembles comes primarily from conventional TEM of developing mouse spermatids (Ho and Wey, 2007; Otani et al., 1988; Pleuger et al., 2020) **(Fig. 1.7)**. In round spermatids, spherical mitochondria are broadly distributed in the cytoplasm. Mitochondria are then recruited to the flagellum in elongating spermatids, where they form ordered rows along the flagellar axis. Finally, mitochondria elongate and twist around the axoneme, forming the mitochondrial sheath. There is strong evidence for kinesin-based microtubule transport in the initial recruitment of mitochondria to the flagellum (Zhang et al., 2012), but the later steps of mitochondrial positioning, elongation, and coiling are much more poorly understood. Three-dimensional stochastic optical reconstruction microscopy recently identified an actin-containing helical super-assembly in the mouse sperm midpiece (Gervasi et al., 2018), which is intriguing because the actin cytoskeleton is also involved in mitochondrial immobilization in yeast, in cultured plant cells, and in neurons (Boldogh

and Pon, 2006; Moore and Holzbaur, 2018). Thus, from a fundamental cell biological perspective, the sperm mitochondrial sheath represents a unique opportunity to study the molecular mechanisms of mitochondria-cytoskeleton interactions. In **Chapter 4**, I present a comparative analysis of mitochondrial organization in sperm from three mammalian species. I show that mitochondrial size and internal ultrastructure vary across species, but that attachment to the cytoskeleton seems to be mediated by conserved macromolecular complexes.

1.5.4 The tail

The sperm tail is essentially a modified motile cilium. Motile cilia, also called flagella, are evolutionarily ancient microtubule-based organelles used by a wide range of single-celled eukaryotes and metazoan cell types to either propel themselves through fluid or to move fluid across their surfaces. As a testament to their ubiquitous roles in cell physiology, ciliary defects cause a range of human diseases. Such pathologies, known collectively as ciliopathies, include chronic respiratory infections, polycystic kidney disease, craniofacial abnormalities and hydrocephaly, and infertility (Lin et al., 2014b; Wallmeier et al., 2020).

The core of the motile cilium is a continuous assembly of compound microtubules whose general architecture is highly conserved across broad swaths of the eukaryotic tree. The base of the cilium is the centriole or basal body, which is a specialized term for a centriole that has nucleated a cilium. The A- and B-tubules of the basal body elongate to form the axoneme, which consists of nine doublet microtubules arrayed radially around a pair of singlets (the 9 + 2 arrangement) **(Fig. 1.8a,f)**. Doublet microtubules consist of a 13-protofilament A-tubule and a 10-protofilament B-tubule, which together anchor a plethora of accessory proteins including thousands of copies of the molecular motor protein dynein **(Fig. 1.8a)**.

Axonemal accessory proteins are arranged on microtubule doublets to form 96-nm structural repeats **(Fig. 1.8a-c)**. The molecular architecture of the 96-nm repeat was first defined by cryo-ET of *Chlamydomonas* flagella and sea urchin sperm (Nicastro et al., 2006). Within each 96-nm unit, dyneins are arranged into two rows on the

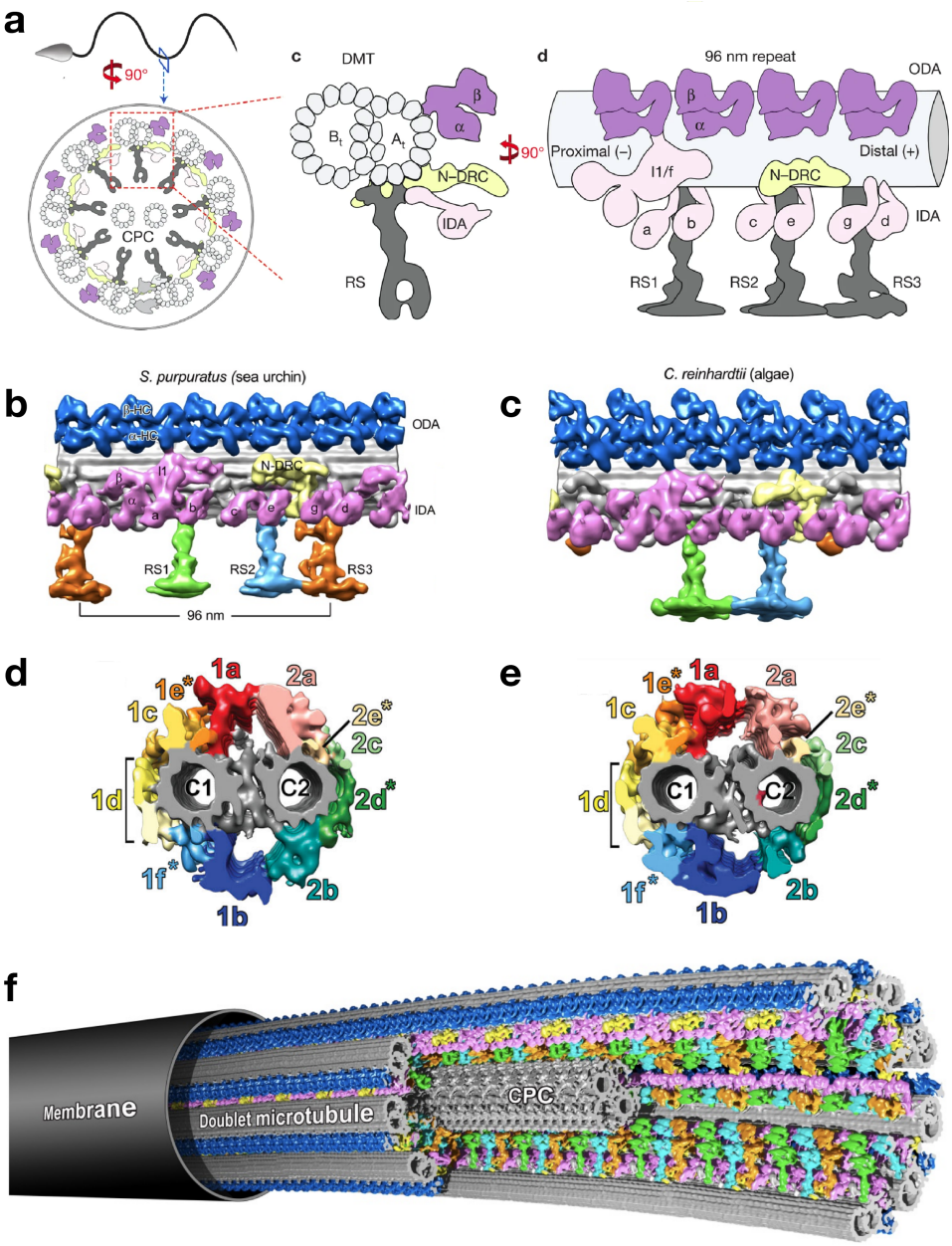


Figure 1.8 | The molecular architecture of the axoneme. Axoneme structure has been studied extensively by cryo-electron tomography, although only in a handful of cell types. **(a)** (left panel) Sea urchin sperm flagella consist of the axoneme surrounded by the plasma membrane. The axoneme has a characteristic 9 + 2 arrangement consisting of nine microtubule doublets arrayed around the central pair apparatus. (right panel) The microtubule doublet (DMT) anchors two rows of dynein arms (outer dynein arms, ODA and inner dynein arms, IDA), the nexin-dynein regulatory complex (N-DRC), and radial spokes (RS1, RS2, RS3). Figure adapted from Lin et al., 2014a. **(b, c)** The overall architecture of the 96-nm doublet repeat is conserved, but metazoans (b) have two-headed ODAs and three radial spokes as opposed to *Chlamydomonas* (c), which has three-headed ODAs and two radial spokes. Figures adapted from Lin and Nicastro, 2018. **(d, e)** The overall architecture of the central pair apparatus is conserved, but there are subtle differences such as the presence of microtubule inner proteins in *Chlamydomonas* (e) but not in sea urchin sperm (d). Images adapted from Carbajal-González et al., 2013. **(f)** An artistic representation of the axoneme, adapted from Lin and Nicastro, 2018.

A-tubule called the inner and outer dynein arms. The outer dynein arms (ODAs) repeat every 24 nm and consist of bundles of two (in metazoans and *Trypanosoma*) or three (in *Chlamydomonas* and *Tetrahymena*) motor domains stacked parallel to one another. The inner dynein arms (IDAs) represent seven different complexes that, together, repeat every 96 nm. Six of the IDAs have a single motor domain and one has two motor domains (called the I1 dynein). Each dynein motor domain extends into a stalk domain, which ends in a microtubule-binding domain that contacts the B-tubule of the neighboring doublet.

In addition to the dynein arms, doublets are connected by the nexin complex, also called the dynein regulatory complex (the N-DRC) (Heuser et al., 2009) **(Fig. 1.8a-c)**. By providing physical resistance to sliding, the N-DRC cross-bridge converts sliding motion from dyneins walking along the neighboring doublet into a bending motion. The N-DRC is also thought to be a major regulatory hub that coordinates dynein activity through signalling, but the precise nature of these signals is unclear.

The inner side of each doublet (that is, the side facing the center of the axoneme) is characterized by large T-shaped assemblies called radial spokes (RSs). In most organisms there are three RSs within every 96-nm repeat, although *Chlamydomonas* only has two RSs per repeat (Pigino et al., 2011) **(Fig. 1.8b,c)**. The overall structure of the RSs is similar, but each one has a distinct protein composition and occupies a defined position along the 96-nm repeat. From the proximal end of the repeat, the three RSs are designated RS1, RS2, and RS3. RS1 and RS2 are spaced 32 nm apart, while RS2 and RS3 are spaced 24 nm apart. Each RS extends ~43 nm from the A-tubule surface, and consists of a base, a stalk, a neck, and a head. The RSs are involved in regulating dynein activity, and the base of each RS makes physical contacts with the IDAs.

Beyond direct interactions with the IDAs, the RSs are thought to regulate ciliary motility through mechanosensory interactions with the central pair apparatus (CPA) (Oda et al., 2014). The CPA is found at the center of the axoneme and consists of two singlet microtubules ensheathed by numerous accessory proteins. Cryo-ET of purified *Chlamydomonas* and sea urchin sperm axonemes revealed that the

accessory proteins form an extensive, inter-connected, and markedly asymmetric network (Carbajal-González et al., 2013) **(Fig. 1.8d,e)**. The CPA microtubules are designated C1 and C2, and each one anchors a biochemically and structurally distinct set of projections. Mutations in the protein hydin, which localizes to the C2 projection network, cause motility defects in both *Chlamydomonas* and mice (Lechtreck et al., 2008). This suggests that CPA architecture is highly conserved; indeed, structures of *Chlamydomonas* and sea urchin sperm CPAs are very similar (Carbajal-González et al., 2013). It must be noted, however, that these are also the only two CPA structures available.

Cryo-ET revealed that the luminal surfaces of microtubule doublets are decorated with a novel class of proteins called microtubule inner proteins (MIPs) (Nicastro et al., 2011, 2006). MIPs have since been identified in centrioles and basal bodies (Greenan et al., 2018, 2020; Guichard et al., 2013), suggesting that they are ubiquitous features of the ciliary cytoskeleton. Although the functions – and even identities – of MIPs are unclear, at least some MIPs contribute to maintaining the integrity and stability of doublet microtubules (Owa et al., 2019). However, some MIPs are only present on specific doublets, conferring asymmetry on the axoneme at the molecular level and hinting that MIPs have a function beyond simply stabilizing doublets (Nicastro et al., 2011). Recent high-resolution structures of purified doublets revealed that MIPs form an intricate network that weaves through the tubulin backbone (Ichikawa et al., 2019, 2017; Khalifa et al., 2020; Ma et al., 2019), which suggests that MIP binding may functionalize the outer surface of doublet microtubules to promote binding or unbinding of other accessory proteins. Although these structures pave the way for mapping specific proteins onto MIP densities, the purification procedures used to prepare axonemal doublets for single particle cryo-EM also resulted in loss of all the external and some internal accessory proteins (Ichikawa et al., 2017; Song et al., 2020). In **Chapter 5**, I present in-cell molecular structures of axonemal doublets and central pair apparatuses from three mammalian species, revealing novel radial spoke accessories and protofilament-bridging MIPs that have so far only been seen in mammalian sperm.

1.5.5 Accessory structures of the mammalian sperm flagellum

The general structure of the axoneme described in the preceding section is conserved across a wide range of organisms and cell types. However, ciliated cells function in a diverse array of fluid environments and their cilia likewise show large variations in waveform (Khan and Scholey, 2018). The quest to understand fundamental mechanisms governing ciliary function would benefit greatly from understanding how variations in motility arise from underlying structural modifications – a goal that is hampered by the fact that detailed structural studies of motile cilia have been limited to a handful of species and cell types.

Sperm represent perhaps the most striking example of ciliary diversity across species (Lüpold and Pitnick, 2018; Pitnick et al., 2009), reflecting the sheer range of reproductive modes and fertilization arenas, from watery media for marine invertebrates and freshwater species to the viscous fluids of the female reproductive tract for mammals. Because motility is crucial to sperm function, natural variations of sperm form present unique opportunities to understand the structural diversification of motile cilia. For instance, mammalian sperm flagella are characterized by large accessory structures that surround and often dwarf the axoneme (Fawcett, 1975) **(Fig. 1.4, Fig. 1.9)**, in stark contrast to marine invertebrate sperm whose tails consist essentially of the axoneme surrounded by the plasma membrane (Fawcett, 1970). Accessory structures are proposed to stabilize beating of the long flagella of mammalian sperm and to facilitate movement of these cells through the viscous fluids of the female reproductive tract (Gadêlha and Gaffney, 2019; Lindemann and Lesich, 2016) **(Fig. 1.9b,c)**. Indeed, many cases of male infertility are linked to defects in these accessory elements (Haidl et al., 1991; Serres et al., 1986; Zhao et al., 2018). However, to date, there is very little structural information on how the accessory structures interact with the axoneme proper.

Axonemal doublets are associated with outer dense fibers (ODFs) for most of their lengths (the 9 + 9 + 2 arrangement) **(Fig. 1.4c,d, Fig. 1.9a)**. The ODFs were initially thought to be active contractile elements, but isolation and biochemical characterization of the ODFs rendered this view untenable (Fawcett, 1975). Instead,

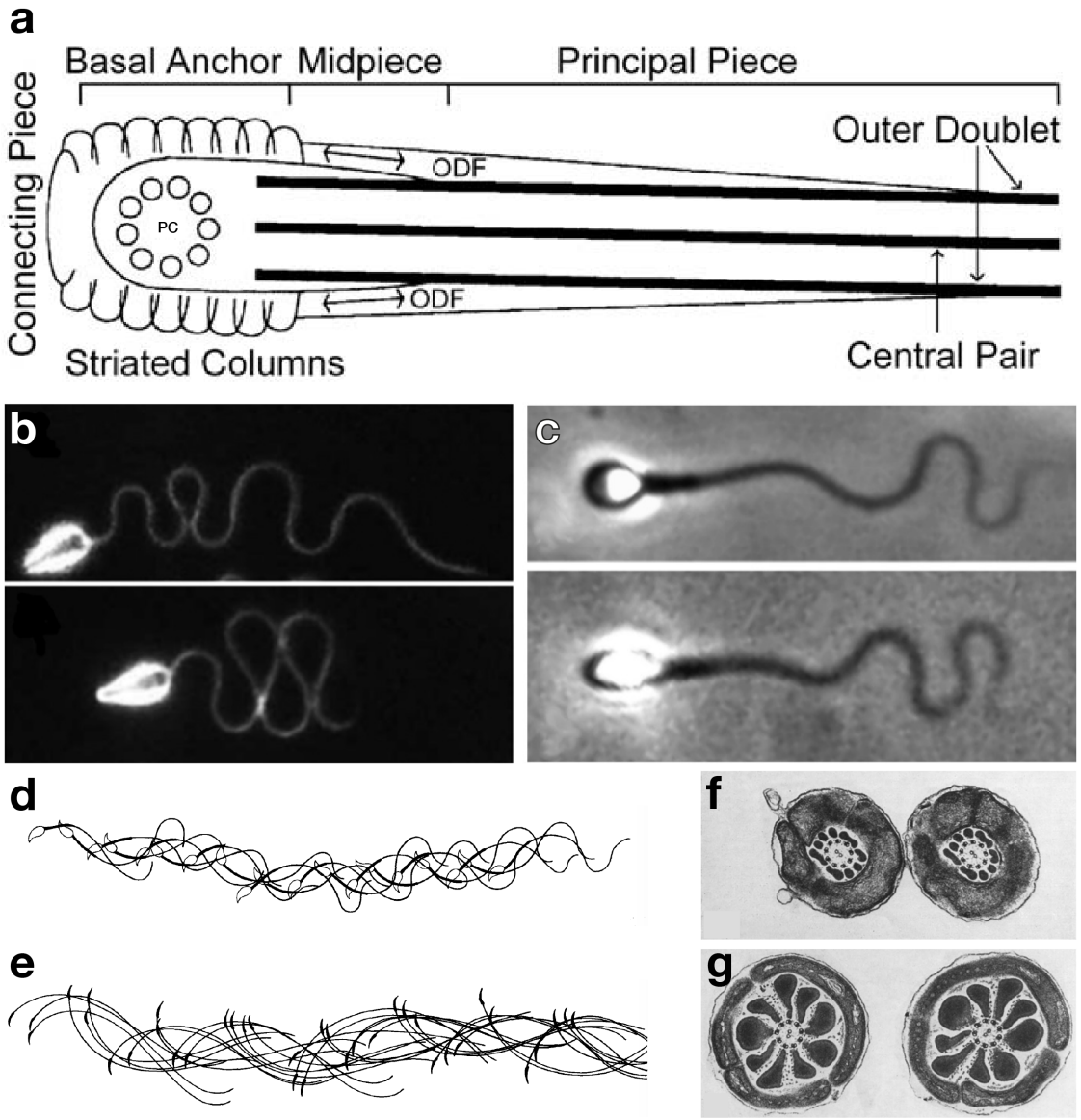


Figure 1.9 | Mammalian sperm flagella are characterized by large accessory structures. **(a)** Outer dense fibers are associated with microtubule doublets along most of the flagellum, and are anchored at the base via the connecting piece. Labels: PC - proximal centriole, ODF - outer dense fibers. Image adapted from Lindemann and Lesich, 2016. **(b, c)** Micrographs of sea urchin (b) and human (c) sperm swimming in low viscosity (top panels) or high viscosity (bottom panels) methycellulose solutions. Note that the sea urchin sperm flagellum exhibits wave compression in high viscosity. Image is reproduced from Gadêlha and Gaffney, 2019, but panels (b, c) are originally from Woolley and Vernon, 2001 and Smith et al., 2009 respectively. **(d, e)** Tracings of mouse (d) and Chinese hamster (e) sperm from film recorded at 300 frames/s and 150 frames/s respectively. **(f, g)** Electron micrographs of transverse sections through midpieces of mouse (f) and Chinese hamster (g) sperm. Note the correlation between radius of flagellar curvature in (d,e) and cross-sectional area of ODFs in (f,g). Panels reproduced from Phillips, 1972.

the ODFs are composed of a number of proteins stabilized by extensive disulfide cross-links (Petersen et al., 1999; Zhao et al., 2018). Thus, the ODFs seem to act as structural scaffolds that stiffen mammalian sperm flagella, possibly protecting them from shear forces encountered during ejaculation (Baltz et al., 1990). The accessory structures also facilitate movement through the viscous fluids of the female reproductive tract by suppressing buckling instabilities that would otherwise cause sperm to swim in circles (Gadêlha and Gaffney, 2019). Comparative studies of mammalian sperm motility found that sperm flagella with larger ODFs formed arcs with larger radii of curvature, revealing a role for the ODFs in modulating the flagellar beat (Phillips, 1972) **(Fig. 1.9d-g)**.

Beyond their passive stiffening effects, ODFs likely play an important role in sperm motility by virtue of their continuity with the connecting piece at the base of the flagellum **(Fig. 1.9a)**. In this manner, forces from axoneme bending would be transmitted to the base of the flagellum via the ODFs; likewise, sliding at the base would be transmitted distally (Lindemann, 1996; Lindemann and Lesich, 2016). Cryo-ET of the isolated bovine sperm connecting piece revealed that it is a large, intricate, asymmetric structure (Ounjai et al., 2012), but the purification procedures resulted in loss of the centrioles. Understanding precisely how the ODFs and the connecting piece modulate the flagellar beat hinges on defining if and how these structures interact with the microtubule-based assemblies of the axoneme – information that is still missing from the literature. In **Chapter 5**, I use cryo-ET to unveil how precisely the ODFs interact with axonemal microtubules, how these interactions vary along the flagellum, and how they are anchored at the base of the tail.

In the midpiece, the axoneme-ODF complex is further surrounded by the mitochondrial sheath **(Fig. 1.4c)**. Distal to this, the axoneme-ODF complex is instead surrounded by a reticular structure called the fibrous sheath, whose extent defines the principal piece. Both the mitochondrial sheath and the fibrous sheath are proposed to constrain movement of the axoneme-ODF complex; they may function analogously to retinacula, which are bands of connective tissue that hold tendons of the wrist and ankle in place (Lindemann and Lesich, 2016).

The fibrous sheath consists of two thick longitudinal columns associated with doublets 3 and 8, which are bridged by thinner circumferential ribs (Fawcett, 1975) **(Fig. 1.4d)**. This asymmetry is thought to limit movement in the plane of the longitudinal columns. However, biochemical characterization of the fibrous sheath revealed that it forms a scaffold for a number of proteins involved in signalling and metabolism (Eddy et al., 2003). The major constituents of the fibrous sheath are the A-kinase anchoring proteins (AKAP) AKAP4 and AKAP3 (Carrera et al., 1994). AKAPs bind to cyclic AMP(cAMP)-dependent protein kinases (PKAs), tethering them close to their substrates and in specific subcellular locations (Smith et al., 2017, 2013). Indeed, AKAP-PKA tethering is implicated in regulating the functional maturation of mammalian sperm (Stival et al., 2018). The fibrous sheath also tethers a number of metabolic enzymes involved in glycolysis, including sperm-specific isoforms of glyceraldehyde 3-phosphate dehydrogenase (GAPDH-S), phosphoglycerate kinase, and lactate dehydrogenase (Krisfalusi et al., 2006; Miki et al., 2004). As discussed earlier, mammalian sperm depend on both mitochondrial respiration and glycolysis to provide enough ATP for their long flagella. In some species, glycolysis seems to contribute a larger portion of this ATP; for instance, sperm from mice deficient in GAPDH-S have only ~10% of the ATP content of sperm from wild-type mice (Miki et al., 2004). Structural studies of the fibrous sheath and how it scaffolds and organizes various signalling and metabolic pathways are clearly warranted.

1.5.6 The endpiece

At the end of the principal piece, the axoneme loses its characteristic 9 + 2 structure, marking the transition to the endpiece. The endpiece consists mainly singlet microtubules ensheathed by the plasma membrane **(Fig. 1.4e)**. Recent cryo-ET work on human and bovine sperm showed that axonemal doublets can split into two complete singlets (Zabeo et al., 2019), which raises the question of how partial B-tubules can close to form full 13-protofilament singlets. The same group used subtomogram averaging to show that human sperm endpiece singlets contain a novel, helical MIP (Zabeo et al., 2018), whose identity and function remain enigmatic. Importantly,

microtubules in the endpiece lack the accessory proteins of the axoneme proper, such as dynein arms and radial spokes, which means that there is likely no active sliding or bending in the most distal part of the sperm tail. Mathematical modelling showed that the presence of an inactive region actually facilitates forward propulsion through viscous media (Neal et al., 2020). These models also predict an optimum length for the endpiece relative to the overall length of the sperm flagellum, motivating comparative studies of endpiece organization across species.

1.5.7 Functional maturation of mammalian sperm

Mammalian sperm must reside in the female reproductive tract for a few hours before they gain the ability to fuse with the egg. During this period, sperm undergo a series of biochemical and morphological changes collectively called capacitation (Austin, 1951; Chang, 1951). Efforts to formulate defined media that could support capacitation *in vitro* ultimately led to the first successful attempts at *in vitro* fertilization (Bavister, 1973; Edwards et al., 1969; Norman et al., 1960; Steptoe and Edwards, 1978; Yanagimachi and Chang, 1963). Despite this practical success, our understanding of the basic biology of sperm functional maturation is far from complete.

There are a multitude of biochemical pathways and signalling cascades involved in sperm capacitation (Aitken and Nixon, 2013; Puga Molina et al., 2018). Capacitation involves the removal of membrane-stabilizing proteins called decapacitation factors and the efflux of cholesterol (Nixon et al., 2020), which conceptually represents a reversal of the membrane stabilization that occurs in the epididymis (Bedford, 2014; Bedford, 1983). The major molecular pathway involves an increase in intracellular Ca^{2+} and HCO_3^-, which stimulate soluble adenylyl cyclase. Adenylate cyclase converts ATP to cAMP, which activates PKA and inhibits serine/threonine phosphatases, leading to a massive phosphorylation cascade. This pathway also leads to cytosolic alkalization and to membrane hyperpolarization, which are thought to promote sustained elevation of intracellular Ca^{2+} (Darszon et al., 2011). The cumulative results of these pathways are two major changes to sperm physiology: hyperactivation, which describes the transition to high-amplitude asymmetric flagellar beating that allows sperm to detach

from the oviductal epithelium and to initiate their final transit towards the egg; and the acrosome reaction, a unique membrane remodelling event that results in the vesiculation of the acrosome and overlying plasma membrane, concomitant with the release of acrosome contents.

Both hyperactivation and the acrosome reaction are prerequisites for fertilization. Hyperactivation is required for sperm to penetrate the zona pellucida (Suarez, 2008), whereas the acrosome reaction is an absolute requirement for fusion with the egg (Yanagimachi, 1981). Although the original definition of capacitation included hyperactivation and the acrosome reaction (Chang, 1984; Gervasi and Visconti, 2016), an opposing view considered capacitation and the acrosome reaction as separate processes, with acrosome-intact sperm being "induced" to acrosome-react by binding to the zona pellucida (Gadella, 2008). However, the latter view is challenged by recent evidence that, at least in mouse, most sperm acrosome-react before encountering the zona pellucida (Jin et al., 2011). Furthermore, acrosome-reacted sperm are capable of penetrating the zona pellucida and go on to fertilize eggs (Inoue et al., 2011). More recently, *in vivo* imaging revealed that most mouse sperm acrosome-react even before entering the vicinity of the oocyte (Hino et al., 2016; La Spina et al., 2016; Muro et al., 2016).

The acrosome reaction is itself a fascinating but deeply mysterious phenomenon. Conventional TEM revealed that the acrosome reaction is a dramatic morphological change involving fusion of the outer acrosomal membrane with the overlying plasma membrane at multiple points (Nagae et al., 1986; Russell et al., 1979). Unlike neuronal exocytosis, in which fusing membranes are recycled, during the acrosome reaction the fusing membranes are shed as vesicles **(Fig. 1.10a-d)**. Thus, sperm lose the entire anterior two-thirds of their plasma membrane, and yet the cell remains intact and in the process the remaining plasma membrane somehow acquires fusogenic capacity. Indeed, mammalian sperm only fuse with eggs via this region of the plasma membrane, also known as the equatorial or post-acrosomal region (Talbot and Chacon, 1982; Tsuiki et al., 1986) **(Fig. 1.10d)**. This immediately raises two fundamental questions: How is sperm integrity maintained throughout such a dramatic vesiculation

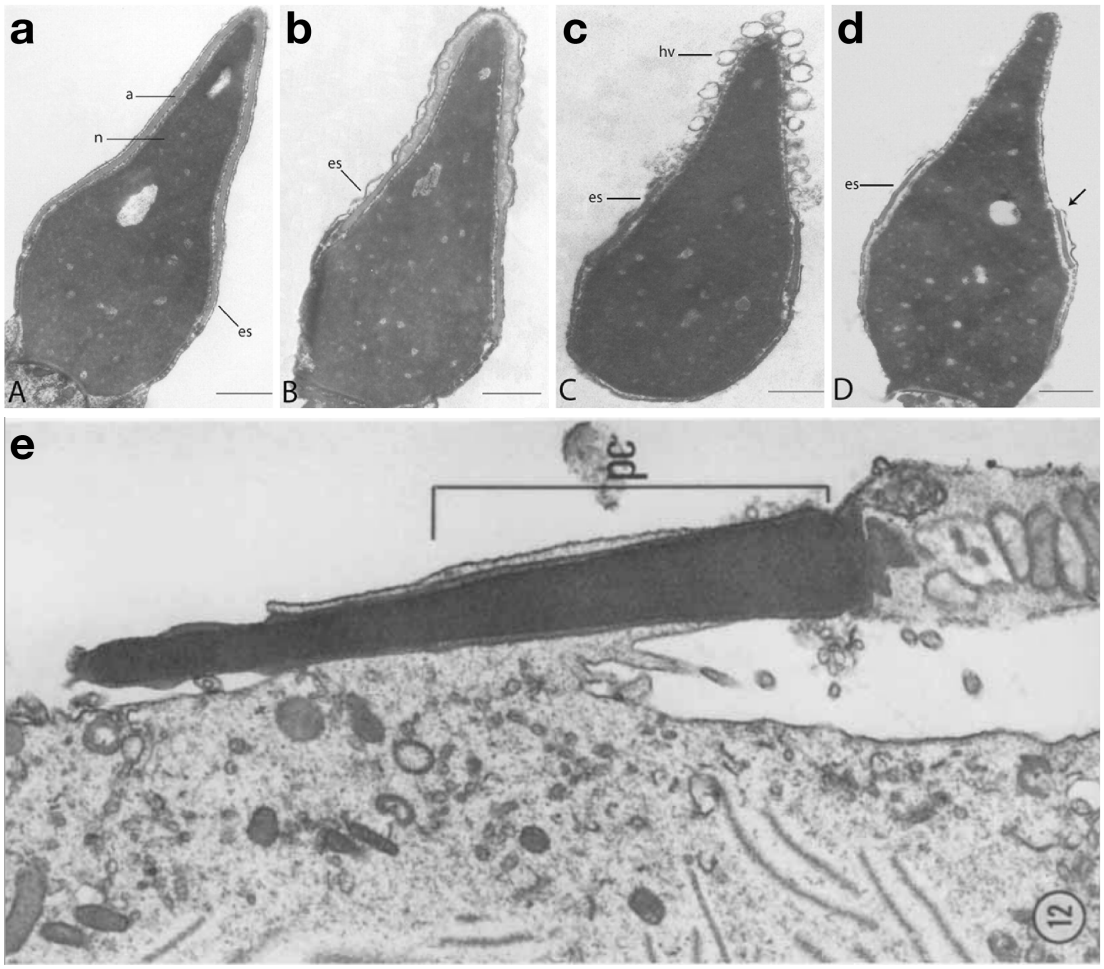


Figure 1.10 | The acrosome reaction is a dramatic membrane remodeling event that prepares the sperm for fusion with the egg. (a-d) Sagittal sections through human sperm in various stages of a calcium ionophore-stimulated acrosome reaction, namely: **(a)** a sperm cell with an intact acrosome, **(b)** a sperm cell with a swollen acrosome, **(c)** a sperm cell with a reacted acrosome that has been shed as vesicles, and **(d)** a reacted sperm cell showing how the plasma membrane over the equatorial and post-acrosomal regions remains intact (arrow). Images from Zanetti and Mayorga, 2009. Labels: n - nucleus, a - acrosome, es - equatorial segment, hv - hybrid vesicles. **(e)** Transmission electron micrograph of sperm-egg fusion in the golden hamster, showing how fusion involves the unreacted plasma membrane of the sperm. Label: pc - post-nuclear cap (post-acrosomal) region. Image adapted from Yanagimachi and Noda, 1970.

process? How does the acrosome reaction change the remaining plasma membrane to render it fusogenic? In **Chapter 6**, I revisit the question of how capacitation-associated membrane modifications lead to the acrosome reaction and ultimately to the acquisition of fusion competence.

2

Materials and Methods

Contents

2.1 Sperm preparation 34
2.1.1 Pig sperm 34
2.1.2 Horse sperm 35
2.1.3 Mouse sperm 35
2.1.4 Bovine sperm 36
2.2 Cryo-ET grid preparation 36
2.3 Cryo-focused ion beam milling 38
2.4 Tilt series acquisition 38
2.5 Tomogram reconstruction 39
2.6 Tomogram segmentation 39
2.7 Subtomogram averaging 39
2.7.1 Proximal centriole triplets, axonemal doublets, central pair apparatus 40
2.7.2 Endpiece singlets 40
2.7.3 Nuclear envelope densities, outer mitochondrial membrane (omm) densities, ATP synthase, microtubule plugs 41
2.7.4 Particles in nuclear clearing zones 41
2.7.5 Acrosome crystalloids 42
2.7.6 Plotbacks 42
2.8 Measurements and quantification 42
2.8.1 Mitochondrial dimensions 42
2.8.2 Internal mitochondrial ultrastructure 43
2.8.3 Membrane distances 43
2.9 Cryo-scanning transmission electron microscopy (cryo-STEM) . 43
2.10 Mass spectrometry 44
2.10.1 Sperm preparation 44
2.10.2 Whole cell proteomics 45
2.10.3 Whole cell cross-linking mass spectrometry 45

2.1 Sperm preparation

2.1.1 Pig sperm

Freshly-ejaculated pig (*Sus scrofa domestica*) semen was purchased from an artificial insemination company (AIM Varkens KI Nederland). Semen was typically diluted in Beltsville's thawing solution (BTS: 205 mM glucose, 20 mM NaCl, 5 mM KCl, 15 mM $NaHCO_3$, 3 mM EDTA) and stored at 18 °C until use. Sperm were used within 1 day of delivery. Sperm were gently layered onto a discontinuous gradient consisting of 2 mL of 70% Percoll overlaid with 4 mL of 30% Percoll, both in HEPES-buffered saline (HBS: 20 mM HEPES, 137 mM NaCl, 10 mM glucose, 2.5 mM KCl, 0.1% kanamycin, pH 7.6) and centrifuged at 750 *g* for 15 min. Pelleted cells were washed once in phosphate-buffered saline (PBS: 137 mM NaCl, 3 mM KCl, 8 mM Na_2HPO_4, 1.5 mM KH_2PO_4, pH 7.4), resuspended in PBS, and counted.

Washed sperm were resuspended in 1X TALP (20 mM HEPES, 90 mM NaCl, 21.7 mM sodium lactate, 15 mM $NaHCO_3$, 5 mM glucose, 3.1 mM KCl, 2 mM $CaCl_2$, 1 mM sodium pyruvate, 0.4 mM $MgSO_4$, 0.3 mM NaH_2PO_4, 100 μg/mL kanamycin, 0.3% w/v fatty acid-free BSA (Sigma), pH 7.4) at ~10-20 x 10^6 cells/mL. Sperm were allowed to capacitate for between 2 and 2.5 hours at 37 °C, 5% CO_2. In order to stimulate the acrosome reaction more rapidly and in a larger percentage of cells, either calcium ionophore A23187 (Sigma) or progesterone (Sigma) was added to capacitated cells to a final concentration of either 5 μM or 3 μM, respectively. Cells were incubated for a further 30 min (for ionophore) or 1 h (for progesterone) at 37 °C, 5% CO_2.

Acrosome status was assessed by fluorescent lectin staining. Approximately 80 μL of naive (Percoll-washed), capacitated, or acrosome-reacted sperm was pipetted into the wells of an 8-well ibidi μ-slide. Cells were fixed with 4% paraformaldehyde for 30 min at room temperature (RT) and washed three times in PBS for 5 min each. When appropriate, cells were permeabilized with PBS + 0.5% Triton X-100 at RT for 30 min and subsequently washed three times in PBS. Wells were then blocked with PBS + 1% BSA overnight at 4 °C, and the samples then incubated for 30 min with peanut agglutinin (PNA)-AlexaFluor568 (Sigma Aldrich) and Hoechst

33342 (LifeTechnologies) in PBS + 1% BSA. Cells were then washed three times with PBS, and a drop of mounting medium (either Fluorsave or ProLong Gold AntiFade) was added to each well. Fluorescence microscopy was performed on a CorrSight (ThermoFisher) light microscope operating in spinning disk mode.

For flow cytometry, cells were first washed with PBS and their concentration adjusted to 30-50 x 10^6 cells/mL. Sperm were then stained with propidium iodide (PI) (LifeTechnologies) and with PNA-fluorescein isothiocyanate (FITC)(Sigma), both at a final concentration of 1 μg/mL. Sperm were then diluted 1/100 to 0.5 x 10^6 cells/mL and analyzed using a BD FACSCanto II flow cytometer. Viable, acrosome-reacted cells were defined as those in the PI^+FITC^+ quadrant of the cytogram.

2.1.2 Horse sperm

Horse sperm were generously provided by Dr. Paula Maitan and Dr. Heiko Henning, both from the Veterinary Faculty of Utrecht University, The Netherlands. Horse (*Equus caballus*) semen was collected from mature Warmblood stallions using a Hanover artificial vagina in the presence of a teaser mare. After collection, semen was filtered through gauze to remove the gel fraction and large debris, then transported to the laboratory at 37 °C and kept at room temperature until further processing. Semen was diluted in INRA96 (IMV Technologies) to obtain a sperm concentration of 30 x 10^6 cells/mL. After this, sperm were centrifuged through a discontinuous Percoll gradient similar to that described for pig sperm for 10 min at 300 *g*, followed by 10 min at 750 *g*. Pelleted cells were washed once in PBS, resuspended in PBS, and counted.

2.1.3 Mouse sperm

Mouse sperm was generously provided by Dr. Elizabeth G. Bromfield from the Veterinary Faculty of Utrecht University, The Netherlands. Mouse (*Mus musculus*) sperm were collected from the cauda epididymis of adult male C75BL/6 mice as described (Hutcheon et al., 2017). Briefly, male mice were culled and the cauda epididymides dissected with the vas deferens attached. Dissected tissue was placed in a 500 μL droplet of modified Biggers, Whitten, and Whittingham media (BWW:

20 mM HEPES, 91.5 mM NaCl, 4.6 mM KCl, 1.7 mM D-glucose, 0.27 mM sodium pyruvate, 44 mM sodium lactate, 5 U/mL penicillin, and 5 μg/mL streptomycin, adjusted to pH 7.4 and an osmolarity of 300 mOsm/kg). To retrieve the mature cauda spermatozoa from the epididymides, forceps were used to first gently push the stored sperm from the vas deferens, after which two incisions were made with a razor blade in the cauda. Spermatozoa were allowed to swim out of the cauda into the BWW over a period of 15 min at 37 °C, after which the tissue was removed and sperm were centrifuged through 27% Percoll and subsequently washed by centrifugation at 400 *g* for 2 min to remove excess Percoll.

2.1.4 Bovine sperm

Bovine sperm was generously provided by Dr. Heiko Henning. Bovine sperm for cryo-EM was collected from highly-fertile Holstein bulls (CRV Delta, The Netherlands). Semen was diluted to a sperm concentration of ~30 x 10^6 cells/mL with either Tris-citrate buffer (96 mM Tris, 27 mM fructose, 35 mM sodium citrate, pH 7, 300 mOsm) or OptiXcell buffer (IMV Technologies).

2.2 Cryo-ET grid preparation

A diagram of the cryo-ET workflow used in this study is shown in **Fig. 2.1**. Approximately 3 μL of a sperm suspension was pipetted onto a glow-discharged 200 mesh Quantifoil R 2/1 holey carbon grid. Cell concentrations were typically around either 2-3 x 10^6 cells/mL (for whole cell tomography) or 20-30 x 10^6 cells/mL (for cryo-FIB milling). One μL of a suspension of BSA-conjugated 10-nm gold beads (Aurion) was added, and the grids then blotted manually from the back (opposite the side of cell deposition) for ~2-3 s (for whole cell tomography) or for ~4-6 s (for cryo-FIB milling) using a manual plunge-freezer (MPI Martinsried) (Dobro et al., 2010). Grids were immediately plunged into either liquid ethane or a liquid ethane-propane mix (37% ethane) cooled to liquid N_2 temperature. Grids were stored under liquid N_2 until imaging.

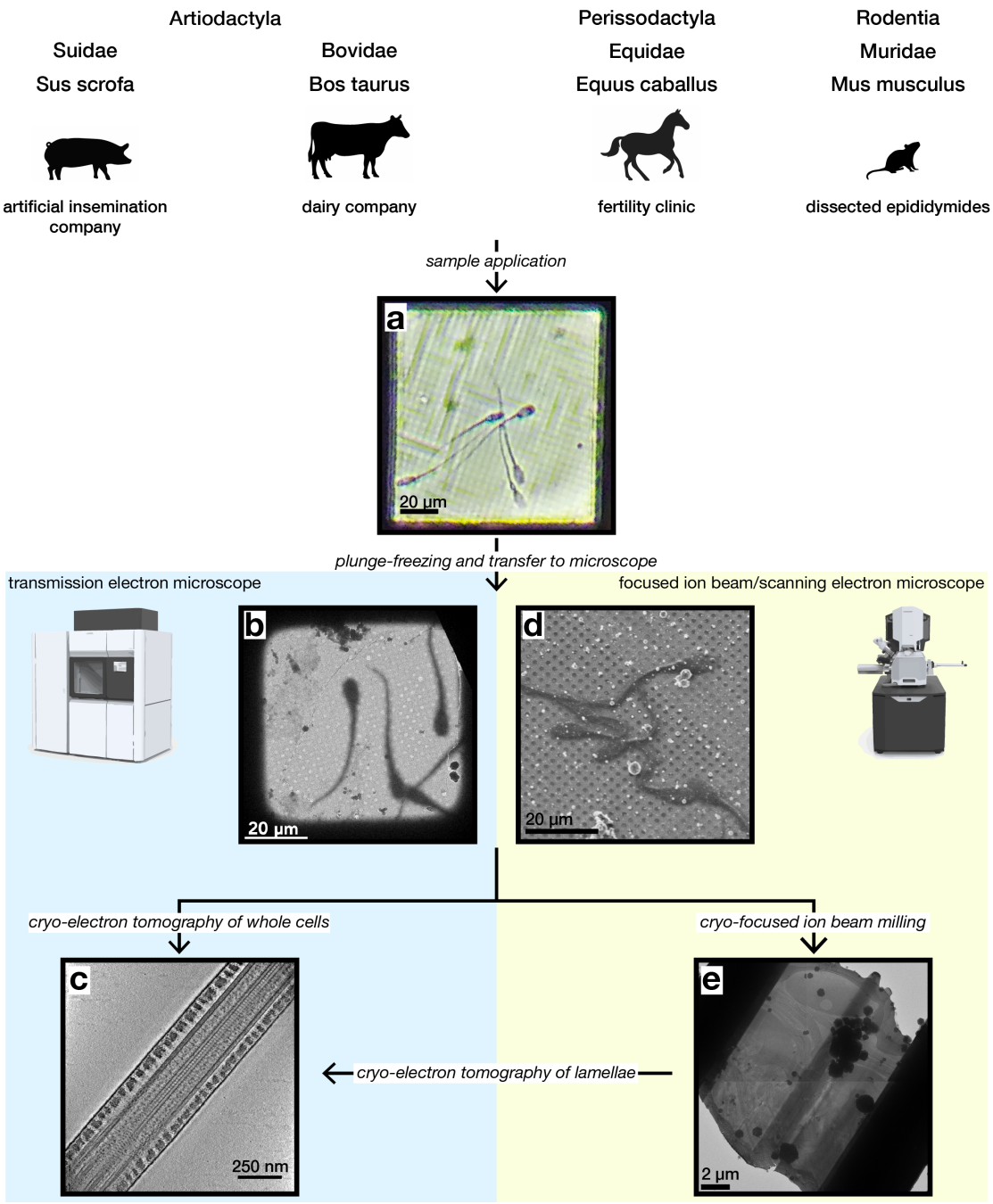


Figure 2.1 | The cryo-electron tomography (cryo-ET) workflow for imaging mammalian sperm. Live sperm were pipetted onto electron microscope (EM) grids and plunge-frozen. Grids were then either imaged directly by cryo-ET (left branch) or first thinned by cryo-focused ion beam (cryo-FIB) milling (right branch). **(a)** shows live pig sperm on an EM grid imaged under a light microscope. **(b)** shows plunge-frozen pig sperm on an EM grid imaged under a transmission electron microscope (TEM, blue background). Thin parts of the cell can be imaged directly by cryo-ET. **(c)** shows a slice through a Volta phase plate cryo-tomogram of the distal region of the principal piece. Grids can also first be transferred to a focused ion beam/scanning electron microscope (FIB/SEM, yellow background) for sample thinning prior to high-resolution imaging. **(d)** shows sperm on an EM grid imaged with a scanning electron microscope. **(e)** shows a cryo-lamella through multiple cells. Lamellae can then be transferred to the TEM for cryo-ET. Icons of the Talos Arctica TEM and Aquilos FIB/SEM were modified from images from ThermoFisher Scientific. **Scale bars:** (a,b,d) 20 µm, (c) 250 nm, (e) 2 µm.

2.3 Cryo-focused ion beam milling

Grids were mounted into notched Autogrids (ThermoFisher) for mechanical support. Clipped grids were loaded into an Aquilos (ThermoFisher) dual-beam cryo-focused ion beam/scanning electron microscope (cryo-FIB/SEM). The temperature of the stage was kept at around −175 °C at all times to prevent devitrification. All SEM imaging was performed at 2 kV and 13 pA, whereas FIB imaging for targeting was performed at 30 kV and 10 pA. After loading, grids were coated with metallic platinum to reduce charging and subsequently with an organometallic platinum layer to protect the milling front. Milling was typically performed with a stage tilt of 18°, so lamellae were inclined at 11° relative to the grid. Each lamella was milled in four stages: an initial rough mill at 1 nA beam current, an intermediate mill at 300 pA, a fine mill at 100 pA, and a polishing step at 30 pA. Lamellae were milled with the wedge pre-milling technique described in Schaffer et al., 2017 and with expansion segments as described in Wolff et al., 2019. Lamellae were then sputter-coated with a thin layer of metallic platinum to reduce charging during cryo-ET imaging.

2.4 Tilt series acquisition

Tilt series were acquired on either a Talos Arctica (ThermoFisher) operating at 200 kV or a Titan Krios (ThermoFisher) operating at 300 kV, both equipped with a post-column energy filter (Gatan) in zero-loss imaging mode with a 20-eV energy-selecting slit. All images were recorded on a K2 Summit direct electron detector (Gatan) in either counting or super-resolution mode with dose-fractionation. Tilt series were collected using SerialEM (Mastronarde, 2005) at a target defocus of between -4 and -6 μm (conventional defocus-contrast) or between -0.5 and -1.5 μm (for tilt series acquired with the Volta phase plate). Tilt series were typically recorded using either strict or grouped dose-symmetric schemes, usually spanning 56° in 2° increments or 54° in 3° increments, with total fluence limited to ∼100 $e^-/Å^2$.

2.5 Tomogram reconstruction

Frames were aligned either post-acquisition with Motioncor2 1.2.1 (Zheng et al., 2017) or on-the-fly using Warp (Tegunov and Cramer, 2019). When used, super-resolution frames were binned 2X during motion correction. Tomograms were reconstructed in IMOD (Kremer et al., 1996) using weighted back-projection, with a simultaneous iterative reconstruction technique (SIRT)-like filter (Zeng, 2012) applied for visualization and segmentation. Defocus-contrast tomograms were CTF-corrected in IMOD using *ctfphaseflip*, while VPP tomograms were left uncorrected.

2.6 Tomogram segmentation

Segmentation was generally performed semi-automatically using the neural network-based workflow implemented in the TomoSeg package in either EMAN 2.1 or EMAN 2.3 (Chen et al., 2017a). Microtubules were traced manually in IMOD. Segmentation was then manually refined in Chimera 1.12 (Pettersen et al., 2004) or in ChimeraX (Goddard et al., 2018). Visualization was performed in either Chimera 1.12 or ChimeraX.

2.7 Subtomogram averaging

Subtomogram averaging with missing wedge compensation was performed using PEET 1.13.0 (Nicastro et al., 2006). Resolution was estimated using the Fourier shell correlation (FSC) at a cut-off of 0.5 (Nicastro et al., 2006). Alignments were generally performed first on binned data, after which aligned positions and orientations were transferred to less-binned data using scripts generously provided by Dr. Daven Vasishtan. These scripts are known as "PEET extensions" (pex scripts) and are based on the TEMPy package (Farabella et al., 2015). After alignment, classification was performed in order to assess heterogeneity and to identify cases of misalignment (Heumann et al., 2011). Missing-wedge corrected classification was performed by first running a principal components analysis using the *pca* function, followed by k-means clustering using the *clusterPca* function. The resulting class averages were manually inspected, and similar classes were combined. Specific averaging strategies

are described below. Details of acquisition parameters and particle numbers are summarized in relevant data tables throughout the results chapters.

2.7.1 Proximal centriole triplets, axonemal doublets, central pair apparatus

Microtubule-based structures were manually traced in IMOD, and model points were added every 8 nm for centrioles (Greenan et al., 2018), 32 nm for the CPA (Carbajal-González et al., 2013), or 96 nm for axonemal doublets (Nicastro et al., 2006) using *addModPts*. These periodicities were also decided based on what could be measured from the raw tomograms. Subtomograms of approximately 70 nm x 42 nm x 70 nm (for centriole triplets), 100 nm x 100 nm x 100 nm (for the CPA), and 100 nm x 100 nm x 100 nm (for doublets) were then aligned and averaged. A randomly chosen particle was used as the initial reference for all alignments involving microtubule-based assemblies. Independent alignments using independent references were performed for datasets from different species. For triplets and doublets, particles with similar orientations (e.g; positions 9, 1, and 2) were first aligned. Sub-averages were manually rotated and/or translated using *modifyMotiveList* to align them with a common reference, followed by an alignment with a restricted search range.

2.7.2 Endpiece singlets

Endpiece singlets were manually traced in IMOD and model points were added every 8 nm using *addModPts*. This periodicity was also decided based on what could be measured from the raw tomograms. Subtomograms of approximately 35 nm x 35 nm x 35 nm were computationally aligned and averaged. An initial alignment was performed to align protofilaments, after which a mask was used to focus alignment on the luminal densities. After classification, a final, restricted alignment was performed with the mask expanded to include the microtubule lattice.

2.7.3 Nuclear envelope densities, outer mitochondrial membrane (omm) densities, ATP synthase, microtubule plugs

Alignment strategies for these complexes were designed to take advantage of their defined orientations relative to the membrane plane or the microtubule tip. Particles were picked manually and their initial orientations were defined using *stalkInit*. Initial references were either a randomly chosen particle (for omm densities) or an average of all particles after roughly aligning them based on their initial orientations (for nuclear envelope densities, ATP synthase, and microtubule plugs). Independent alignments using independent initial references were performed for datasets from different species. Alignments allowed for large rotational search ranges around the particle long axis (defined as the y-axis, perpendicular to the membrane plane), with limited search ranges around the x- and z-axes (the membrane plane).

All initial alignments were performed without symmetry. After visual inspection of the maps, threefold symmetry was applied for nuclear envelope densities and twofold symmetry for omm densities. Symmetrization involved using the aligned positions from the unsymmetrized runs as seed points and rotating particles around the axis of symmetry to generate virtual particles. A symmetrized volume was generated by averaging all particles and virtual particles and used as a reference for a final, restricted alignment.

2.7.4 Particles in nuclear clearing zones

Particles in nuclear clearing zones appeared rectangular in side views and donut-shaped in top views, suggesting that they were cylindrical. Particles were manually picked and their initial orientations estimated by defining a line through the cylindrical long axis using the *stalkInit* program. Particle long axes were then aligned, and all particles were averaged to generate an initial reference. Alignments allowed for large rotational search ranges around the particle long axis (the cylinder long axis), with limited search ranges around the x- and z-axes. All initial alignments were performed without symmetry, after which aligned positions and orientations were used to seed sevenfold-symmetrized alignment and averaging runs.

2.7.5 Acrosome crystalloids

Particle positions were seeded by generating a three-dimensional grid of points in crystalloid patches using the *gridInit* program. All particle orientations were randomized and initial alignments allowed for full rotational searches around all axes. To ensure consistency, two independent initial alignments were performed, each using a randomly-selected particle from a separate tomogram as an initial reference. Since both alignments converged on similar structures, alignments were continued. The dataset was cleaned by (i) removing all particles with a cross-correlation value less than one standard deviation above the mean (which removed poorly-aligning particles such as those at the edges of crystalloid patches) and by (ii) removing overlapping particles. The orientations of the remaining particles were again randomized and another alignment performed using a new randomly-selected particle as a reference. After a final particle clean-up by classification, a final restricted alignment was performed.

2.7.6 Plotbacks

Plotbacks were generated in IMOD by first running *createAlignedModel* to generate model files reflecting updated particle positions and orientations after alignment. The relevant subtomogram average was then thresholded for visualization and saved as an isosurface model, which was then placed back into the tomograms using *clonemodel*.

2.8 Measurements and quantification

2.8.1 Mitochondrial dimensions

All measurements were performed in IMOD on VPP tomograms filtered with a SIRT-like filter. Mitochondrial width was measured in the non-missing wedge direction at five points along the length of each mitochondrion. Only mitochondria that were entirely in the field of view were included in the measurements. Tomograms and corresponding measurements were then grouped based on their locations relative to the connecting piece.

2.8.2 Internal mitochondrial ultrastructure

Internal mitochondrial ultrastructure was quantified from tomograms from cryo-FIB milled lamellae. The volume occupied by the matrix (V_{matrix}, the volume enclosed by the inner mitochondrial membrane) was measured relative to the volume occupied by the entire mitochondrion (V_{mito}, the volume enclosed by the outer mitochondrial membrane). Mesh volumes were extracted from segmentations using *imodinfo*. Because neural network-based segmentation often resulted in gaps, mitochondrial membranes were segmented manually in IMOD for quantification. Only slices in which both the inner and outer mitochondrial membranes were clearly defined were used for segmentation.

2.8.3 Membrane distances

Most inter-membrane distances were estimated in two-dimensional tomographic slices in IMOD. However, three-dimensional inter-membrane distance measurements shown in Chapter 6 were performed on membranes segmented in Avizo 9.2.0 (ThermoFisher). Membrane surfaces were approximated as triangular meshes. Membrane distance was defined for each triangle in the mesh as the closest distance to the neighboring mesh. For visualization, the plasma membrane was color-coded based on its distance relative to the outer acrosomal membrane.

2.9 Cryo-scanning transmission electron microscopy (cryo-STEM)

Pig sperm used for cryo-STEM experiments described in Chapter 4 were incubated in capacitating conditions and plunge-frozen after a ~30 min ionophore treatment as described in Sections 2.1.1 and 2.2 above. Grids were mounted onto a Gatan 626 cryo-holder and loaded into a Tecnai 20 (FEI/Philips Electron Optics, now ThermoFisher) scanning/transmission electron microscope equipped with a Schottky field emission gun and operated at an accelerating voltage of 200 kV. Dark-field imaging was performed with a high-angle annular dark field (HAADF) detector

(Fischione) and chemical characterization with an energy-dispersive X-ray (EDX) detector (Si/Li, EDAX). Images were collected on a 2048 x 2048 charge-coupled device (CCD) camera (Tietz Video and Image Processing Systems) using the Tecnai Imaging & Analysis (TIA) software.

2.10 Mass spectrometry

All mass spectrometry experiments were performed by Dr. Riccardo Zenezini-Chiozzi and Johannes Hevler, who are part of the Biomolecular Mass Spectrometry Group at Utrecht University, The Netherlands. I was directly involved in sample preparation and data analysis.

2.10.1 Sperm preparation

Two biological replicates (that is, two animals) were used for all mass spectrometry experiments. Pig sperm were Percoll-washed as described above (Section 2.1.1) in order to remove residual components of seminal fluid. After the Percoll wash, sperm were washed in PBS and pelleted. The pellet was then flash-frozen in liquid nitrogen and stored at −80 °C until further processing. Approximately 50 x 10^6 cells were used for each whole cell proteomics experiment, while approximately 300 x 10^6 cells were used for cross-linking experiments.

Head-tail separation was performed according to Miyata et al. (2015). Approximately 100 x 10^6 Percoll-washed sperm were resuspended in PBS and sonicated on ice using a Branson tip sonicator with a 3.2-mm microprobe at 40% power output for a total of 5 cycles of 15-s pulses followed by 30-s rests. The suspension was centrifuged at 500 *g* for 15 min to pellet out sperm heads. The resulting supernatant was subsequently centrifuged at 20 000 *g* for 30 min to pellet out sperm tails. The pellets were then flash-frozen in liquid nitrogen and stored at −80 °C until further processing.

2.10.2 Whole cell proteomics

Sperm pellets were resuspended in 100-200 µL lysis buffer (100 mM Tris pH 8.5, 5 mM Tris(2-carboxyethyl)phosphine TCEP, 30 mM 2-chloroacetamide CAA, 1 mM pervanadate, 10 U/mL DNase 1, 1% sodium deoxycholate, supplemented with 1 tablet each of broad-spectrum phosphatase and proteinase inhibitors, both from Roche) and sonicated on ice for 2 min with a UP100H tip sonicator operating at 80% power output. After sonication, the sample was centrifuged at 200 000 *g* for 1 h at 4 °C. A small aliquot (5-10 µL) of the clarified supernatant was used for determining protein concentration using a Pierce™ BCA protein assay. The remaining volume was then diluted 3 X with 100 mM Tris pH 8.5 supplemented with 1% benzonase and 2 mM $MgCl_2$ and incubated with shaking for 2 h at room temperature. Proteins were then precipitated with the addition of 4 X (v/v) methanol, 1 X (v/v) $CHCl_3$, and 3 X (v/v) H_2O, with vortexing after each solvent addition. Samples were mixed thoroughly and centrifuged at 5000 *g* for 10 min at room temperature. The upper (H_2O/methanol) phase was removed, leaving the protein phase undisturbed. Methanol (3 X v/v) was added to the protein phase and the sample subsequently centrifuged at 5000 *g* for 10 min at room temperature. The supernatant was aspirated off and the protein pellet allowed to dry, after which the pellet was resuspended in digestion buffer (100 mM Tris pH 8.5, 5 mM TCEP, 30 mM CAA, 1% SDC) with a Trypsin/Lys-C protease mix (ThermoFisher).

Approximately 500 ng of total protein was injected onto a QExactive HF-X quadrupole orbitrap mass spectrometer (ThermoFisher). Spectra were analyzed with MaxQuant 1.6 using a 1% false discovery rate.

2.10.3 Whole cell cross-linking mass spectrometry

Sperm pellets were resuspended in 540 µL PBS with 1 mM disuccinimidyl sulfoxide (DSSO, ThermoFisher) and incubated at room temperature for 20 min. The reaction was quenched with 50 mM Tris, pH 8.0 and the sample then centrifuged at 5000 *g* for 5 min at room temperature. The cell pellet was then solubilized in 1 mL of 50 mM ammonium bicarbonate, 1% TritonX-100, 8 M urea.

Solubilized cross-linked protein was analyzed by liquid chromatography/mass spectrometry (LC/MS) as described in Liu et al. (2018). Briefly, cross-linked proteins were analyzed using an ultra-HPLC Agilent 1200 (Agilent Technologies) equipped with a C18 column packed with Poroshell 120 EC-C18 (Agilent Technologies) coupled online to an Orbitrap Fusion mass spectrometer (ThermoFisher). Spectra were analyzed with XlinkX v2.0 and interactome maps were generated with Cytoscape v3.4 and xiNET. Cross-linked lysines were mapped onto either crystal structures from the PDB or homology models generated with the Robetta server (Kim et al., 2004).

3

The molecular architecture of the sperm head-tail junction, a specialized nucleus-cytoskeleton contact site

Contents

3.1 Introduction **47**
3.2 Results and Discussion **49**
3.2.1 The sperm head is compact. 49
3.2.2 A conserved supramolecular array of proteins in the nuclear envelope forms the base of the head-tail junction. 52
3.3 Concluding Remarks **59**

3.1 Introduction

Beyond its canonical role as the cellular command center, the nucleus is a dynamic organelle that is itself reshaped and repositioned in response to the changing environment (Gundersen and Worman, 2013; Webster et al., 2009). This plasticity ultimately depends on coupling between the nucleus and the cytoskeleton, which is mediated by linker of nucleoskeleton and cytoskeleton (LINC) complexes that span the nuclear envelope (Chang et al., 2015; Starr and Fridolfsson, 2010). Nucleus-cytoskeleton interactions are critical for a diverse range of processes, including cell migration, DNA repair, and chromosome segregation (Kirby and Lammerding, 2018). However, despite their important roles in cell physiology, the architecture of nucleus-cytoskeleton contacts remains largely undefined.

One of the most dramatic examples of nuclear remodeling occurs during spermiogenesis, the process by which haploid round spermatids transform into mature spermatozoa. During spermiogenesis, sperm chromatin becomes repackaged into a highly compact, highly stable form through the replacement of histones with protamines (Rathke et al., 2014). Concomitant with chromatin compaction, the nucleus itself is remodeled into a streamlined form through its interactions with a transient microtubule-based assembly called the manchette (Dunleavy et al., 2019; Pereira et al., 2019). As a result, sperm nuclei occupy less than a tenth of the volume of their somatic counterparts (Miller et al., 2010). The nucleus is then coupled to the flagellum through a specialized nucleus-cytoskeleton contact site called the head-tail junction (Wu et al., 2020).

Disruption of the head-tail junction causes infertility manifested by acephalic or decapitated sperm. Genomic screens and mouse genetics have now uncovered a small set of proteins that are essential for the integrity of the head-tail junction. These include the testis-specific Sad1 and UNC84 domain containing (SUN) protein isoform SUN5, a LINC complex component (Elkhatib et al., 2017; Shang et al., 2018, 2017); spermatogenesis-associated protein 6 (SPATA6), a pericentriolar matrix protein (Yuan et al., 2015); and polyamine modulated factor 1 binding protein 1 (PMFBP1), a testis-specific protein that localizes to the sperm connecting piece (Sha et al., 2019; Zhu et al., 2018). Despite these molecular advances, however, we know comparatively little about the structural organization of the head-tail junction beyond gross morphological details from classical TEM.

In this chapter, I use cryo-FIB milling-enabled cryo-ET to unveil the molecular architecture of the head and the head-tail junction in mature mammalian sperm. These analyses revealed a supramolecular array of nuclear envelope proteins at the core of the head-tail junction. This assembly appears to be conserved between the pig and the mouse despite drastic differences in overall head shape.

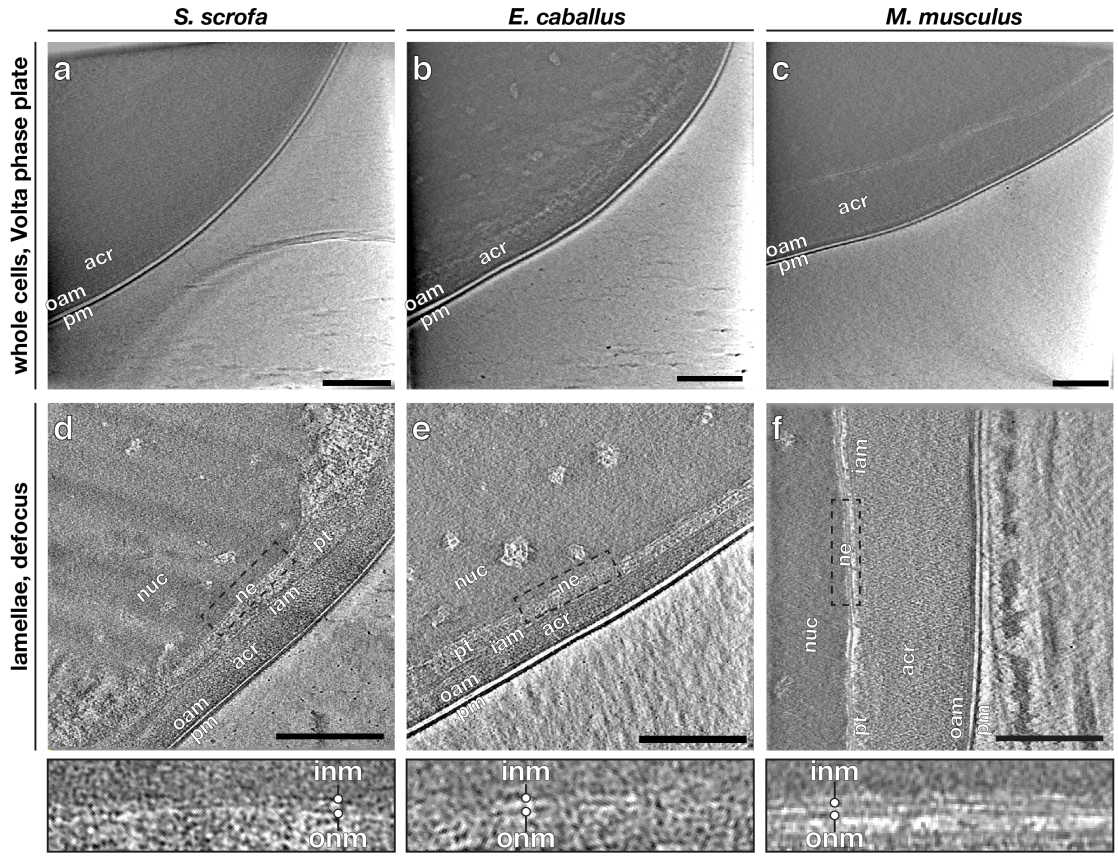


Figure 3.1 | The sperm head is compact. (a-c) Slices through Volta phase plate cryo-tomograms of whole pig (a), horse (b), and mouse (c) sperm heads. **(d-f)** Upper panels show slices through defocus-contrast cryo-tomograms from FIB-milled lamellae of pig (d), horse (e), and mouse (f) sperm heads. Lower panels show digital zooms of regions boxed out in the upper panels. **Labels:** pm – plasma membrane, oam – outer acrosomal membrane, iam – inner acrosomal membrane, acr – acrosome, pt – perinuclear theca, ne – nuclear envelope, nuc – nucleus, onm – outer nuclear membrane, inm – inner nuclear membrane. **Scale bars:** 250 nm.

3.2 Results and Discussion

3.2.1 The sperm head is compact.

Although mammalian sperm heads are relatively flat, they are still too thick for direct imaging by cryo-ET, even with enhanced contrast from the Volta phase plate (VPP) **(Fig. 3.1a-c)**. As such, I used cryo-ET of cryo-FIB milled lamellae to image fine details of the structural organization of the sperm head **(Fig. 3.1d-f)**. This revealed the compact arrangement of the sperm head, which consists – from the inside out – of a nucleus, a dense layer of residual cytoplasm called the perinuclear theca, and a large

vesicle called the acrosome, all surrounded by the plasma membrane. The plasma membrane and the outer acrosomal membrane are closely apposed all along the sperm head **(Fig. 3.1)**, in contrast to their typical wavy appearance in classical TEM images (Tsai et al., 2010). The lumen of the acrosome is electron dense, suggesting that the enzymes therein are densely packed. The inner acrosomal membrane is laminated to the perinuclear theca, which in turn overlies the nuclear envelope. Notably, the inner and outer nuclear membranes (INM and ONM, respectively) of the sperm nuclear envelope are separated by ~10 nm in this region, which is a much smaller separation than the ~45 nm typical of somatic cells **(Fig. 3.1d-f, lower panels)** (Franke et al., 1981; Mahamid et al., 2016).

Sperm nuclei are highly condensed, driven by the exchange of histones for protamines during spermatogenesis (Johnson et al., 2010; Rathke et al., 2014). As such, most of the nucleus appears electron-dense and relatively featureless, even in thin lamellae **(Fig. 3.1d-f)** and even with enhanced contrast from the VPP **(Fig. 3.2)**. However, imaging cryo-FIB-milled lamellae with the VPP allowed detection of macromolecular complexes in an otherwise densely-packed environment **(Fig. 3.2)**. For instance, an array of membrane proteins is visible on the inner leaflet of the outer acrosomal membrane **(Fig. 3.2i)**, as are locally-ordered densities within the acrosomal matrix **(Fig. 3.2ii)**, and small particles within nuclear pockets **(Fig. 3.2iii)**. These nuclear pockets likely correspond to the "clearing zones" or "nuclear vacuoles" typically seen by classical EM (Mortimer, 2018); however, it is clear from cryo-tomograms that these regions are neither membrane-bound nor empty **(Fig. 3.3a-c)**.

Particles inside the nuclear pockets are present in all three species and appear donut-shaped in top views and rectangular in side views **(Fig. 3.3a-c)**. Subtomogram averaging revealed that these particles are cylinders ~16 nm long and ~11 nm wide, with a shape that resembles the 20S proteasome core particle **(Fig. 3.3d-g, Table 3.1)**. This is consistent with immunofluorescence and immunogold labelling experiments that localized the 20S proteasome to decondensed regions within nuclei of both developing spermatids and mature sperm (Haraguchi et al., 2007). Furthermore, proteasome subunits are detected in whole-cell proteomics of pig sperm **(Table 3.2)**,

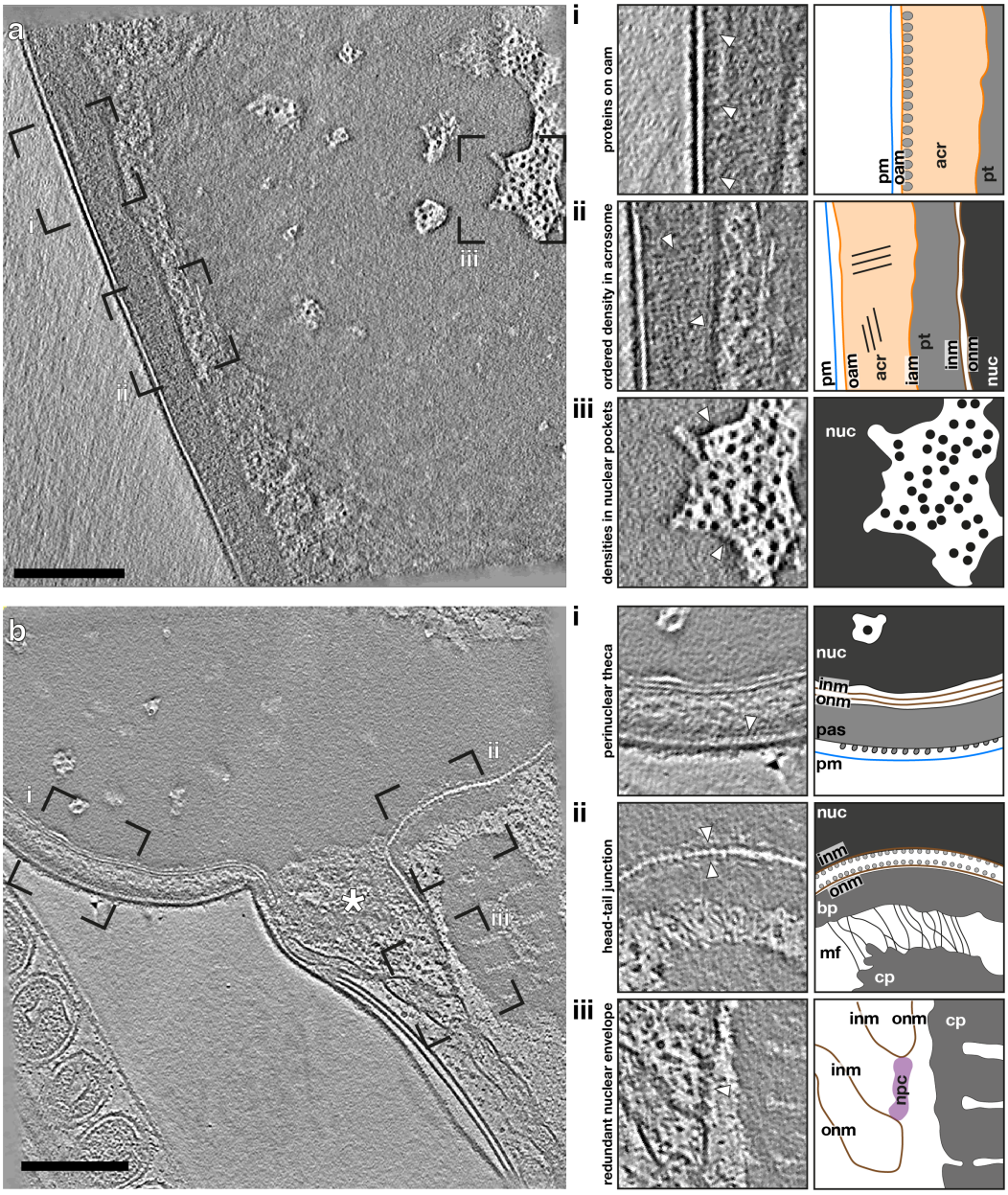


Figure 3.2 | The sperm nuclear envelope consists of discrete domains characterized by distinct protein signatures. Slices through Volta phase plate cryo-tomograms of FIB-milled pig sperm, collected at **(a)** the nuclear periphery in the pre-equatorial region, and **(b)** at the head-tail junction. Right panels show digital zooms and schematics of boxed-out regions in the left panels, emphasizing (a) the different protein densities directly visible in the tomograms: (a-i) proteins on the outer acrosomal membrane, (a-ii) ordered protein density in the acrosomal matrix, and (a-iii) discrete particles in nuclear pockets; and (b) the different regions of the nuclear envelope: (b-i) the nuclear envelope underlying the perinuclear theca, (b-ii) the nuclear envelope overlying the head-tail junction, and (b-iii) the redundant nuclear envelope extending into the neck, which encloses a region of nuclear material that is less dense than that in the rest of the nucleus (asterisk). **Labels:** pm – plasma membrane, oam – outer acrosomal membrane, iam – inner acrosomal membrane, acr – acrosome, pt – perinuclear theca, ne – nuclear envelope, nuc – nucleus, onm – outer nuclear membrane, inm – inner nuclear membrane, pas – postacrosomal sheath, bp – baseplate, mf – microfilaments, cp – connecting piece, npc – nuclear pore complex. **Scale bars:** 250 nm.

Table 3.1 | Image acquisition and processing metrics for subtomogram averaging of protein complexes in the mammalian sperm nucleus and nuclear envelope.

Parameter	Species		
	Sus scrofa	*Equus caballus*	*Mus musculus*
nuclear particles			
sample type	lamellae	lamellae	lamellae
microscope (accelerating voltage)	Arctica (200 kV)	Arctica (200 kV)	Arctica (200 kV)
pixel size (Å)	4.34	5.66	5.66
symmetry	C1/C7	C1/C7	C1/C7
number of particles	52/364	137/959	122/854
estimated resolution (Å)	39/39	35/25	37/28
nuclear envelope proteins			
sample type	lamellae	-	lamellae
microscope (accelerating voltage)	Arctica (200 kV)	-	Arctica (200 kV)
pixel size (Å)	4.34	-	5.66
symmetry	C1/C3	-	C1/C3
number of particles	268/536	-	561/1611
estimated resolution (Å)	39/35	-	31/27

and the α and β subunits of the 20S core particle are enriched in sperm heads relative to tails **(Fig. 3.4)**. Proteasomes degrade acetylated core histones as part of the histone-to-protamine transition (Qian et al., 2013), so the particles in nuclear clearing zones may represent residual proteasomes that become "trapped" in nuclear pockets as chromatin around them condenses.

3.2.2 A conserved supramolecular array of proteins in the nuclear envelope forms the base of the head-tail junction.

Nuclear reshaping necessitates remodeling of the nuclear envelope (Ho, 2010; Pereira et al., 2019; Ungricht and Kutay, 2017). Cryo-ET revealed that the sperm nuclear envelope consists of three morphological domains, characterized by distinct protein profiles and by different spacings between the inner and the outer nuclear membranes **(Fig. 3.2b)**. Along most of the nucleus, the nuclear envelope separates nuclear material from a region of condensed cytoplasm called the perinuclear theca **(Fig. 3.2b-i)**. Here, the INM and ONM are devoid of large membrane proteins and are

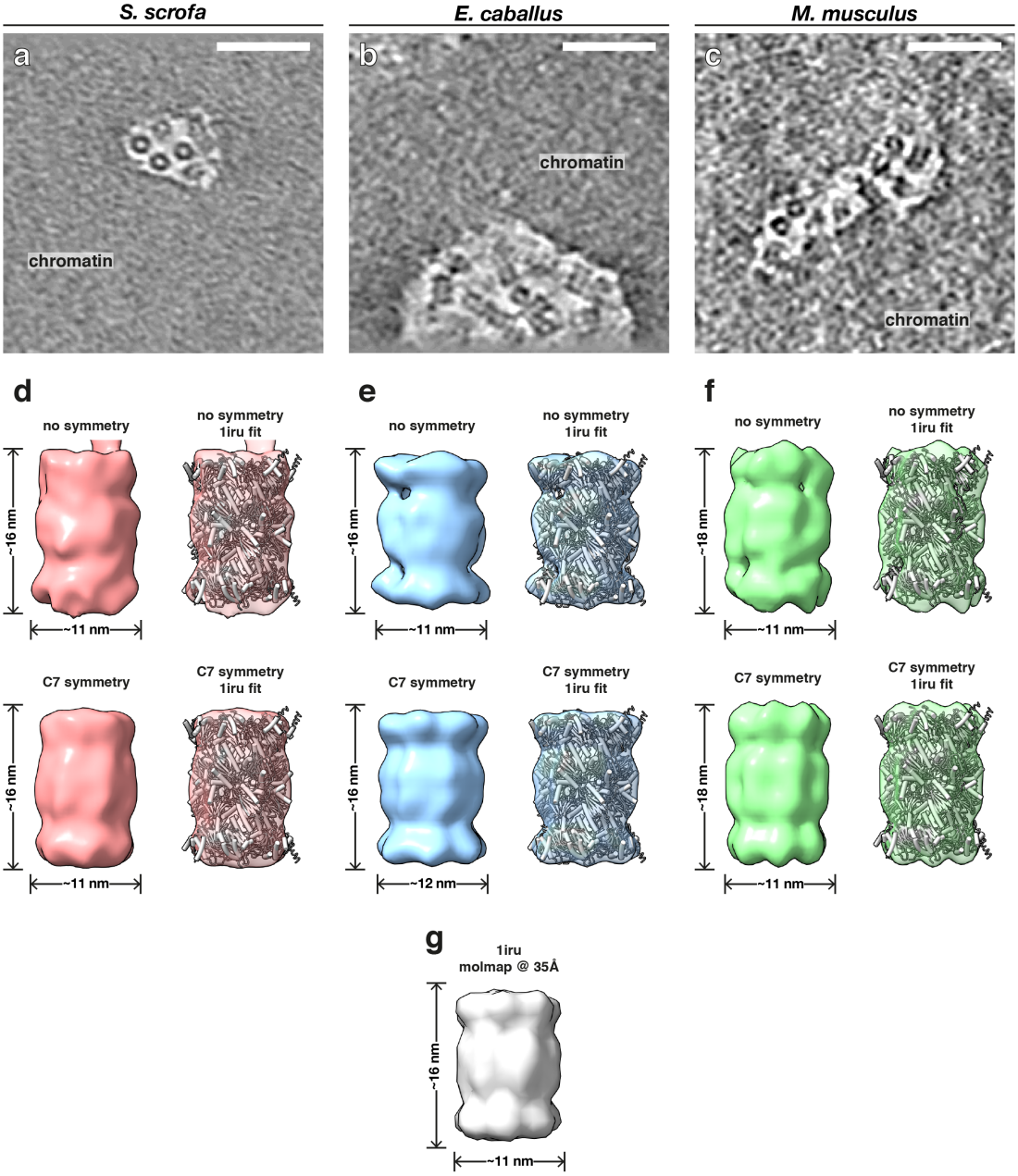


Figure 3.3 | Nuclear pockets contain particles that resemble 20S proteasomes. (a-c) Slices through defocus-contrast cryo-tomograms of FIB-milled pig (a), horse (b), and mouse (c) sperm. Note the cylindrical particles clustered in regions of much lower electron density than the surrounding chromatin. **(d-f)** Subtomogram averages of the nuclear particles without (top panels) and with (bottom panels) C7 symmetry applied. The crystal structure of the human 20S proteasome (PDB ID 1IRU) is fitted into the density in right panels in (d-f) and shown as a molecular map filtered to 35 Å in **(g)**. **Scale bars:** 50 nm.

Table 3.2 | Proteasome subunits in pig sperm identified through label-free mass spectrometry.

Gene name	Protein name	iBAQ	Peptides	Unique peptides	Sequence coverage (%)	Sequence length	MW (kDa)
PSMA1	Proteasome subunit alpha type-1	7.9342	27	27	94.3	263	29.555
PSMA2	Proteasome subunit alpha type-2	7.768	13	13	59.8	234	25.898
PSMA3	Proteasome subunit alpha type-3	7.86936	17	17	51	255	28.433
PSMA4	Proteasome subunit alpha type-4	7.89629	15	15	74.7	261	29.483
PSMA5	Proteasome subunit alpha type-5	8.1752	17	17	67.6	241	26.411
PSMA6	Proteasome subunit alpha type-6	7.84333	21	21	81.7	246	27.399
PSMA7	Proteasome subunit alpha type-7	7.10258	18	13	66.9	248	27.867
PSMA8	Proteasome subunit alpha-type 8	7.96434	18	13	68	250	27.928
PSMB1	Proteasome subunit beta type-1	8.031	16	16	62.7	241	26.33
PSMB2	Proteasome subunit beta type-2	7.76911	17	17	74.1	201	22.78
PSMB3	Proteasome subunit beta type-3	7.92444	13	13	60	205	23.008
PSMB4	Proteasome subunit beta type-4	7.96251	12	12	56.1	264	29.053
PSMB5	Proteasome subunit beta type-5	7.79592	18	18	56.7	275	30.16
PSMB6	Proteasome subunit beta type-6	7.70767	14	14	75.1	241	25.692
PSMB7	Proteasome subunit beta type-7	7.74641	13	13	71.8	277	29.98
PSMC1	26S proteasome regulatory subunit 4	7.23164	28	28	63.6	440	49.184
PSMC2	26S proteasome regulatory subunit 7	7.31698	44	44	83.1	433	48.633
PSMC3	26S proteasome regulatory subunit 6A	7.42892	31	31	69.9	442	49.573
PSMC4	26S proteasome regulatory subunit 6B	7.33726	34	34	80.4	418	47.366
PSMC5	26S proteasome regulatory subunit 8	7.35687	30	30	70.2	406	45.626
PSMC6	26S proteasome regulatory subunit 10B	7.12111	29	29	69.5	403	45.855
PSMD1	26S proteasome non-ATPase regulatory subunit 1	7.28051	53	53	66	953	105.81
PSMD11	26S proteasome non-ATPase regulatory subunit 11	7.3176	34	34	71.2	420	47.321
PSMD12	26S proteasome non-ATPase regulatory subunit 12	7.12713	29	28	62.9	456	53.024
PSMD13	26S proteasome non-ATPase regulatory subunit 13	7.3897	24	24	71.3	376	42.867
PSMD14	26S proteasome non-ATPase regulatory subunit 14	7.13847	15	15	52.9	310	34.577
PSMD2	26S proteasome non-ATPase regulatory subunit 2	7.18937	54	54	64.4	908	100.24
PSMD3	26S proteasome non-ATPase regulatory subunit 3	7.02808	34	34	61	534	60.966
PSMD4	26S proteasome non-ATPase regulatory subunit 4	7.24371	15	15	38.4	380	41.106
PSMD6	26S proteasome non-ATPase regulatory subunit 6	6.981	21	21	44.9	450	52.205
PSMD7	26S proteasome non-ATPase regulatory subunit 7	7.45161	21	21	63.3	324	37.011
PSMD8	26S proteasome non-ATPase regulatory subunit 8	6.86713	13	13	32.2	351	39.732
PSMD9	26S proteasome non-ATPase regulatory subunit 9	7.6342	14	14	84.3	223	24.416
PSME4	Proteasome activator complex subunit 4	5.62226	11	11	9.7	1756	201.3
PSMF1	Proteasome inhibitor PI31 subunit	6.7463	2	2	9.3	270	29.532
PSMG2	Proteasome assembly chaperone 2	7.1206	8	8	28	264	29.121

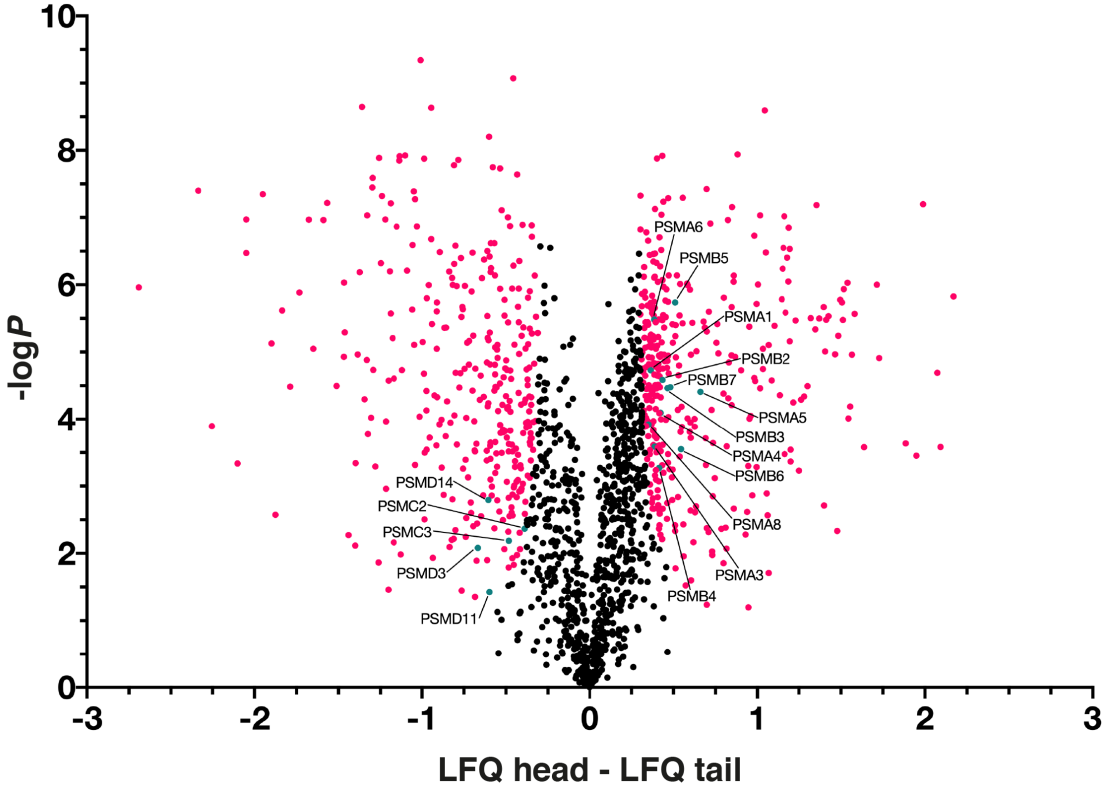


Figure 3.4 | Subunits of the 20S proteasome are enriched in sperm heads relative to sperm tails. Mass spectrometry-based label-free quantification of protein abundance in pig sperm heads and tails separated by sonication. Data are taken from two experiments from two different animals. Significantly enriched proteins are colored in pink, and proteasome subunits are colored in green. Note how α and β subunits of the 20S core particle are enriched in heads, while regulatory subunits are enriched in tails.

spaced ~10 nm apart, which is closer than the 30-50 nm in somatic cells (Franke et al., 1981; Mahamid et al., 2016). In mature sperm, nuclear pore complexes are relegated to a zone of the NE that extends into the connecting piece, called the redundant nuclear envelope (Mortimer, 2018) **(Fig. 3.2b-iii)**. Here, NE spacing is more variable and approaches ~30 nm in the vicinity of NPCs. This is consistent with freeze-fracture EM, which also concluded that NPCs concentrate in this region (Ho, 2010). The redundant NE also encloses a pocket that contains particles similar to those interspersed throughout the nucleus **(Fig. 3.2b, asterisk)**.

The head-tail junction is a specialized nucleus-cytoskeleton contact site **(Fig. 3.2b-ii, Fig. 3.5)**. Here, the nuclear envelope overlies an electron-dense structure called the baseplate, which couples to the connecting piece through ~3-nm microfilaments

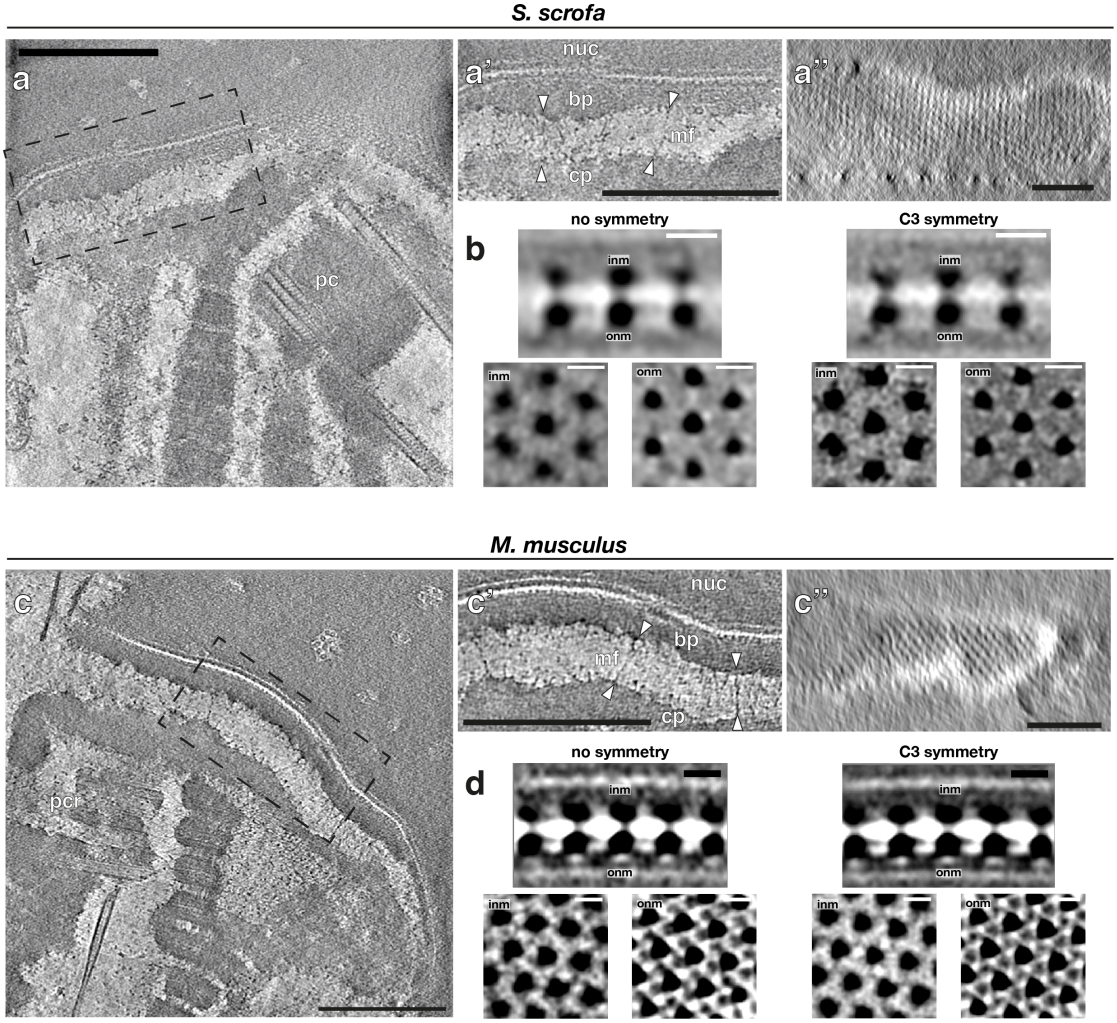


Figure 3.5 | A hexagonal array of trimeric protein densities in the nuclear envelope forms the base of the head-tail junction. **(a,c)** Slices through defocus-contrast cryo-tomograms of FIB-milled pig (a) and mouse (c) sperm. Tomograms were collected at the head-tail junction; note the presence of the proximal centriole (pc) in pig sperm and of proximal centriole remnants (pcr) in mouse sperm. (a',c') Digital zooms of boxed-out regions in (a,c) showing microfilaments connecting the baseplate to the connecting piece (arrowheads). (a",c") Views perpendicular to the plane of the nuclear envelope showing that it is studded with protein densities that form an ordered array. **(b,d)** Slices through subtomogram averages of nuclear envelope densities from pig (b) and mouse (d) sperm without (left panels) and with (right panels) C3 symmetry. **Labels:** pc[r] - proximal centriole [remnants], nuc - nucleus, bp - baseplate, mf - microfilaments, cp - connecting piece, inm - inner nuclear membrane, onm - outer nuclear membrane. **Scale bars:** (a,a',c,c') 250 nm, (a", c") 100 nm, (b,d) 10 nm.

(Fig. 3.2b-ii, Fig. 3.5a' & c'). The INM and the ONM are 14 nm apart and are studded with protein particles arranged in an ordered array **(Fig. 3.5a" & c")**.

I then characterized these particles by subtomogram averaging **(Fig. 3.5b & d, Fig. 3.6, Table 3.1)**. The averages revealed that these particles are arranged in a hexagonal lattice with a 12-13 nm spacing, which is conserved between the pig and the mouse. These particles consist of two prominent densities – one embedded in the inner nuclear membrane and the other associated with the inner leaflet of the outer nuclear membrane – with weaker density connecting them. Individual proteins are three-fold symmetric, most prominently in the ONM-proximal densities **(Fig. 3.5b & d)**. These proteins bridge the nuclear envelope and interact with structural proteins of the baseplate that in turn couple to the connecting piece via 3-nm microfilaments.

The most likely candidates for the components of the hexagonal array are SUN proteins, which are INM-resident proteins that consist of a transmembrane domain, a coiled-coil domain, and a SUN domain. SUN protein trimerization is necessary to form binding sites for partner KASH (Klarsicht, ANC-1, and SYNE/Nesprin-1 and -2 homology)-peptide containing proteins in the ONM (Sosa et al., 2012). Together, these proteins form the core of LINC complexes (Chang et al., 2015). Indeed, the crystal structure of the trimeric SUN domain from human SUN2 (Sosa et al., 2012) (PDB 4DXR) fits into our ONM-proximal densities **(Fig. 3.6)**, where the SUN domain is expected to be.

I propose that the hexagonal arrays consist of the sperm-specific SUN5, which localizes specifically to the head-tail junction (Shang et al., 2017). SUN5-knockout mice produce acephalic sperm in which the connecting piece and baseplate are fully formed but fail to attach to the NE (Shang et al., 2017). Human SUN5 mutations result in male infertility characterized by acephalic spermatozoa (Elkhatib et al., 2017; Shang et al., 2018). SUN5 is also shorter than its somatic counterparts, SUN1 and SUN2, with its coiled-coil domain predicted to span 12 nm as opposed to 45 nm in the latter two isoforms (Sosa et al., 2013). This is consistent with the 14 nm nuclear envelope spacing resolved in the tomograms and averages **(Fig. 3.5)**.

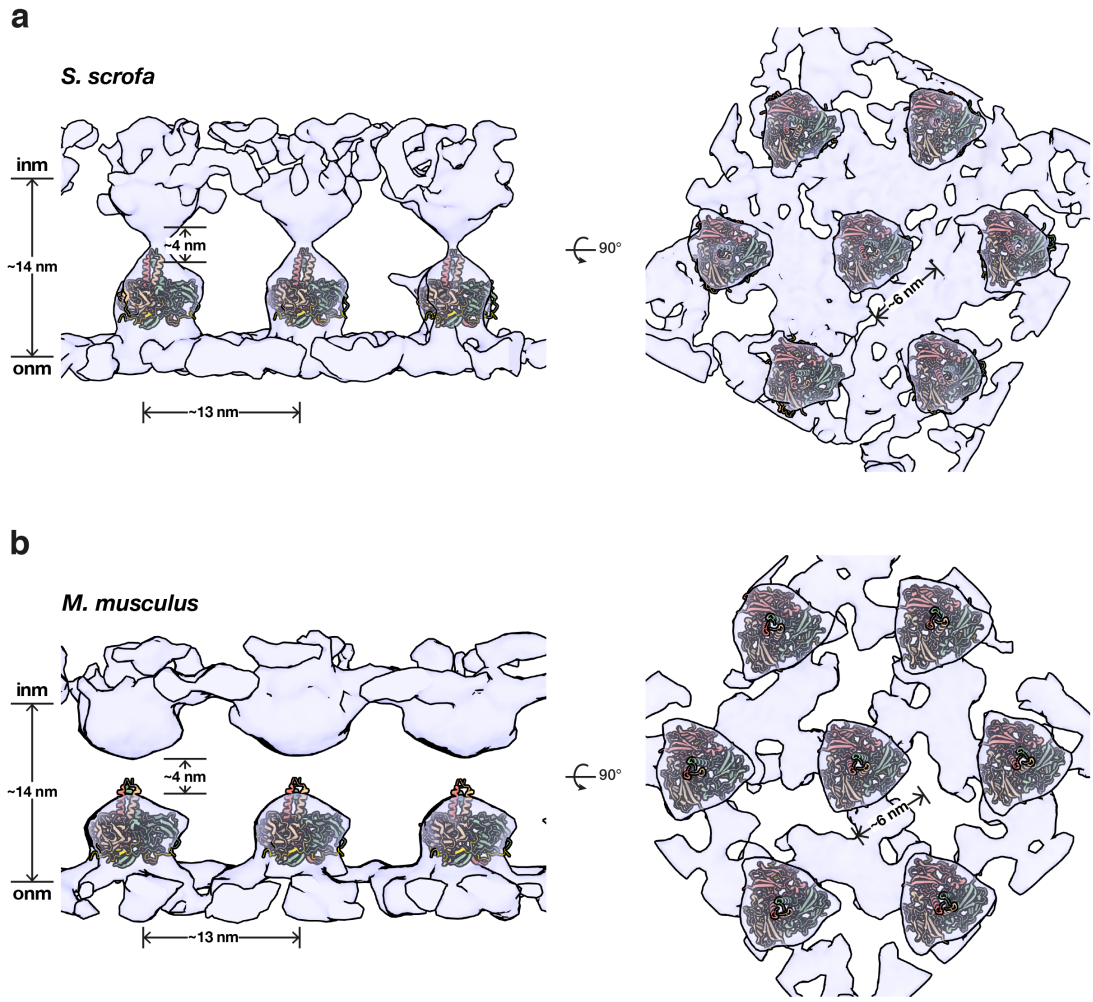


Figure 3.6 | Nuclear envelope densities have molecular dimensions consistent with SUN proteins. Isosurface rendering of threefold-symmetrized nuclear envelope densities from pig **(a)** and mouse **(b)** sperm, viewed parallel (left) or perpendicular (right) to the membrane plane. The crystal structure of human SUN2 (PDB 4DXR) is fitted into the density.

Assembly of LINC complexes into an ordered superstructure may stabilize the head-tail junction, which is particularly important given that this is the major point of articulation between the head and the tail and would hence be subjected to mechanical stress during sperm movement. In migrating fibroblasts and in smooth muscle cells, nuclear positioning is mediated by linear arrays of LINC complexes that assemble along actin fibers (Luxton et al., 2010; Nagayama et al., 2014). Because direct interactions between putative SUN proteins are not immediately obvious in the subtomogram averages, their assembly into ordered arrays may be mediated by oligomerization of their partner proteins in the ONM. Indeed, crystal structures of 3:3 SUN/KASH

complexes suggest that the three KASH peptides that bind to a SUN trimer likely do not all come from the same KASH protein (Sosa et al., 2012). However, although SUN5 is essential for sperm head-tail coupling, sperm KASH proteins are not essential for male fertility (Dunleavy et al., 2019), suggesting that an alternative LINC complex forms the foundation of the head-tail coupling apparatus in mammalian sperm.

3.3 Concluding Remarks

In this chapter, I used cryo-FIB milling-enabled cryo-ET to image fine structural details of the sperm head and head-tail junction, revealing previously-undetected macromolecular complexes that appear to be conserved across mammalian species. I find proteasome-like particles in locally decondensed regions of chromatin, previously thought to be empty based on classical electron micrographs. I also find an ordered array of nuclear envelope proteins and propose that these represent SUN5, which is essential for head-tail coupling. Direct confirmation of the identities of these proteins awaits direct labelling or genetic perturbation. Immense insight will likely come from using these methods combined with cryo-FIB-ET to image the process of chromatin compaction and nuclear reshaping during spermiogenesis.

4

A conserved supramolecular array anchors mitochondria to the cytoskeleton in the sperm mitochondrial sheath

Contents

4.1 Introduction 60
4.2 Results and Discussion 62
4.2.1 Mitochondrial dimensions vary across species and spatially along the midpiece. 62
4.2.2 Cristae architecture varies across species. 66
4.2.3 Inter-mitochondrial junctions are associated with novel linker complexes. 67
4.2.4 Mitochondria are anchored to the cytoskeleton through a conserved ladder-like array in the outer mitochondrial membrane. 69
4.2.5 Glycerol kinase-like proteins and voltage dependent anion channels are probable constituents of the ladder-like array. . 72
4.2.6 Amorphous calcium granules form in mitochondria of sperm incubated in capacitating conditions. 76
4.3 Concluding Remarks 78

4.1 Introduction

In many cell types, mitochondria collectively form a dynamic network whose members divide, fuse, and communicate with one another (Glancy et al., 2015; Viana et al., 2020; Vincent et al., 2017). Through interactions with the cytoskeleton, mitochondria

are transported – sometimes across large distances – and positioned in response to dynamic stimuli (Moore and Holzbaur, 2018). Interactions with the cytoskeleton can also restrain mitochondria to specific subcellular localizations. In neurons, axonal mitochondria can be immobilized by interactions with the microtubule or actin cytoskeletons (Chen and Sheng, 2013; Kang et al., 2008; Moore and Holzbaur, 2018). In cardiac and skeletal muscle, mitochondria are constrained by myofibrils and by the sarcoplasmic reticulum (Huang et al., 2013; Lavorato et al., 2017). However, despite the prevalence of inter-mitochondria and mitochondria-cytoskeleton interactions and their integral roles in cellular function, there is very little information on the molecular architectures of these interaction sites in any cell type.

One of the most striking mitochondrial configurations occurs in amniote sperm, where mitochondria are arranged in a spiral around the axoneme, defining a region called the midpiece (Fawcett, 1970, 1975). Mitochondria are among the few organelles in mature sperm, which otherwise lose most of their cytoplasm and organelles *en route* to becoming highly streamlined cells specialized for finding and fusing with the egg. The extensive mitochondrial sheath in amniote sperm may be an adaptation needed to power the large, long flagellum in these lineages. Variations in midpiece morphometry affect sperm motility and competitiveness (Firman and Simmons, 2010; Fisher et al., 2016), and different species rely on energy from mitochondrial respiration to different extents (Marin et al., 2003; Tourmente et al., 2015), warranting comparative studies of mitochondrial structure across species.

Although the gross ultrastructure of the mitochondrial sheath has been described in a wide range of species, the molecular underpinnings of this unique arrangement remain undefined. For instance, we do not know whether mitochondria within the sheath communicate with one another. Understanding how sperm mitochondria communicate has important implications for sperm metabolism, especially since mammalian sperm rapidly change their metabolic requirements during capacitation and hyperactivation (Hidalgo et al., 2020). We also do not understand how sperm mitochondria are anchored to the underlying cytoskeleton. Defining the basis for this interaction is imperative for understanding how the mitochondrial sheath assembles,

which in turn is of practical importance since malformation of the mitochondrial sheath is associated with many cases of male infertility (Chen et al., 2017b).

The structure and development of the mitochondrial sheath have been imaged with a range of electron microscopy (EM) methods, including scanning EM, freeze-fracture EM, and serial section transmission EM (Bahr and Engler, 1970; Gervasi et al., 2018; Ho and Wey, 2007; Otani et al., 1988). However, these techniques require harsh sample preparation methods that can distort fine cellular structure and limit achievable resolution. In this chapter, I use cryo-FIB milling, cryo-ET, and image processing to image the mitochondrial sheath in mature sperm from three mammalian species. I take advantage of the uniquely multi-scale capabilities of cryo-ET to unveil new aspects both of the overall organization of the mitochondrial sheath and of the molecular structures important for its assembly.

4.2 Results and Discussion

4.2.1 Mitochondrial dimensions vary across species and spatially along the midpiece.

I imaged the mitochondrial sheath in mature sperm from three mammalian species, namely the pig (*Sus scrofa*), the horse (*Equus caballus*), and the mouse (*Mus musculus*). These species differ in terms of sperm size, motility patterns, and metabolism. To visualize the overall organization of the mitochondrial sheath, I imaged whole sperm with the Volta phase plate (VPP) **(Fig. 4.1)** (Danev et al., 2014; Fukuda et al., 2015). Neural-network based segmentation (Chen et al., 2017a) of the mitochondrial membrane revealed how mitochondria are organized in three dimensions **(Fig. 4.2a-f)**. I also measured the width of each mitochondrion at multiple points along its length. I then divided mitochondria into groups based on their positions along the midpiece, as measured by their distance from the neck **(Fig. 4.2g,h)**. The midpiece is ~10 μm long in both pig and horse sperm, but ~20 μm long in mouse sperm, so each group represents 2 μm in the pig and the horse and 4 μm in the mouse.

Mouse sperm mitochondria were ~1.5 X wider than pig and horse sperm mitochondria overall **(Fig. 4.2g)**. Because mitochondria wrap around the axoneme,

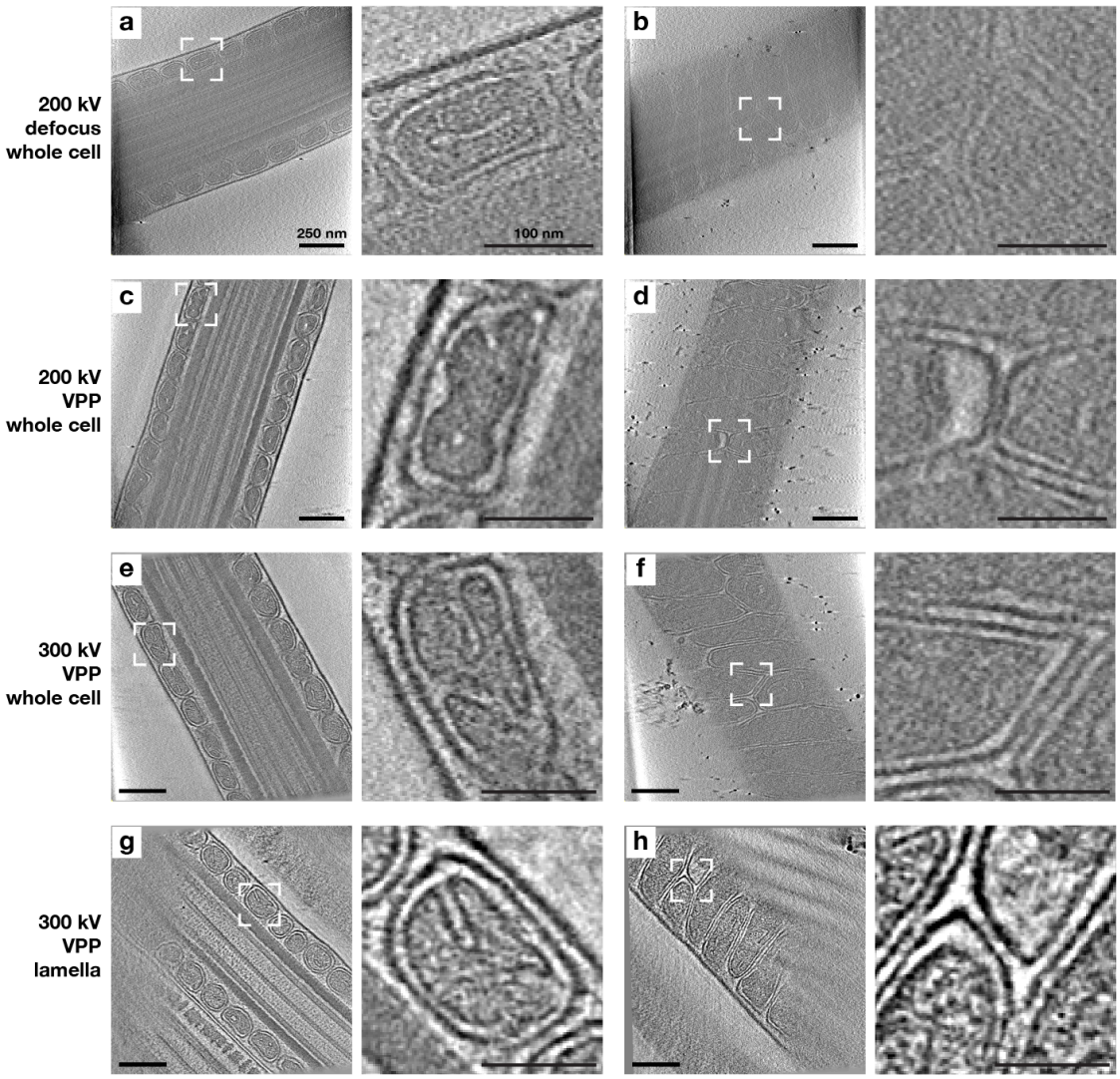


Figure 4.1 | Cryo-focused ion beam milling and use of the Volta phase plate (VPP) improve cryo-ET imaging of the midpiece. Slices through cryo-tomograms of pig sperm midpieces, acquired **(a,b)** on whole cells with an accelerating voltage of 200 kV and without the VPP; **(c,d)** on whole cells with an accelerating voltage of 200 kV and with the VPP; **(e,f)** on whole cells with an accelerating voltage of 300 kV and with the VPP; **(g,h)** on lamellae (~300-nm thick) with an accelerating voltage of 300 kV and with the VPP. Left panels (a,c,e,g) show central longitudinal slices, while right panels (b,d,f,h) show tangential slices. **Scale bars:** left panels – 250 nm, right panels (digital zooms) – 100 nm.

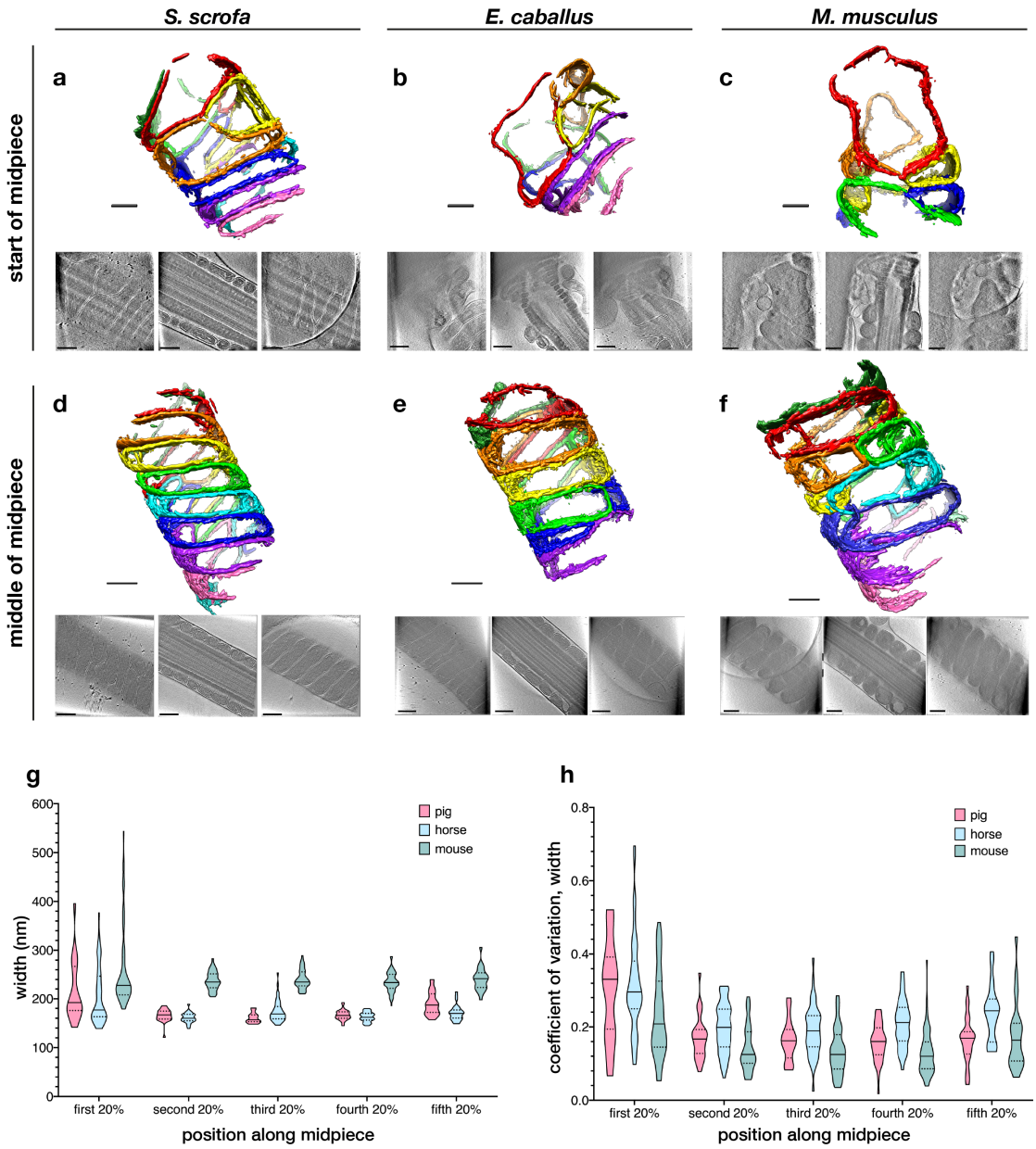


Figure 4.2 | Mitochondrial dimensions vary across species and spatially along the midpiece. (a-f) Segmentation of sperm mitochondria from the start (a-c) or middle (d-f) of the midpiece from pig (a,d), horse (b,e), and mouse (c,f) sperm. Slices through VPP cryo-tomograms used to generate the segmentations are shown in bottom panels. **(g)** Plotting the average width of mitochondria from different regions of the midpiece shows that mouse sperm mitochondria are larger than pig and horse sperm mitochondria. Note also that, in all three species, mitochondria at the start of the midpiece are larger than those in more distal parts. **(h)** Mitochondrial width was measured at five points along the length of each mitochondrion, and plotting the coefficient of variation from different regions along the midpiece shows that mitochondria at the start of the midpiece have more variable widths along their lengths. In (g,h) solid lines represent the median and dotted lines represent the first and third quartiles. **Scale bars:** 250 nm.

Table 4.1 | Measurements of mitochondrial width in different regions of the midpiece in sperm from three mammalian species.

species	mitochondria width (nm, mean ± s.d.) in fraction of midpiece				
	first 20%	second 20%	third 20%	fourth 20%	last 20%
S. scrofa	215 ± 64 (n=19)	166 ± 12 (n=29)	161 ± 11 (n=17)	166 ± 10 (n=38)	166 ± 10 (n=38)
E. caballus	206 ± 58 (n=48)	161 ± 10 (n=67)	174 ± 22 (n=43)	163 ± 10 (n=49)	171 ± 16 (n=30)
M. musculus	262 ± 83 (n=63)	238 ± 19 (n=48)	240 ± 20 (n=47)	235 ± 20 (n=63)	240 ± 23 (n=23)

this difference has fairly large implications for the overall width of the midpiece. Most mitochondria in the middle ~60% of the midpiece are crescent-shaped tubes **(Fig. 4.2d-f)** with consistent widths along their lengths **(Fig. 4.2h)**. Intriguingly, mitochondria at the start of the midpiece **(Fig. 4.2a-c)** are larger **(Fig. 4.2g, Table 4.1)** than their more distal counterparts. Moreover, these mitochondria had more variable shapes, evidenced by greater variation in their widths at different point along their lengths **(Fig. 4.2h, Table 4.1)**.

Mitochondria are generally packed into left-handed helices along most of the midpiece in all three species, although precise arrangements differ **(Fig. 4.2d-f)**. In the mouse, they are arranged in double helices packed end-to-end **(Fig. 4.2f)**. In the horse and pig, helices are often interrupted when the end of one mitochondrion is sandwiched between two neighboring mitochondria **(blue in Fig. 4.2e)**.

Overall, mitochondrial dimensions are remarkably consistent in sperm, which contrasts with other mitochondria-rich tissues such as muscle, in which there are massive variations in mitochondrial size and morphology (Vincent et al., 2019). It is unclear how this consistency is regulated during spermiogenesis. Spatial variation in mitochondrial packing may be driven by changes in the diameter of the midpiece, which decreases distally from the head concomitant with gradual thinning of the outer dense fibers (ODFs).

4.2.2 Cristae architecture varies across species.

To visualize the internal organization of sperm mitochondria in a near-native state, I imaged sperm thinned by cryo-FIB milling **(Fig. 4.3)**. This revealed unexpected diversity in the internal ultrastructure of mitochondria across mammalian species, especially in terms of cristae morphology **(Fig. 4.3)**. Horse sperm mitochondria have an expanded intermembrane space and a condensed matrix **(Fig. 4.3c,d)**. Mouse sperm mitochondria have an expanded matrix, with a narrow intermembrane space and thin cristae **(Fig. 4.3e,f)**. Pig sperm mitochondrial morphology is intermediate **(Fig. 4.3a,b)**, and although the mitochondrial matrix was dense, I could identify individual complexes that resembled ATP synthase on cristae of FIB-milled mitochondria **(Fig. 4.3h,i)**, which was confirmed by subtomogram averaging **(Fig. 4.3i')**.

These cross-species differences correlate with measurements of matrix volume relative to mitochondrial volume **(Fig. 4.3g)**. In this regard, horse sperm mitochondria resemble "condensed" mitochondria, which correlate with higher rates of oxidative activity (De Martino et al., 1979; Perkins and Ellisman, 2011). Indeed, horse sperm are dependent on oxidative phosphorylation (Davila et al., 2016), whereas pig (Marin et al., 2003) and mouse sperm (Mukai and Okuno, 2004; Odet et al., 2013) rely on a glycolytic mechanism.

A striking feature of mouse sperm mitochondria was prominent trans-mitochondrial cristae alignment **(Fig. 4.3e,f)**, that was not observed in pig or in horse sperm **(Fig. 4.3a-d)**. Trans-mitochondrial cristae alignment has also been reported in muscle tissue of various organisms (Picard et al., 2015), and is proposed to mediate electrochemical coupling between adjacent mitochondria. To my knowledge, this is the first time this phenomenon has been observed in mature sperm from any lineage. It is particularly curious, however, that trans-mitochondrial cristae alignment in sperm is species-specific. Coupled with differences in mitochondrial morphology and cristae architecture, these observations suggest fundamental differences in mitochondrial energetics across species.

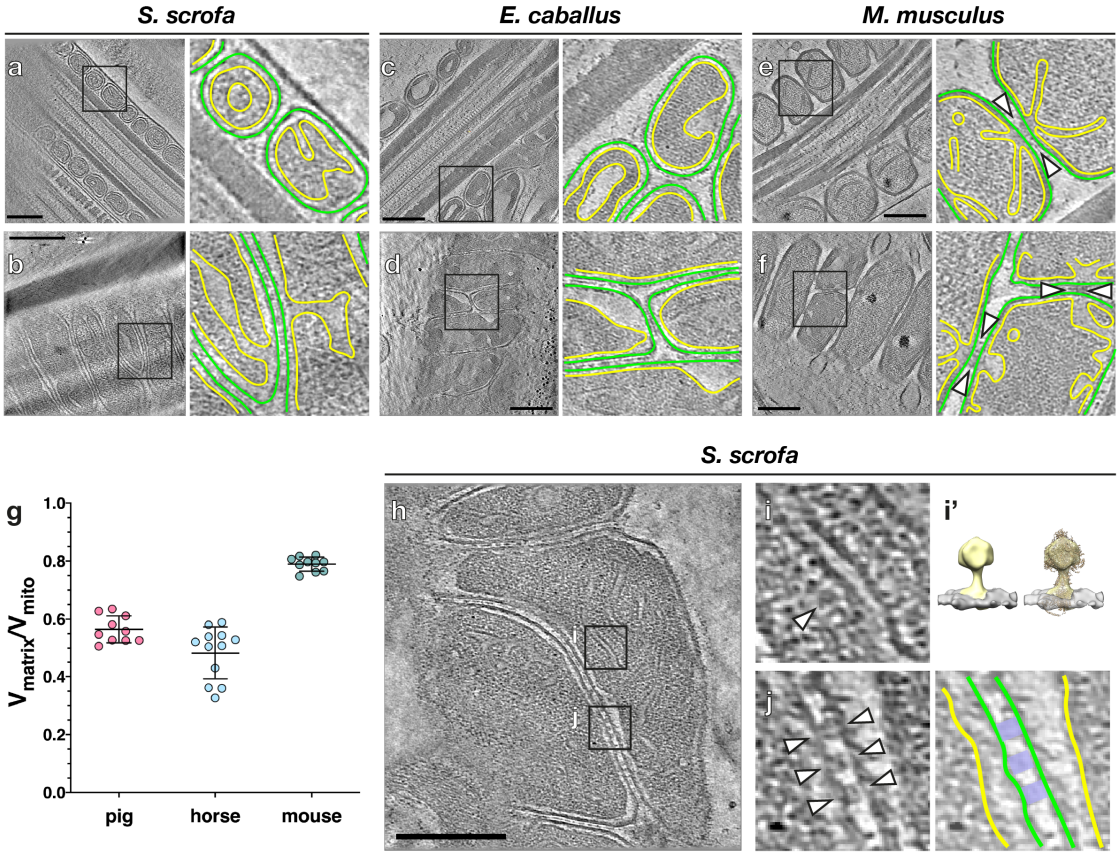


Figure 4.3 | Cristae organization varies across species. **(a-f)** Slices through cryo-tomograms of FIB-milled pig **(a,b)**, horse **(c,d)**, and mouse **(e,f)** sperm midpieces. Right panels show digital zooms of the regions boxed out in the left panels. The outer mitochondrial membrane (OMM) is traced in green and the inner mitochondrial membrane (IMM) is drawn in yellow. **(g)** Quantifying the volume enclosed by the mitochondrial matrix relative to the volume enclosed by the whole mitochondrion reveals that pig and horse sperm mitochondria have more expanded cristae and more condensed matrices than mouse sperm mitochondria. Lines represent mean ± standard deviation. **(h)** Slice through a cryo-tomogram of FIB-milled pig sperm mitochondria close to the connecting piece. **(i)** ATP synthase can be directly identified on cristae based on its characteristic shape, which is confirmed by subtomogram averaging (i'). **(j)** Novel inter-mitochondrial linkers tether neighboring mitochondria to each other (arrowheads in left panel, purple in right panel). **Scale bars:** 250 nm.

4.2.3 Inter-mitochondrial junctions are associated with novel linker complexes.

The organization of the mitochondrial sheath means each mitochondrion has three distinct surfaces – one facing the plasma membrane, one facing the axoneme, and one facing neighboring mitochondria. Imaging cryo-FIB-milled sperm revealed that each domain is associated with a distinct molecular signature **(Figs. 4.3 - 4.6)**, consistent with observations from freeze-fracture EM of guinea pig sperm (Olson and

Table 4.2 | Image acquisition and processing metrics for subtomogram averaging of mitochondrial protein complexes in mammalian sperm.

Parameter	Species		
	Sus scrofa	*Equus caballus*	*Mus musculus*
ATP synthase			
sample type	lamellae	-	-
microscope (accelerating voltage)	Arctica (200 kV)	-	-
pixel size (Å)	4.34	-	-
symmetry	C1	-	-
number of particles	209	-	-
estimated resolution (Å)	38	-	-
outer mitochondrial membrane arrays			
sample type	lamellae	lamellae	lamellae
microscope (accelerating voltage)	Arctica (200 kV)	Arctica (200 kV)	Arctica (200 kV)
pixel size (Å)	4.34	5.66	5.66
symmetry	C1/C2	C1/C2	C1/C2
number of particles	268/536	962/1924	972/1944
estimated resolution (Å)	39/35	38/33	38/22

Winfrey, 1992). Cryo-ET revealed that inter-mitochondrial linkers span the ~8-nm distance between outer membranes of neighboring mitochondria and are positioned at regularly spaced intervals in both the pig and the horse **(Fig. 4.3a-d, h-j)**. In the mouse, inter-mitochondrial linkers are more sparsely distributed, but are consistently associated with trans-mitochondrial cristae alignment **(Fig. 4.3e,f, right)**.

Inter-mitochondrial linkers may represent a molecular basis for generating and maintaining the unique packing arrangement of the mitochondrial sheath. The linker complexes could also represent the molecular underpinnings of the electron-dense inter-mitochondrial junctions seen by classical EM in other cell types (Huang et al., 2013; Picard et al., 2015). I did not observe mitochondrial nanotunnels in any of the species examined, in contrast to their relative abundance in muscle tissue (Vincent et al., 2019, 2017).

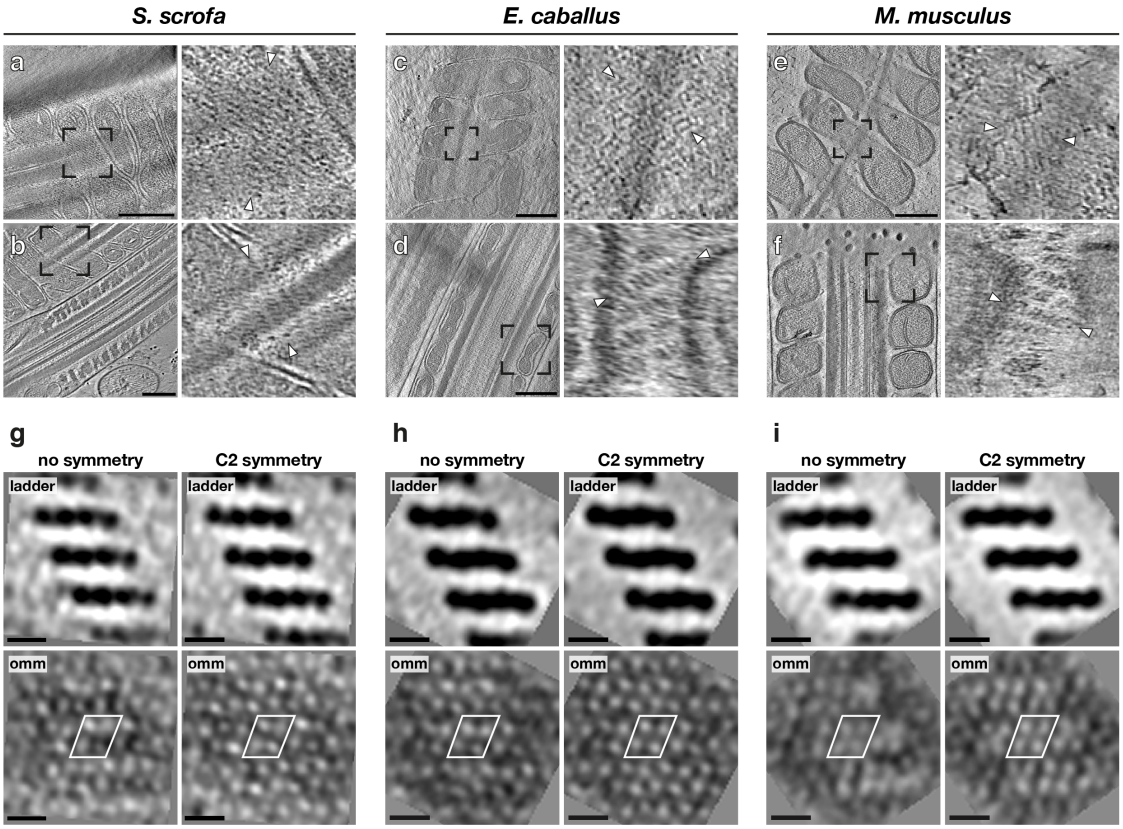


Figure 4.4 | Ladder-like arrays on the axoneme-facing surface of the outer mitochondrial membrane (OMM) are conserved. (a-f) Slices through cryo-tomograms of FIB-milled pig (a,b), horse (c,d), and mouse (e,f) mitochondria. Right panels show digital zooms of the regions boxed out in the left panels, with arrowheads indicating ladder-like arrays. **(g-i)** Subtomogram averages of the ladder-like array and the OMM before (left panels) and after (right panels) applying twofold symmetry. **Scale bars:** (a-f) 250 nm, (g-i) 10 nm.

4.2.4 Mitochondria are anchored to the cytoskeleton through a conserved ladder-like array in the outer mitochondrial membrane.

The axoneme-facing surface of the outer mitochondrial membrane (OMM) is characterized by an ordered array **(Fig. 4.4, 4.5)** that is absent from the plasma membrane-facing surface **(Fig. 4.6a)**. These arrays are present in all three species and along the entire midpiece **(Fig. 4.4a-f)**, and closely resemble the particle rows seen in guinea pig sperm by freeze-fracture EM (Friend and Heuser, 1981).

I averaged the ladder-like arrays from cryo-FIB-milled lamellae and found that they consist of ~22-nm-long two-fold symmetric boat-shaped particles that rise ~5-nm above the membrane **(Fig. 4.4g-i, 4.5)**. Assuming an average protein density

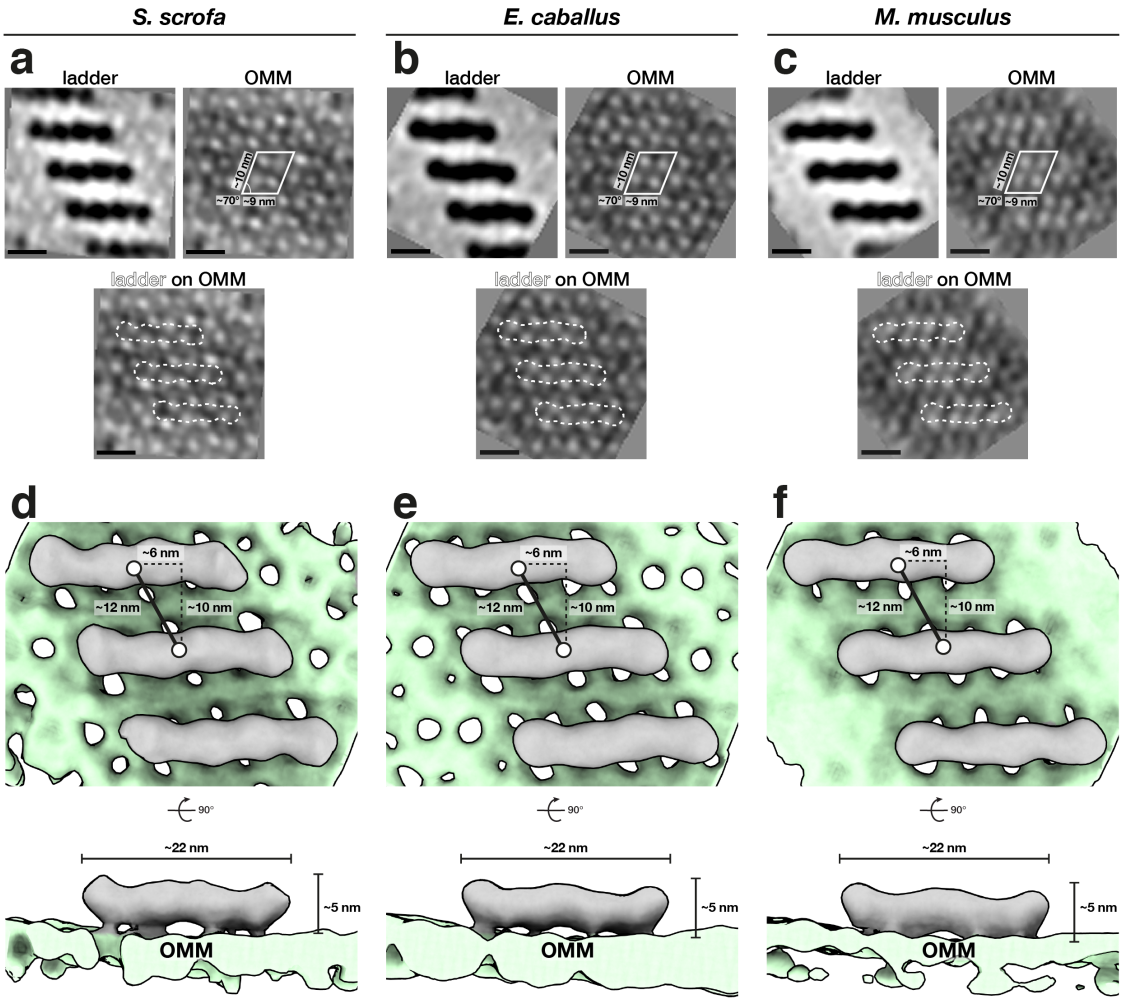


Figure 4.5 | Structural details of ladder-like arrays on sperm mitochondria. (a-c) Subtomogram averages of the ladder-like array and the outer mitochondrial membrane (OMM) with twofold symmetry applied. **(d-f)** Isosurface renderings of the subtomogram averages in (a-c) with ladder-like arrays in grey and the OMM in green. **Scale bars:** (a-c) 10 nm.

of 1.43 g/cm^3 (Quillin and Matthews, 2000), equivalent to 0.861 Da/Å^3, I estimate that each particle is ~250-kDa based on its volume. When viewed orthogonal to the membrane, it is evident that the ladder-like arrays are formed by rows of these boat-shaped particles arranged parallel to each other. Each particle is related to its closest neighbors by a ~10 nm translation perpendicular to the particle long axis and a ~6 nm shift along the particle long axis, yielding a center-to-center spacing of ~12 nm **(Fig. 4.5d-f)**. Because of the offset along the particle long axis, the line through neighboring particle centers is oriented ~60° relative to the long axis of each particle. Each row of particles is spaced ~12 nm from the adjacent one, and the rows overall

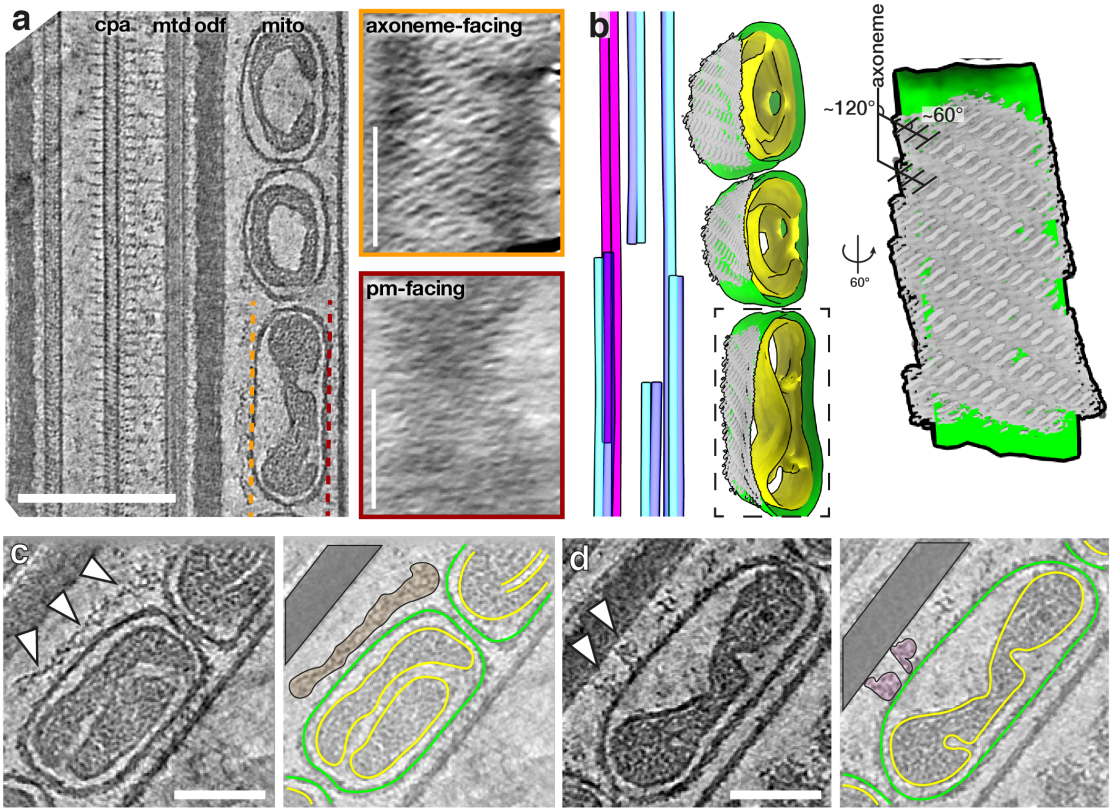


Figure 4.6 | Ladder-like arrays anchor sperm mitochondria to the cytoskeleton. (a) Slice through a cryo-tomogram of a FIB-milled horse sperm midpiece, showing mitochondria (mito), outer dense fibers (odf), microtubule doublets (mtd), and the central pair apparatus (cpa). The ladder-like array is only found on the axoneme-facing surface (yellow) of midpiece mitochondria, and not on the plasma membrane-facing surface (red). **(b)** Left panel: Segmentation of the tomogram shown in (a), with the OMM in green, the IMM in yellow, ladder-like arrays in grey, microtubule doublets in blue, and the cpa in pink. Right panel: Rotated and zoomed-in view of the axoneme-facing surface of a mitochondrion. The axoneme is oriented vertically, so the ladder-like arrays are oriented ~120° to the flagellar long axis, and individual particles within the array are oriented ~60° to this axis. **(c,d)** Slices through a cryo-tomogram of a FIB-milled horse sperm midpiece showing how the ladder-like array interacts with the submitochondrial reticulum to anchor mitochondria to the ciliary cytoskeleton. **Scale bars:** (a) left - 250 nm, insets - 100 nm; (c,d) 100 nm.

are oriented ~120° relative to the long axis of the flagellum **(Fig. 4.6b)**. The OMM underlying the ladder-like arrays also has a strikingly regular structure. Here, the OMM is studded with ~3-4 nm-wide pores arranged in a lattice whose unit cell is a parallelogram with a = ~9 nm, b = ~10 nm, and α = ~70° **(Fig. 4.4g-i, 4.5a-c)**. Each boat-shaped particle stretches across 3 unit cells. The boat-shaped particles may thus be peripheral membrane proteins that are anchored through interactions with the membrane-embedded proteins that make up the OMM lattice.

Remarkably, the ladder-like arrays and the OMM lattices are conserved across the three species examined, both in terms of individual particle dimensions and in terms of their supramolecular arrangement **(Fig. 4.5)**. This conservation suggests that the ladder-like arrays are a crucial structural element of the mitochondrial sheath. Consistent with this, we observed direct interactions between the ladder-like array and cytoskeletal filaments surrounding the ODFs **(Fig. 4.6c,d)**, suggesting that these arrays anchor mitochondria to the midpiece cytoskeleton. Indeed, cytoskeletal filaments in the midpiece, also called the submitochondrial reticulum, co-purify with sperm mitochondria (Olson and Winfrey, 1986, 1990), suggesting that they are tightly associated. At this point, it is unclear whether these arrays function in the initial microtubule-based transport of mitochondria from the cytoplasm to the elongating flagellum or in later stages of midpiece formation where mitochondria coil around the axoneme (Pleuger et al., 2020). A more comprehensive understanding of the role of the ladder-like array in the morphogenesis of the mitochondrial sheath will likely come from studies of spermiogenesis and from gene-modified animals with midpiece dysplasia.

4.2.5 Glycerol kinase-like proteins and voltage dependent anion channels are probable constituents of the ladder-like array.

As a step towards determining the molecular composition of the ladder-like arrays, I collaborated with Dr Riccardo Zenezini-Chiozzi and Johannes Hevler of the Mass Spectrometry Group at Utrecht University. Together, we performed label-free quantitative proteomics and whole-cell cross-linking mass spectrometry of pig sperm. Our proteomics experiments show that the most abundant OMM proteins in pig sperm are two isoforms of the voltage-dependent anion channel (VDAC), VDAC2 and VDAC3 **(Table 4.3)**. VDAC is a strong candidate for the OMM pores because it folds into a 19-stranded β-barrel with a pore diameter of ~3.5 nm (Bayrhuber et al., 2008), which matches the sizes of the pores resolved in our averages **(Fig. 4.7a)**. Crucially, VDAC forms ordered supramolecular arrays in the outer mitochondrial membrane (Gonçalves et al., 2007; Guo and Mannella, 1993; Hoogenboom et al.,

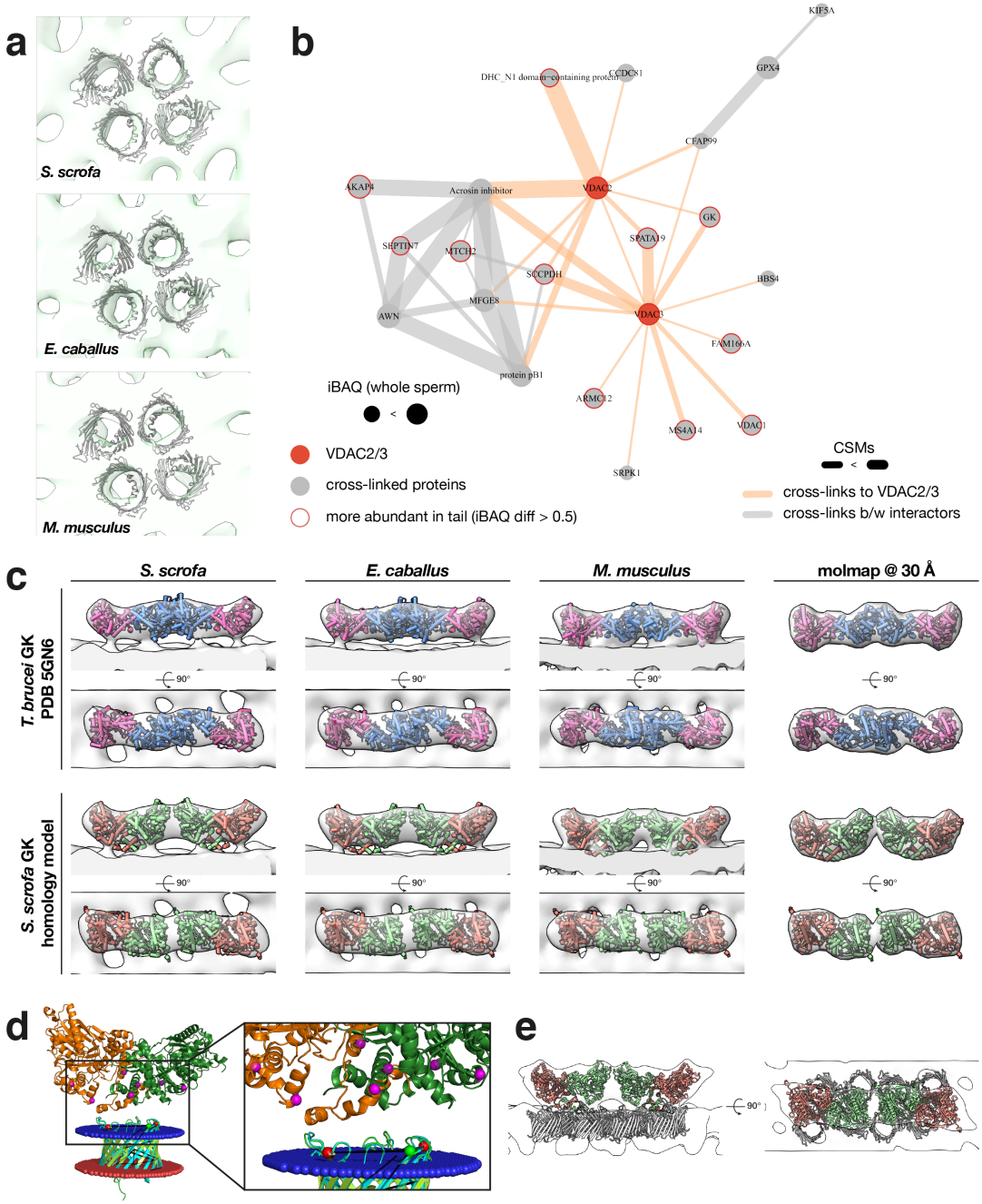


Figure 4.7 | Glycerol kinase (GK)-like proteins and voltage dependent anion channels (VDAC) are probable constituents of the ladder-like array. **(a)** The VDAC pore size is consistent with the pore sizes resolved in our averages. The crystal structure of VDAC2 from zebrafish (PDB 4BUM) is shown in grey, fitted into our averages (green). **(b)** Whole-cell cross-linking mass spectrometry (XL-MS) identified three proteins, SPATA19, GPX4, and GK, known to localize to the OMM in mature sperm and whose disruption causes defects in the mitochondrial sheath. **(c)** The molecular dimensions of two GK or GK-like protein dimers end-to-end match the boat-shaped particles. Top panels: fit two copies of a crystal structure of GK from *Trypanosoma brucei* (PDB 5GN6). Bottom panels: fit two copies of a pig GK Robetta homology model. **(d)** Mapping cross-linked Lys residues onto homology models of pig GK (pink spheres) and pig VDAC2/3 (red/green spheres) suggests an orientation consistent with subtomogram averages. **(e)** A model of a GK-like dimer-of-dimers (homology models of pig GK) on a VDAC scaffold (PDB 4BUM) fitted into our pig subtomogram average (outline).

2007; Mannella, 1982), and the lattice parameters of our OMM array closely resemble those of one form of the VDAC lattice (Guo and Mannella, 1993; Mannella, 1998). Importantly, the other β-barrel OMM proteins (e.g; components of the translocase of the outer membrane, TOM, and sorting and assembly machinery, SAM, complexes) were much less abundant **(Table 4.3)**.

To search for candidates for the boat-shaped particles, we then used whole cell cross-linking mass spectrometry (XL-MS) to find potential VDAC2/3 interaction partners on the OMM. We treated cells with disuccinimidyl sulfoxide (DSSO), which cross-links free lysines that are within 30 Å (Cα-Cα) of each other, and screened for cross-links present in at least two biological replicates. We found two major interaction hubs centered around VDAC2/3 **(Fig. 4.7b)**, one comprising mitochondria-associated proteins and one comprising acrosome-associated proteins, which is consistent with immunofluorescence studies localizing VDAC2/3 both to the midpiece and to the acrosome (Hinsch et al., 2004; Kwon et al., 2013). Of the proteins in the mitochondria-associated interaction hub, three proteins are particularly noteworthy because they are known to localize to the OMM and because their disruption results in dysplasia of the mitochondrial sheath: spermatogenesis-associated protein 19 (SPATA19) (Mi et al., 2015), glutathione peroxidase 4 (GPX4) (Imai et al., 2009; Schneider et al., 2009), and glycerol kinase (GK) (Chen et al., 2017b; Shimada et al., 2019).

SPATA19 and GK cross-link directly to VDAC2/3 **(Fig. 4.7b)**, suggesting that they are in close proximity to the OMM, as would be expected for the boat-shaped particles in our averages. SPATA19 is a small protein with an estimated molecular weight of 18 kDa in the pig; to fit into our densities, it must either be present in multiple copies or form a complex with other proteins. GK has an estimated molecular weight of 60 kDa, and crystal structures suggest that GK forms an S-shaped dimer that is conserved from bacteria (Bystrom et al., 1999; Fukuda et al., 2016) to eukaryotes (Balogun et al., 2019; Schnick et al., 2009). Two GK dimers arranged end-to-end fit surprisingly well into our boat-shaped densities **(Fig. 4.7c)**. We then mapped the cross-links between GK and VDAC2/3 onto homology models of these proteins. All cross-links were consistent with how GK and VDAC2/3 would be oriented based on

Table 4.3 | Outer mitochondrial membrane proteins in pig sperm identified through label-free mass spectrometry.

Gene name	Protein name	iBAQ	Unique peptides	Seq coverage (%)	Seq length	MW (kDa)
VDAC3	Voltage-dependent anion-selective channel protein 3	9.65132	17	66.8	283	30.603
VDAC2	Voltage-dependent anion-selective channel protein 2	9.62553	21	76.2	294	31.604
SPATA19	Spermatogenesis-associated protein 19, mitochondrial	9.1826	16	91.6	154	17.97
PPP1CC	Serine/threonine-protein phosphatase PP1-gamma catalytic subunit	9.17373	13	82.5	337	38.548
GK	Glycerol kinase	8.94769	19	81.7	553	60.681
SPATA18	Mitochondria-eating protein	8.86132	51	57.9	560	63.3
PEBP1	Phosphatidylethanolamine-binding protein 1	8.83808	19	92	187	20.971
FUNDC2	FUN14 domain-containing protein 2	8.72412	19	77.2	189	20.571
CYB5B	Cytochrome b5 type B	8.71029	12	71.5	144	16.199
HK1	Hexokinase-1	8.61928	98	68	915	102.29
HADHB	Trifunctional enzyme subunit beta, mitochondrial	8.59686	47	77.7	475	51.25
MAOA	Amine oxidase [flavin-containing] A	8.57693	36	66.2	527	59.802
CISD1	CDGSH iron-sulfur domain-containing protein 1	8.55178	7	76.4	106	11.965
PHB	Prohibitin	8.52293	30	93	272	29.804
VDAC1	Voltage-dependent anion-selective channel protein 1	8.45978	9	53.4	283	30.726
RPS27A	Ubiquitin-40S ribosomal protein S27a	8.43921	2	15.9	132	15.227
UBA52	Ubiquitin-60S ribosomal protein L40	8.37732	8	53.1	128	14.728
CYB5R3	NADH-cytochrome b5 reductase 3	8.10106	23	77.2	272	30.83
PHB2	Prohibitin-2	8.06555	22	72.2	299	33.387
ACSL6	Long-chain-fatty-acid–CoA ligase 6	8.03162	1	76.2	722	80.706
MTX2	Metaxin-2	7.78606	11	54.7	267	30.106
SAMM50	Sorting and assembly machinery component 50 homolog	7.70276	32	63.8	469	51.871
NME1	Nucleoside diphosphate kinase A	7.67576	5	61.2	152	17.109
TOMM40	Mitochondrial import receptor subunit TOM40 homolog	7.562	12	63.2	361	37.758
BRI3BP	BRI3-binding protein	7.5364	4	16.1	242	26.985
VAT1	Synaptic vesicle membrane protein VAT-1 homolog	7.42728	27	74	400	42.687
DNAJC11	DnaJ homolog subfamily C member 11	7.42552	31	61.4	559	63.352
SYNJ2BP	Synaptojanin-2-binding protein	7.40987	3	21.4	145	15.774
COASY	Bifunctional coenzyme A synthase	7.37311	18	53.2	562	61.748
SH3GLB1	Endophilin-B1	7.33594	22	53	402	45.075
BPHL	Valacyclovir hydrolase	7.2781	15	64	297	33.278
PGAM5	Serine/threonine-protein phosphatase PGAM5, mitochondrial	7.27757	16	60.2	289	32.028
TOMM22	Mitochondrial import receptor subunit TOM22 homolog	7.22293	6	61	141	15.351
TOMM34	Mitochondrial import receptor subunit TOM34	6.98055	11	37.9	309	34.553
MFF	Mitochondrial fission factor	6.88656	2	4.6	217	25.006
MAOB	Amine oxidase [flavin-containing] B	6.88568	22	59.4	520	58.252
LETMD1	LETM1 domain-containing protein 1	6.7699	12	46.6	341	39.801
FIS1	Mitochondrial fission 1 protein	6.75893	5	39.5	152	16.838
CPT1B	Carnitine O-palmitoyltransferase 1, muscle isoform	6.75627	16	30.5	734	84
OPA1	Dynamin-like 120 kDa protein, mitochondrial	6.646	40	50.9	997	115.79
AGPAT5	1-acyl-sn-glycerol-3-phosphate acyltransferase epsilon	6.63189	6	23	365	41.923
ACSL3	Long-chain-fatty-acid–CoA ligase 3	6.62267	28	49	720	80.275
NIPSNAP2	Protein NipSnap homolog 2	6.59304	8	39.6	268	31.341
MARCH5	E3 ubiquitin-protein ligase MARCH5	6.5689	8	42.1	278	31.231
RHOT1	Mitochondrial Rho GTPase 1	6.48603	9	21	599	68.582
ACSL1	Long-chain-fatty-acid–CoA ligase 1	6.37754	8	12.6	699	78.032
AGK	Acylglycerol kinase, mitochondrial	6.22886	10	34.9	421	46.939
ACSL5	Long-chain-fatty-acid–CoA ligase 5	5.71818	10	20.9	669	75.224
BID	BH3-interacting domain death agonist	5.57155	2	11.8	186	20.86
ARG1	Arginase-1	5.33887	3	11.5	322	35.018

our averages; that is, all cross-links were between the cytosolic face of VDAC2/3 and the putative OMM-facing surface of GK **(Fig. 4.7d,e)**. Interpreting the boat-shaped particles as GK-like proteins would also be consistent with known OMM localization of GK in mature sperm, and with the mitochondrial dysplasia in sperm from mice lacking sperm-specific GK isoforms (Chen et al., 2017b; Shimada et al., 2019).

4.2.6 Amorphous calcium granules form in mitochondria of sperm incubated in capacitating conditions.

As a step towards understanding the roles of mitochondria in capacitation and hyperactivation, I imaged pig sperm incubated in *in vitro* capacitation media for ~2 h **(Fig. 4.8)**. Electron-dense granules were visible in mitochondrial matrices of sperm incubated in capacitating conditions with or without the addition of calcium ionophore **(Fig. 4.8a-b)**. Mitochondrial granules were amorphous **(Fig. 4.8c)** and granules were present in ~50% of cryoEM projection images acquired from capacitated or ionophore-treated sperm, but were absent from only Percoll-washed sperm **(Fig. 4.8d)**. Ionophore-treated sperm had similar numbers of granules per mitochondrion (mean ± s.d. 10 ± 5) to only capacitated sperm (11 ± 6) **(Fig. 4.8e)**. Granules in ionophore-treated cells were only slightly larger (58 ± 18 nm) than those in only capacitated sperm (49 ± 15 nm) **(Fig. 4.8f)**.

To probe the chemical nature of mitochondrial granules, I then imaged ionophore-treated capacitated sperm with cryo-high angle annular dark field scanning transmission electron microscopy (cryo-HAADF-STEM). In HAADF-STEM, annular dark-field detector is used to collect electrons that are inelastically scattered at high angles; image contrast thus comes from differences in scattering propensity, so elements of higher atomic number appear brighter than those of lower atomic number. I observed bright spots in mitochondria that stood out from other cellular structures such as the connecting piece and the nucleus **(Fig. 4.8h,i)**, which suggests that granules contain elements heavier than carbon, oxygen, and phosphorus.

To define the elemental content of mitochondrial granules, I interfaced cryo-HAADF-STEM with energy dispersive X-ray spectroscopy (EDX). The electron beam

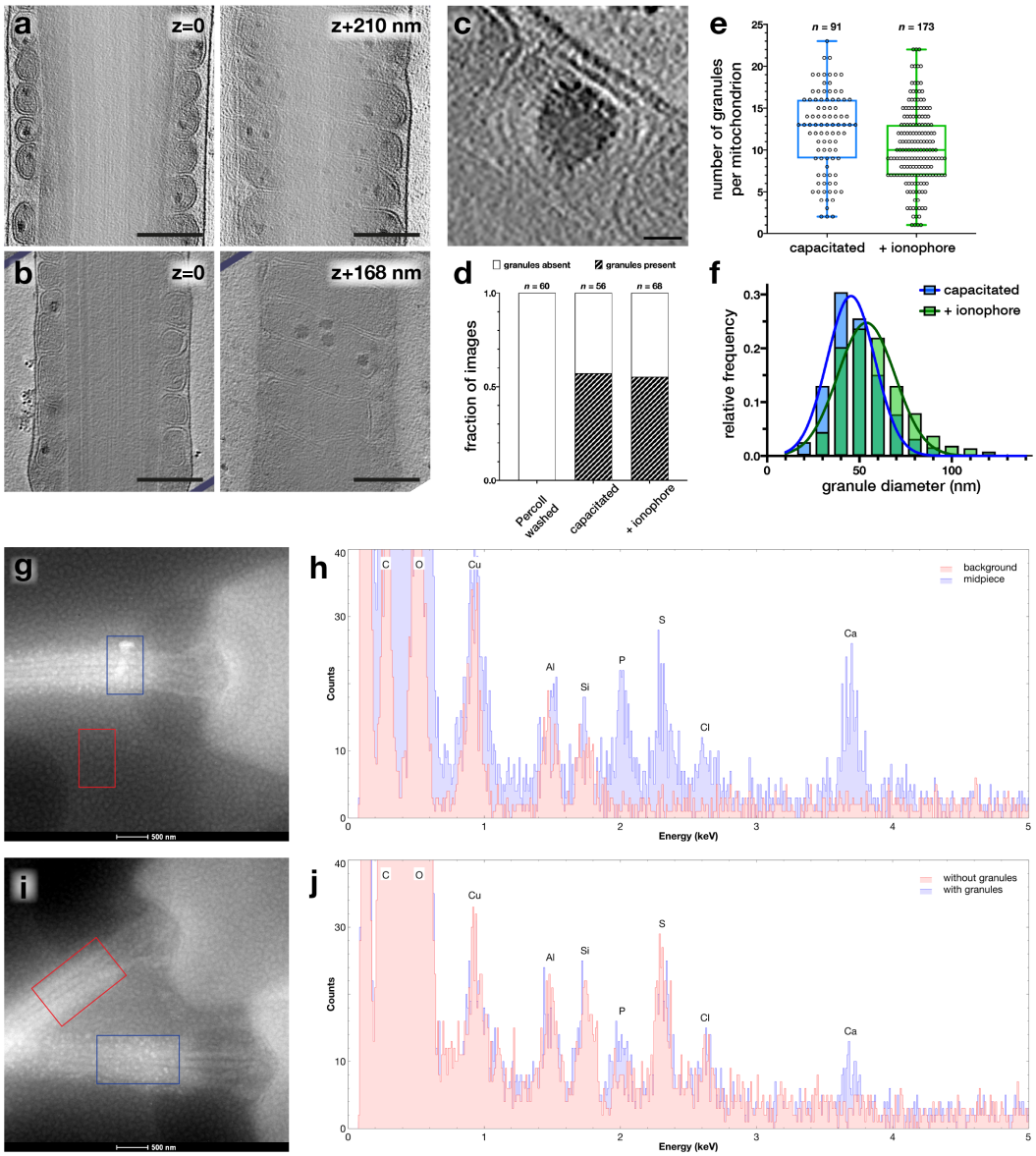


Figure 4.8 | Amorphous calcium granules form in mitochondria of pig sperm incubated in capacitating conditions. **(a,b)** Central longitudinal (left) and tangential (right) tomographic slices through midpieces of pig sperm incubated in capacitating conditions without (a) or with (b) the addition of calcium ionophore A23187. **(c)** A large granule in the mitochondrial matrix of a cell incubated in capacitating media + ionophore. **(d)** Granules were only visible in sperm incubated in capacitating conditions, either with or without ionophore treatment. **(e)** Quantifying number of granules per mitochondrion in cryo-tomograms shows that there is no appreciable increase after ionophore addition (capacitated: mean = 11 ± 6; + ionophore: mean = 10 ± 5. **(f)** Quantifying granule size in cryo-tomograms shows that granules in sperm incubated with ionophore are slightly larger than those incubated only in capacitating media (capacitated: mean = 49 ± 15 nm; + ionophore: mean = 58 ± 18 nm). **(g-j)** Cryo-high-angle annular dark field scanning transmission electron micrographs (g,i) and corresponding energy-dispersive X-ray spectra (h,j) of ionophore-treated capacitated sperm. Spectra in (h,j) are colored according to where they were collected as indicated by boxes in (g,i). Calcium is enriched in granule-containing mitochondria relative to buffer (g,h) and to granule-lacking mitochondria (i,j). **Scale bars:** (a,b) 250 nm, (c) 50 nm, (g,i) 500 nm.

used for imaging may also excite electrons in the sample, ejecting them from their respective energy shells. An electron from a higher energy shell may then "relax" into the gap left by the lower-energy ejected electron, and the difference may be given off as an X-ray. EDX exploits the fact that different elements have characteristic energy differences between electron shells, and thus give off X-rays of characteristic energies as well. EDX revealed that calcium and, to a lesser extent, phosphorus were enriched in mitochondria with granules relative to both the surrounding medium **(Fig. 4.8h)** and to mitochondria without granules **(Fig. 4.8i)**.

Thus, sperm mitochondrial granules likely represent amorphous calcium phosphate stores, as has been reported for morphologically-similar granules in other cell types (Greenawalt et al., 1964; Jacob et al., 1994; Wolf et al., 2017). Mitochondrial granules may represent transient calcium stores that cells can mobilize in response to changing metabolic requirements (Wolf et al., 2017), but large granules are also linked to calcium overload and to inhibited mitochondrial respiration (Malyala et al., 2019; Strubbe-Rivera et al., 2020). Determining whether mitochondrial granules are restricted to either live or dead sperm through cryo-correlative light and electron microscopy would help shed light on the roles of mitochondrial calcium signaling in sperm capacitation.

4.3 Concluding Remarks

In this chapter, I used cryo-FIB milling-enabled cryo-ET to image the sperm mitochondrial sheath. The data reveal that the internal architecture of sperm mitochondria varies across species. Comparative studies of how mitochondrial structure varies with sperm metabolism across different species will undoubtedly contribute to a broader understanding of how mitochondrial from relates to function. Studies on how mitochondrial architecture changes with capacitation and hyperactivation are also highly anticipated. The data also suggest that, despite this diversity, the molecular underpinnings of mitochondrial sheath architecture are conserved, at least in mammals. Specifically, cryo-ET unveiled novel inter-mitochondrial linkers that tether adjacent mitochondria and ladder-like arrays that anchor mitochondria to the

cytoskeleton. Defining whether similar arrays are present in other differentiated cell types – and whether they use a similar pool of protein components – is an area ripe for study.

5

The multi-scale architecture of mammalian sperm flagella

Contents

5.1 Introduction 80
5.2 Results and Discussion 83
5.2.1 The conserved ciliary microtubule core is accessorized in a diverse manner across lineages and across cell types. 83
5.2.2 Accessory structures are integral parts of mammalian sperm flagella and impose large mechanical asymmetries on the core axoneme. 98
5.3 Concluding Remarks 109

5.1 Introduction

Cilia, also called flagella, are evolutionarily ancient organelles used by a myriad of eukaryotic cell types and organisms to propel themselves through fluid environments (Mitchell, 2017; Wan, 2018). These intricate molecular machines are paragons of self-organization built from a bewildering array of active and passive structural elements that, together, are able to spontaneously generate oscillatory wave-like motion (Gaffney et al., 2011). The basic architecture of motile cilia is conserved across broad swaths of the eukaryotic tree, providing information on the minimal structures needed for spontaneous undulation (Brokaw, 2009). However, because they operate in a wide range of environments, cilia from different cell types generate

different waveforms (Khan and Scholey, 2018) that are further modulated by fluid viscosity (Smith et al., 2009).

The motile cilium is a continuous assembly of compound microtubules (Ishikawa, 2017). The base of the cilium is the centriole or basal body, which is typically a cylinder of triplet microtubules **(Fig. 1.6)**. The centriole transitions into the axoneme, which consists of nine doublet microtubules arrayed around a central pair of singlet microtubules **(Fig. 1.8)**. Axonemal microtubules anchor hundreds of dynein motors and accessory proteins to power and regulate movement. Axoneme structure has been studied extensively by cryo-electron tomography (cryo-ET) in *Chlamydomonas*, *Tetrahymena*, and sea urchin sperm (Nicastro et al., 2011, 2006; Owa et al., 2019; Pigino et al., 2012). Recent studies have begun to shed light on species- and cell type-specific specializations (Greenan et al., 2020; Imhof et al., 2019; Lin et al., 2014b; Yamaguchi et al., 2018), motivating efforts to expand the pantheon of organisms and cell types used in axoneme research.

Perhaps the most striking example of ciliary diversity across species is in sperm, which are highly specialized for a defined function – to find and fuse with the egg. Sperm consist of a head, which contains the genetic payload, and a tail, which is a modified motile cilium. Despite their streamlined structure, sperm are simultaneously the most diverse eukaryotic cell type (Gage, 2012; Lüpold and Pitnick, 2018), reflecting the sheer range of reproductive modes and fertilization arenas, from watery media for marine invertebrates and freshwater species to the viscous fluids of the female reproductive tract for mammals. Because motility is crucial to sperm function, the natural variation of sperm form presents a unique opportunity to understand the structural diversification of motile cilia.

Mammalian sperm flagella are characterized by accessory structures that surround and dwarf the axoneme (Fawcett, 1975), unlike marine invertebrates whose sperm tails consist essentially of the axoneme (Fawcett, 1970). In mammalian sperm, axonemal doublets are associated with filamentous cytoskeletal elements called outer dense fibers (ODFs) for most of their lengths **(Fig. 1.9)**. The ODFs are further surrounded by a sheath of mitochondria in the midpiece and by a reticular structure

called the fibrous sheath in the principal piece. These accessory structures are proposed to stabilize beating of the long flagella of mammalian sperm (Lindemann, 1996; Lindemann and Lesich, 2016). The accessory structures may also facilitate movement through viscous media by suppressing buckling instabilities that would otherwise cause sperm to swim in circles (Gadêlha and Gaffney, 2019). Indeed, many cases of male infertility are linked to defects in these accessory elements (Haidl et al., 1991; Serres et al., 1986; Zhao et al., 2018). However, we still do not fully understand how these accessory structures modulate the flagellar beat since there is very little structural information on how they interact with the axoneme proper.

Sperm have two centrioles that are located in the neck, where the nucleus attaches to the flagellum **(Fig. 1.6)**. The centriole closer to the nucleus is referred to as the proximal centriole (PC) and the one at the base of the flagellum the distal centriole (DC). During spermiogenesis in mammals, the DC is remodeled to the point that it no longer resembles a canonical centriole. This was thought to represent a process of degeneration (Manandhar et al., 2000), but recent work showed that the DC is in fact a functional centriole that participates in orchestrating the first zygotic division (Fishman et al., 2018). Such drastic deviations from canonical centriole architecture have not been investigated in detail.

The atypical structure of the DC leads to another distinguishing feature of mammalian sperm flagella: they are not anchored by a basal body (Avidor-Reiss, 2018). Instead, the base of the mammalian sperm flagellum is surrounded by a large cytoskeletal scaffold called the connecting piece. The isolated bovine sperm connecting piece was characterized by cryo-ET, revealing a complex asymmetric assembly (Ounjai et al., 2012). However, the purification process resulted in loss of the centrioles. Thus, there is still a paucity of structural information on the flagellar base in intact cells and on how it varies across species that often have very different head shapes.

In this chapter, I combine cryo-focused ion beam (cryo-FIB) milling-enabled cryo-ET (Marko et al., 2007; Rigort et al., 2012) with subtomogram averaging to image mature sperm from three mammalian species – the pig (*Sus scrofa*), the horse (*Equus caballus*), and the mouse (*Mus musculus*) – that differ in terms of gross morphology,

motility, and metabolism. Leveraging the uniquely multiscale capabilities of cryo-ET, I attempt to define the molecular architecture of microtubule-based assemblies and their critical interactions with accessory structures. Taking advantage of the highly streamlined shape of sperm, I attempt to define how these structures and relationships change throughout the flagellum.

5.2 Results and Discussion

5.2.1 The conserved ciliary microtubule core is accessorized in a diverse manner across lineages and across cell types.

The proximal centriole in mammalian sperm contains novel microtubule inner proteins.

Sperm centrioles are located in the neck, where the nucleus attaches to the flagellum. Here, the centrioles are surrounded by a large cytoskeletal scaffold called the connecting piece (CP). The neck is too thick (~600-700 nm) for direct imaging by cryo-ET, so previous attempts to image this area relied on fractionation and purification (Ounjai et al., 2012). That study generated a highly informative three-dimensional model of the CP, but the purification process resulted in loss of the centrioles. In order to image sperm centrioles in their native subcellular milieu, I used cryo-FIB milling to generate thin lamellae suitable for high-resolution imaging **(Fig. 5.1)**.

Cryo-ET of lamellae containing the proximal centriole (PC) confirmed that it is indeed composed of triplet microtubules in pig and in horse sperm **(Fig. 5.1a-b)**. Unexpectedly, triplets of the pig sperm PC are not all the same length **(Fig. 5.1a, 5.2a)**. Shorter triplets are grouped on one side of the centriole, giving the PC a striking dorsoventral asymmetry **(Fig. 5.2a)**. Consistent with previous reports that the PC degenerates in rodents (Manandhar et al., 1998; Woolley and Fawcett, 1973), the PC was not prominent in mouse sperm. However, cryo-ET showed unequivocally that some centriolar microtubules remain **(Fig. 5.1c)**, suggesting that degeneration is incomplete. Complete triplets can be observed alongside triplets in various stages of degeneration, including triplets in which only the B-tubule had degraded **(Fig. 5.1c')**.

Table 5.1 | Image acquisition and processing metrics for subtomogram averaging of microtubule-based assemblies in mammalian sperm.

Parameter	Species		
	Sus scrofa	*Equus caballus*	*Mus musculus*
proximal centriole			
sample type	lamellae	-	-
microscope (accelerating voltage)	Arctica (200 kV)	-	-
pixel size (Å)	8.68	-	-
symmetry	C1	-	-
number of particles	202	-	-
estimated resolution (Å)	30	-	-
distal centriole			
sample type	lamellae	-	-
microscope (accelerating voltage)	Arctica (200 kV)	-	-
pixel size (Å)	8.68	-	-
symmetry	C1	-	-
number of particles	120	-	-
estimated resolution (Å)	30	-	-
96-nm axonemal repeat			
sample type	whole cells	whole cells/lamellae	whole cells
microscope (accelerating voltage)	Arctica (200 kV)	Arctica (200 kV)	Krios (300 kV)
pixel size (Å)	11.32	11.32	14.16
symmetry	C1	C1	C1
number of particles	1438	634	1112
estimated resolution (Å)	37	40	40
central pair apparatus			
sample type	whole cells	whole cells/lamellae	whole cells/lamellae
microscope (accelerating voltage)	Arctica (200 kV)	Arctica (200 kV)	Arctica (200 kV)
pixel size (Å)	11.32	11.32	11.32
symmetry	C1	C1	C1
number of particles	978	461	281
estimated resolution (Å)	36	34	49
endpiece singlets			
sample type	whole cells	whole cells	whole cells
microscope (accelerating voltage)	Arctica (200 kV)	Arctica (200 kV)	Krios (300 kV)
pixel size (Å)	3.50	5.66	7.08
symmetry	C1	C1	C1
number of particles	5799	9136	1581
estimated resolution (Å)	19	19	30

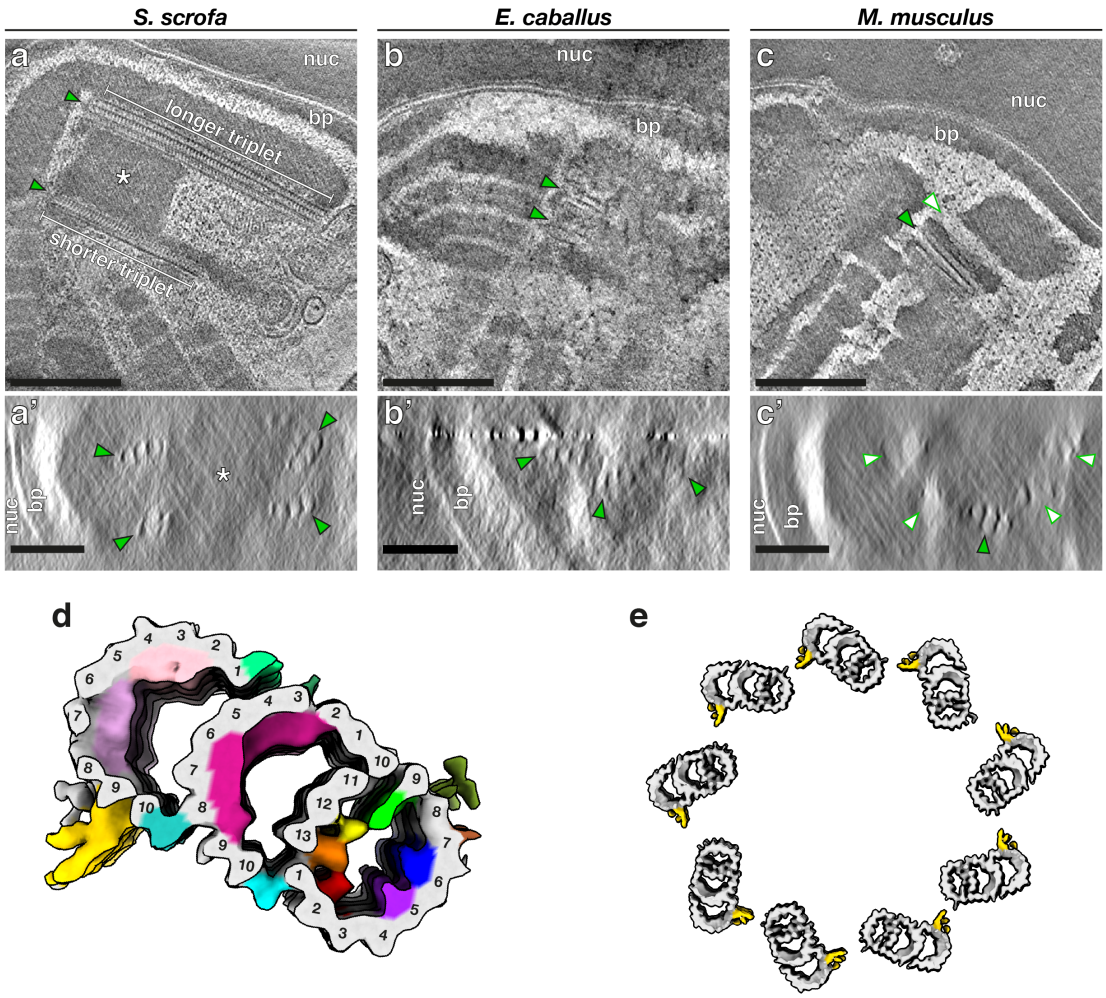


Figure 5.1 | The proximal centriole (PC) in mammalian sperm contains novel microtubule inner proteins. (a-c) Tomographic slices through cryo-FIB milled lamellae of pig (a), horse (b), and mouse (c) sperm. Transverse slices (a'-c') show complete triplets in the pig (a') and the horse (b'), but not in the mouse (c'). **(d)** *In situ* structure of the pig sperm PC with the tubulin backbone in grey and microtubule inner protein densities colored individually. **(e)** Reconstruction of the pig sperm PC with the A-C linker colored in yellow. **Scale bars:** (a,b,c) 250 nm; (a',b',c') 100 nm.

I then determined the *in situ* structure of the pig sperm PC by subtomogram averaging **(Fig. 5.1d)**. While the overall structure of the PC triplet is similar to other centriole structures (Greenan et al., 2018, 2020; Guichard et al., 2013; Le Guennec et al., 2020; Li et al., 2012), it differs in terms of the microtubule inner protein densities (MIPs) **(Fig. 5.2b)**. Nine MIPs are resolved in the average: six in the A-tubule, one in the B-tubule, and two in the C-tubule **(Fig. 5.2c)**. In the A-tubule most of the MIPs are unique, including MIP2 (yellow) that binds to protofilament

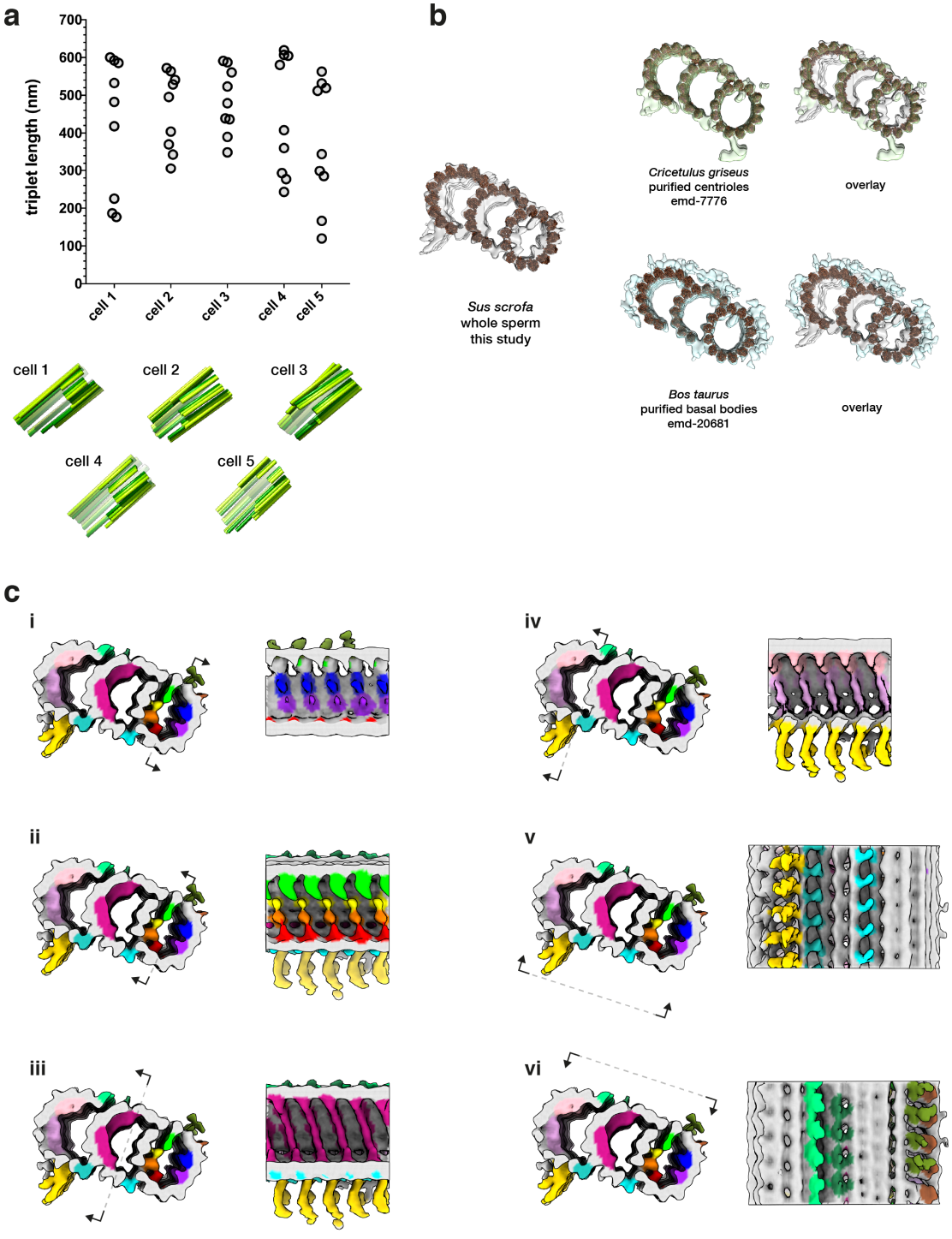


Figure 5.2 | Structural features of the pig sperm proximal centriole (PC). (a) PC triplets have unequal lengths (top panel) and shorter triplets are grouped on one side, giving the PC dorsoventral asymmetry (bottom panel). **(b)** Many of the microtubule inner proteins (MIPs) in the pig sperm PC are not found in other mammalian centriole structures. **(c)** Details of the MIP densities in the pig sperm PC.

A12, MIP3 (orange) bridging protofilaments A13 and A1, MIP4 (red) that binds to A2, MIP5 (purple) that binds to A5, and MIP6 (blue) bridging A6 and A7. MIP1 (green), a prominent MIP associated with protofilament A9, was also reported in centrioles isolated from CHO cells (Greenan et al., 2018) and in basal bodies from bovine respiratory epithelia (Greenan et al., 2020). Protofilaments A9 and A10 are proposed to be the location of the seam (Ichikawa et al., 2017), which suggests that MIP1 is a highly-conserved seam-stabilizing or seam-recognizing structure.

In the B-tubule, there is a unique helical MIP7 (magenta) bridging protofilaments B3-9. There are also two groups of unique MIPs in the C-tubule, MIP8 (light pink) associated with C2-C4 and MIP9 (pink) with C5-C7. The inner junctions between A- and B-tubules (cyan) and between B- and C-tubules (turquoise) are non-tubulin proteins that repeat every 8 nm and are staggered relative to each other when viewed from the luminal side of the triplet. The average also shows density for the A-C linker (gold), which is associated with protofilaments C9 and C10 **(Fig. 5.1e)**.

The B- and C-tubule MIPs in the structure reported herein are not present in other centriole structures. However, helical MIPs have been observed in the transition zone of bovine respiratory cilia (Greenan et al., 2020). Unlike other mammalian centriole structures, I do not observe MIPs that bridge B1-B2 or C1-C2 **(Fig. 5.2b,c)**. It is difficult to tell whether these differences in MIP patterns are due to differences in cell type or species. As this is the first *in situ* structure of any mammalian centriole, these differences may also be because previous structures were of isolated centrioles. Nonetheless, it is clear that there is great diversity in how core centriolar microtubules are accessorized, which raises questions about the functions of these MIPs.

The distal centriole in mammalian sperm is composed of doublet microtubules arrayed asymmetrically around a pair of singlet microtubules.

In mammals, the distal centriole (DC) at the base of the flagellum is remodeled so dramatically during spermiogenesis that it no longer resembles a typical centriole. This was thought to represent a process of degeneration (Manandhar et al., 2000), but recent work has shown that the DC is in fact a functional centriole that participates in

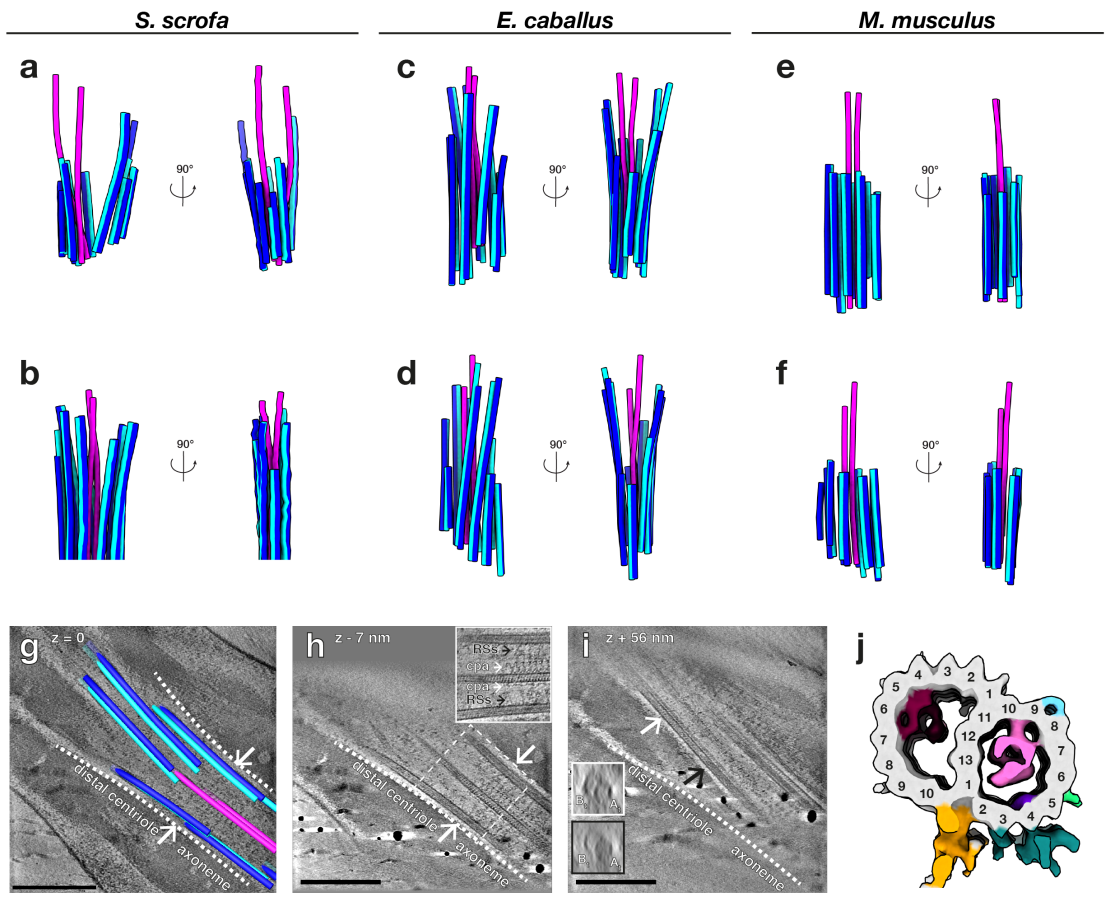


Figure 5.3 | The distal centriole (DC) in mammalian sperm is composed of doublet microtubules arrayed asymmetrically around a pair of singlet microtubules. (a-f) Microtubules in the DC of pig (a,b), horse (c,d), and mouse (e,f) sperm traced from Volta phase plate cryo-tomograms of intact sperm. **(g-i)** Tomographic slices through cryo-FIB milled lamellae of the DC-to-axoneme transition in pig sperm show how the change in geometry (g) coincides with the appearance of axoneme accessory structures (h) and with density in the A-tubule (i). **(j)** *In situ* structure of the pig sperm DC with the tubulin backbone in grey and microtubule inner protein densities colored individually. **Scale bars:** 250 nm.

orchestrating the first zygotic division (Fishman et al., 2018). Such drastic deviations from canonical centriole structure have not been characterized.

To determine the organization of the sperm DC, I traced microtubules through Volta phase plate (VPP) cryo-tomograms of whole sperm **(Fig. 5.3)**. The DC consists of doublet microtubules, with a pair of singlets extending through the lumen **(Fig. 5.3a-f)**. In pig and in horse sperm **(Fig. 5.3a-d)**, doublets extend almost as far proximally as the central pair. In a further departure from canonical centriole structure, DC doublets are splayed open and arranged asymmetrically around the singlets. The central singlets themselves are spaced inconsistently, suggesting that they lack the

projections characteristic of the central pair apparatus (CPA). Mouse sperm lack the splayed doublets, but they also have a pair of singlets extending beyond the axoneme **(Fig. 5.3e-f)**.

To more precisely define the DC-to-axoneme transition, I imaged cryo-FIB-milled sperm **(Fig. 5.3g-j)**. I directly observed this transition *in situ* in pig sperm, defined by the appearance of axonemal accessory proteins such as the radial spokes (RSs) and the projections of the CPA **(Fig. 5.3g-h)**. The onset of the axoneme coincides with a change in microtubule geometry **(Fig. 5.3g)**, suggesting that the splayed-open doublets are indeed characteristic of the DC. The transition zone also coincides with an increase in density in the A-tubule **(Fig. 5.3i)**, suggesting that binding of axonemal accessory structures is related to the regulated binding of A-tubule MIPs. I then determined the structure of DC doublets, revealing the presence of MIPs distinct from those in the PC **(Fig. 5.3j)**.

The mammalian sperm central pair complex has a conserved projection network but species-specific microtubule inner proteins.

To gain insight into the molecular architecture of the axoneme, I determined structures of the central pair apparatus **(Fig. 5.5)** and of the 96-nm axonemal repeat **(Fig. 5.6)**. The overall architecture of the CPA projection network is similar across the three species examined **(Fig. 5.4)** and resembles that of the CPA from *Chlamydomonas* and from sea urchin sperm (Carbajal-González et al., 2013; Fu et al., 2019). Indeed, mutations in hydin, a component of the C2b projection, impair ciliary motility in both *Chlamydomonas* and mice (Lechtreck et al., 2008). However, the mammalian sperm CPA lacks the C1f projection found between the C1b and C1d projections in *Chlamydomonas* flagella and sea urchin sperm (Carbajal-González et al., 2013) **(Fig. 1.8d,e)**.

Mammalian sperm CPAs have several MIPs **(Fig. 5.5)** that are absent from *Chlamydomonas* and from sea urchin sperm, which have only small MIPs or no MIPs respectively **(Fig. 1.8d,e)**. Similar to the PC **(Fig. 5.1d)**, pig and horse sperm have large helical MIPs in the C1 microtubule that bridge protofilaments 1-7 and repeat every 8 nm **(Fig. 5.5a-b, panels i)**. Mouse sperm have smaller MIPs in the same area, but these bridge fewer protofilaments and repeat with an overall periodicity of 32

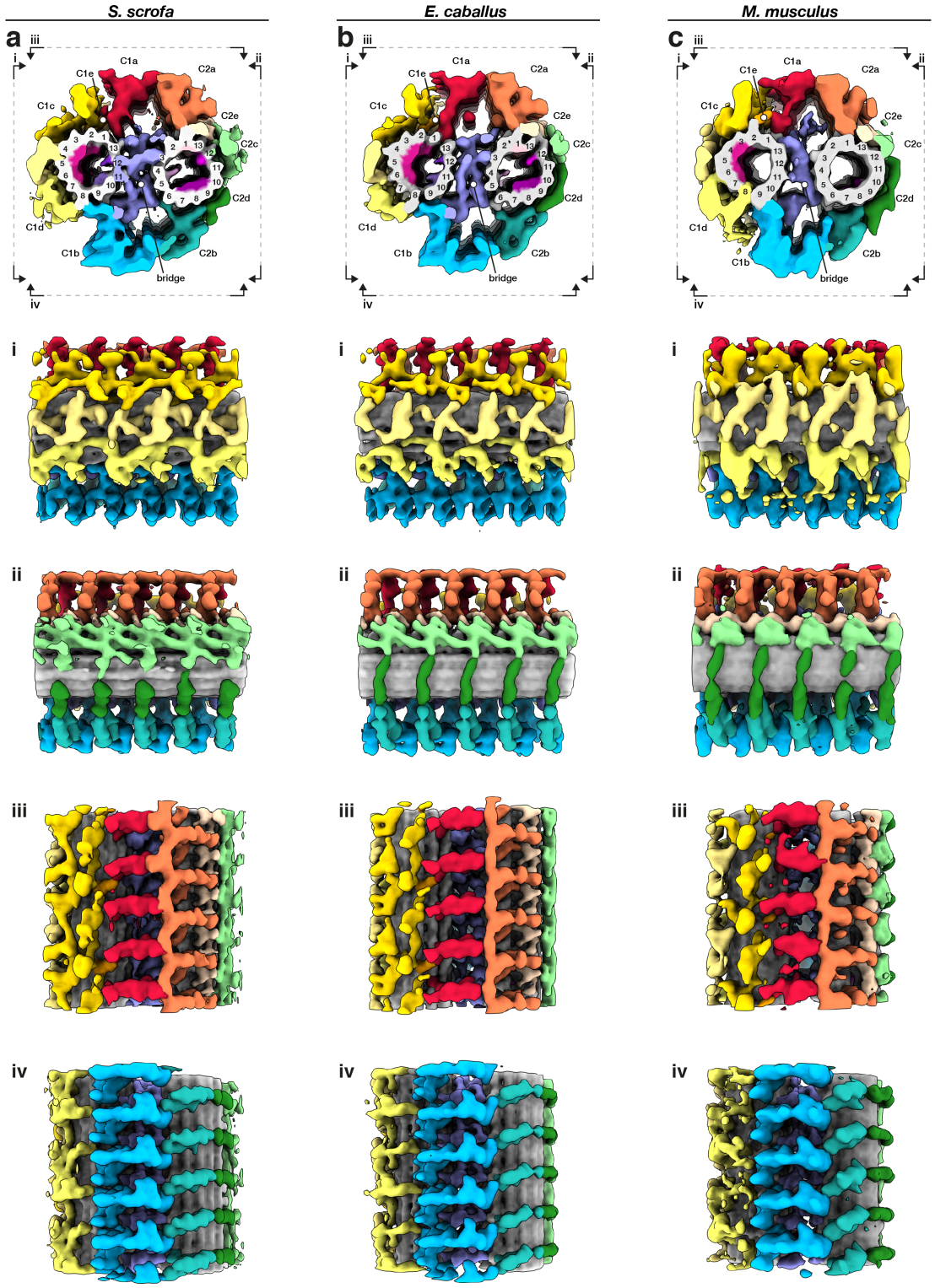


Figure 5.4 | Structural details of the central pair apparatus projection network in mammalian sperm. **(a-c)** Whole-population *in situ* structures of the 32-nm CPA repeat from pig (a), horse (b), and mouse (c) sperm. Individual rotated views show details of C1 projections (i), C2 projections (ii), the interface between C1a and C2a projections (iii), and the interface between C1b and C2b projections (iv). Projections are segmented and colored according to Carbajal-González et al., 2013.

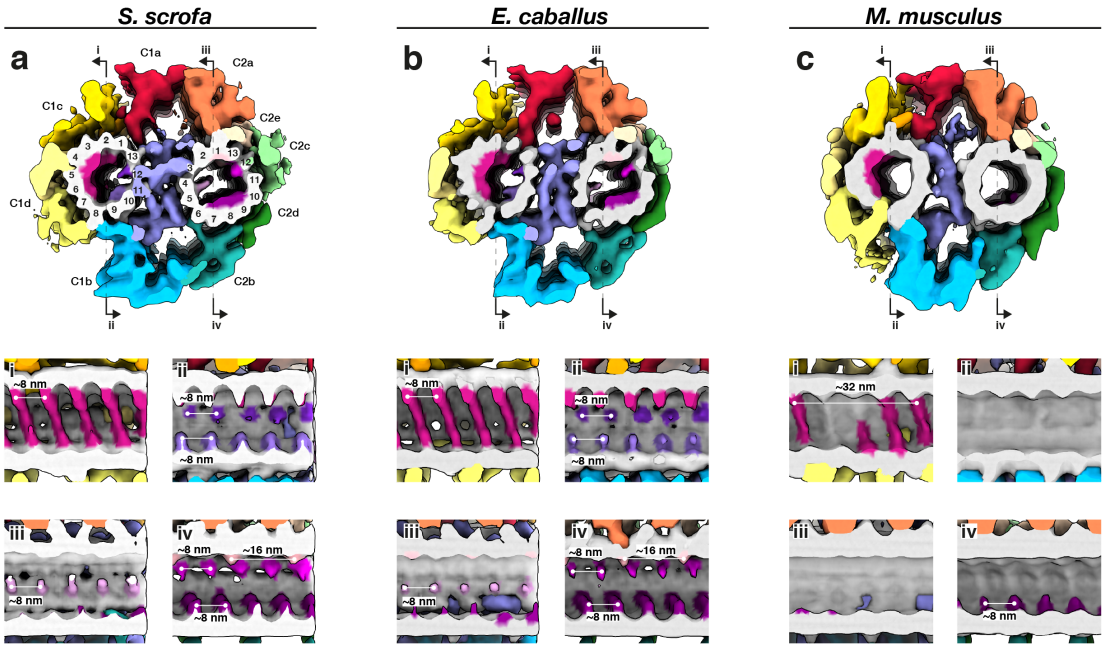


Figure 5.5 | The mammalian sperm central pair apparatus (CPA) has a conserved projection network but species-specific microtubule inner proteins. (a-c) Whole-population *in situ* structures of the 32-nm CPA repeat from pig (a), horse (b), and mouse (c) sperm.

nm **(Fig. 5.5c, panel i)**. Pig and horse sperm also have smaller C1 MIPs on the side facing the bridge, with one bridging protofilaments 9 and 10 and the other jutting out from between protofilaments 12 and 13 **(Fig. 5.5a-b, panels ii)**. Both of these MIPs repeat every 8 nm and both are absent from the mouse **(Fig. 5.5c, panel ii)**. In the C2 microtubule, the pig and the horse have several other MIPs that are also absent from the mouse. These include a MIP that protrudes out from between protofilaments 4 and 5 and repeats every 8 nm **(Fig. 5.5a-b, panel iii)**, a MIP that binds between protofilaments 1 and 13 and repeats every 16 nm, and a MIP that extends from protofilament 12 and repeats every 8 nm **(Fig. 5.5a-b, panel iv)**. A fourth B-tubule MIP bridges protofilaments 7-9 in the pig and the horse, but this MIP is smaller and only bridges protofilaments 8 and 9 in the mouse **(Fig. 5.5a-c, panels iv)**.

The mammalian sperm axoneme anchors unique accessory structures and species-specific microtubule inner proteins.

The 96-nm axonemal repeat from mammalian sperm shares most of the general features seen in other organisms and cell types **(Fig. 5.6a-c, Fig. 5.7a-g)**. In addition,

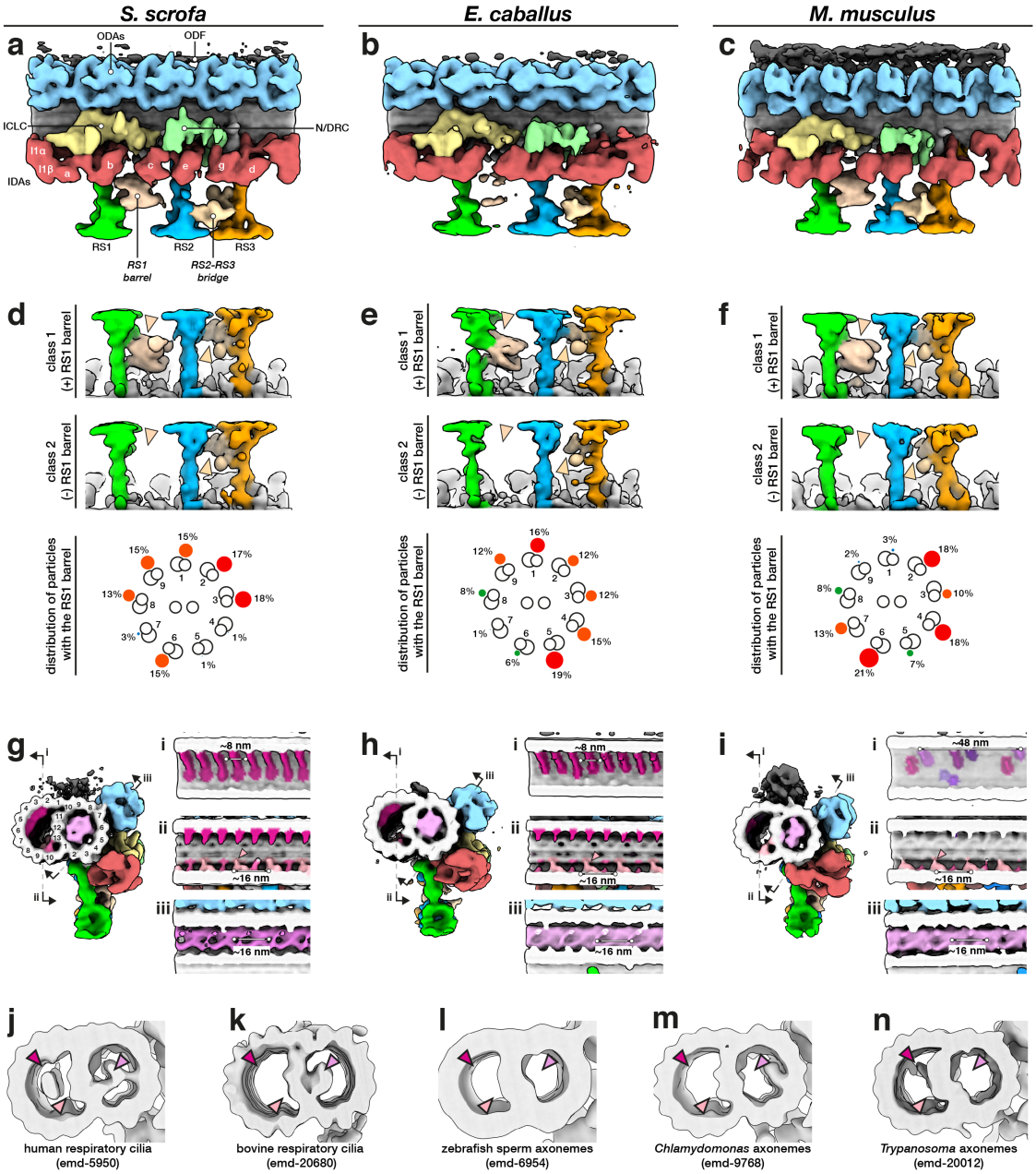


Figure 5.6 | The mammalian sperm axoneme anchors unique accessory structures and species-specific microtubule inner proteins. (a-c) Whole-population *in situ* structures of the 96-nm repeat from pig (a), horse (b), and mouse (c) sperm. **(d-f)** Classification focused on the RS1 barrel revealed two distinct classes of particles, one with (top panels) and one without (middle panels) the structure. Particles with the RS1 barrel are distributed asymmetrically around the axoneme (bottom panels). **(g-i)** Microtubule inner proteins in axonemes from pig (g), horse (h), and mouse (i) sperm. **(j-n)** Microtubule inner proteins in axonemes from other cell types and organisms.

the averages show densities for attachment to the outer dense fibers (ODFs) as well as other novel structural features associated with the radial spokes (RSs). In particular, I observed a barrel-shaped structure associated with RS1 (the RS1 barrel) and an extensive bridge linking the stalks of RS2 and RS3 (the RS2-RS3 bridge). An independent study recently confirmed the presence of these structures in mouse sperm flagella (Gadadhar et al., 2021). Importantly, The RS1 barrel and the RS2-RS3 bridge are absent from other axoneme structures reported so far **(Fig. 5.7a-g)**.

Focused classification resolved two distinct classes of particles, one with and the other without density for the RS1 barrel **(Fig. 5.6d-f)**. By separating out only particles with the barrel, classification also improved the density for this structure. The RS1 barrel is ~18 nm long and ~16 nm wide and makes two major contacts with RS, one at the base of the head and one at the middle of the stalk. Interestingly, particles that do have the RS1 barrel are distributed asymmetrically around the axoneme. Although the RS1 barrel is not particularly enriched in any individual doublet position, it occurs less frequently in specific positions. In the pig, only 1% of the particles were found in each of doublets 4 and 5, while only 3% were in doublet 7. In the horse, only 1% were found in doublet 7. In the mouse, only 2% were found in doublet 9 and 3% in doublet 1.

Comparing mammalian sperm axonemes to those from other species reveals large variations in MIP densities **(Fig. 5.6j-n)**. Mammalian sperm have a large MIP that fills almost the entire lumen of the A-tubule **(the A-MIP, Fig. 5.6g-i, bottom panels)**, which explains why the A-tubule appears dark in cross-section. The A-MIP makes extensive contacts with the A-tubule, including protofilaments A1-A3, A5-A6, and A8-A13, and has an overall periodicity of ~16 nm. Because the sperm A-MIP makes contacts with nearly all protofilaments of the A-tubule, it seems plausible that it would affect the mechanics of the doublet. The A-MIP also makes contacts with the same protofilament to which the ODFs attach, which suggests that it may also functionalize the outer surface of the A-tubule for ODF docking. A-tubule MIPs are present in axonemes from human **(Fig. 5.6j)** (Lin et al., 2014b) and bovine **(Fig. 5.6k)** respiratory cilia (Greenan et al., 2020), but these are not as extensive as the A-MIP in mammalian sperm **(Fig. 5.7h)**. Zebrafish **(Fig. 5.6l)** (Yamaguchi et al.,

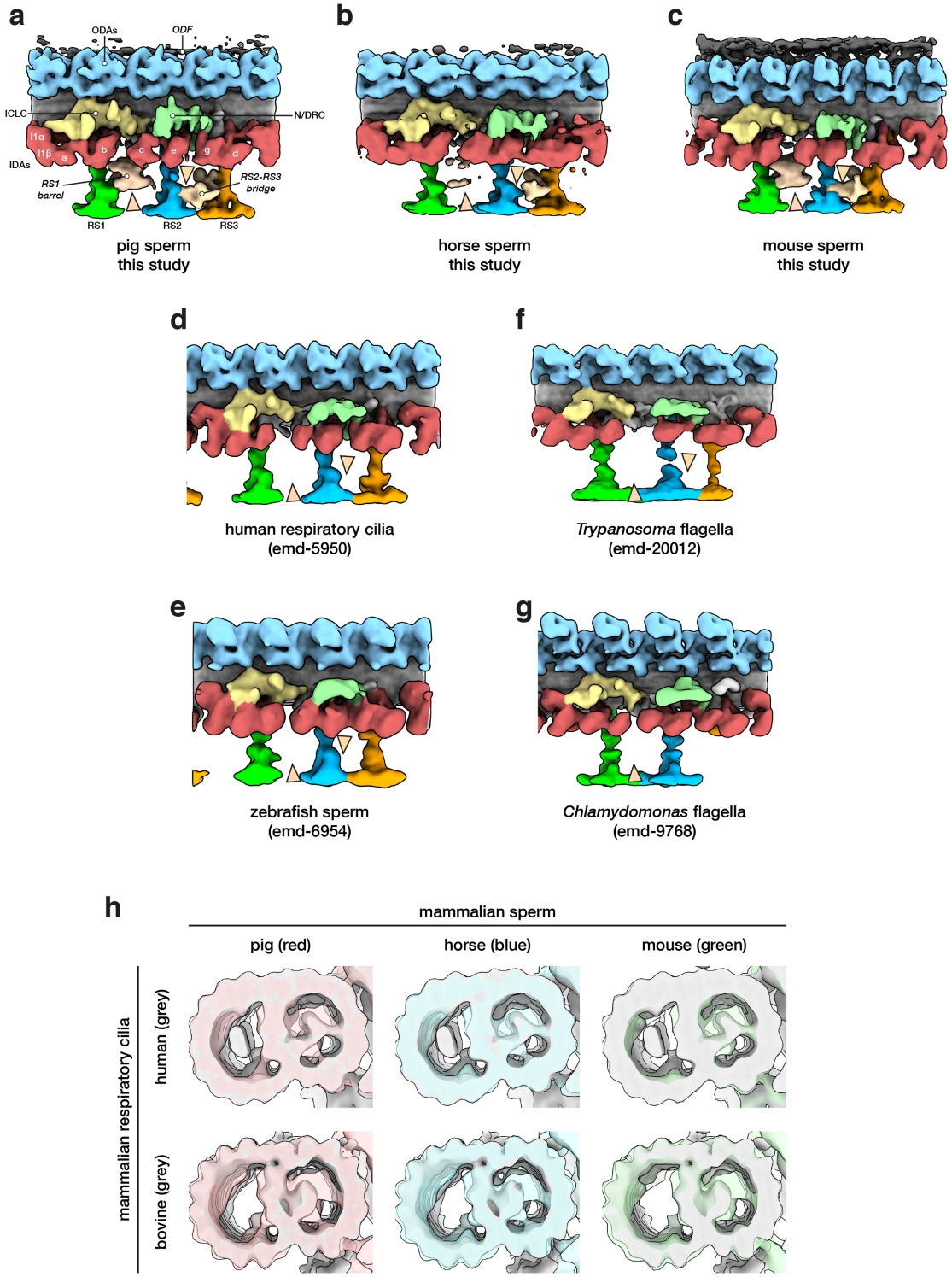


Figure 5.7 | Comparing the mammalian sperm axoneme with other structures. (a-g) Structures of the 96-nm axonemal repeat from various species in cell types. Arrowheads mark the novel RS1 barrel and RS2-RS3 bridge so far seen only in mammalian sperm. **(h)** A-tubule MIPs are present in mammalian respiratory cilia, but the A-MIP in mammalian sperm is larger and makes more extensive connections with the A-tubule itself.

2018) and sea urchin sperm (Lin et al., 2014a; Nicastro et al., 2011) do not have large MIPs in the A-tubule, nor do *Chlamydomonas* **(Fig. 5.6m)** (Nicastro et al., 2011; Owa et al., 2019) or *Trypanosoma* **(Fig. 5.6n)** (Imhof et al., 2019).

In all axonemes so far, B-tubules contain MIP3a and MIP3b, which bind to protofilaments B9 and B10 with staggered ~16-nm repeats **(Fig. 5.6g-i)**. However, in mammalian sperm, MIP3a has an additional density that links it to protofilament A13 **(Fig. 5.6g-i, panels ii, pink arrowheads; Fig. 5.7h)**. In pig and horse sperm, a helical MIP with an ~8-nm repeat bridges protofilaments B2-B7 **(Fig. 5.6g-i, panels i)**. Mouse sperm do not have this large MIP and instead have smaller MIPs that bind with an overall apparent periodicity of ~48-nm **(Fig. 5.6i, panel i)**. Large B-tubule MIPs have so far only been seen in human respiratory cilia **(Fig. 5.6j)** and in *Trypanosoma* (the ponticulus, **Fig. 5.6n)**, but the morphometry of these MIPs differs from the helical MIPs in mammalian sperm.

A crucial comparison comes from the structure of axonemes from mouse respiratory cilia (Ueno et al., 2012). Mouse respiratory cilia lack the large A-MIP that is so prominent in mouse sperm, which points to cell-type specific differences in the MIP repertoire. Similarly, the RS1 barrel and the RS2-RS3 bridge **(Fig. 5.6)** are present in sperm, but not in respiratory cilia **(Fig. 5.7a-e)**. Because the radial spokes are key regulators of flagellar motility, as evidenced by the fact that radial spoke defects cause a number of ciliopathies (Lin et al., 2014b), the RS1 barrel and the RS2-RS3 bridge are likely to play a significant role in modulating sperm motility. As with many of the structures reported here, defining why exactly they are needed in mammalian sperm would help us better understand the intricacies of flagellar organization.

Singlet microtubules in the endpiece are capped by a conserved plug but contain species-specific microtubule inner proteins.

I then determined how the doublets of the axoneme transition into singlets of the endpiece **(Fig. 5.8a-c)**. The data revealed that doublets can transition into singlets by two possible arrangements, either by a doublet splitting into two independent singlets **(Fig. 5.8d-f, left panels)** or by the B-tubule terminating abruptly **(Fig. 5.8d-f, right panels)**. Similar patterns have been observed in human sperm (Zabeo et al.,

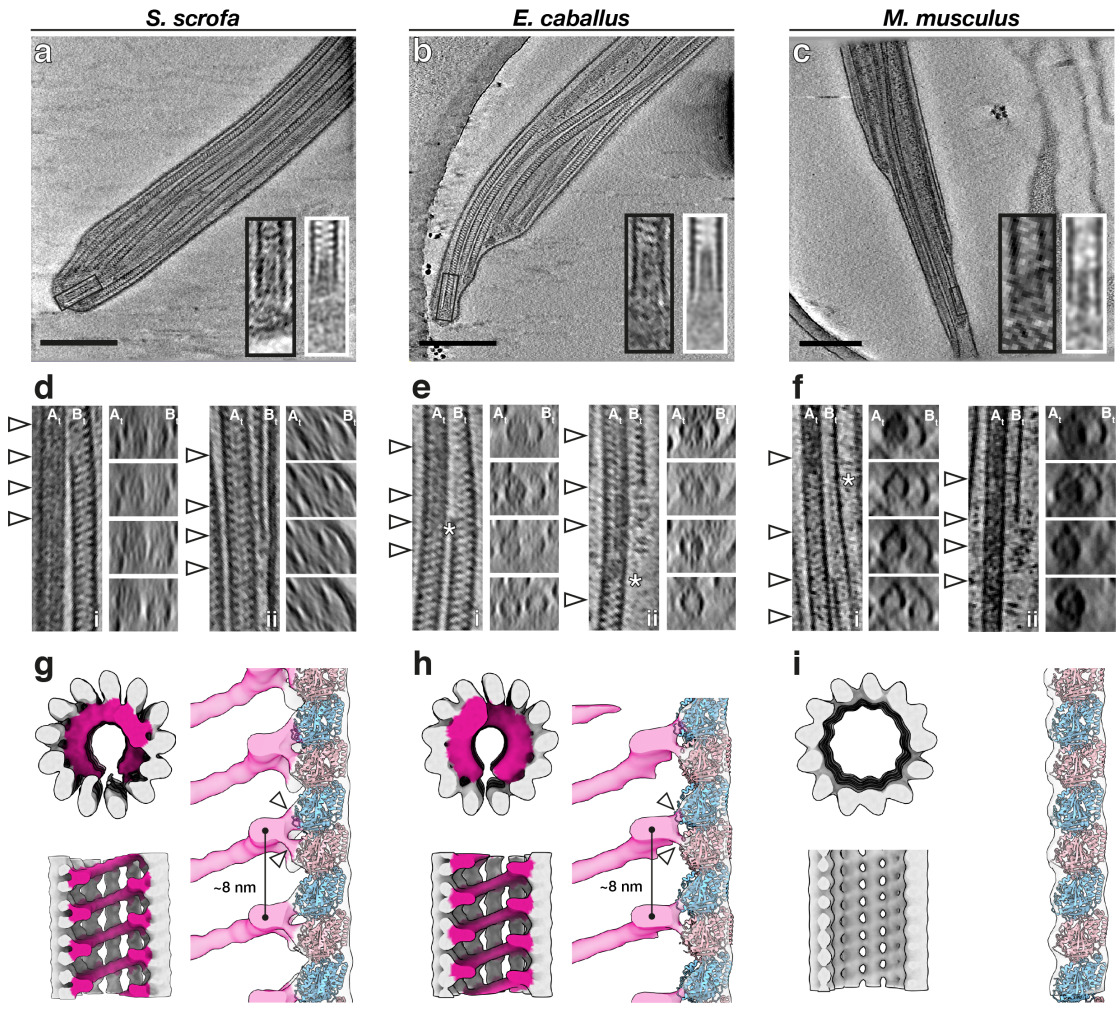


Figure 5.8 | Singlet microtubules in the endpiece are capped by a conserved plug but contain species-specific microtubule inner proteins. (a-c) Slices through defocus cryo-tomograms of the endpiece in pig (a), horse (b), and mouse (c) sperm. **(d-f)** Representative examples of the mechanisms by which doublets can transition into singlets. Doublets can split into two complete singlets (panels i), or the B-tubule can terminate abruptly with the A-tubule extending as a singlet (panels ii). **(g-i)** *In situ* structures of singlet microtubules from pig (g), horse (h), and mouse (i) sperm endpieces. **Scale bars:** 250 nm.

2019). The doublet-to-singlet transition is also associated with loss of density in the A-tubule **(Fig. 5.8d-f, asterisks)**, although the precise location of this change relative to the splitting event varies. After the splitting event, 8-nm striations previously seen only in the B-tubule were visible in both singlets. The A-MIP thus seems to be a marker of the axoneme proper; the A-tubule lumen transitions from "empty" to "full" at the DC-to-axoneme transition **(Fig. 5.3i)**, whereas it goes from "full" to "empty" at the doublet-to-singlet transition.

I then averaged endpiece singlets from the three species and found that they are consistently comprised of 13 protofilaments **(Fig. 5.8g-i)**. In the pig and the horse, singlets contain a helical MIP that follows the microtubule lattice, similar to the MIP previously described for human sperm endpieces (Zabeo et al., 2018). The higher-resolution averages here now reveal that this helical MIP makes independent contacts with both tubulin monomers **(Fig. 5.8g-h, arrowheads in right panels)**. This MIP is similar to MIP7 in the B-tubule of the proximal centriole **(Fig. 5.1d)**, to the helical MIP on the outer wall of the B-tubule of the axonemal doublets **(Fig. 5.6g-i)**, and to the helical MIPs in the CPA **(Fig. 5.5a-b)**. Intriguingly, this MIP is absent from endpiece singlets in the mouse **(Fig. 5.8i)**, where axonemal B-tubules and CPA microtubules also lack the large multi-protofilament-spanning MIPs present in the pig and horse **(Fig. 5.5c, Fig. 5.6i)**.

I also observed that microtubule termini are capped in all three species **(Fig. 5.8a-c, black boxes)**. Averaging confirmed the presence of a plug extending 30 nm into the microtubule lumen **(Fig. 5.8a-c, white boxes)**. Normally, ciliary length control and turnover of axonemal components is mediated by the intraflagellar transport (IFT) system. However, IFT is absent in mature spermatozoa (San Agustin et al., 2015), which raises the question of how microtubule length and stability are maintained in these cells. These capping structures may stabilize free microtubule ends and prevent them from depolymerizing.

In summary, the structures reported here show that ciliary MIPs are highly diverse, both within a single cilium and across cell types **(Figs. 5.1, 5.3, 5.5, 5.6, 5.8)**. Comparing several ciliary assemblies reveals that there are fundamental differences in the MIP repertoire across cell types and lineages. Most notably, large helical protofilament-bridging MIPs are present in essentially all microtubule-based assemblies throughout the sperm flagellum in pig and in horse, although they are reduced in corresponding structures in mouse sperm **(Figs. 5.5, 5.6)**. These MIPs seem to be characteristic of mammalian sperm flagella as they are absent from axonemes of zebrafish sperm, sea urchin sperm, and mammalian respiratory cilia **(Fig. 5.7)**. Similar MIPs are present in human sperm endpiece singlets and in bovine respiratory

epithelia, although in the latter they are restricted to the transition zone (Greenan et al., 2020). It is plausible that the helical MIPs are formed by variations of the same core protein complex, but direct confirmation awaits higher-resolution structures, genetic perturbation experiments, and direct labelling. If this were the case, however, this complex would have to adapt to the subtle differences in curvature between the walls of the centriolar/axonemal B-tubules and the 13-protofilament singlets.

The intimate and extensive contacts that these MIPs make with the tubulin lattice suggest that they would affect the mechanical properties of the microtubule itself. Microtubules are characterized by a paradoxical length-dependent bending stiffness attributed to the low shear modulus between adjacent protofilaments (Kurachi et al., 1995; Pampaloni et al., 2006; Taute et al., 2008). The protofilament-bridging MIPs observed here may decrease inter-protofilament shearing, increasing the shear modulus and the resulting bending stiffness of sperm microtubules. This adaptation might be necessary to withstand the large forces involved in moving the long flagellum of mammalian sperm, potentially reducing the length-dependency of bending stiffness in MIP-reinforced microtubules. These MIPs may also act as structural braces that suppress internal buckling within the axoneme under large loading in high viscosity fluids.

5.2.2 Accessory structures are integral parts of mammalian sperm flagella and impose large mechanical asymmetries on the core axoneme.

Structural organization of the fibrous sheath.

To resolve the structural organization of mammalian sperm accessory structures, I first imaged the fibrous sheath **(Fig. 5.9a-c)**. The fibrous sheath extends the length of the principal piece **(Fig. 5.11)** and consists of two thickenings called longitudinal columns that are interconnected by circumferential ribs. Cryo-ET of FIB-milled principal pieces revealed that the fibrous sheath consists of a dense meshwork of filaments **(Fig. 5.9d-f)**. Filaments that comprise the circumferential ribs are oriented perpendicular to the flagellar long axis **(Fig. 5.9d-f)** while those in the longitudinal columns are oriented parallel to this axis **(Fig. 5.9d'-f')**. Intriguingly, while AKAP4-null sperm completely

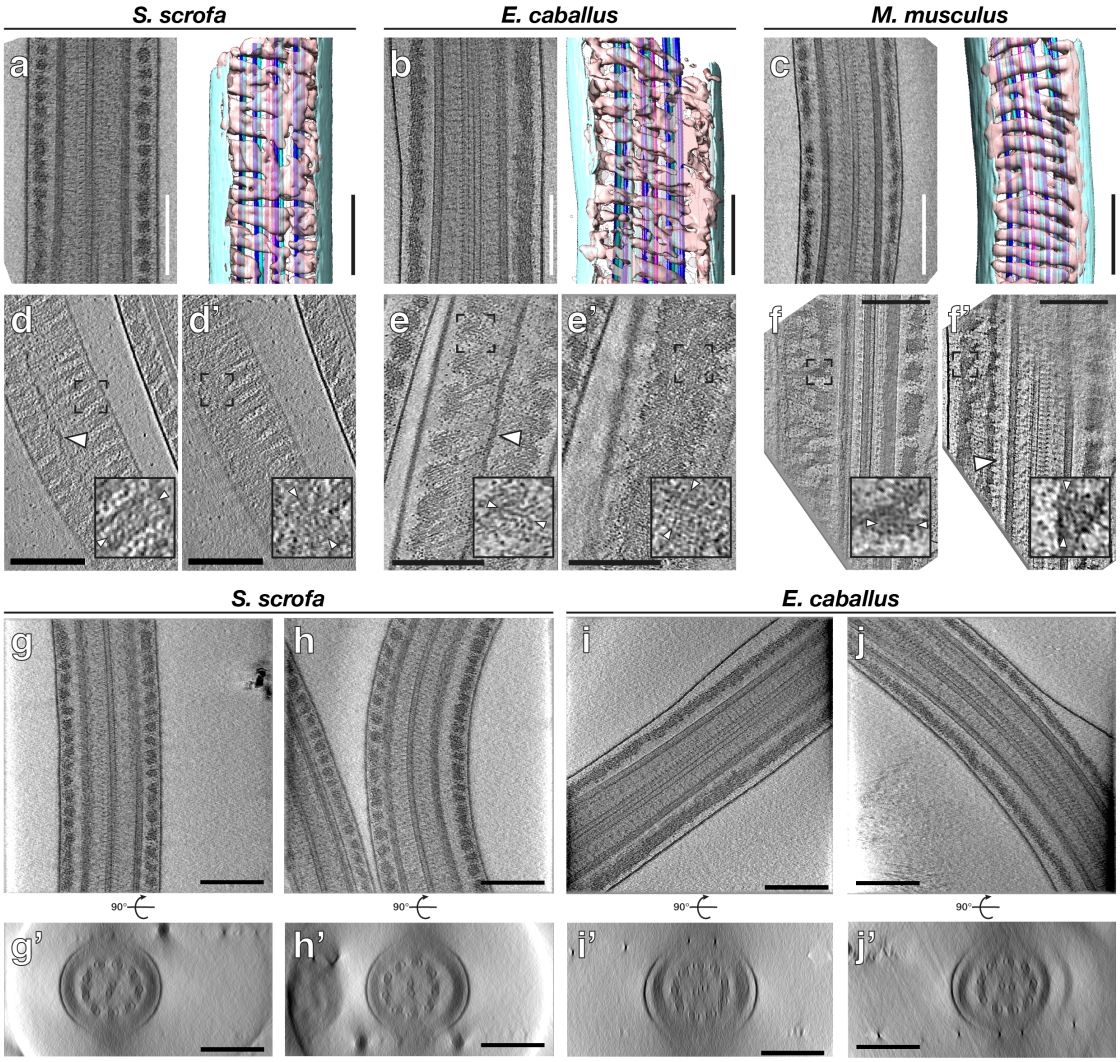


Figure 5.9 | Structural organization of the fibrous sheath in relation to the axoneme. **(a-c)** Central longitudinal tomographic slices (left panels) and segmentations (right panels) of the principal piece from pig (a), horse (b), and mouse (c) sperm. The plasma membrane is shown in sky blue, the fibrous sheath in red, the doublets in blue, and the central pair in pink. **(d-f)** Slices through cryo-tomograms of cryo-FIB milled pig (d), horse (e), and mouse (f) sperm principal pieces. Filaments composing the fibrous sheath appear to be oriented perpendicular to the flagellar long axis in the circumferential ribs (arrowheads in insets d, e, f), but parallel to it in the longitudinal columns (arrowheads in insets d', e', f'). **(g-j)** Computational slices through defocus-contrast cryo-tomograms of straight (g,i) and bent (h,j) regions of pig (g,h) and horse (i,j) sperm flagella. Note how the fibrous sheath compresses on the inside of the bend and extends on the outside of the bend (h,j). Note also how the axoneme appears to be free to move within the fibrous sheath in the plane perpendicular to the longitudinal columns (h',j'). **Scale bars:** 250 nm.

lack the fibrous sheath, AKAP3-null sperm only lack the circumferential ribs, suggesting that there is compositional modularity within the fibrous sheath (Xu et al., 2020).

Preliminary cryo-ET data comparing straight and curved regions of sperm flagella revealed that the fibrous sheath itself undergoes structural rearrangements during motility **(Fig. 5.9g-j)**. Specifically, the spacing between circumferential ribs decreases on the inside of the bend and increases on the outside of the bend **(Fig. 5.9g,h)**. Furthermore, the axoneme is free to move within the fibrous sheath **(Fig. 5.9g'-j')**. These observations need to be quantified more rigorously, but they suggest avenues for future research into how the fibrous sheath changes during sperm movement.

Outer dense fibers are directly coupled to axonemal doublets in the principal piece but are not directly linked in the midpiece.

To resolve how the ODFs associate with the microtubule doublets of the axoneme, I aligned particles from the principal piece and classified them with a mask on the ODF-doublet attachment. The resulting structures reveal that the ODFs are directly, physically linked to protofilament 9 of the A-tubule **(Fig. 5.10a-c)**. The ODF-doublet attachment consists of a pair of linkers spaced ~8 nm apart, with each pair spaced ~16 nm from the next, yielding an apparent overall periodicity of ~16 nm that is consistent across species. Direct ODF-microtubule linkages provide a mechanism by which forces from axoneme bending can be transmitted through the ODFs to the base of the flagellum. As such, in the principal piece, the ODFs should be considered a part of the axoneme proper, which increases the effective diameter of the axoneme. This increase in diameter translates to an increase in bending torque (Lindemann, 1996; Lindemann and Lesich, 2016), but because the ODFs themselves are not all the same size and terminate at different points, this increase is not uniform **(Fig. 5.11)**.

To determine how ODF-doublet association changes along the flagellum, I then separately averaged the 96-nm repeat from the midpiece, proximal principal piece, and distal principal piece **(Fig. 5.10d-l)**. Structures from the distal principal piece, after the ODFs had terminated, did not show density for the ODFs **(Fig. 5.10f',i',l')**. In the proximal principal piece, the ODFs are directly attached to the axoneme via the A-tubule as described above **(Fig. 5.10e',h',k')**. In the midpiece, the ODFs are at

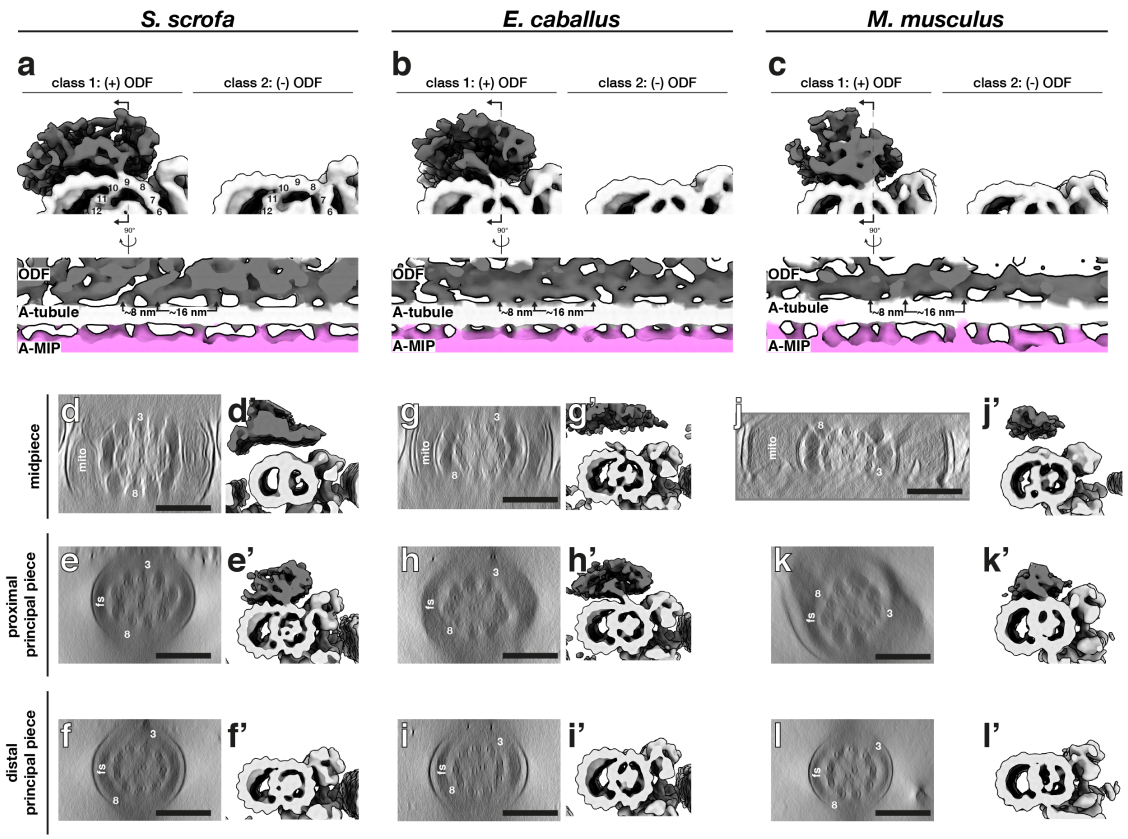


Figure 5.10 | The attachment of outer dense fibers to axonemal doublets varies along the length of the sperm flagellum. (a-c) *In situ* structures of the 96-nm axonemal repeat from the principal piece of pig (a), horse (b), and mouse (c) sperm after classification focused on the ODF attachment. **(d-l)** Axoneme structures with particles from tomograms from (d,g,j) only the midpiece, (e,h,k) only the proximal principal piece, and (f,i,l) only the distal principal piece. **Labels:** mito - mitochondria, fs - fibrous sheath. **Scale bars:** 250 nm.

their largest but, surprisingly, are not directly connected to the microtubule doublets **(Fig. 5.10a',g',j')**. This pattern of association seems to be a more general feature of mammalian sperm, as I observed it in all three species.

Thus, beyond the gradual tapering and staggered termination of the ODFs, a further source of proximal-distal asymmetry is the association of the ODFs with the axonemal doublets themselves. Intriguingly, this arrangement has actually been suggested previously based on measurements of ODF-doublet spacing in thin section TEM of bull sperm (Lesich et al., 2014), and cryo-ET now shows that it holds true at the molecular level in three other mammalian species. This configuration would allow the ODFs to slide relative to the axoneme while being restrained by the mitochondrial sheath, lending flexibility to the midpiece. This is proposed to support formation of the

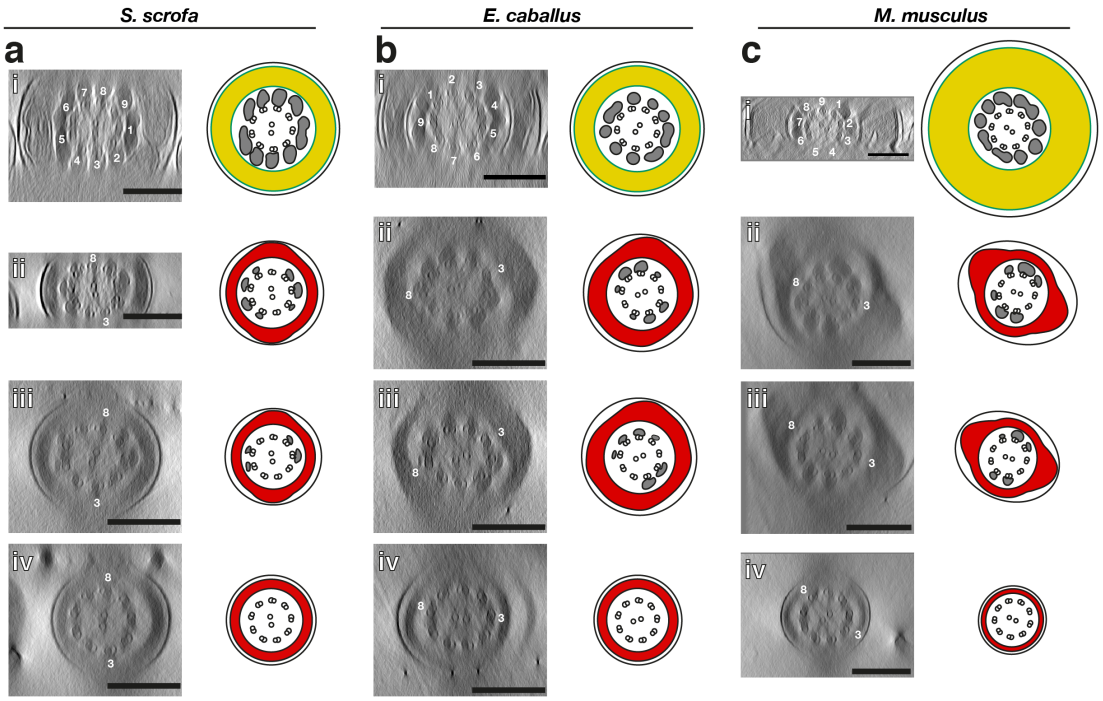


Figure 5.11 | Outer dense fibers impose mechanical asymmetry on the mammalian sperm flagellum. (a-c) Transverse sections (left panels) through tomograms of pig (a), horse (b), and mouse sperm flagella (c). Schematic renderings (right panels) of the positions of accessory structures in the flagellum, with mitochondria in green and yellow, outer dense fibers in grey, and the fibrous sheath in red. Tomograms were taken at various locations along the flagellum, from the midpiece (top) to the end of the principal piece (bottom). For all three species, tomograms from the midpiece (a-i, b-i, c-i) and, additionally for the pig the proximal principal piece (a-ii), were from lamellae. In pig and horse sperm, ODFs associated with doublets 3 and 8 terminate first and are replaced by attachments to the fibrous sheath, followed by ODFs at doublets 2, 4, and 7, while ODFs at doublets 9, 1, 5, and 6 are the last to terminate. The termination pattern is similar in mouse sperm, with the exception that ODF 9 terminates before ODF 2. **Scale bars:** 250 nm.

extreme bends in the midpiece seen during hyperactivation (Lindemann and Lesich, 2016). At least in the mouse, midpiece flexibility is crucial for sperm motility and hyperactivation, and mice lacking the catalytic subunit of a sperm-specific calcineurin isoform are infertile because they have more rigid midpieces (Miyata et al., 2015). Midpiece stiffness decreases as sperm transit through the epididymis (Jeulin et al., 1996; Miyata et al., 2015), which suggests that ODFs start out directly linked to the axoneme along their entire lengths and later locally detach in the midpiece.

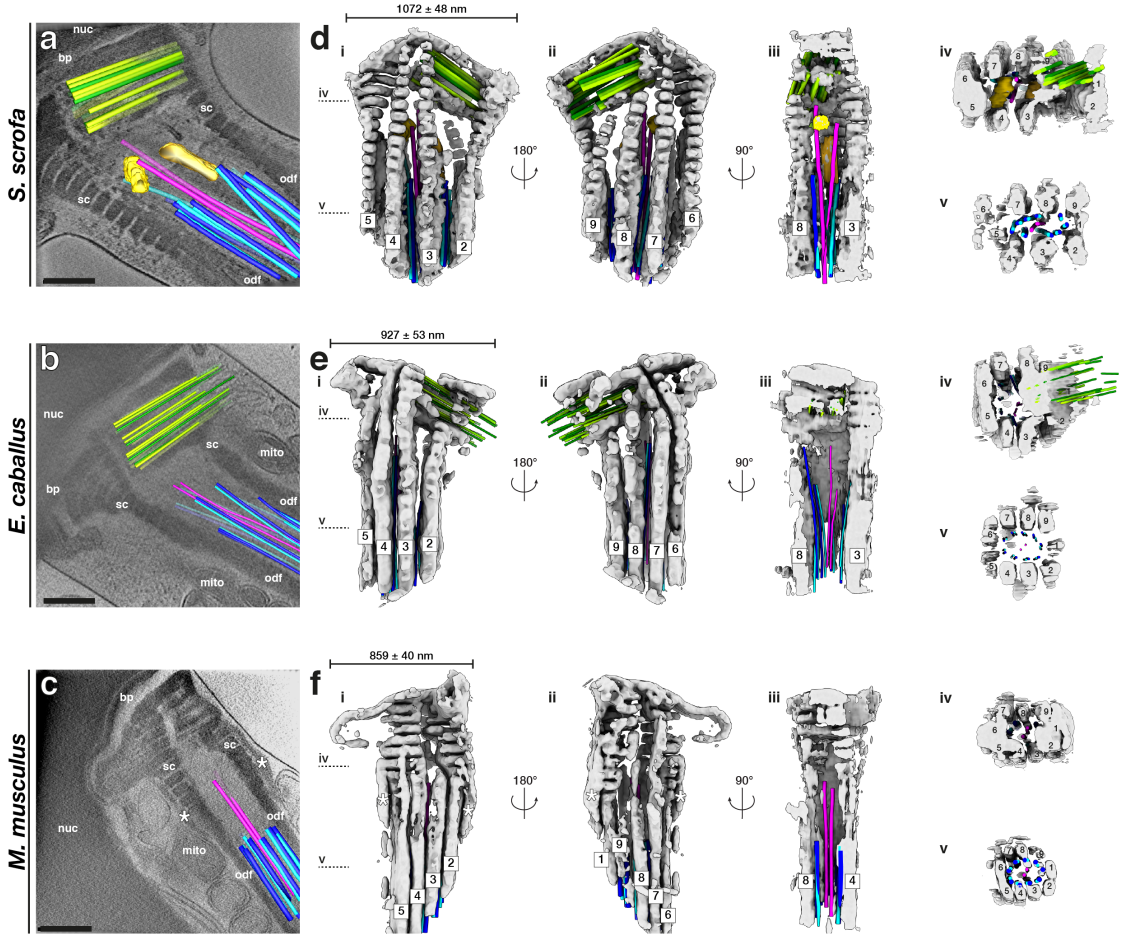


Figure 5.12 | The connecting piece forms a large, asymmetric chamber around the sperm centrioles. (a-c) Slices through Volta phase plate cryo-tomograms of the neck region in intact pig (a), horse (b), and mouse (c) sperm. **(d-f)** Three-dimensional architecture of the flagellar base, with the connecting piece in grey, the proximal centriole in green, distal centriole doublets in blue and singlets in pink, and electron-dense bars in yellow. The connecting piece was segmented semi-automatically with a neural network, while microtubules were traced manually. **Labels:** nuc - nucleus, bp - baseplate, sc - segmented columns, odf - outer dense fibers, mito - mitochondria. **Scale bars:** 250 nm.

The connecting piece forms a large, asymmetric chamber around the sperm centrioles at the base of the flagellum.

The mammalian sperm flagellum is not anchored by a basal body, and I show here that the distal centriole adopts an asymmetric, splayed-out structure **(Fig. 5.3)**. Instead, the connecting piece plays the role of the basal anchorage. Although properties of the flagellar waveform depend greatly on the properties of the base, there is very little information on how this region is organized in three dimensions. In order to capture the full three-dimensional complexity of the neck, I took advantage of the enhanced

contrast provided by the Volta phase plate, which facilitated tracing microtubules in the neck region while retaining the context of the surrounding CP **(Fig. 5.12a-c)**. Semi-automated neural-network-based segmentation (Chen et al., 2017a) revealed that the CP forms a large chamber enclosing the sperm centrioles. Although precise dimensions and shapes of the CP differ across species **(Fig. 5.12d-f)**, its general architecture appears to be conserved across mammalian species.

The proximal region of the CP consists of striated columns (SCs), which are continuous distally with the ODFs. In all three species, the CP displays both dorsoventral and left-right asymmetry. Following the numbering scheme laid out in (Ounjai et al., 2012), we found that the SCs follow a conserved pattern of grouping and splitting. The proximal CP can be grossly divided into left and right regions. The right region forms the proximal centriolar vault and comprises fused columns 8, 9, 1, 2, and 3, whereas the left region comprises fused columns 4, 5, 6, and 7 **(Fig. 5.12d-f, panels iv)**. The columns gradually separate, eventually splitting into nine separate columns that fuse distally with the ODFs **(Fig. 5.12d-f, panels v)**.

The PC is embedded within the proximal region of the CP. The material of the CP extends through the interstices of the PC triplets **(Fig. 5.1a-c)** and is continuous with electron-dense material within the proximal lumen of the PC **(Fig. 5.1a')**. Indeed, conventional EM suggests that the material within the PC is the precursor of the CP (Fawcett and Phillips, 1969). Intriguingly, the dorsoventral asymmetry of the pig sperm PC is defined relative to the CP, with the side of the shorter triplets always facing the Y-shaped segmented column 9 **(Fig. 5.12d)**. The asymmetry of the PC may therefore play a role in defining the asymmetry of the CP as a whole.

The pig sperm CP also has two electron-dense bars associated with the central singlets of the DC **(Fig. 5.12a,d, yellow and goldenrod)**, which resemble the bars observed in the bovine sperm CP (Ounjai et al., 2012). These bars are conspicuously absent from horse and from mouse sperm. Instead, mouse sperm have two electron-dense structures flanking the SCs **(asterisks in Fig. 5.12c,f)**, an arrangement reminiscent of the distribution pattern of the centrosomal protein speriolin (Goto et al., 2010; Ito et al., 2019).

The connecting piece is an elastic scaffold that is remodelled during the beat cycle.

Although dynein-driven inter-doublet sliding is well-understood to form the basis of flagellar bending, we do not know how bending is regulated in order to generate flagellar oscillation. For instance, it is unclear whether there are structural changes at base of the flagellum during the beat cycle. This question is even more complicated in mammalian sperm, where the flagellum is no longer anchored by a basal body, but by the connecting piece (CP). Light microscopy and thin-section EM of chinchilla sperm (Vernon and Woolley, 2004) and guinea pig sperm (Woolley et al., 2008) suggest that the CP is remodelled during a beat cycle. Furthermore, Riedel-Kruse and Hilfinger (2007) found that computational models of bull sperm movement could only recapitulate experimental data if the models allowed for basal sliding to occur. However, there is no three-dimensional structural information on how the CP moves in intact cells and in relation to other cellular components such as the centrioles. Thus, to determine whether and how the connecting piece changes during the flagellar beat, I imaged bull sperm plunge-frozen while actively swimming **(Figs.5.13-5.14)**. I imaged whole bull sperm with the Volta phase plate and compared sperm that had straight necks with sperm that had curved necks **(Fig. 5.13a-c)**.

The overall architecture of the bull sperm neck closely resembled that of the pig **(Fig. 5.13a'-c')**. Consistent with cryo-ET reconstructions from this study and from Ounjai et al. (2012) that show the proximal region of the CP consists of two fused masses, I designate the side of the PC as the "right" side. The "left" side is thus characterized by a nose-shaped extension where the CP attaches to the baseplate. The angle between the PC and the DC was 53 ± 5° in straight sperm, but this increased to 60 ± 2° in slightly curved sperm and 78 ± 7° in curved sperm **(Fig. 5.14a,b)**. If the DC (and thus the base of the axoneme) is fixed as a reference, this means that the PC moves approximately 25° towards the DC. However, because the PC is embedded in the proximal part of the CP, this displacement actually represents a larger-scale motion of the CP itself **(Fig. 5.13a"-c")**.

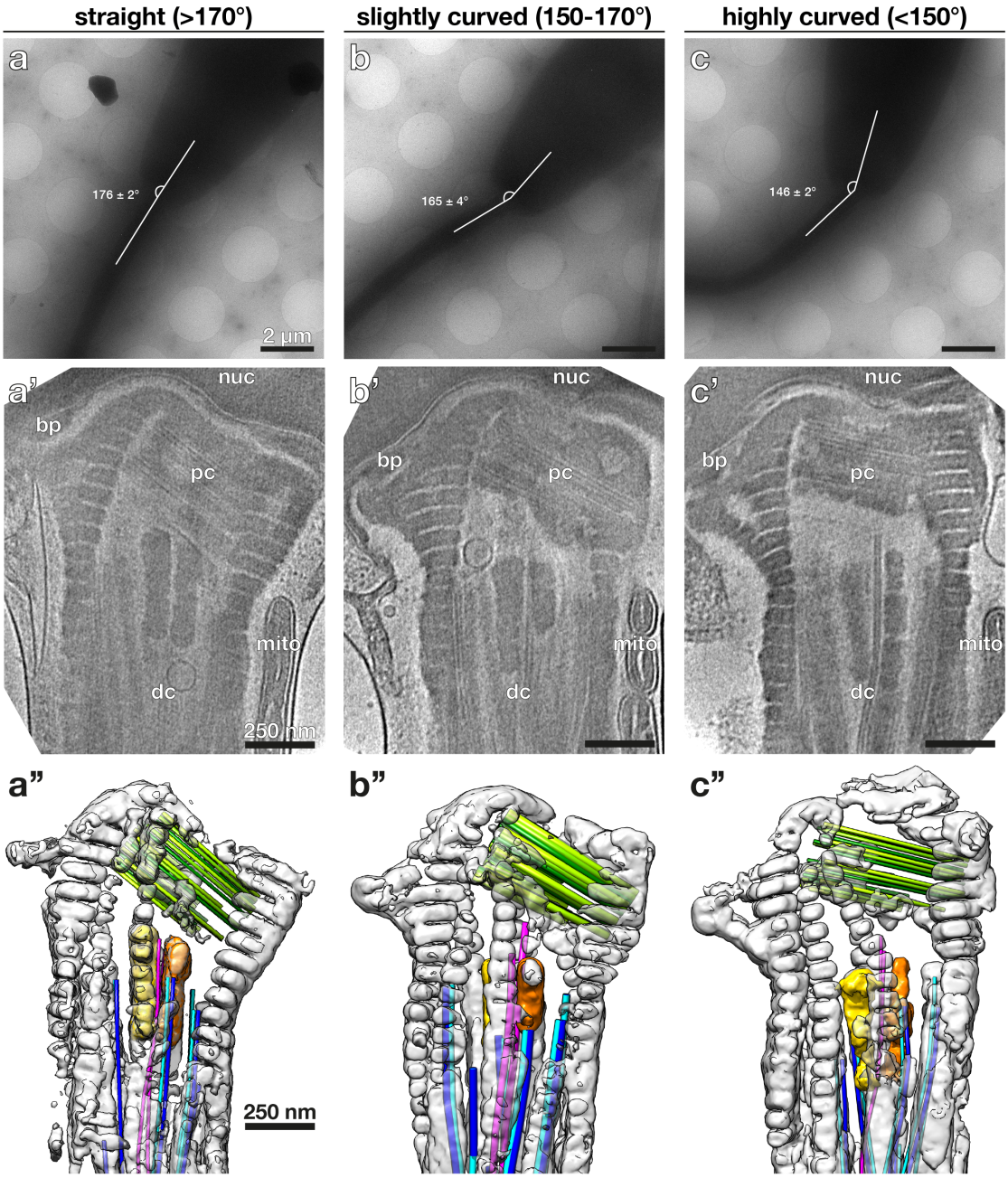


Figure 5.13 | The connecting piece is an elastic scaffold that is remodelled during the beat cycle. (a-c) Low-magnification cryo-electron micrographs of straight (a), slightly curved (b), and highly curved (c) bovine sperm. **(a'-c')** Slices through VPP cryo-tomograms of the cells shown in (a-c). **(a"-c")** Segmentations of the cells shown in (a-c). Proximal centriole triplets are shown in green, distal centriole doublets in blue, distal centriole singlets in pink, electron-dense bars in yellow (left bar) and orange (right bar), and the connecting piece in grey. **Labels:** nuc - nucleus, bp - baseplate, pc - proximal centriole, dc - distal centriole, mito - mitochondria. **Scale bars:** (a-c) 2 µm, (a'-c', a"-c") 250 nm.

When I measured the relative angles between individual segments of the SCs **(Fig. 5.14e,f)**, I found that movement of the CP was localized to a very specific point. In particular, the angle between segments 8 and 9 of the left SCs changes from -1 ± 3° in straight sperm to -23 ± 6° in highly curved sperm **(Fig. 5.14f, left)**. In the right SCs, the angle between segments 8 and 9 changes from +5 ± 4° in straight sperm to -13 ± 4° in curved sperm **(Fig. 5.14f, right)**. This displacement is consistent with the ~25° movement of the PC towards the DC. The angles between other segments do not change significantly between straight and curved sperm. Note that segments 8 and 9 are located just proximal to the mitochondrial sheath, which suggests that the mitochondria collectively act as a retinaculum to restrain movement of the flagellum. Interestingly, the mitochondrial sheath is itself asymmetric at the region of the neck, with the mitochondria on the right side of the neck extending further proximally than those on the left. This may provide at least some structural basis for the observation that I only observed strong curvature towards the left (that is, opposite the side of the PC).

To measure the extent of basal sliding, I measured the displacement between the segmented columns along the axis of the flagellum **(Fig. 5.14c,d)**. As fixed reference points, I oriented the head-tail axis vertically and drew lines perpendicular to this axis extending from segments 9 of the left and right SCs. I then measured the distance between these lines (d), which I defined to be negative if segment 9 on the right SC was lower than segment 9 on the left. In straight sperm, segment 9 of the right SCs was typically lower than the corresponding segment 9 on the left (-189 ± 61 nm). In highly curved sperm, segment 9 of the right SCs was higher than that on the left (+116 ± 81 nm). This translates to sliding on the order of ~150-300 nm, which is of the same range estimated by Riedel-Kruse and Hilfinger (2007).

Thus, the CP is an elastic structure that is itself remodelled during the beat cycle, at least in bull sperm. Both the PC/DC angle **(Fig. 5.14g)** and the relative sliding between the left and right SCs **(Fig. 5.14h)** correlate with neck angle (Pearson r = -0.9285 and -0.9347, respectively). PC/DC angle and SC sliding also correlate with each other (Pearson r = 0.9138) **(Fig. 5.14i)**. As such, the different components of the

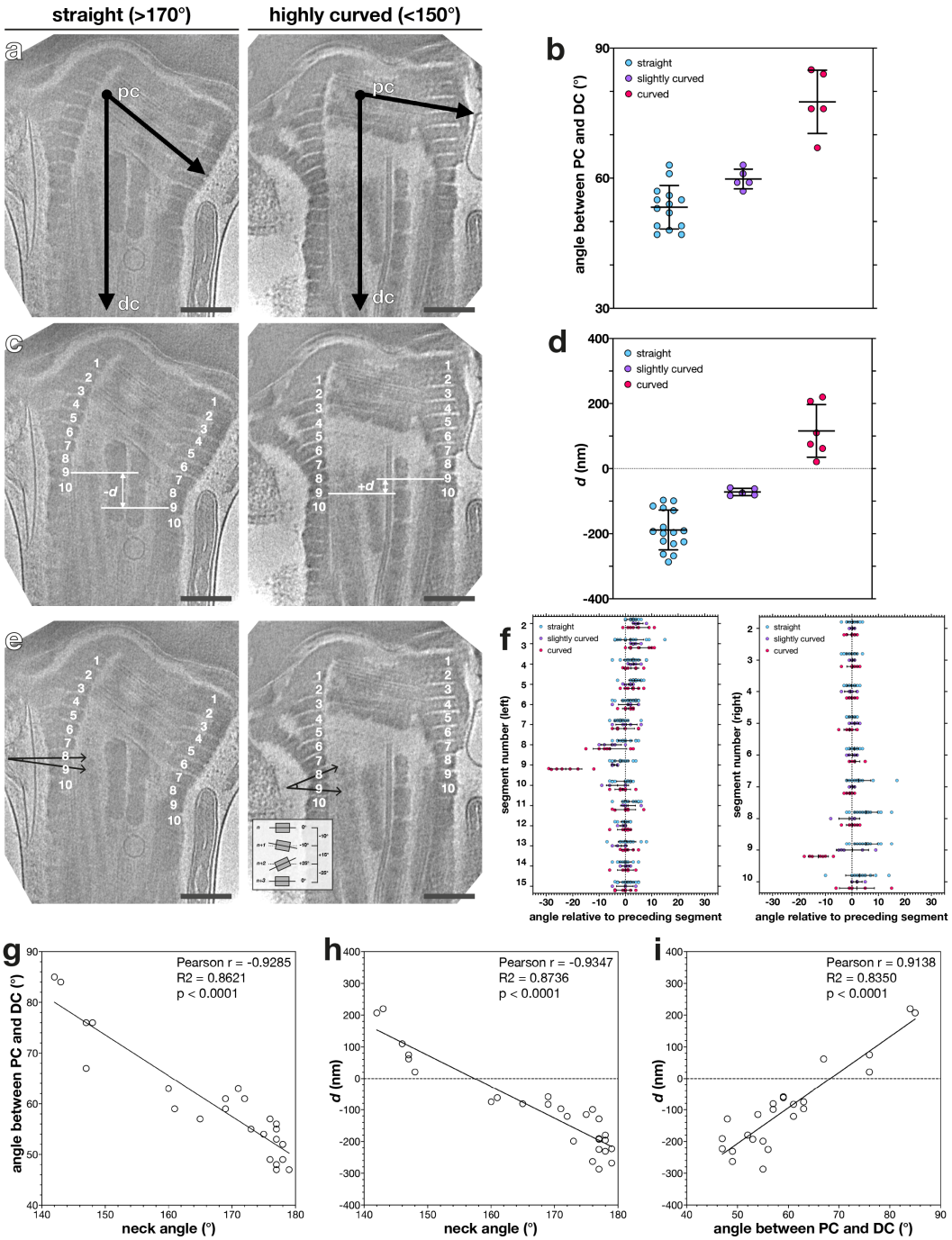


Figure 5.14 | Quantifying structural deformations in the sperm neck. Three quantities were measured to compare deformations of the connecting piece in sperm with curved necks relative to sperm with straight necks, namely: **(a,b)** the angle between the proximal centriole (PC) and the distal centriole (DC); **(c,d)** the relative distance (*d*) between a fixed segment (segment 9) in the left segmented columns and its corresponding segment in the right segmented columns; and **(e,f)** the relative angles between each segment of the segmented columns. Left panels (a, c, e) show schematics of how these quantities were defined, while right panels (b, d, f) show the measurements grouped according to neck angle. Segmented columns are labelled and numbered based on the convention used for measurements. Every data point represents a cell, and lines represent mean ± standard deviation. **(g)** PC-DC angle correlates with neck angle. **(h)** Segmented column sliding (*d*) correlates with neck angle. **(i)**PC-DC correlates with segmented column sliding. **Scale bars:** 250 nm.

sperm neck move concertedly, suggesting that they form a coordinated micron-scale assembly. Reversal of the elastic remodelling of the CP may provide the mechanism for reversing the direction of the propagating wave. In this context, the segmented nature of the CP may be an adaptation to allow it to be both strong and flexible, akin to vertebrae of the spine. This raises intriguing biomechanical questions of how differences in CP architecture translate to differences in flagellar waveform. For instance, in pig sperm, mitochondria only appear distal to the segmented columns, unlike in bull and horse sperm where they wrap around the lower ends of the segmented columns. In mouse sperm, the left side of the CP is adjacent to the basal hook of the head, which could reasonably be expected to provide resistance to bending. There are also the larger outstanding questions of the evolutionary significance of the CP. For instance, the CP seems to be a feature of internal fertilizers and is absent from sea urchin or *Xenopus* sperm. In fowl sperm and turtle sperm, the CP is present but is not segmented (Wu et al., 2020). It would also be interesting to trace whether the appearance and elaboration of the CP relates to the progressive remodelling of the distal centriole.

5.3 Concluding Remarks

This study exemplifies the need for comparative studies of cilia and flagella, both from different species and from different cell types of the same species. This work motivates future efforts to define how species-specific features of flagellar architecture affect the hydrodynamics of sperm motility. Such endeavours will likely involve the synthesis of structural cell biology, motility analysis, and mathematical modelling. The structures presented here provide crucial resources for understanding how the ancient and conserved ciliary microtubule core is ornamented to support motility through diverse fluid environments.

6

Acrosome destabilization transforms the molecular landscape of the mammalian sperm surface

Contents

6.1 Introduction 110
6.2 Results and Discussion 112
6.2.1 The plasma membrane and outer acrosomal membrane are closely apposed even in non-capacitated sperm. 112
6.2.2 Acrosome swelling and membrane destabilization already occur during capacitation. 114
6.2.3 Acrosome destabilization results in release of morphologically heterogeneous, protein-decorated vesicles along with patches of crystalloid material. 121
6.2.4 An atypical fission-fusion pathway maintains cell integrity after acrosome destabilization. 124
6.2.5 The acrosome reaction leads to topographical and molecular remodelling of the sperm surface. 126
6.2.6 An updated model of how capacitation-associated membrane destabilization restructures the sperm surface. 130
6.3 Concluding Remarks 134

6.1 Introduction

Mammalian sperm must reside in the female reproductive tract for up to a few hours before they gain the ability to fuse with the egg. During this time, sperm undergo a plethora of biochemical changes collectively called capacitation (Aitken and Nixon, 2013; Bailey, 2010; Gervasi and Visconti, 2016). The discovery of this phenomenon

was crucial to the development of *in vitro* fertilization (Austin, 1951; Chang, 1951, 1959). Capacitation is characterized by cholesterol efflux, phospholipase activation, and altered membrane fluidity (Bailey, 2010; Harrison and Gadella, 2005; Nolan and Hammerstedt, 1997; Travis and Kopf, 2002), which render sperm capable of undergoing the acrosome reaction – a unique membrane remodeling event that is an absolute requirement for sperm to become fusion-competent (Yanagimachi, 1981).

Classical EM revealed that the acrosome reaction is a dramatic morphological change involving fusion of the plasma membrane and the outer membrane of the acrosome, a large vesicle overlying the anterior two-thirds of the nucleus, at multiple points along its surface (Nagae et al., 1986; Russell et al., 1979; Stock and Fraser, 1987; Yudin et al., 1988). Mechanistic models of the acrosome reaction often treat it with direct parallels to synaptic vesicle exocytosis (Tsai et al., 2010; Zanetti and Mayorga, 2009); however, membrane recycling does not occur during the acrosome reaction, and fusing membranes are instead shed as vesicles. Light microscopy has also shown that, as a result of the acrosome reaction, Izumo1 re-localizes onto the plasma membrane, allowing it to interact with its oocyte-borne partner, Juno, to mediate sperm-egg adhesion (Satouh et al., 2012). Acrosome swelling and membrane docking are clear intermediates in this process (Sosa et al., 2015; Tsai et al., 2010; Zanetti and Mayorga, 2009), but how exactly these stages lead to vesiculation while maintaining cellular integrity, and how this ultimately leads to protein re-localization and the acquisition of fusion competence, remain uncertain.

Classical models of fertilization treat capacitation and the acrosome reaction as two independent events, with capacitated sperm being "induced" to acrosome react when they bind the zona pellucida (Mayorga et al., 2007; Tsai et al., 2010). However, the contents of the acrosome are exposed even during capacitation, which suggests that the acrosome does not remain completely intact until zona binding (Kim et al., 2011; Kim and Gerton, 2003). Furthermore, elegant studies in the mouse showed that most sperm acrosome-react before encountering the zona (Jin et al., 2011), and that acrosome-reacted sperm are capable of penetrating the zona and go on to fertilize eggs (Inoue et al., 2011). More recently, *in vivo* imaging revealed that most mouse sperm

acrosome-react even before entering the vicinity of the oocyte (Hino et al., 2016; La Spina et al., 2016; Muro et al., 2016). The growing body of evidence challenging the classical view necessitates a re-examination of how capacitation-associated membrane destabilization leads to the acrosome reaction.

In this chapter, I use cellular cryo-ET, three-dimensional segmentation, and subtomogram averaging to study capacitation and the acrosome reaction in whole, unfixed, unstained mammalian sperm. This analysis reveals that acrosome swelling and membrane destabilization begin during capacitation and ultimately lead to a complete restructuring of the sperm surface.

6.2 Results and Discussion

6.2.1 The plasma membrane and outer acrosomal membrane are closely apposed even in non-capacitated sperm.

I imaged sperm from highly-fertile commercial artificial insemination pigs (*Sus scrofa domestica*) in various stages of *in vitro* capacitation and the acrosome reaction. Pig sperm are ideal for cryo-ET as their heads are flat (several hundred nanometers to one micron), which facilitates vitrification and imaging without the need for sample thinning. Both membrane-intact and membrane-disrupted cells could be clearly identified in low-magnification cryo-EM projection images of non-capacitated sperm **(Fig. 6.1)**. Disrupted cells were surrounded by vesicles and, crucially, had lost the plasma membrane overlying the post-acrosomal region **(Fig. 6.1d-f)**. This is likely to result in a loss of cell integrity and therefore in cell death, so I excluded cells with this morphological signature from further analysis.

A striking feature of intact, non-capacitated sperm was the uniform spacing between the plasma membrane (PM) and the outer acrosomal membrane (OAM) **(Fig. 6.1a-c, 6.2a)**. The PM and the OAM are ~8-10 nm apart and lie parallel to each other until the end of the acrosome, where the vesicle tapers **(Fig. 6.2b-d)**. This differs from many classical EM images of sperm, in which the PM and OAM appear wavy, with estimated interbilayer distances of >10 nm (Sosa et al., 2015; Tsai et al., 2010; Zanetti and Mayorga, 2009). These observations underscore the

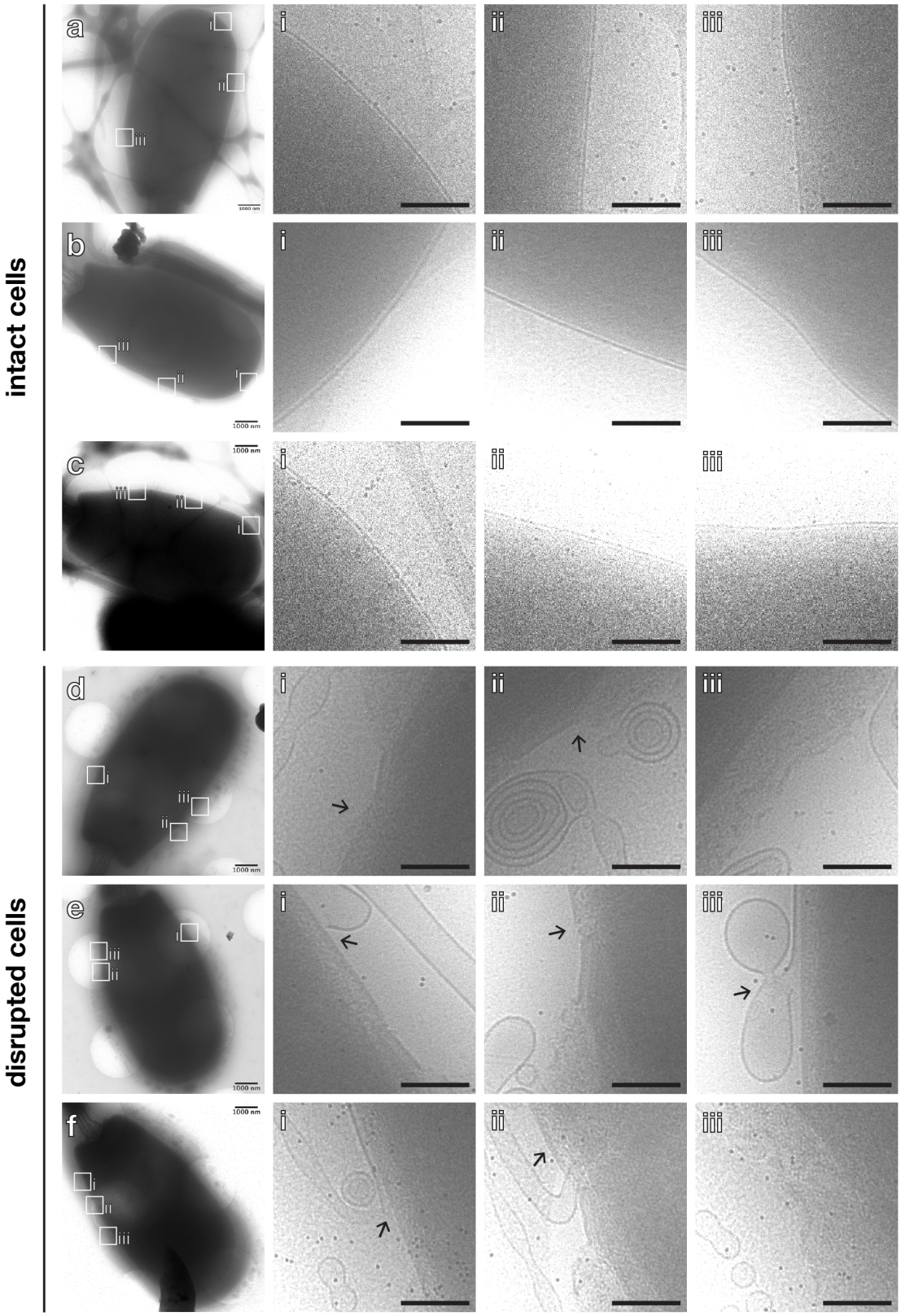


Figure 6.1 | Representative micrographs of intact and disrupted non-capacitated sperm. Cryo-EM projection images of **(a-c)** intact and **(d-f)** disrupted non-capacitated sperm. Panels (i), (ii), and (iii) are digital zooms of the areas boxed out in (a-f). **Scale bars:** left panels - 1 μm, panels i-iii - 250 nm.

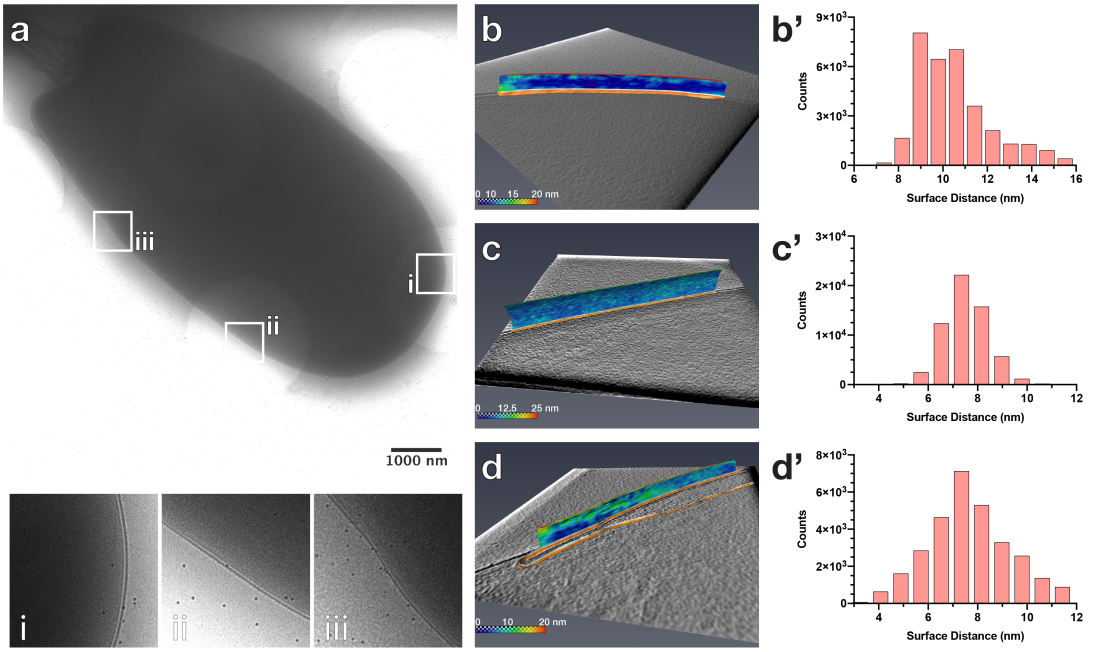


Figure 6.2 | The plasma membrane and the outer acrosomal membrane are closely apposed even in non-capacitated sperm. (a) Cryo-EM projection image of an intact, non-capacitated sperm head with insets (i-iii) showing close spacing between the locally-parallel plasma and outer acrosomal membranes. **(b-d)** Segmentation of tomograms from the apical (b), pre-equatorial (c), and equatorial (d) regions, with the plasma membrane colored by closest distance to the outer acrosomal membrane (orange). Corresponding distance distributions are shown in (b'-d'). **Scale bars:** (a) 1 μm.

advantages afforded by rapid vitrification and highlights why cryo-EM is appropriate for the study of membrane remodelling.

6.2.2 Acrosome swelling and membrane destabilization already occur during capacitation.

To track intermediates leading to the acrosome reaction, I imaged sperm incubated under capacitating conditions (i.e; in media containing HCO_3^-, BSA, and Ca^{2+}) with or without the addition of calcium ionophore A23187 or progesterone, which artificially stimulate the acrosome reaction in capacitated cells **(Fig. 6.3)**. Sperm within an ejaculate are inherently variable (Buffone et al., 2014), which precludes a strictly timepoint-based assessment of the reaction coordinate. Instead, I imaged several cells from several different animals, analyzed the dataset for membrane remodeling intermediates that I could observe consistently **(Table 6.1)**, and attempted to order

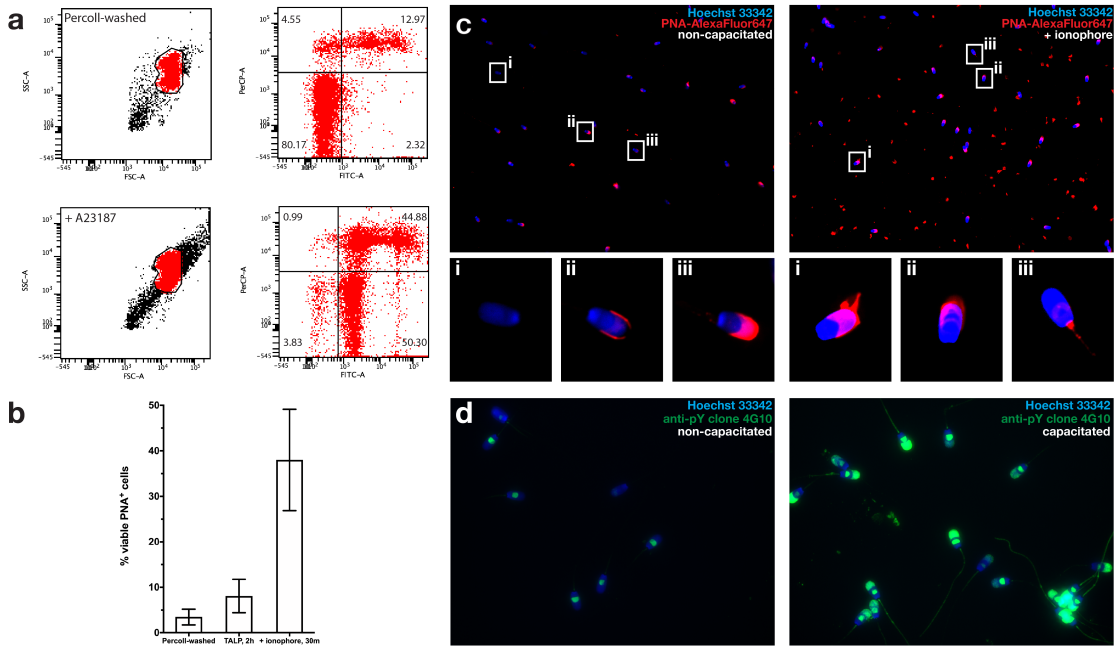


Figure 6.3 | Assessment of capacitation and acrosome status by flow cytometry and fluorescence microscopy. **(a)** Flow cytometry of non-capacitated (top) and acrosome-reacted (bottom) sperm allows for **(b)** quantification of viable, acrosome-reacted cells. **(c)** Fluorescent lectin staining of permeabilized non-capacitated (left) and acrosome-reacted (right) cells. **(d)** Phosphotyrosine staining of non-capacitated (left) and capacitated (right) cells.

these stages relative to one another.

Sperm incubated in capacitating conditions (for simplicity, capacitated sperm) showed an overall increase in head dimensions **(Fig. 6.4)** (length: non-capacitated = 8.69 ± 0.14 μm, capacitated = 8.96 ± 0.21 μm; width: non-capacitated = 4.66 ± 0.09 μm, capacitated: 4.84 ± 0.17 μm). Cryo-ET revealed that this was associated with swelling of the acrosome and with decondensation of acrosome contents **(Fig. 6.5c-f)**. Decondensation of the acrosomal matrix improved contrast within the acrosome lumen, making protein arrays on the OAM visible in whole cells **(arrowheads in Fig. 6.5c-f)** whereas in non-capacitated sperm they were only visible in thin lamellae **(Fig. 3.2)**. Acrosome swelling was previously observed by classical EM of ionophore-treated cells (Zanetti and Mayorga, 2009), but cryo-ET reveals that swelling already occurs during capacitation. An atomic force microscopy (AFM)-based study also found evidence of acrosome swelling during capacitation, and found it to be dependent on cholesterol efflux and on the presence of bicarbonate (Boerke et al., 2014).

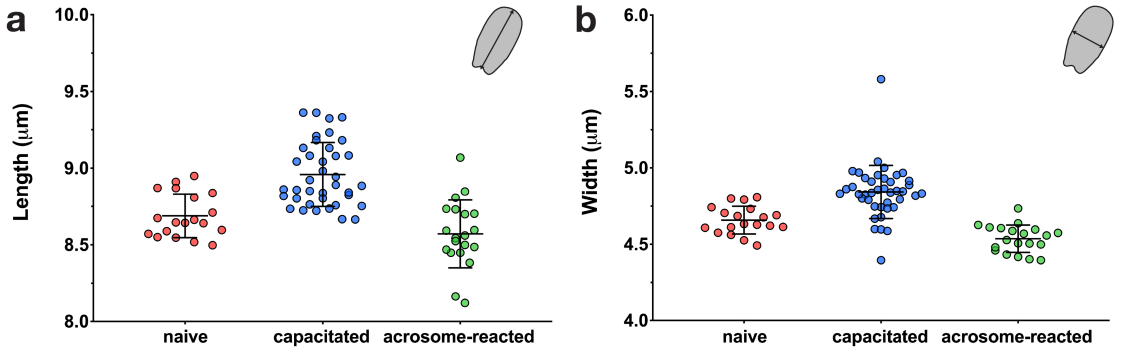


Figure 6.4 | Changes in sperm head dimensions with capacitation and ionophore-stimulated acrosome reaction. (a,b) Sperm head dimensions change with swelling and subsequent vesiculation and loss of the acrosome, as measured from cryo-EM projection images. Every point represents a cell and lines represent mean ± standard deviation.

Various membrane remodelling intermediates were present in capacitated cells, and all of them involve the loss of uniform PM-OAM spacing. Particularly striking were points of close apposition between these membranes, including instances where the bilayers appeared to be <1 nm apart **(Fig. 6.6)**. These represent long contact zones and not hemifusion intermediates as there is a clear central density throughout, indicating that the proximal leaflets have not merged **(Fig. 6.6a,b)**. These contact zones can be up to several hundred nanometers long, but appear to be flat **(Fig. 6.6c,d)** and not circular as previously suggested (Zanetti and Mayorga, 2009).

Some capacitated cells with profusely-swollen acrosomes exhibited clear signs of membrane destabilization **(Fig. 6.5, Fig. 6.7)**. One intriguing intermediate observed was rupture of the OAM, which caused it to locally buckle away from the PM. Surprisingly, I observed what seem to be membrane edges at the ends of these regions, where the OAM curves towards the PM **(asterisks in Fig. 6.5e,f, Fig. 6.7a-c)**. In a number of cells, the OAM had clearly destabilized whereas the overlying PM was still intact, which means that these cells might appear "acrosome-intact" as assessed by fluorescent lectin-based assays. Capacitated cells also showed signs of vesiculation **(Fig. 6.7a,b)**, suggesting that cells are not arrested at the OAM rupture stage. I also imaged cells plunge-frozen within ~2-6 minutes of ionophore treatment and found further evidence of OAM rupture, along with direct evidence that these intermediates lead to formation of mixed vesicles consisting of both PM and OAM **(Fig. 6.8)**.

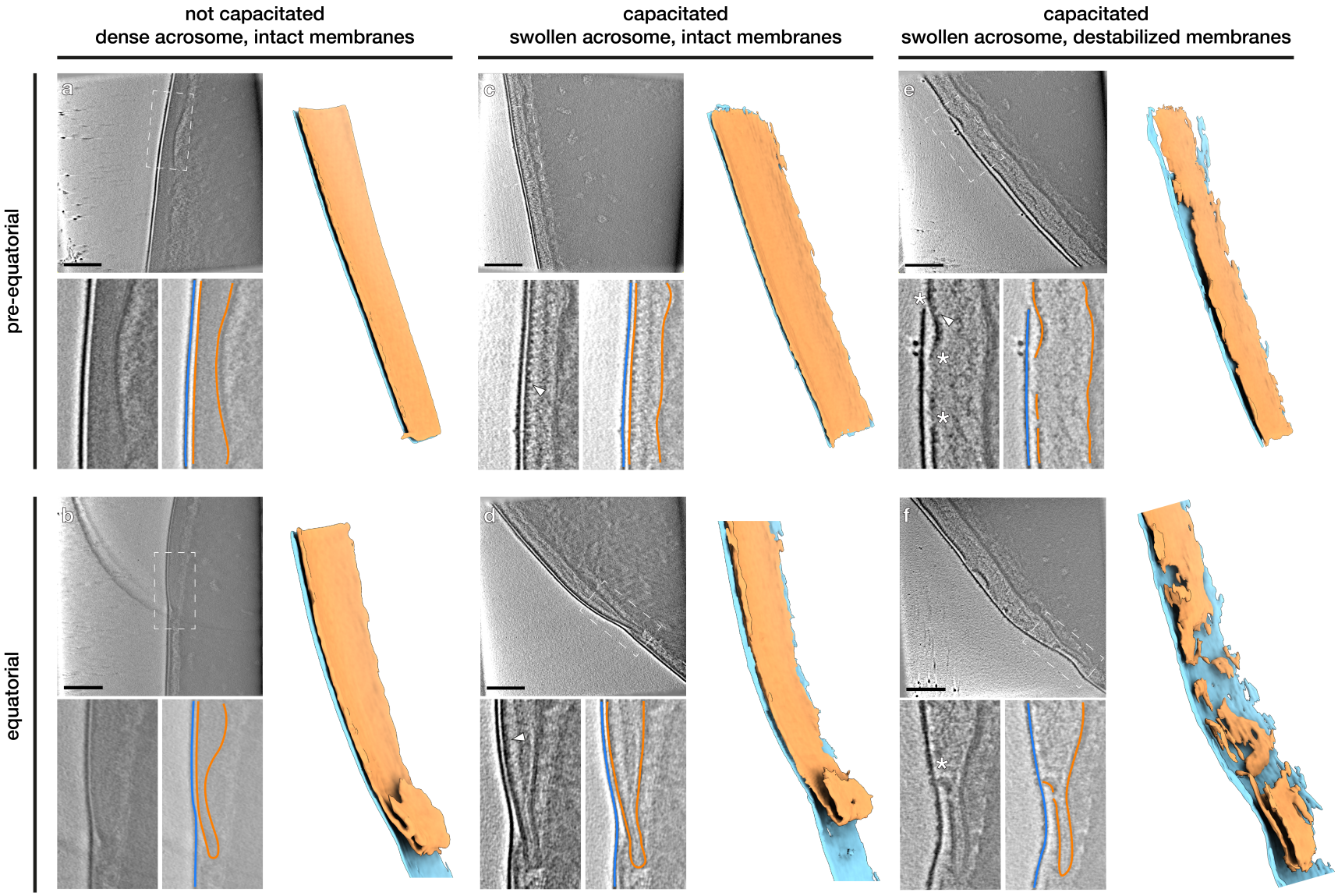


Figure 6.5 | Capacitation is associated with acrosome swelling and membrane destabilization. Computational slices (2.1-nm thick) (upper left panels) and corresponding segmentations (right panels) of VPP cryo tomograms of non-capacitated **(a, b)** and capacitated **(c-f)** cells representing various stages of acrosome swelling and membrane disruption around the pre-equatorial (a, c, e) and equatorial (b, d, f) regions. For clarity, the plasma membrane (blue) and outer acrosomal membrane (orange) are manually annotated in digital zooms (lower left panels); in these panels, arrowheads indicate outer acrosomal membrane protein densities and asterisks indicate sites of membrane rupture. **Scale bars:** 250 nm.

Table 6.1 | Number of tomograms in the dataset representing each membrane remodelling intermediate.

condition / description	capacitated	AR ionophore	AR progesterone
dense acrosome, membranes intact	10	4	-
swollen acrosome, membranes intact	15	4	-
swollen acrosome, OAM destabilized	8	2	1
swollen acrosome, PM destabilized	2	-	-
swollen acrosome, OAM and PM destabilized	5	2	1
reacted, apical, shroud present	-	10	5
reacted, apical, shroud absent	-	6	-
reacted, equatorial	-	32	5
total number of tomograms	**40**	**60**	**12**
total number of animals	**5**	**6**	**1**

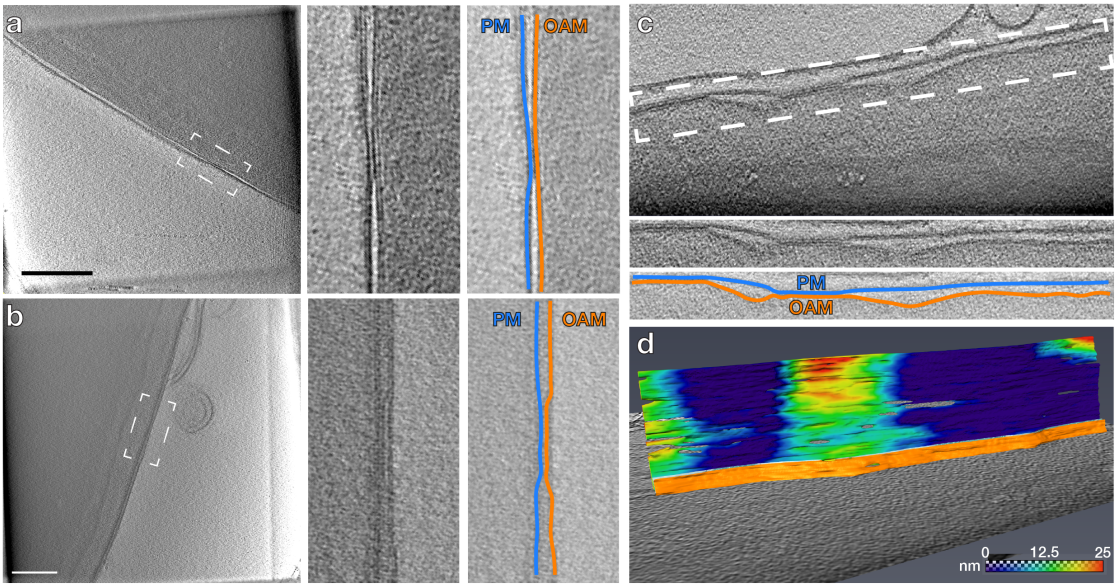


Figure 6.6 | Long contact zones are visible in capacitated and acrosome-reacting sperm. **(a, b)** Slices through defocus-contrast tomograms taken at the pre-equatorial region, with digital zooms showing long, flat regions of membrane docking. **(c)** Computational slice through defocus-contrast tomogram of a cell plunge-frozen ~6 min after ionophore addition, with **(d)** segmentation of the plasma membrane colored by closest distance to the outer acrosomal membrane. **Labels:** PM - plasma membrane, OAM - outer acrosomal membrane. **Scale bars:** 250 nm.

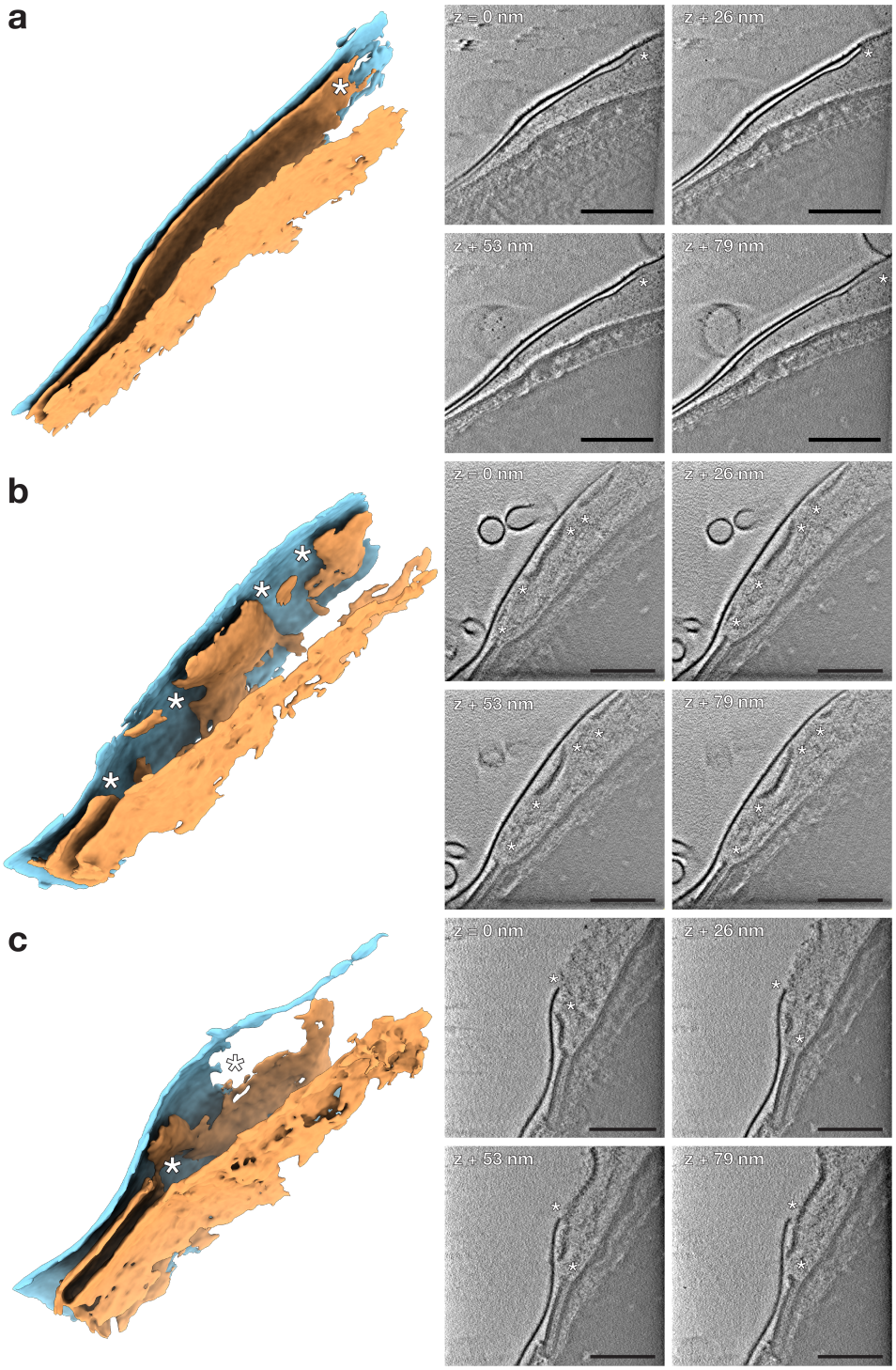


Figure 6.7 | Additional examples of membrane fission-fusion intermediates in late-stage capacitated sperm. Segmentation (left) of VPP tomograms (representative slices, right). **(a)** The plasma membrane remains intact, but the outer acrosomal membrane has begun to rupture locally (asterisks). **(b)** The plasma membrane remains mostly intact, but the outer acrosomal membrane has ruptured extensively. **(c)** Both the plasma membrane and the outer acrosomal membrane have ruptured. Note the presence of vesicles in (a) and (b), which indicate that vesiculation has occurred in neighboring regions of the cell. **Scale bars:** 250 nm.

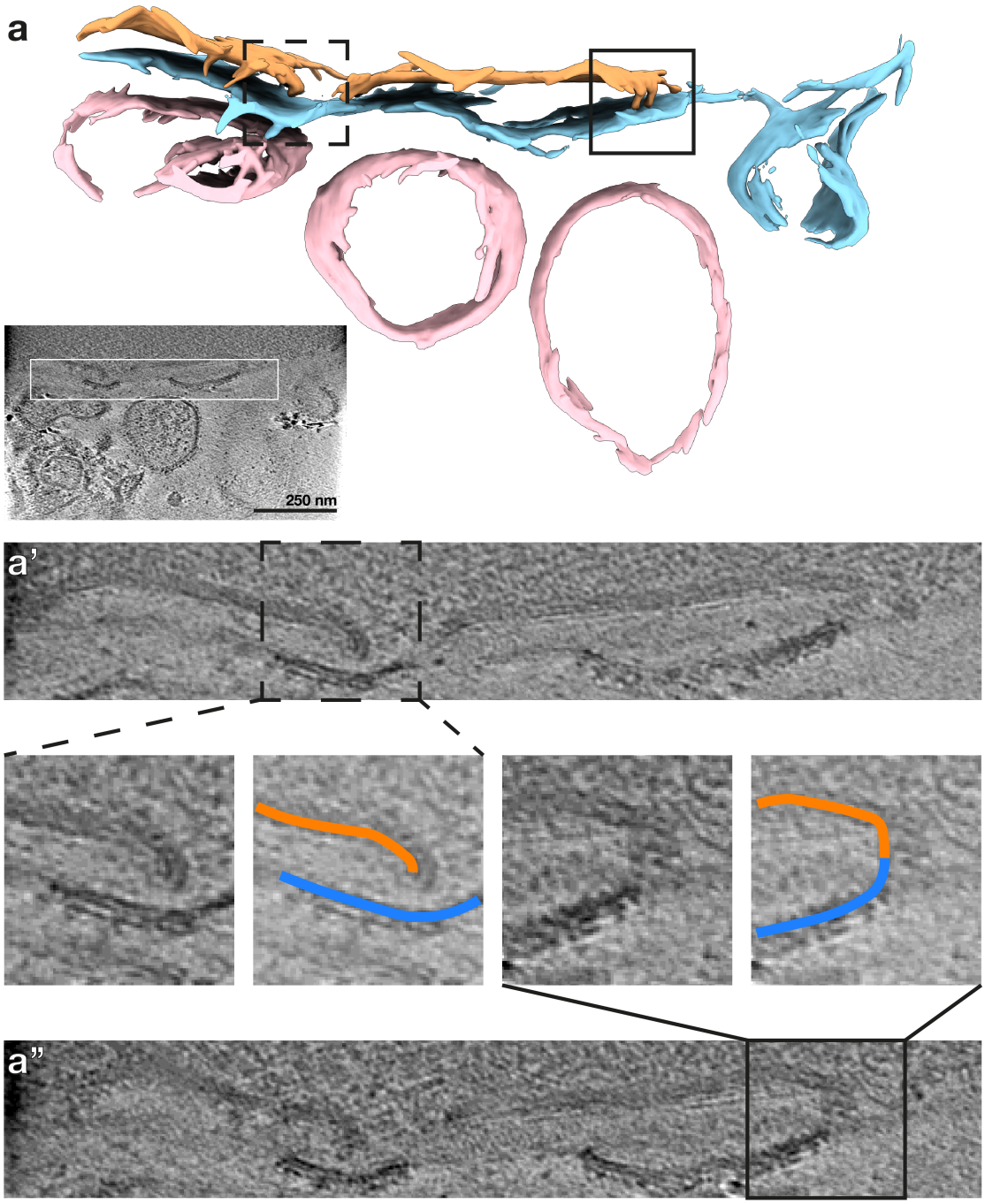


Figure 6.8 | Membrane destabilization, fusion, and vesiculation of the plasma membrane and the outer acrosomal membrane. (a) Segmentation of a defocus-contrast cryo tomogram from a cell plunge-frozen 6 min after addition of calcium ionophore (tomographic slice shown in inset) showing how membrane destabilization leads to vesiculation. **(a', a")** Computational slices through the tomogram in (a), with annotated examples of membrane rupture (dashed frame) and membrane fusion (solid frame). **Scale bars:** 250 nm.

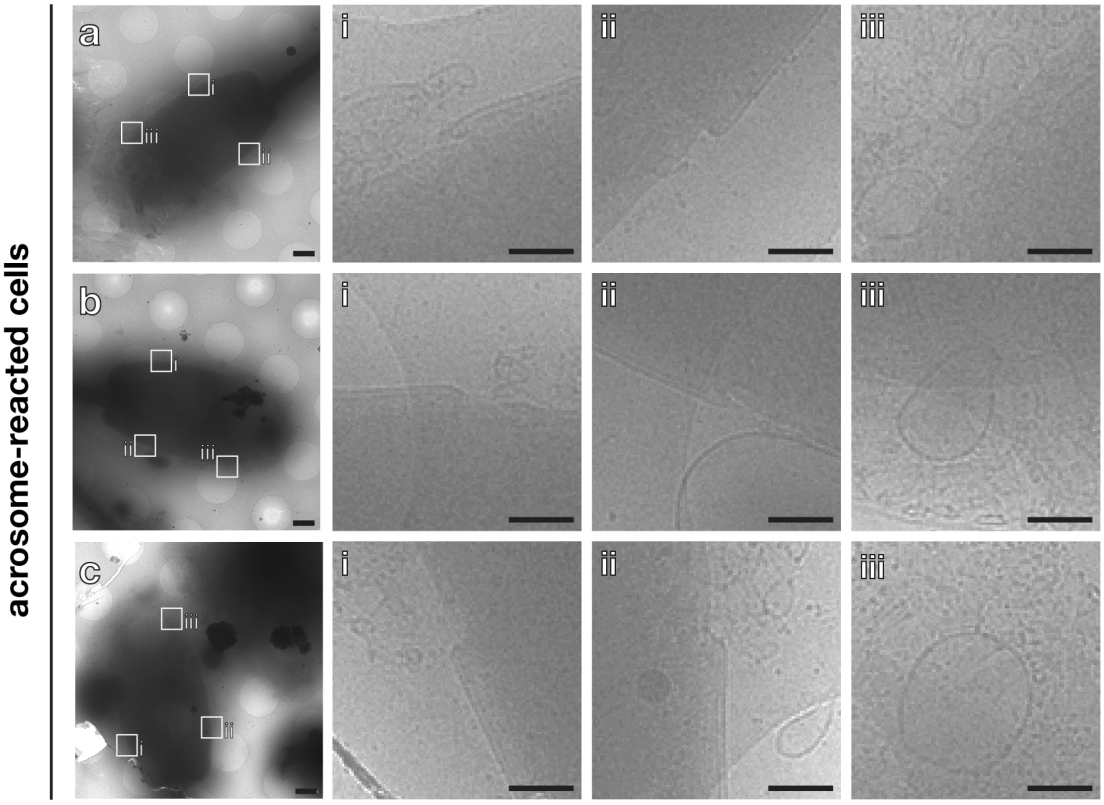


Figure 6.9 | Representative micrographs of fully acrosome-reacted sperm. (a-c) Cryo-EM projection images of fully acrosome-reacted sperm. Panels (i), (ii), and (iii) are digital zooms of the areas boxed out in (a), (b), and (c). **Scale bars:** left panels - 1 μm, panels i-iii - 250 nm.

Thus, the cryo-ET data here reveal that acrosome swelling and decondensation, membrane docking, and membrane destabilization all occur during capacitation. Capacitated cells are therefore not arrested at the membrane docking stage, as has been proposed (Mayorga et al., 2007; Tsai et al., 2010). This has important functional consequences, as it suggests that the acrosome reaction is not a discrete process separate from capacitation. Instead, acrosome vesiculation likely occurs as a direct consequence of capacitation-associated membrane destabilization.

6.2.3 Acrosome destabilization results in release of morphologically heterogeneous, protein-decorated vesicles along with patches of crystalloid material.

In order to assess how the acrosome reaction remodels the sperm surface, I then imaged capacitated sperm plunge-frozen after a ~30 min ionophore treatment. Fully

acrosome-reacted cells could be easily recognized even in low-magnification cryo-EM images **(Fig. 6.9)**. Acrosome-reacted cells were surrounded by a shroud of vesicles along with liberated acrosomal contents. In addition, the apical regions of these cells had become very thin due to the loss of the acrosome. Cryo-ET revealed that the vesicles of the acrosomal shroud were morphologically heterogeneous –some were spherical, others tubular, and others had more complex shapes – yet most of them were protein-decorated **(Fig. 6.10, Fig. 6.11a, Fig. 6.12a)**.

I also observed striking lattice-like structures in the shroud **(asterisks in Fig. 6.10, Fig. 6.11b, Fig. 6.12a)**. These structures are visible in swollen acrosomes of capacitated cells **(Fig. 6.12d)**, and persist around acrosome-reacted cells even after dispersal of the shroud **(Fig. 6.12e)**. Acrosome crystalloids have also been seen by classical EM in rabbit (Olson and Winfrey, 1994) and in ram sperm (Fléchon, 2016), where they form a larger structure extending across almost the entire anterior acrosome. Cryo-ET of sperm thinned by cryo-FIB milling revealed that the crystalloids are present in the acrosomes of non-capacitated pig sperm as well **(Fig. 3.2a-ii, Fig. 6.12c)**, suggesting that the smaller crystalloid patches in the acrosomal shroud are a result of the disassembly of an initial larger superstructure. It is tempting to speculate that these crystalloids represent a structural scaffold onto which soluble components of the acrosomal matrix are anchored, and that their progressive disassembly represents a mechanism for controlled release of acrosome contents.

I then attempted to define the structure of the crystalloids by subtomogram averaging. I averaged crystalloid patches from capacitated sperm since the surrounding material was too dense in non-capacitated sperm. The patches were also larger in capacitated sperm than in the shrouds of acrosome-reacted sperm, which facilitated averaging by increasing particle numbers. Subtomogram averaging of crystalloid patches revealed a complex architecture consisting of staggered columns of saddle-shaped densities (dark blue) and horseshoe-shaped densities (light blue) **(Fig. 6.13a)**. Within each column, individual densities are spaced every ~14 nm. Both ends of the saddle-shaped densities make contacts with a horseshoe-shaped density, yielding rows of alternating densities with a saddle-to-saddle or horseshoe-to-horseshoe spacing

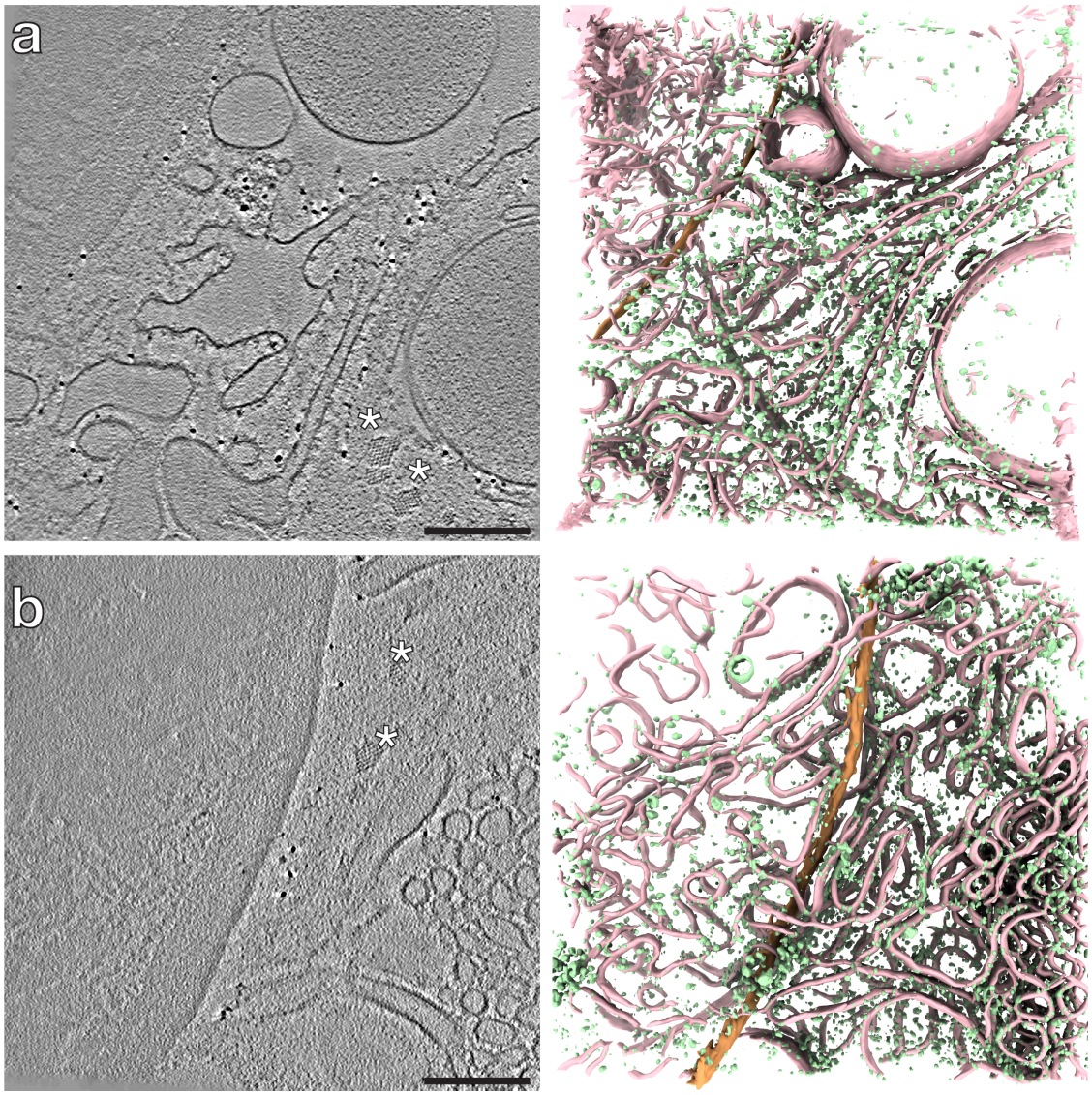


Figure 6.10 | The acrosomal shroud consists of morphologically heterogeneous protein-decorated vesicles. (a, b) Computational slices through VPP cryo-tomograms of the acrosomal shroud in sperm samples plunge-frozen 30 min after ionophore treatment. Crystalloid patches are marked with asterisks. Right panels show three-dimensional segmentations of the tomograms in (a) and (b), respectively. **Colors:** orange - inner acrosomal membrane; pink - vesicles; green - membrane protein densities. **Scale bars:** 250 nm.

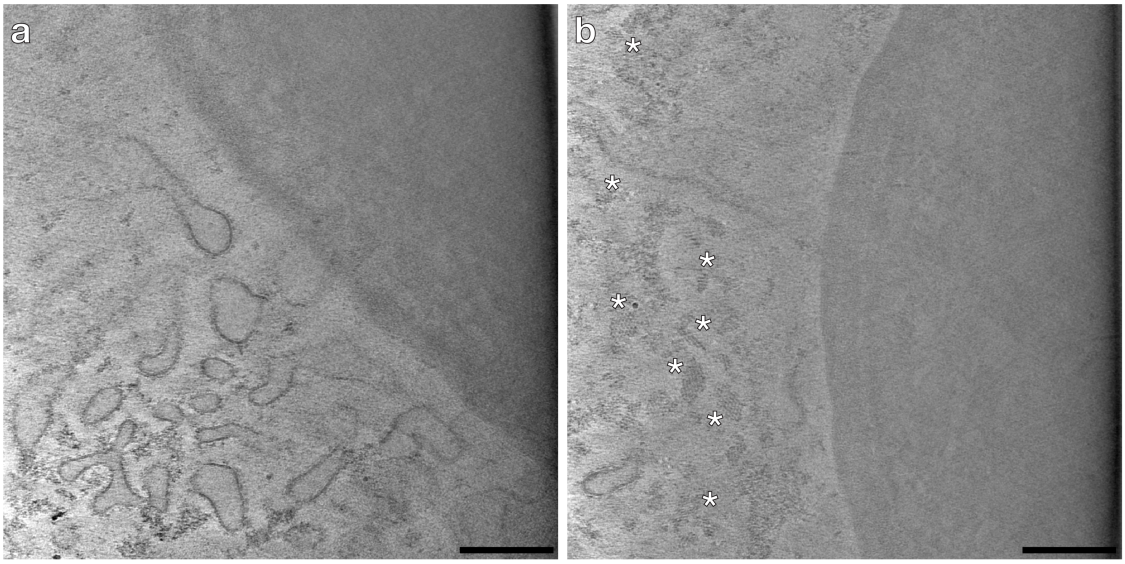


Figure 6.11 | The acrosomal shroud in acrosome-reacted sperm after progesterone stimulation. (a, b) Computational slices through defocus-contrast cryo-tomograms of the acrosomal shroud in sperm samples plunge-frozen 30 min after progesterone treatment. Note the membrane protein-decorated vesicles and crystalloid patches, which are marked with asterisks in (b). **Scale bars:** 100 nm.

of ~24 nm **(Fig. 6.13a,b)**. The overall structure appears to be two-fold rotationally symmetric, and a two-fold axis can be placed through the centerline of every column **(Fig. 6.13b, leftmost panel)**

6.2.4 An atypical fission-fusion pathway maintains cell integrity after acrosome destabilization.

One of the distinguishing features of the acrosome reaction is that the fusing membranes are not recycled – the sperm thus loses a large portion of its plasma membrane and yet remains intact. In order to determine how cell integrity is maintained throughout such a drastic membrane vesiculation process, I focused on imaging the area around the end of the acrosome. Even in capacitated cells not stimulated with ionophore or progesterone, I observed that the OAM ruptures and fuses with the overlying PM where the acrosome begins to taper **(Fig. 6.5f, Fig. 6.7b,c, Fig. 6.14)**, leaving a hairpin-shaped membrane that extends several hundred nanometers anterior to the post-acrosomal sheath **(Fig. 6.14)**. Inspection of fully acrosome-reacted cells revealed that this membrane pinches off; as a result, the new limiting membrane follows

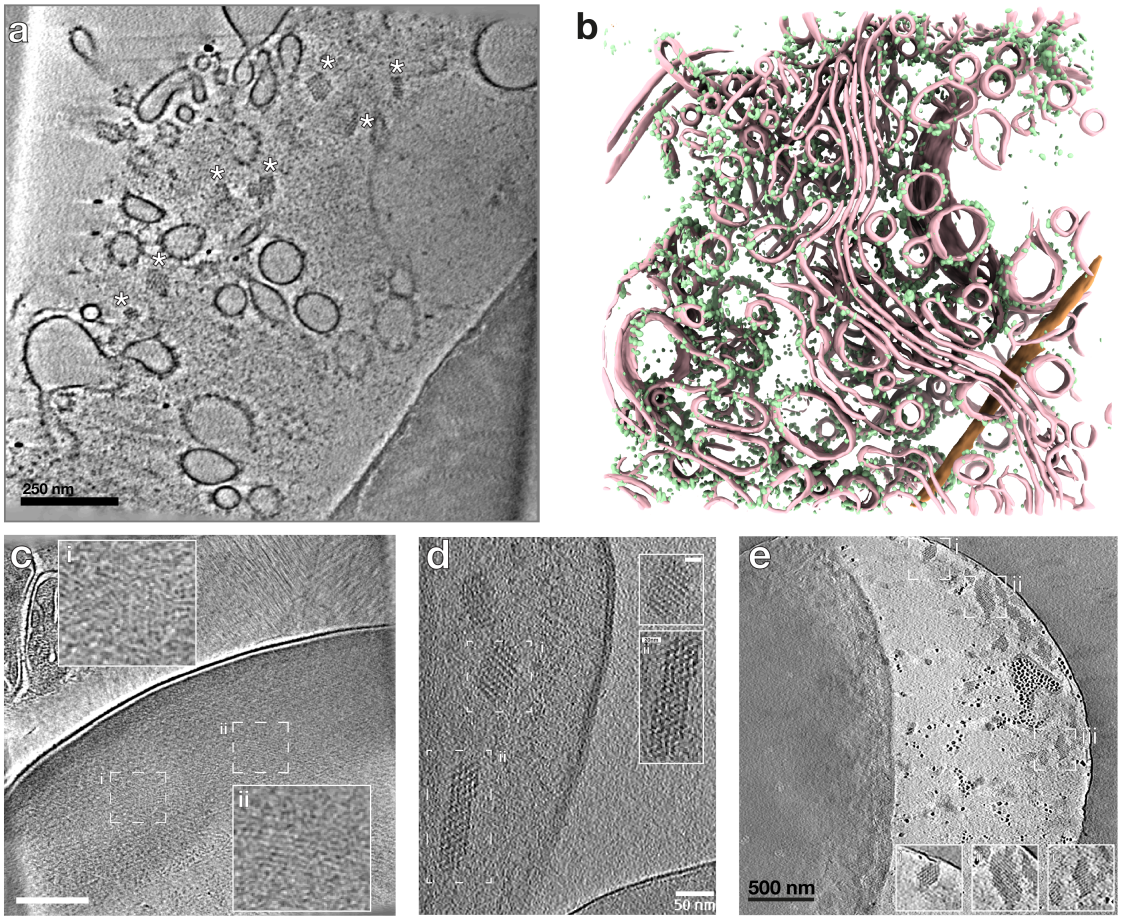


Figure 6.12 | Membrane destabilization leads to acrosome vesiculation and to the dispersal of acrosome contents. (a) VPP tomogram and **(b)** corresponding segmentation of a cell plunge-frozen 30 min after ionophore addition. Crystalloid patches are marked with asterisks in (a). **(c-e)** Computational slices through cryo-tomograms showing that crystalloids are present in the acrosome of non-capacitated **(c)** and capacitated **(d)** cells and that they persist after dispersal of the shroud **(e)**. The tomogram in (c) was collected with the VPP on a cryo-FIB milled cell, while those in (d) and (e) were collected with defocus-contrast on whole capacitated or acrosome-reacted cells, respectively. **Scale bars:** (a, c) 250 nm, (d) 50 nm, (e) 500 nm.

the shape of the post-acrosomal sheath **(Fig. 6.15, Fig. 6.16)**. This fission-fusion process joins the inner acrosomal membrane (IAM) and the PM overlying the post-acrosomal sheath, maintaining membrane continuity. The IAM is tightly laminated to the perinuclear theca, which prevents it from destabilization. In a similar manner, the post-acrosomal sheath may function to physically support the overlying plasma membrane, preventing it from vesiculating and thereby preserving cell integrity.

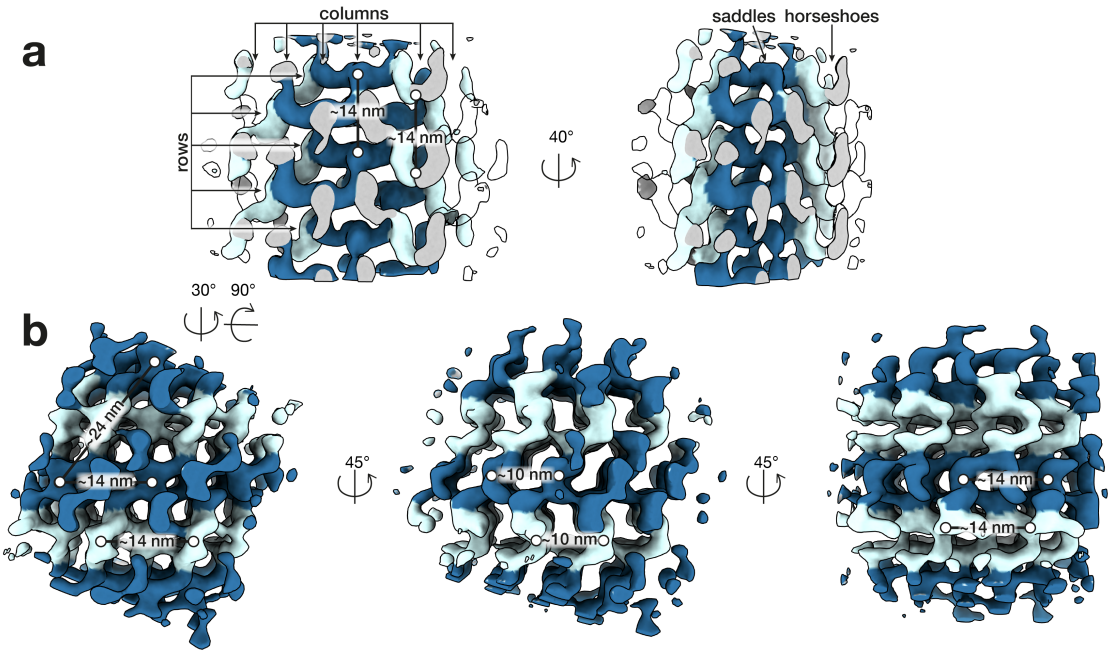


Figure 6.13 | Subtomogram averaging of crystalloid patches from acrosomes of capacitated sperm. (a) Crystalloids consist of staggered columns of saddle-shaped (dark blue) and horseshoe-shaped (light blue) densities. Every saddle-shaped density makes contacts with a horseshoe-shaped density at both ends, forming rows of alternating saddles and horseshoes. **(b)** Viewing the average at different orientations suggests that the overall structure is rotationally two-fold symmetric about an axis through the center of each column.

6.2.5 The acrosome reaction leads to topographical and molecular remodelling of the sperm surface.

In the apical region of acrosome-reacted sperm, the IAM is the new limiting membrane of the cell **(Fig. 6.12a, Fig. 6.15a)**. The PM overlying the post-acrosomal region remains intact and is now continuous with the IAM. Segmentation of high-contrast tomograms acquired with a VPP revealed that the PM forms a sheath around the post-acrosomal region **(Fig. 6.15)**. An extended non-vesiculated region is present over the equatorial region **(Fig. 6.15, Fig. 6.16)**, but we could only image its periphery due to sample thickness. Nonetheless, our tomograms revealed the presence of tubulovesicular projections in this region.

Comparing the post-acrosomal PM in acrosome-reacted sperm with the same region in non-capacitated sperm revealed major differences in protein decoration **(Fig. 6.17)**. In non-capacitated cells, the post-acrosomal PM was relatively smooth, with only a few small protein densities protruding from the membrane **(Fig. 6.17a,c)**. In acrosome-

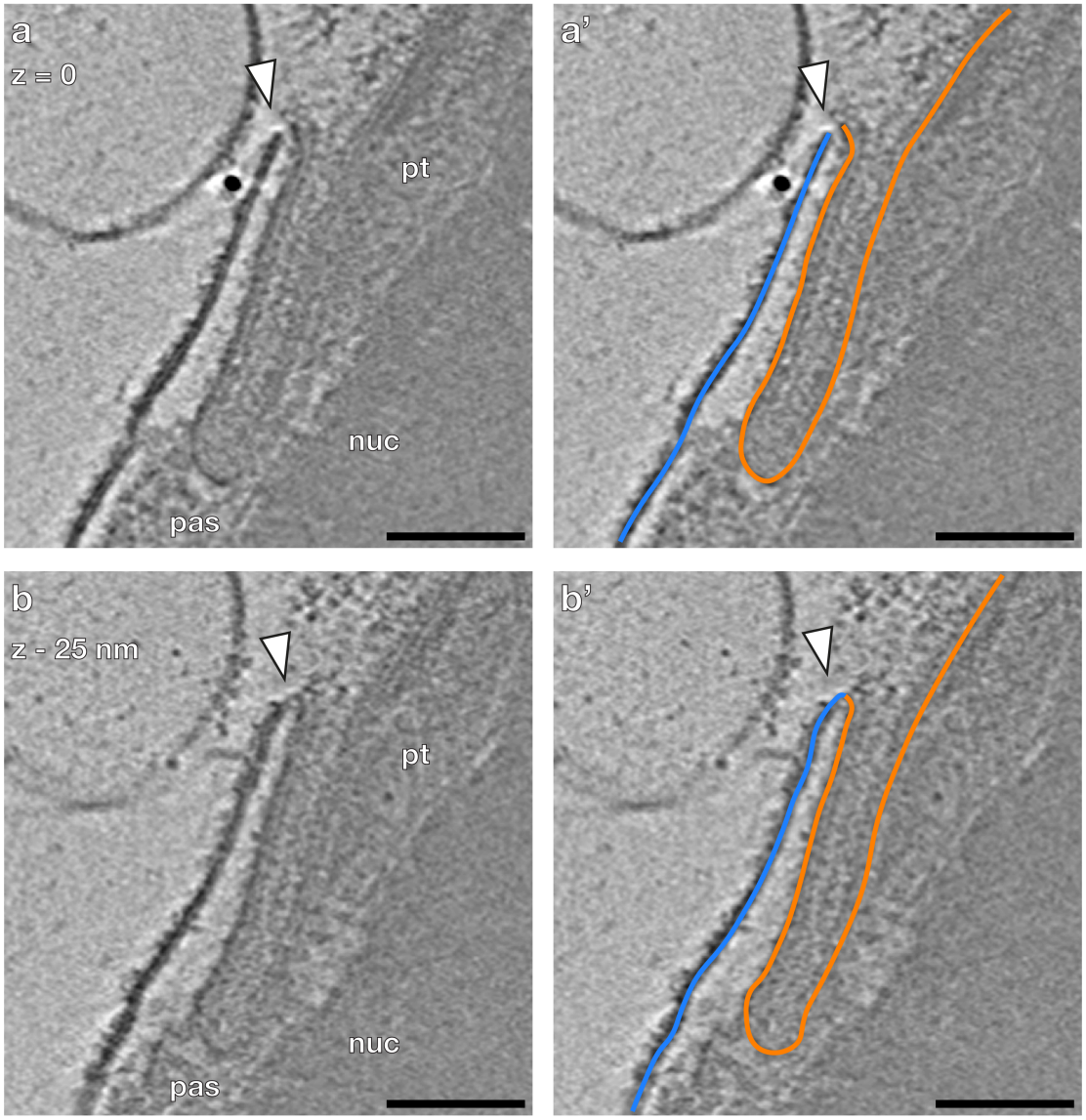


Figure 6.14 | An atypical fission-fusion pathway maintains cell integrity after acrosome destabilization. (a, b) Computational slices through VPP cryo-tomograms of capacitated sperm with corresponding annotations in **(a', b')** showing how a membrane fission-fusion event reseals the sperm at the equatorial/post-acrosomal region. **Labels:** pas - post-acrosomal sheath, pt - perinuclear theca, nuc - nucleus. **Scale bars:** 100 nm.

reacted cells, the post-acrosomal PM was packed with membrane protein densities **(Fig. 6.17b,d, Fig. 6.18)**. These densities do not appear to be ordered, which suggests that they represent a number of different proteins or protein complexes. Indeed, although until recently only the immunoglobulin superfamily member IZUMO1 was known to be necessary for sperm-egg binding, there are now a number of sperm proteins known to be essential for this event (Fujihara et al., 2020; Inoue et al., 2005;

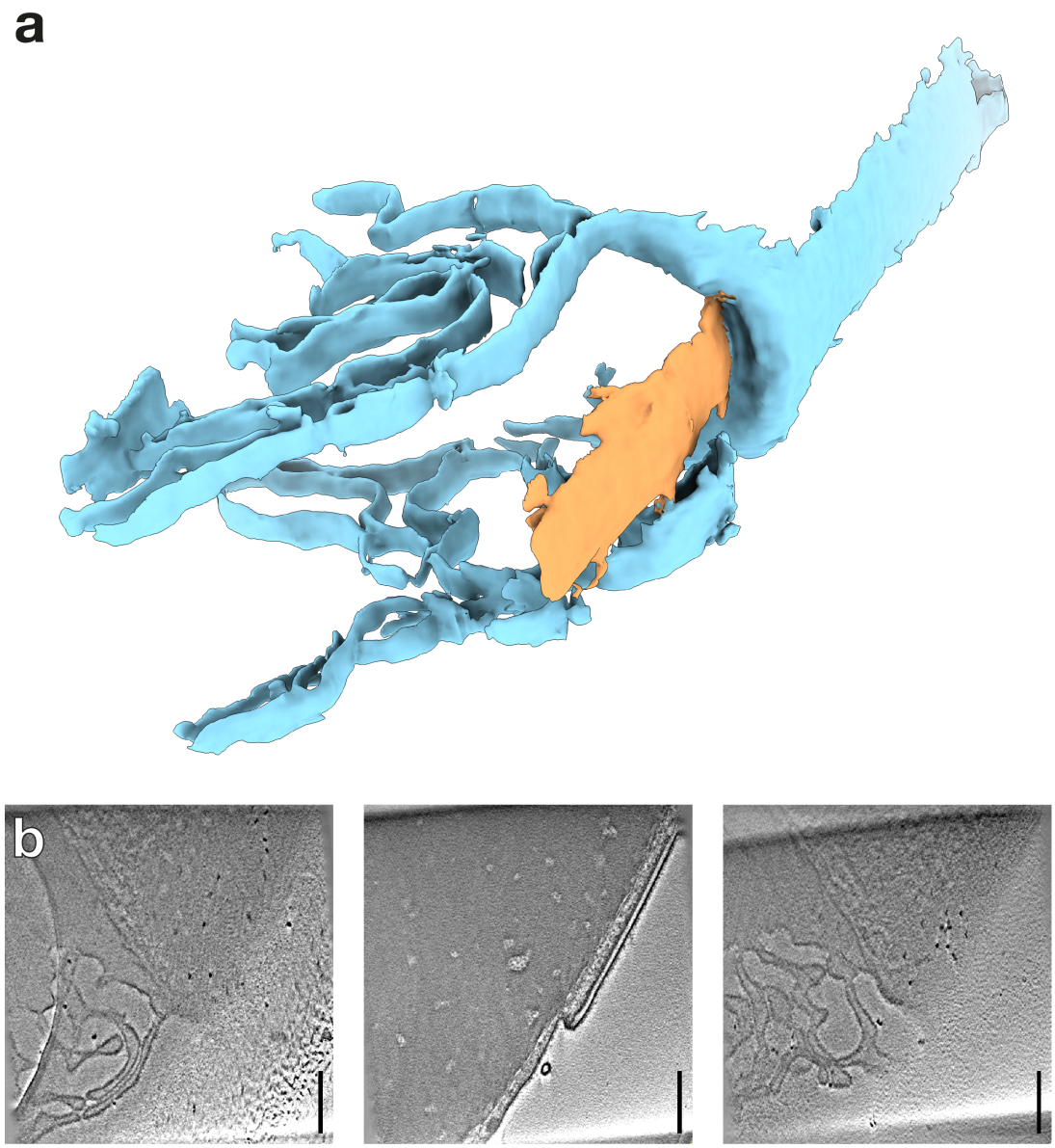


Figure 6.15 | The acrosome reaction transforms the topography of the sperm surface. **(a)** Segmentation of a VPP tomogram showing how the plasma membrane overlying the post-acrosomal region forms a continuous sheath around the remaining inner acrosomal membrane. **(b)** Computational slices through the cryo-tomogram that was segmented in (a). **Scale bars:** 250 nm.

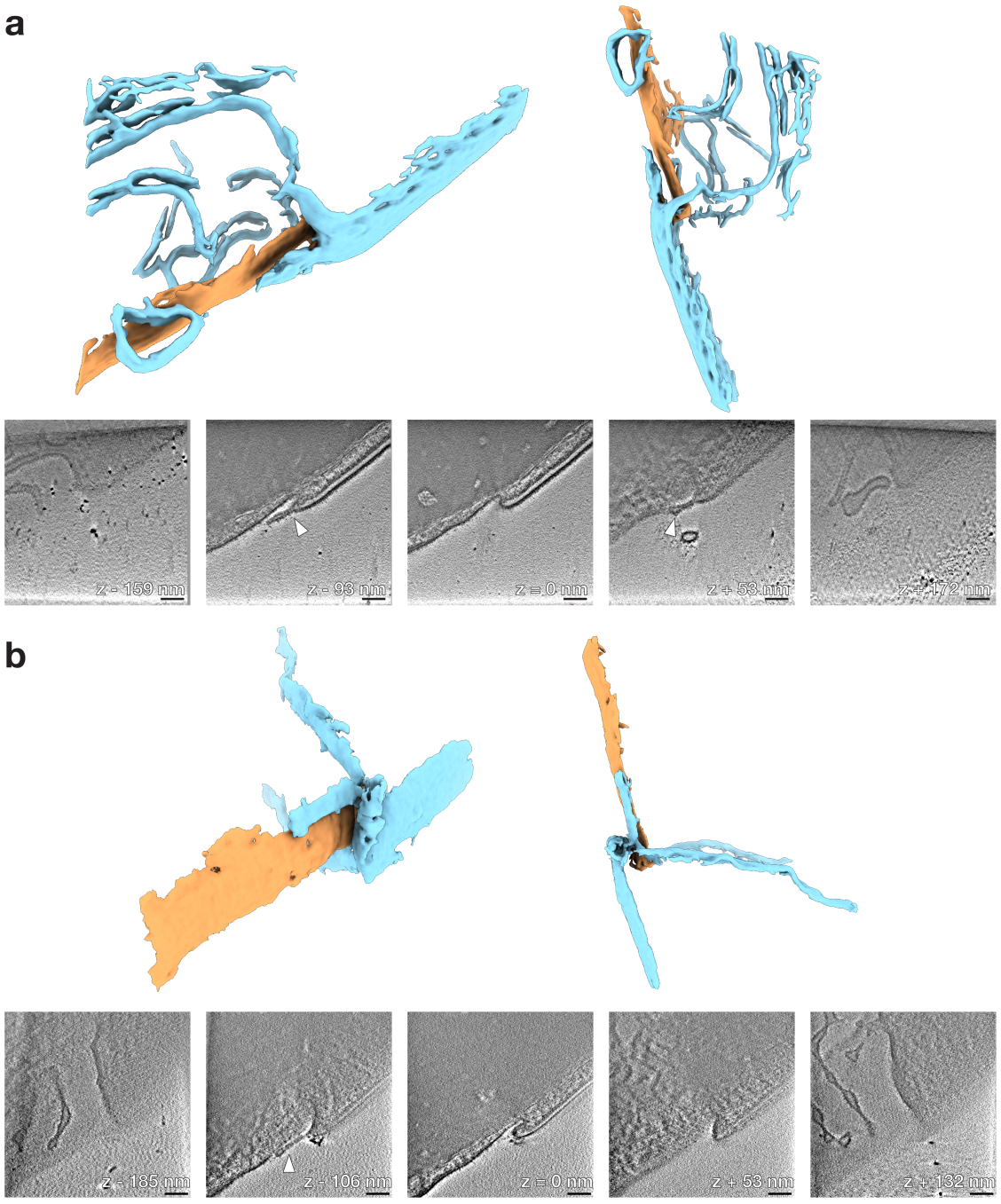


Figure 6.16 | Additional examples of the new topography of acrosome-reacted sperm. **(a, b)** Segmentation of VPP tomograms of the acrosome-reacted cells, with computational slices through the tomograms shown in lower panels. **Scale bars:** 250 nm.

Lamas-Toranzo et al., 2020; Noda et al., 2020). The fact that we do not see ordered densities does not rule out the possibility that these proteins may assemble into larger complexes when the sperm comes into contact with the egg.

Given its putative role as a physical support for the post-acrosomal PM, we sought to determine whether the post-acrosomal sheath itself changes during the acrosome reaction. The post-acrosomal sheath is characterized by a linear array of densities with an ~8 nm periodicity, which does not change after the acrosome reaction **(Fig. 6.17d-f)**. Interestingly, subtomogram averaging revealed that the distance between the post-acrosomal sheath and the overlying PM increases from ~5 nm in unreacted cells to ~13 nm in acrosome-reacted cells **(Fig. 6.17e,f)**. This may represent a "loosening" of the interactions between the PM and the post-acrosomal sheath, since continual stabilization of the PM could hinder subsequent fusion with the egg. Thus, the acrosome reaction changes both the micron-scale topography and the molecular landscape of the sperm surface.

6.2.6 An updated model of how capacitation-associated membrane destabilization restructures the sperm surface.

Based on our cryo-ET data, we propose a model of the acrosome reaction as a direct consequence of membrane destabilization that occurs gradually during capacitation **(Fig. 6.19)**. (a) The PM and OAM are closely-spaced even in non-capacitated cells. (b) An initial influx of Ca^{2+} could induce membrane docking, presumably via trans-SNARE complex formation. The acrosome subsequently swells and the acrosomal matrix decondenses, although which of these events occurs upstream of the other is unclear. It is possible that swelling is driven by decondensation of matrix material in a process analogous to polymer swelling, although it is also possible that decondensation is driven by the influx of water from small, transient fusion events involving the docked PM and OAM. I propose that the increase in acrosomal osmotic pressure and in membrane surface area, coupled with changes in membrane composition driven by cholesterol efflux and phospholipase activation (Abi Nahed et al., 2016; Asano et al., 2013), destabilize the PM and the OAM. The OAM then begins to rupture (c), buckles,

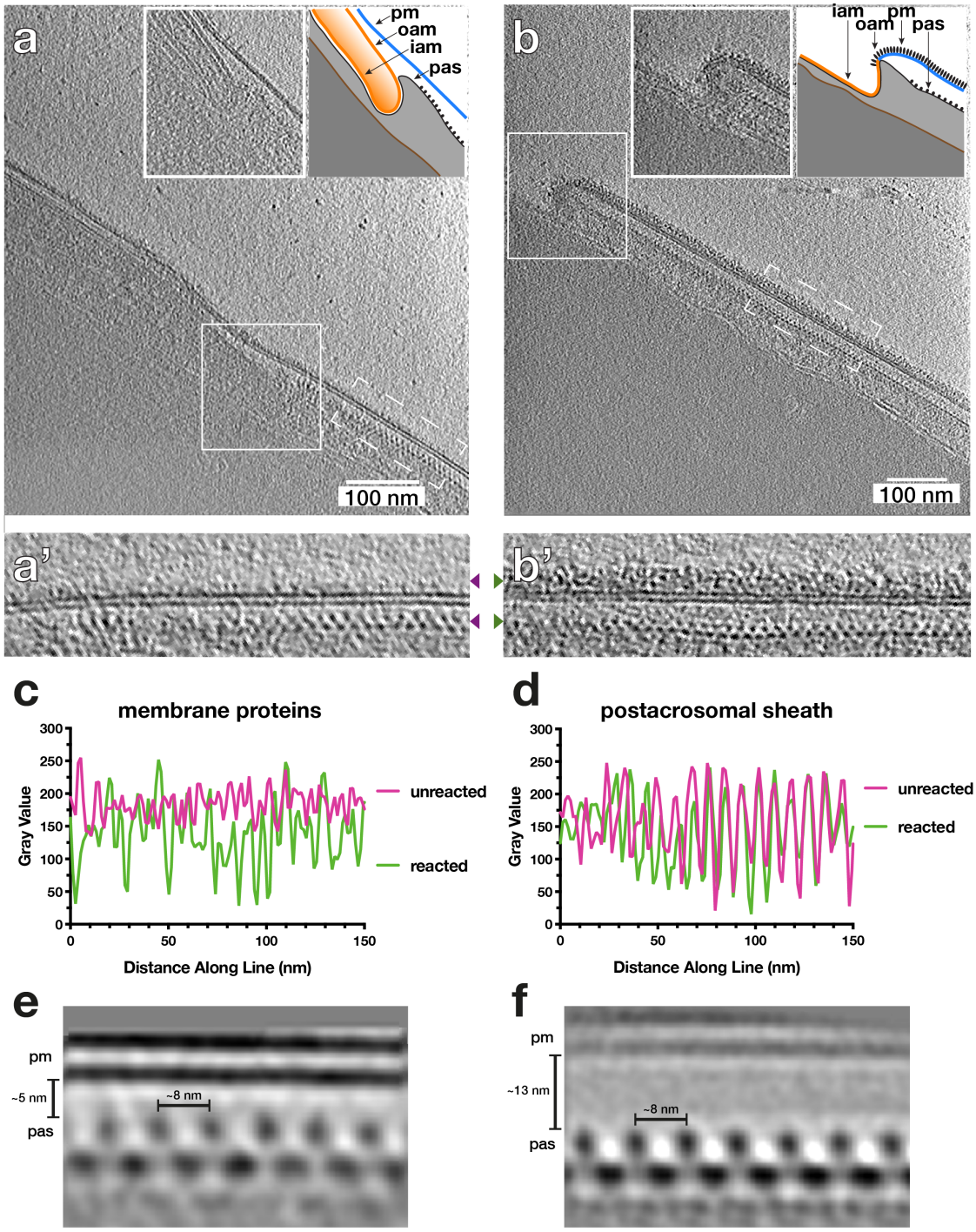


Figure 6.17 | The acrosome reaction transforms the molecular landscape of the sperm surface. **(a, b)** Slices through defocus-contrast cryo-tomograms of the equatorial/post-acrosomal region of unreacted (a) and acrosome-reacted (b) cells. Insets are digital zooms taken from the locations indicated by solid frames. **(a', b')** Digital zooms of the plasma membrane overlying the post-acrosomal sheath, taken from the approximate locations indicated by dashed frames in (a) and (b). **(c, d)** Linescans above the plasma membrane (c, top arrows in a' and b') and through the post-acrosomal sheath (d, bottom arrows in a' and b'). **(e, f)** Slices through subtomogram averages of the post-acrosomal sheath and overlying plasma membrane from unreacted (e) and acrosome-reacted (f) sperm. **Labels:** pm - plasma membrane, oam - outer acrosomal membrane, iam - inner acrosomal membrane, pas - post-acrosomal sheath. **Scale bars:** (a, b) 100 nm.

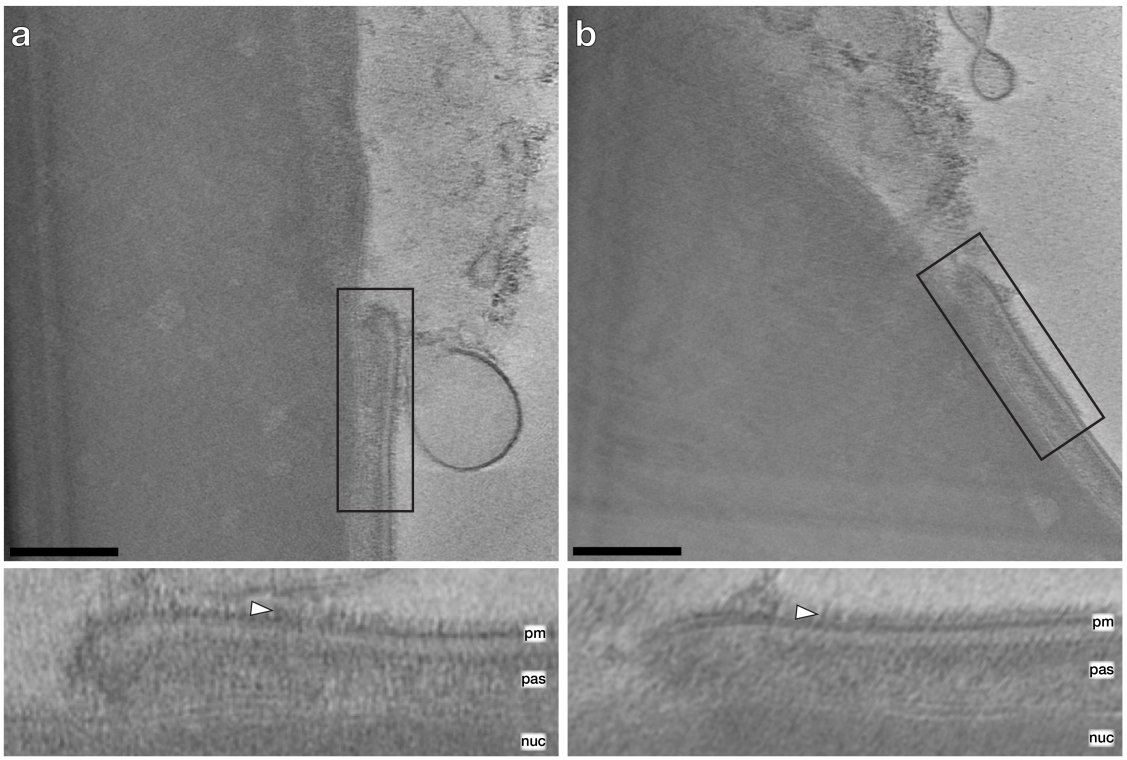


Figure 6.18 | Membrane protein decoration on the post-acrosomal plasma membrane of acrosome-reacted sperm after progesterone stimulation. (a, b) Slices through defocus-contrast cryo-tomograms of the equatorial/post-acrosomal region of acrosome-reacted sperm. Cells were incubated for 2 h in capacitating media, treated with 3 μM progesterone, and incubated for 30 min. Insets are digital zooms taken from the locations indicated by solid frames. Note how the plasma membran overlying the post-acrosomal sheath is densely packed with membrane proteins. **Labels:** pm - plasma membrane, pas - post-acrosomal sheath, nuc - nucleus. **Scale bars:** (a, b) 100 nm.

and fuses (e) with the overlying PM at the rupture sites. (d) I also observed instances of PM rupture upstream of fusion in cells with ruptured OAM, and it is possible that fusion occurs between the free edges of both membranes. (f) During the acrosome reaction, as these fission-fusion events propagate along the sperm head, the PM and the OAM are shed as mixed vesicles. (g) This leaves the IAM as the new limiting membrane of the anterior portion of the cell.

At the equatorial region (h), the acrosome tapers, but the close spacing between the PM and the OAM is maintained. (i) As in the anterior region, the acrosome swells and acrosomal contents decondense. (j) The OAM ruptures and fuses with the PM at a defined area, which coincides with the point that the acrosome begins to taper. At the equatorial/post-acrosomal region, the post-acrosomal sheath seems

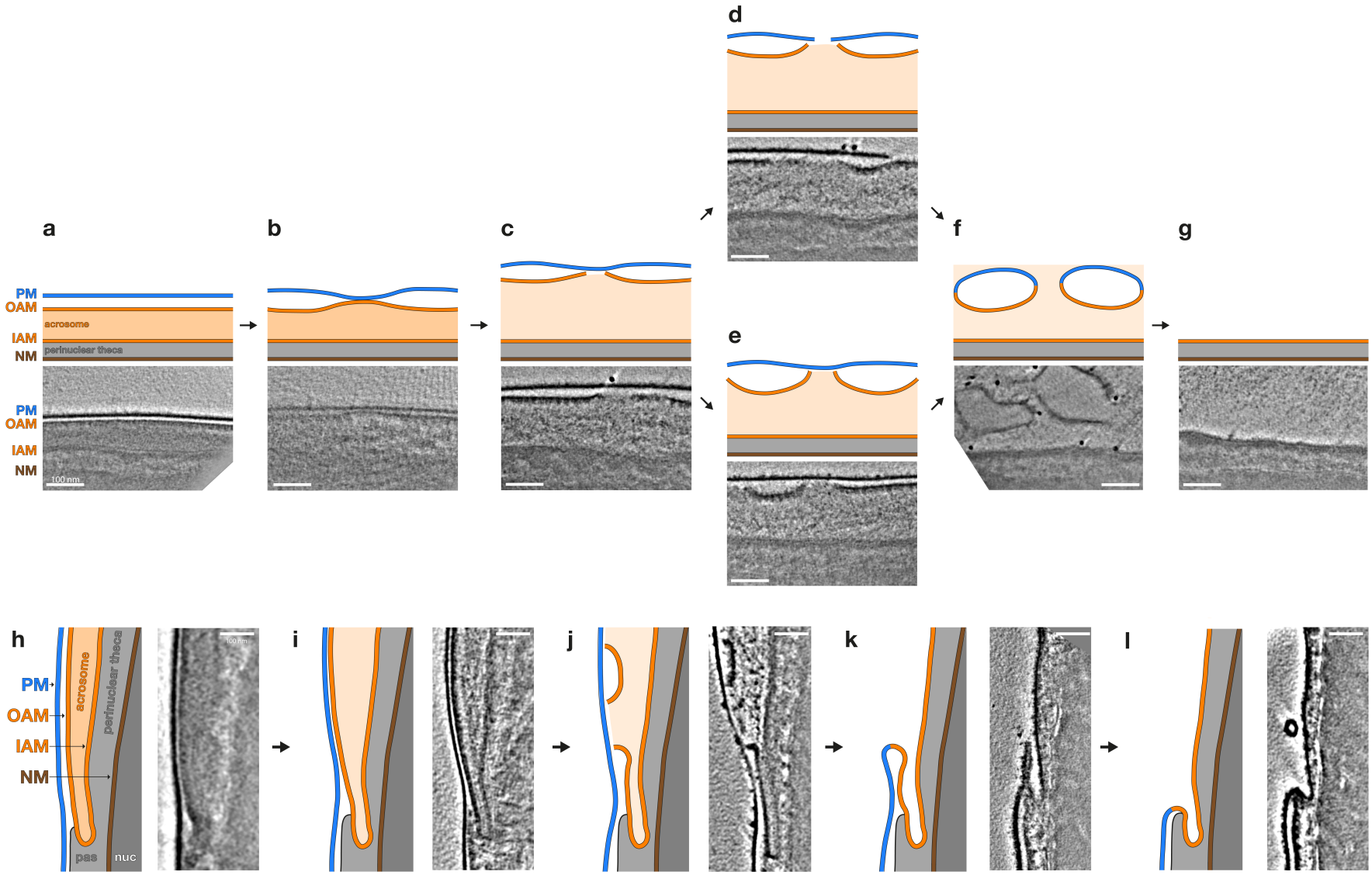


Figure 6.19 | A revised model of how capacitation-related membrane destabilization leads to the acrosome reaction. Schematic diagrams and representative tomographic slices showing how membrane remodeling events lead to vesiculation **(a-g)** and ensure cell continuity at the equatorial/post-acrosomal region **(h-l)**. See Section 6.2.6 for a full discussion of the proposed pathway. **Labels:** PM - plasma membrane, OAM - outer acrosomal membrane, IAM - inner acrosomal membrane, NM - nuclear membrane. **Scale bars:** 100 nm.

to support the overlying plasma membrane, preventing it from vesiculating. (k) The excess membrane anterior to the post-acrosomal sheath buds off. (l) As a result, the plasma membrane of the equatorial/post-acrosomal region becomes continuous with the anterior IAM, ensuring that cellular integrity is maintained during the acrosome reaction. As a result, membrane proteins relocalize onto the "new" post-acrosomal PM, presumably from the IAM.

6.3 Concluding Remarks

The model presented here provides an update to the classical view of capacitation and the acrosome reaction as two distinct events. Classically, capacitated sperm are thought to remain "acrosome-intact" until they bind to the zona pellucida, which then "triggers" the multipoint fusion that leads to acrosome vesiculation. However, there is a growing body of evidence challenging this view (Hino et al., 2016; Inoue et al., 2011; Jin et al., 2011; La Spina et al., 2016; Muro et al., 2016). The results presented in this chapter support the more nuanced view that arises from these recent observations, in which gradual changes in membrane properties lead to a topographical restructuring of the sperm surface, facilitating the relocalization of membrane proteins and creating a platform for interaction and fusion with the egg.

7 Summarizing Discussion

Contents

7.1 Major findings, implications, and future directions 136
7.1.1 Organelle-cytoskeleton interaction sites are characterized by conserved and highly ordered supramolecular assemblies. . 136
7.1.2 Asymmetry and anisotropy in mammalian sperm flagella. . . 139
7.1.3 Sperm centrioles present an opportunity to study the remodeling of an otherwise conserved structure. 140
7.1.4 Microtubule inner proteins are diverse both within the flagellum and across cell types and lineages. 141
7.1.5 The acrosome reaction is a unique membrane fission-fusion event that reflects the structural organization of the mammalian sperm head. 145
7.2 Challenges and opportunities in structural cell biology 147
7.2.1 "What's that blob?" 147
7.2.2 All samples great and small 148
7.2.3 Out of the lab and into the field 149

This thesis is fundamentally a curiosity-driven exploration of the mesoscale cellular landscape of one of the most specialized metazoan cell types – the sperm. Before discussing the overarching themes that emerge from this thesis, it is important to contextualize the work by briefly describing how it began and how it evolved over time. Nearly all of the structures resolved here were not targets that I initially set out to image. The initial goal was to define the membrane remodelling pathways involved in the acrosome reaction (Chapter 6). Given that there are many decades of excellent conventional EM work on sperm, I did not expect to be able to contribute much to the literature on sperm structure in general. However, gaining access to and building up expertise in more advanced technologies, such as the Volta phase

plate (VPP) and cryo-focused ion beam (cryo-FIB) milling, gave way to the gradual realization that sperm structure remains, in the words of Aitken and Nixon (2013), "a distant landscape glimpsed but unexplored". This led me to invest my efforts towards building a comprehensive account of the molecular architecture of sperm, from head to tail, from organelles to macromolecular complexes (Chapters 3 to 5) **(Fig. 7.1)**. This thesis is by no means a definitive compendium of sperm structure, but I hope it shows what is possible with a comparative multi-scale structural approach.

7.1 Major findings, implications, and future directions

7.1.1 Organelle-cytoskeleton interaction sites are characterized by conserved and highly ordered supramolecular assemblies.

Cryo-ET and subtomogram averaging reveal that the major organelle-cytoskeleton contact sites in sperm, namely the head-tail junction and the mitochondrial sheath, are characterized by ordered supramolecular assemblies that are conserved across mammalian species. In Chapter 3, I show that the base of the head-tail junction is a hexagonal array of proteins that bridge the nuclear envelope **(Fig. 3.5)**. Based on their size, shape, and localization, I propose that these densities represent SUN proteins, specifically the sperm-specific SUN5. In Chapter 4, I show that the axoneme-facing surfaces of mitochondria bear ladder-like arrays of boat-shaped particles anchored by a network of pores in the outer mitochondrial membrane **(Fig. 4.5)**. Based on proteomics, cross-linking mass spectrometry, and the molecular dimensions of cryo-ET maps, I propose that the pores represent VDAC2/3, while the boat-shaped particles represent glycerol kinase (GK) or GK-like proteins.

What determines the organization of these supramolecular arrays? The structures I obtained suggest that there are no direct interactions between the soluble domains of putative SUN trimers in the nuclear envelope, nor between GK-like proteins on the outer mitochondrial membrane. Assembly may be mediated by interactions among the membrane-embedded components of these complexes; for instance, the relative orientations of VDAC2/3 pores may set the spacing for GK-like proteins. This

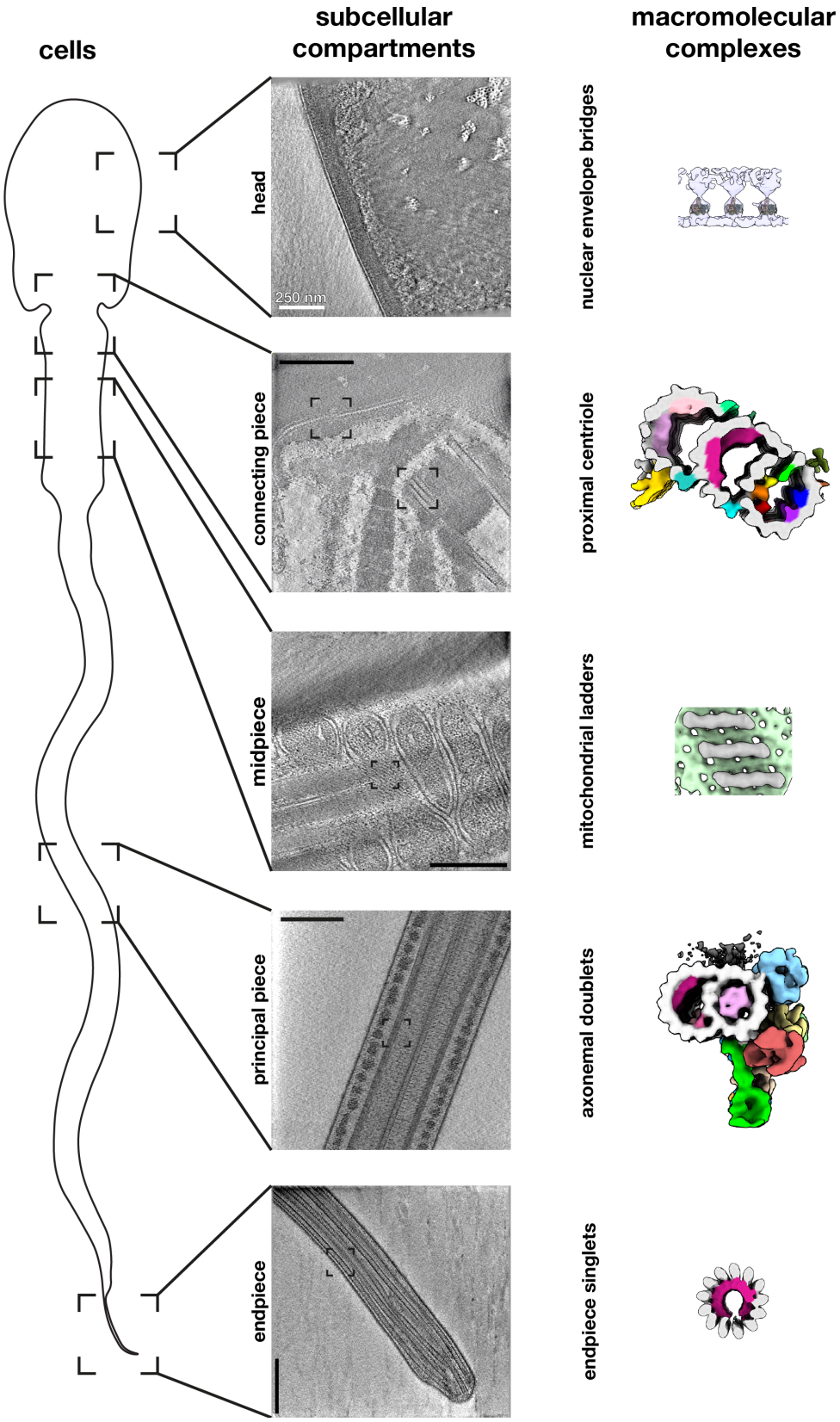


Figure 7.1 | Cryo-electron tomography of mammalian sperm across scales. A diagram summarizing the main subcellular compartments and macromolecular complexes studied in this thesis.

will need to be revisited with structures that are better resolved in the membrane region. Another intriguing possibility is that these arrays could be organized by their cytoskeletal binding partners. The periodicity of relevant motifs on cytoskeletal filaments could dictate the spacing of the membrane-associated arrays. However, the direct cytoskeletal binding partners of either complex remain shrouded in mystery.

The fact that mitochondrial ladder-like arrays and SUN protein arrays are conserved across mammalian species suggests that they play important structural roles in the cell. Indeed, improper formation of either the mitochondrial sheath or the head-tail junction results in infertility. Assembly of proteins into large, ordered assemblies likely reflects the need to maintain the integrity of these organelle-cytoskeleton contacts, stabilizing them against shear stresses during sperm motility and hyperactivation. Conceptually, this could be similar to a focal adhesion in which avidity effects from integrin clustering promote interactions with integrin ligands in the extracellular matrix. However, whereas focal adhesions are constantly assembled and disassembled, it seems likely that the mitochondrial ladders and SUN protein arrays are less dynamic.

To my knowledge, this is the first time such assemblies have been visualized at any organelle-cytoskeleton interface in any cell type. Whether similar ordered arrays are present in other cell types or at other organelle-cytoskeleton contacts remains to be seen. An interesting precedent is found in the similarly highly-polarized *Plasmodium*, the causative agent of malaria, where cryo-ET resolved periodic linker densities that tether organelles to the cytoskeleton, keeping organelles fixed with respect to the cell during the high-velocity stop-and-go gliding motion characteristic of the parasite (Kudryashev et al., 2010). In striated muscle, proper mitochondrial positioning is critical for muscle function and depends on direct associations between mitochondria and intermediate filaments (Konieczny et al., 2008; Milner et al., 2000). Similarly, in skin cells, mitochondrial organization depends on keratin (Steen et al., 2020). The structural bases for these associations is unknown, but cryo-ET may prove useful in these contexts as well.

7.1.2 Asymmetry and anisotropy in mammalian sperm flagella.

Mammalian sperm flagella are characterized by large accessory structures, namely the mitochondrial sheath in the midpiece, the fibrous sheath in the principal piece, and the outer dense fibers (ODFs) that extend throughout most of the tail. The ODFs are continuous with the connecting piece, which anchors them at the base of the flagellum. In Chapter 5, I explore the architecture of the connecting piece-ODF system and show that, in addition to their passive role in increasing the bending stiffness of the flagellum, these accessory structures likely also modulate the flagellar beat by imposing large asymmetries and anisotropies on the sperm tail.

Of particular relevance to wave generation, I found prominent asymmetry in the connecting piece at the base of the flagellum **(Fig. 5.12)**. This large-scale asymmetry could bias basal sliding to one side relative to the head, consequently polarizing inter-doublet sliding moments transmitted to the rest of the axoneme. Indeed, in order to swim forward, mouse sperm balance out intrinsic asymmetry of the waveform with episodic side-to-side switching of asymmetric bends (Babcock et al., 2014). Counter-bend experiments on rat sperm flagella showed that shear developed in the distal flagellum is not identical when the flagellum is bent in two opposing bending directions relative to the head (Lindemann et al., 2005). Cryo-ET data comparing bovine sperm with straight versus curved necks show unequivocally that basal sliding *can* occur, and that basal sliding is asymmetric relative to the head **(Fig. 5.14)**. I only ever observed sperm necks curved away from the side of the proximal centriole (PC), and thus only the segmented columns on the side of the PC slid towards the head. This reflects the intrinsic asymmetry of the neck and demonstrates how structure can influence motility.

Subtomogram averaging resolved direct coupling between ODFs and axonemal doublets in the principal piece **(Fig. 5.10)**, which provides a structural mechanism by which asymmetric basal sliding can be transmitted to more distal parts of the tail, thus polarizing the overall waveform. Indeed, polarized waveforms have been reported for human sperm and bull sperm (Friedrich et al., 2010; Gadêlha et al., 2020; Saggiorato et al., 2017). In contrast, the ODFs are not directly coupled to doublets in the midpiece **(Fig. 5.10)**. This configuration would allow the ODFs to slide relative to the axoneme

while being restrained by the mitochondrial sheath, lending flexibility to the midpiece. This is proposed to support formation of the extreme bends in the midpiece seen during hyperactivation (Lesich et al., 2014; Lindemann and Lesich, 2016).

The current work only scratches the surface of what is possible with cellular cryo-ET. Future work could relate flagellar curvature to structural changes in the accessory structures, in the vein of how Lin and Nicastro (2018) directly correlated dynein activation states to their positions on the axoneme relative to the bend direction. Preliminary data suggest that the fibrous sheath compresses on the inside of the bend and that the axoneme can move within the sheath in the plane of the circumferential ribs **(Fig. 5.9)**. Cryo-ET could also help shed light on the structural changes that occur during hyperactivation, which changes the flagellar waveform dramatically.

7.1.3 Sperm centrioles present an opportunity to study the remodeling of an otherwise conserved structure.

In Chapter 5, I describe the atypical structure of the distal centriole (DC) at the base of the mammalian sperm flagellum **(Fig. 5.3)**. I show that, in non-rodent mammals, the DC is comprised of doublet microtubules splayed out asymmetrically around two singlet microtubules. In mice, the doublet microtubules are missing but the central singlets remain. In contrast, conventional TEM suggests that the DC remains a ninefold-symmetric barrel of triplet microtubules in marine invertebrates, fish, reptiles, amphibians, and birds (Avidor-Reiss, 2018).

How might a typical centriole be remodeled into an atypical DC? Recently, cryo-ET revealed the presence of a conserved helical scaffold in the inner lumen of centrioles (Le Guennec et al., 2020). Loss of POC16/WDR90, a component of the inner scaffold, results in centrioles that are not circular but elliptical in cross-section (Steib et al., 2020). POC16/WDR90 appears to recruit other components of the inner scaffold because loss of POC16/WDR90 alters the localization of other inner scaffold proteins such as POC5, POC1B, and FAM161A (Steib et al., 2020). Indeed, POC5, POC1B, and FAM161A are associated with the sperm DC, but instead of forming a cylindrical structure they form two asymmetric rods (Fishman et al., 2018). Reorganization of

these proteins may thus contribute to the loss of the inner scaffold and thus to the asymmetric splayed-out architecture of the DC microtubules **(Fig. 5.3)**. Consistent with this model, POC16/WDR90 is absent from our pig sperm proteome.

Why would the DC need to be remodeled, and why so dramatically, in mammalian sperm? One possibility is that DC remodeling represents the loss of its function as a basal anchor, which is taken over by the connecting piece. There is no structure resembling the connecting piece in sperm of marine invertebrates or fish (Wu et al., 2020). In these sperm, only the DC can fulfill the role of the basal anchor. Electron-dense material surrounds the centrioles in the sperm of reptile, amphibian, and birds, but there is no defined connecting piece in these lineages (Wu et al., 2020). In reptile sperm, the electron-dense material is continuous with accessory fibers associated with the axoneme (Healy and Jamieson, 1994; Hess et al., 1991; Jamieson et al., 1997), although the extent to which these fibers extend along the tail is unclear. The connecting piece is most elaborate in mammalian sperm, where the outer dense fibers are also the most pronounced. Could remodeling of the DC reflect loss of selection pressure for it to act as a basal anchor while maintaining its role in organizing the first zygotic division?

Why would the role of the basal anchor need to shift from the DC to the connecting piece? This could be related to capacitation and the structural changes needed to support hyperactivated motility in mammalian sperm. Higher torques are required to generate the high-amplitude beating of hyperactivated sperm, leading to greater shear stress at the base and necessitating the elaboration of the connecting piece into a large elastic scaffold. Broadening the scope of comparative cryo-ET studies to include sperm from different lineages and integrating structural models with mathematical analysis of flagellar waveforms could help test these relationships.

7.1.4 Microtubule inner proteins are diverse both within the flagellum and across cell types and lineages.

The cryo-ET data presented in this thesis reveal that the structural elaborations of mammalian sperm flagella extend across scales (Chapter 5), from large accessory

structures that increase the overall diameter and rigidity of the entire flagellum to protofilament-bridging microtubule inner proteins (MIPs) that likely reinforce the microtubules themselves. Because interactions between protofilaments are much weaker than interactions between tubulin monomers along a protofilament (Nogales et al., 1999; VanBuren et al., 2002), microtubules cannot be modelled as simple cylinders. Protofilaments can slide relative to one another, conferring shearability onto the microtubule. Indeed, protofilament shearing is thought to contribute to microtubule instability during periods of catastrophe within the cell (Hunyadi et al., 2005). Protofilament-bridging MIPs would likely decrease inter-protofilament shearing, thus increasing microtubule bending stiffness. It thus seems more than coincidental that such MIPs are present in mammalian sperm, which swim through viscous media, but not in sea urchin or zebrafish sperm, which swim through watery environments.

The head-to-tail approach applied here also revealed diversity among MIPs within the sperm flagellum **(Fig. 7.2)**, hinting at functions beyond stabilizing microtubules. MIP diversity manifests in the central pair apparatus, where a large discontinuous helical MIP is present in the C1 microtubule but not the C2 microtubule. In addition, while discontinuous helical MIPs are present in endpiece singlets, they are absent from A-tubules of either the axonemal doublets or the proximal centriole. Instead, similar MIPs are associated with the B-tubules in the latter two structures. Because axonemal doublets can split into two complete singlets, the large A-MIP in the doublet must at some point be replaced by the helical MIP in the singlet. The appearance of the large A-MIP coincides with the appearance of radial spokes and dynein arms at the distal centriole-to-axoneme transition **(Fig. 5.3)**, and its disappearance likewise coincides with the doublet-to-singlet transition **(Fig. 5.8)**.

How would structures in the microtubule lumen affect structures on the external surface? In *Drosophila*, substitution of a single conserved glycine residue in β-tubulin prevents outer dynein arms from properly associating with sperm axonemes (Raff et al., 2008). Remarkably, this residue projects into the microtubule lumen, which suggests that it may regulate binding of MIPs that then permit ODA docking. Recent single-particle cryo-EM structures of decorated doublet microtubules revealed that MIPs form

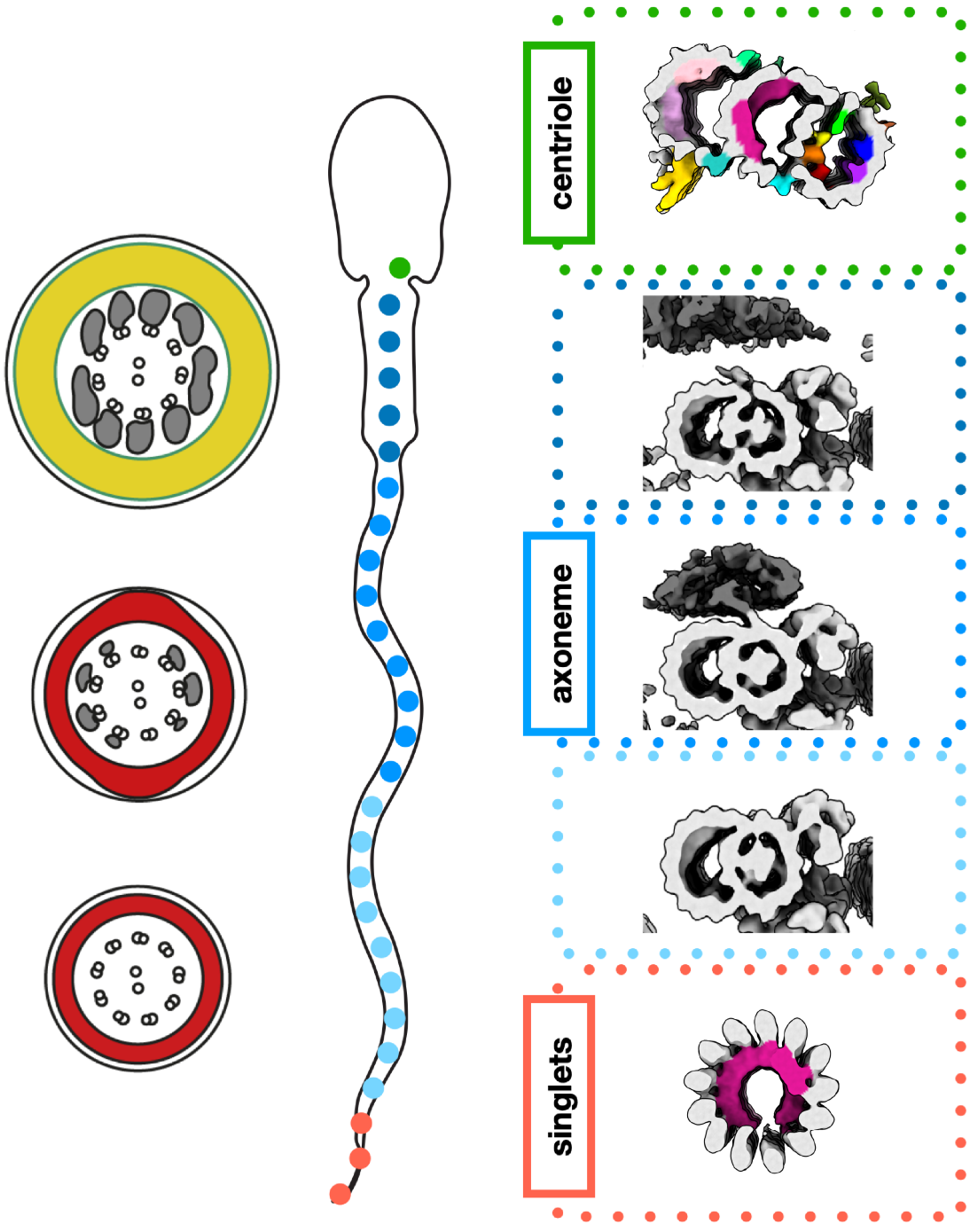


Figure 7.2 | The diversity of microtubule-based assemblies within a single motile cilium. Tracing microtubule-based assemblies along a single motile cilium reveals structural diversity both in terms of microtubule inner protein signatures and in terms of association with accessory elements.

an extensive network that weaves through the tubulin lattice (Ichikawa and Bui, 2018; Ichikawa et al., 2017; Ma et al., 2019) and even alters the spacing between tubulin dimers (Ichikawa et al., 2019; Ma et al., 2019). Thus, MIP binding or unbinding may also functionalize the microtubule to support association or dissociation of accessory structures on the external surface.

How is microtubule identity regulated? The answer might lie at least partially in the building blocks of microtubules themselves. Variations in microtubule properties can result from incorporating different tubulin isoforms or from tubulins with different post-translational modifications – the "tubulin code" (Janke and Magiera, 2020). Eukaryotes have several different tubulin isoforms that differ primarily in the C-terminal region; humans have nine isoforms of both α- and β-tubulin (Roll-Mecak, 2020). In *Drosophila*, basal bodies and axonemes use the same α-tubulin isoform but different β-tubulin isoforms (Dutcher, 2001). The β1 isoform is involved in assembly of basal bodies and nonmotile cilia, whereas the testis-specific β2 isoform is used to build sperm axonemes (Kemphues et al., 1982). Postmitotic male germ cells expressing only β1 cannot assemble the central pair, but replacing the C-terminus of β1 with that from β2 allows the chimera to support assembly of a 9 + 2 axoneme (Nielsen et al., 2001). There is also proteomic evidence from the tunicate *Ciona intestinalis* that ciliary axonemes in different cell types preferentially use different tubulin isoforms and recruit different dynein arm complexes (Konno et al., 2015).

Understanding the interplay of the tubulin code, MIPs, and accessory structures will likely require a synergistic approach. Mass spectrometry-based approaches to probe differential enrichment of specific tubulin isoforms or post-translational modifications could be integrated with cryo-ET-based profiling of cell type-specific MIP and accessory protein repertoires. All of these experiments would benefit from a comparative approach, both within a cilium and across cilia from different cell types and species, and would help shed light on how the ancient and conserved microtubule core is ornamented to support motility in diverse fluid environments.

7.1.5 The acrosome reaction is a unique membrane fission-fusion event that reflects the structural organization of the mammalian sperm head.

In Chapter 6, I revisit the morphological changes that occur during capacitation and the acrosome reaction, which are prerequisite events for sperm to become fusion-competent **(Fig. 6.19)**. Cryo-ET suggests that capacitation is primarily a membrane destabilization event, which leads to a fission-fusion pathway in which the apical regions of the plasma membrane (PM) and the outer acrosomal membrane (OAM) are shed as vesicles. The cryo-ET data also reveal how this fission-fusion process maintains cell integrity and leads to both topographical and molecular remodeling of the sperm surface.

The architecture of the sperm head imposes certain constraints that may influence how the acrosome reaction proceeds. In neuronal exocytosis, synaptic vesicles are typically small and highly curved relative to the PM. In contrast, the acrosome is a large vesicle that covers the anterior two-thirds of the sperm head, and hence it is locally parallel to the overlying PM. Another important feature of the acrosome is that its inner membrane is stably laminated to the underlying perinuclear theca. Only the OAM is available for fusion, and the fusing membranes end up being shed as vesicles, as opposed to being recycled. However, a consequence of the IAM being so stable is that it is likely not fusogenic, which explains why mammalian sperm fuse with eggs exclusively via the equatorial/post-acrosomal region of the PM.

The membrane remodeling intermediates observed in this study do not appear to fit the canonical fusion-by-hemifusion pathway; instead, the presence of membrane edges is reminiscent of the rupture-insertion pathway (Chlanda et al., 2016; Haldar et al., 2019). Whether fusion proceeds via hemifusion or via rupture-insertion depends on membrane spontaneous curvature and hence on lipid composition, strongly favoring cholesterol-poor bilayers (Chlanda et al., 2016; Haldar et al., 2019). This may be particularly relevant given that one of the molecular signatures of capacitation is cholesterol efflux. Although the rupture-insertion pathway has so far only been observed for viral fusion, and although there are no putative viral fusogen-like

proteins in the sperm acrosome, recent structural studies have shown that the SNARE protein VAMP2/synaptobrevin contains a juxtamembrane peptide whose membrane-destabilizing properties are necessary for fusion (Rathore et al., 2019). Such a peptide may contribute both to acrosomal membrane rupture and to stabilizing the free edges of ruptured membranes.

As a result of acrosome destabilization, the plasma membrane overlying the equatorial/post-acrosomal regions becomes highly decorated with membrane protein densities. These densities appear heterogeneous, suggesting that they represent a number of different molecular species. Consistent with this, there is now a growing list of sperm proteins essential for sperm-egg fusion in mammals, including IZUMO1, SPACA6, FIMP, SOF1, and TMEM95 (Fujihara et al., 2020; Inoue et al., 2005; Lamas-Toranzo et al., 2020; Noda et al., 2020). It would be interesting to map the spatial organization of these proteins on the surface of acrosome-reacted sperm by combining cryo-ET with localization tags such as aptamer-based DNA origami.

Another change that occurs during the acrosome reaction is an increase in spacing between the plasma membrane and the post-acrosomal sheath. Although our data suggest that the post-acrosomal sheath physically stabilizes the overlying plasma membrane during the acrosome reaction, how this actually happens is unclear. Furthermore, the very nature of the post-acrosomal sheath is enigmatic; fortunately, its highly ordered structure suggests that it is a suitable target for subtomogram averaging in future work.

Imaging sperm-egg fusion directly by cryo-ET will be extremely challenging, both due to the sheer size of the egg and to the difficulty of capturing a sperm-egg fusion event in the small volume of a cryo-lamella. An intriguing approach to begin to address the molecular architecture of the fertilization synapse would be to generate model membrane systems mimicking the egg. This could be done by reconstituting egg-specific factors necessary for fusion, such as Juno and the tetraspanin CD9, on artificial membranes and subsequently imaging how these membranes interact with acrosome-reacted sperm. Such a bottom-up approach would also permit enquiries into the effects of lipid composition and membrane curvature on sperm-egg interaction.

7.2 Challenges and opportunities in structural cell biology

7.2.1 "What's that blob?"

Because contrast in cryo-EM/ET comes directly from biological material, EM data captures everything, not just the signal from a protein of interest. Thus, it is often difficult to identify individual densities in information-rich cellular tomograms. One solution to the localisation problem is to integrate the molecular specificity of fluorescence microscopy into the EM pipeline. This technique is called correlative light and electron microscopy (CLEM) and has in fact been applied quite successfully for conventional TEM-based methods (Kremer et al., 2015). However, cryo-CLEM is much more difficult. The technical challenges involved in optimising the optical set-up while minimising chances for ice contamination and sample devitrification cannot be overstated. Several promising approaches now exist, including light microscopes integrated within the FIB/SEM chamber (Gorelick et al., 2019) and algorithms that enable super-resolution CLEM with low laser intensities (Moser et al., 2019). Cryo-FIB/SEM based "mill-and-view" strategies can also be integrated with cryo-fluorescence microscopy to define sites of interest for subsequent cryo-FIB milling and high-resolution cryo-ET (Wu and Lander, 2020).

Because CLEM methods often involve genetic tags and thus require the system to be genetically manipulable, they will always be challenging to apply to gamete biology. Although mRNA microinjection is a viable alternative for oocytes, sperm pose a more difficult challenge as they are transcriptionally and translationally silent. Surface proteins can be targeted through antibody- or nanobody-based labelling, or through aptamer-based DNA origami strategies. However, most applications will likely involve the generation of transgenic animal lines, and thus will benefit greatly from efforts to extend the range of species for which genetic tools are available (Hirose et al., 2020).

Unfortunately, fluorescent labelling will simply not be practical for many samples, either because genetic manipulation is unfeasible or because labelling may disrupt the localization or function of the protein of interest. In such cases, signal from

the target itself must be used directly for [putative] identification (Böhning and Bharat, 2020). This concept is already exploited in template matching, a strategy to localize a target within a cellular tomogram by searching for densities that match the shape and size of a given template structure (such as a lowpass-filtered crystal structure or cryo-EM map) (Albert et al., 2020; Asano et al., 2015; Frazier et al., 2017; Fukuda et al., 2017). Some protein complexes, such as ATP synthase and the nuclear pore complex, can also be recognised directly by virtue of their distinct shapes and by the fact that they occupy defined subcellular locations (Mahamid et al., 2016; Mühleip et al., 2017). Another intriguing possibility to help identify unknown densities is to interface cellular tomography with bottom-up structural proteomics. In one approach, protein complexes are fractionated and enriched directly from cell lysates, then analyzed in parallel by mass spectrometry and single particle cryo-EM (Ho et al., 2020). Cryo-EM and mass spectrometry results are then integrated into a program called cryoID, which essentially sequences proteins by structure in maps with resolutions higher than about 4Å (Ho et al., 2020).

7.2.2 All samples great and small

Although cryo-FIB milling makes thicker cells accessible to cryo-ET, it is still limited to samples than can be reliably vitrified by plunge-freezing (that is, a few microns thick). This precludes the analysis of larger cells, like the oocyte, and tissues, like the testes. Several groups are actively developing methods to address these limitations. One promising strategy involves first producing ~20-μm thick slabs from high-pressure-frozen samples either with a cryo-ultramicrotome or a cryo-FIB/SEM, followed by finer milling with a cryo-FIB/SEM to 150-300 nm (Schaffer et al., 2019; Zhang et al., 2019). Currently, however, these methods are technically challenging and low-throughput. Furthermore, even when milling and transfer steps are successful, each 150-nm-thick lamella represents a volume of only ~0.24 μm^3 (Rast et al., 2019), which is only ~0.00005% of the volume of a 100-μm oocyte. As such, there will be biological questions for which cryo-FIB-ET simply will not be the method of choice.

A family of EM methods known as volume electron microscopy would be applicable in cases where entire cells or tissues need to be imaged. Volume EM encompasses methods such as serial block-face electron microscopy (SBEM), focused ion beam scanning electron microscopy (FIB/SEM), and automated tape-collecting ultramicrotome scanning electron microscopy (ATUM-SEM) (Titze and Genoud, 2016). In SBEM, a microtome is mounted inside the microscope chamber and a diamond knife is used to shave a thin layer off the top of the sample, which is then imaged by SEM. In FIB/SEM, a gallium beam is used instead of a diamond knife, allowing for finer milling on the order of 2-5 nm. In ATUM-SEM, the entire sample is first sectioned outside the microscope with a diamond knife, and the sections are automatically collected on tape, which can then be loaded into an SEM. These volume EM methods have been applied to muscle biology (Glancy et al., 2015; Vincent et al., 2019), large-scale connectomics of the brain (Scheffer et al., 2020; Xu et al., 2017, 2019), and recently to oocyte biology as well (Baena and Terasaki, 2019; So et al., 2019) .

Although most applications of volume EM still use conventional EM sample preparation, these methods have also recently started to interface with cryo-EM. FIB/SEM in particular can be used to image high pressure-frozen samples at cryo-temperatures (Schertel et al., 2013). Among other applications, cryo-FIB/SEM has been used for large-scale comparative studies of biomineralising protists (Hörning et al., 2020), and for whole-cell ultrastructural studies of mitochondrial morphology directly on patient samples (Zhu et al., 2020).

7.2.3 Out of the lab and into the field

One factor that limits the more general applicability of cellular cryo-ET is the need for specialized sample preparation equipment. This requirement makes it difficult to use cryo-ET to image labile samples that cannot easily be transported to a specialized lab. This includes samples that need to be collected in the field, such as unculturable microorganisms from extreme environments or sperm from non-domestic animals. Fortunately, a number of labs are developing solutions to this problem, centered around modifying the plunge-freezing device to make it compact and portable (Comolli et al.,

2012; Depelteau et al., 2020). Modified plunge-freezing devices have enabled cryo-EM of uncultivable archaea from extreme environments, such as acidic runoff from mines (Baker et al., 2010). Plunge-freezing in the field has also been integrated with metagenomics and metatranscriptomics to profile microbial communities in groundwater (He et al., 2020; Luef et al., 2015). In terms of reproductive biology, portable plunge-freezing devices could in principle be used to prepare cryo-EM-ready sperm samples directly from wildlife, which could help conservation programs assess and monitor fertility in natural populations. In a similar vein, one could also envision using portable plunge-freezers to complement surveys of microbial diversity in the oceans (Sunagawa et al., 2020).

The effort to make cellular cryo-ET more accommodating of environmental samples is a pursuit that is of paramount importance in a changing world. As pressure grows for researchers to reach higher and higher resolution in cryo-EM/ET, we must not lose sight of the fact that there is immense value in imaging "messy" samples as well, even though they may not be the best candidates for obtaining high-resolution structures. As cryo-FIB milling, data acquisition, and image processing all become more rapid and robust, cellular cryo-ET has the potential to become a tool for genuine hypothesis-enabling research.

References

Abi Nahed, R., G. Martinez, J. Escoffier, S. Yassine, T. Karaouzène, J.-P. Hograindleur, J. Turk, G. Kokotos, P. F. Ray, S. Bottari, G. Lambeau, S. Hennebicq, and C. Arnoult (2016). Progesterone-induced Acrosome Exocytosis Requires Sequential Involvement of Calcium-independent Phospholipase A2β (iPLA2β) and Group X Secreted Phospholipase A2 (sPLA2). *Journal of Biological Chemistry* 291 (6):3076–89. DOI: 10.1074/jbc.M115.677799.

Aitken, R. J. and B. Nixon (2013). Sperm capacitation: A distant landscape glimpsed but unexplored. *Molecular Human Reproduction* 19 (12):785–793. DOI: 10.1093/molehr/gat067.

Albert, S., M. Schaffer, F. Beck, S. Mosalaganti, S. Asano, H. F. Thomas, J. M. Plitzko, M. Beck, W. Baumeister, and B. D. Engel (2017). Proteasomes tether to two distinct sites at the nuclear pore complex. *Proceedings of the National Academy of Sciences of the United States of America* 114 (52):13726–13731. DOI: 10.1073/pnas.1716305114.

Albert, S., W. Wietrzynski, C. W. Lee, M. Schaffer, F. Beck, J. M. Schuller, P. A. Salomé, J. M. Plitzko, W. Baumeister, and B. D. Engel (2020). Direct visualization of degradation microcompartments at the ER membrane. *Proceedings of the National Academy of Sciences of the United States of America* 117 (2):1069–1080. DOI: 10.1073/pnas.1905641117.

Allen, M. J., E. M. Bradbury, and R. Balhorn (1997). AFM analysis of DNA-protamine complexes bound to mica. *Nucleic Acids Research* 25 (11):2221–2226. DOI: 10.1093/nar/25.11.2221.

Anderson, P. W. (1972). More Is Different. *Science* 177 (4047):393–396. DOI: 10.1126/science.177.4047.393.

Asano, A., J. L. Nelson-Harrington, and A. J. Travis (2013). Phospholipase B is activated in response to sterol removal and stimulates acrosome exocytosis in murine sperm. *The Journal of Biological Chemistry* 288 (39):28104–15. DOI: 10.1074/jbc.M113.450981.

Asano, S., Y. Fukuda, F. Beck, A. Aufderheide, F. Förster, R. Danev, and W. Baumeister (2015). A molecular census of 26S proteasomes in intact neurons. *Science* 347 (6220):439–442. DOI: 10.1126/science.1261197.

Austin, C. (1951). Observations on the Penetration of the Sperm into the Mammalian Egg. *Australian Journal of Biological Sciences* 4 (4):581. DOI: 10.1071/BI9510581.

Avidor-Reiss, T. (2018). Rapid Evolution of Sperm Produces Diverse Centriole Structures that Reveal the Most Rudimentary Structure Needed for Function. *Cells* 7 (7):67. DOI: 10.3390/cells7070067.

Avidor-Reiss, T. and M. R. Leroux (2015). Shared and distinct mechanisms of compartmentalized and cytosolic ciliogenesis. *Current Biology* 25 (23):R1143–R1150. DOI: 10.1016/j.cub.2015.11.001.

Avidor-Reiss, T., M. Mazur, E. L. Fishman, and P. Sindhwani (2019). The Role of Sperm Centrioles in Human Reproduction – The Known and the Unknown. *Frontiers in Cell and Developmental Biology* 7:1–15. DOI: 10.3389/fcell.2019.00188.

Baba, T., S. Azuma, S. I. Kashiwabara, and Y. Toyoda (1994). Sperm from mice carrying a targeted mutation of the acrosin gene can penetrate the oocyte zona pellucida and effect fertilization. *Journal of Biological Chemistry* 269 (50):31845–31849.

Babcock, D. F., P. M. Wandernoth, and G. Wennemuth (2014). Episodic rolling and transient attachments create diversity in sperm swimming behavior. *BMC Biology* 12 (1):1–12. DOI: 10.1186/s12915-014-0067-3.

Baena, V. and M. Terasaki (2019). Three-dimensional organization of transzonal projections and other cytoplasmic extensions in the mouse ovarian follicle. *Scientific Reports* 9 (1):1–13. DOI: 10.1038/s41598-018-37766-2.

Bahr, G. F. and W. F. Engler (1970). Considerations of volume, mass, DNA, and arrangement of mitochondria in the midpiece of bull spermatozoa. *Experimental Cell Research* 60 (3):338–340. DOI: 10.1016/0014-4827(70)90526-4.

Bailey, J. L. (2010). Factors regulating sperm capacitation. *Systems Biology in Reproductive Medicine* 56 (5):334–348. DOI: 10.3109/19396368.2010.512377.

Baker, B. J., L. R. Comolli, G. J. Dick, L. J. Hauser, D. Hyatt, B. D. Dill, M. L. Land, N. C. VerBerkmoes, R. L. Hettich, and J. F. Banfield (2010). Enigmatic, ultrasmall, uncultivated Archaea. *Proceedings of the National Academy of Sciences of the United States of America* 107 (19):8806–8811. DOI: 10.1073/pnas.0914470107.

Balbach, M., M. G. Gervasi, D. M. Hidalgo, P. E. Visconti, L. R. Levin, and J. Buck (2020). Metabolic changes in mouse sperm during capacitation. *Biology of Reproduction*:1–5. DOI: 10.1093/biolre/ioaa114.

Balogun, E. O., D. K. Inaoka, T. Shiba, C. Tsuge, B. May, T. Sato, Y. Kido, T. Nara, T. Aoki, T. Honma, A. Tanaka, M. Inoue, S. Matsuoka, P. A. Michels, Y. I. Watanabe, A. L. Moore, S. Harada, and K. Kita (2019). Discovery of trypanocidal coumarins with dual inhibition of both the glycerol kinase and alternative oxidase of Trypanosoma brucei brucei. *FASEB Journal* 33 (11):13002–13013. DOI: 10.1096/fj.201901342R.

Baltz, J. M., P. Oneeka Williams, and R. A. Cone (1990). Dense Fibers Protect Mammalian Sperm Against Damage. *Biology of Reproduction* 43 (3):485–491. DOI: 10.1095/biolreprod43.3.485.

Bavister, B. D. (1973). Capacitation of golden hamster spermatozoa during incubation in culture medium. *Journal of Reproduction and Fertility* 35 (1):161–163. DOI: 10.1530/jrf.0.0350161.

Bayrhuber, M., T. Meins, M. Habeck, S. Becker, K. Giller, S. Villinger, C. Vonrhein, C. Griesinger, M. Zweckstetter, and K. Zeth (2008). Structure of the human voltage-dependent anion channel. *Proceedings of the National Academy of Sciences of the United States of America* 105 (40):15370–15375. DOI: 10.1073/pnas.0808115105.

Bedford, J. M. (2014). Singular features of fertilization and their impact on the male reproductive system in eutherian mammals. *Reproduction* 147 (2):43–52. DOI: 10.1530/REP-13-0436.

Bedford, J. (1983). Significance of the Need for Sperm Capacitation Before Fertilization in Eutherian Mammals. *Biology of Reproduction* 28:108–120.

Boerke, A., J. van der Lit, F. Lolicato, T. A. Stout, J. B. Helms, and B. M. Gadella (2014). Removal of GPI-anchored membrane proteins causes clustering of lipid microdomains in the apical head area of porcine sperm. *Theriogenology* 81 (4):613–624. DOI: 10.1016/j.theriogenology.2013.11.014.

Böhning, J. and T. A. Bharat (2020). Towards high-throughput in situ structural biology using electron cryotomography. *Progress in Biophysics and Molecular Biology*:DOI: 10.1016/j.pbiomolbio.2020.05.010.

Boldogh, I. R. and L. A. Pon (2006). Interactions of mitochondria with the actin cytoskeleton. *Biochimica et Biophysica Acta - Molecular Cell Research* 1763 (5-6):450–462. DOI: 10.1016/j.bbamcr.2006.02.014.

Brokaw, C. J. (2009). Thinking about flagellar oscillation. *Cell Motility and the Cytoskeleton* 66 (8):425–436. DOI: 10.1002/cm.20313.

Brugh, V. M. and L. I. Lipshultz (2004). Male factor infertility: Evaluation and management. *Medical Clinics of North America* 88 (2):367–385. DOI: 10.1016/S0025-7125(03)00150-0.

Buffone, M. G., N. Hirohashi, and G. L. Gerton (2014). Unresolved Questions Concerning Mammalian Sperm Acrosomal Exocytosis. *Biology of Reproduction* 90 (5):1–8. DOI: 10.1095/biolreprod.114.117911.

Bystrom, C. E., D. W. Pettigrew, B. P. Branchaud, P. O'Brien, and S. J. Remington (1999). Crystal structures of Escherichia coli glycerol kinase variant S58→W in complex with nonhydrolyzable ATP analogues reveal a putative active conformation of the enzyme as a result of domain motion. *Biochemistry* 38 (12):3508–3518. DOI: 10.1021/bi982460z.

Carbajal-González, B. I., T. Heuser, X. Fu, J. Lin, B. W. Smith, D. R. Mitchell, and D. Nicastro (2013). Conserved structural motifs in the central pair complex of eukaryotic flagella. *Cytoskeleton* 70 (2):101–120. DOI: 10.1002/cm.21094.

Cardullo, R. A. and J. M. Baltz (1991). Metabolic regulation in mammalian sperm: Mitochondrial volume determines sperm length and flagellar beat frequency. *Cell Motility and the Cytoskeleton* 19 (3):180–188. DOI: 10.1002/cm.970190306.

Carrera, A., G. L. Gerton, and S. B. Moss (1994). The Major Fibrous Sheath Polypeptide of Mouse Sperm: Structural and Functional Similarities to the A-Kinase Anchoring Proteins. *Developmental Biology* 165 (1):272–284. DOI: 10.1006/dbio.1994.1252.

Ceballos, G., P. R. Ehrlich, A. D. Barnosky, A. García, R. M. Pringle, and T. M. Palmer (2015). Accelerated modern human-induced species losses: Entering the sixth mass extinction. *Science Advances* 1 (5):9–13. DOI: 10.1126/sciadv.1400253.

Ceballos, G., P. R. Ehrlich, and P. H. Raven (2020). Vertebrates on the brink as indicators of biological annihilation and the sixth mass extinction. *Proceedings of the National Academy of Sciences of the United States of America* 117 (24):13596–13602. DOI: 10.1073/pnas.1922686117.

Chang, M. C. (1951). Fertilizing capacity of spermatozoa deposited into the fallopian tubes. *Nature* 168 (4277):697–698. DOI: 10.1038/168697b0.

— (1959). Fertilization of rabbit ova in vitro. *Nature* 184 (4684):466–467. DOI: 10.1038/184466a0.

— (1984). The Meaning of Sperm Capacitation: A Historical Perspective. *Journal of Andrology* 5 (2):45–50. DOI: 10.1002/j.1939-4640.1984.tb00775.x.

Chang, W., H. J. Worman, and G. G. Gundersen (2015). Accessorizing and anchoring the LINC complex for multifunctionality. *Journal of Cell Biology* 208 (1):11–22. DOI: 10.1083/jcb.201409047.

Chen, M., W. Dai, S. Y. Sun, D. Jonasch, C. Y. He, M. F. Schmid, W. Chiu, and S. J. Ludtke (2017a). Convolutional neural networks for automated annotation of cellular cryo-electron tomograms. *Nature Methods* 14 (10):983–985. DOI: 10.1038/nmeth.4405.

Chen, Y. and Z. H. Sheng (2013). Kinesin-1-syntaphilin coupling mediates activity-dependent regulation of axonal mitochondrial transport. *Journal of Cell Biology* 202 (2):351–364. DOI: 10.1083/jcb.201302040.

Chen, Y., P. Liang, Y. Huang, M. Li, X. Zhang, C. Ding, J. Feng, Z. Zhang, X. Zhang, Y. Gao, Q. Zhang, S. Cao, H. Zheng, D. Liu, Z. Songyang, and J. Huang (2017b). Glycerol kinase-like proteins cooperate with Pld6 in regulating sperm mitochondrial sheath formation and male fertility. *Cell Discovery* 3 (1):17030. DOI: 10.1038/celldisc.2017.30.

Chlanda, P., E. Mekhedov, H. Waters, C. L. Schwartz, E. R. Fischer, R. J. Ryham, F. S. Cohen, P. S. Blank, and J. Zimmerberg (2016). The hemifusion structure induced by influenza

virus haemagglutinin is determined by physical properties of the target membranes. *Nature Microbiology* 1 (6):1–8. DOI: 10.1038/nmicrobiol.2016.50.

Chung, J.-J., S.-H. Shim, R. A. Everley, S. P. Gygi, X. Zhuang, and D. E. Clapham (2014). Structurally Distinct Ca^{2+} Signaling Domains of Sperm Flagella Orchestrate Tyrosine Phosphorylation and Motility. *Cell* 157 (4):808–822. DOI: 10.1016/j.cell.2014.02.056.

Cleland, J., S. Bernstein, A. Ezeh, A. Faundes, A. Glasier, and J. Innis (2006). Family planning: the unfinished agenda. *The Lancet* 368 (9549):1810–1827. DOI: 10.1016/S0140-6736(06)69480-4.

Comizzoli, P. and W. V. Holt (2019). Breakthroughs and new horizons in reproductive biology of rare and endangered animal species. *Biology of Reproduction* 101 (3):514–525. DOI: 10.1093/biolre/ioz031.

Comolli, L. R., R. Duarte, D. Baum, B. Luef, K. H. Downing, D. M. Larson, R. Csencsits, and J. F. Banfield (2012). A portable cryo-plunger for on-site intact cryogenic microscopy sample preparation in natural environments. *Microscopy Research and Technique* 75 (6):829–836. DOI: 10.1002/jemt.22001.

Cui, W. (2010). Mother or nothing: the agony of infertility. *Bulletin of the World Health Organization* 88 (12):881–882. DOI: 10.2471/blt.10.011210.

Danev, R., B. Buijsse, M. Khoshouei, J. M. Plitzko, and W. Baumeister (2014). Volta potential phase plate for in-focus phase contrast transmission electron microscopy. *Proceedings of the National Academy of Sciences of the United States of America* 111 (44):15635–40. DOI: 10.1073/pnas.1418377111.

Darszon, A., T. Nishigaki, C. Beltran, and C. L. Treviño (2011). Calcium Channels in the Development, Maturation, and Function of Spermatozoa. *Physiological Reviews* 91 (4):1305–1355. DOI: 10.1152/physrev.00028.2010.

Davila, M. P., P. M. Muñoz, J. M. Bolaños, T. A. Stout, B. M. Gadella, J. A. Tapia, C. Balao Da Silva, C. Ortega Ferrusola, and F. J. Peña (2016). Mitochondrial ATP is required for the maintenance of membrane integrity in stallion spermatozoa, whereas motility requires both glycolysis and oxidative phosphorylation. *Reproduction* 152 (6):683–694. DOI: 10.1530/REP-16-0409.

De Martino, C., A. Floridi, M. L. Marcante, W. Malorni, P. S. Barcellona, M. Bellocci, and B. Silvestrini (1979). Morphological, histochemical and biochemical studies on germ cell mitochondria of normal rats. *Cell and Tissue Research* 196 (1):1–22. DOI: 10.1007/BF00236345.

Depelteau, J. S., G. Koning, W. Yang, and A. Briegel (2020). An Economical, Portable Manual Cryogenic Plunge Freezer for the Preparation of Vitrified Biological Samples for Cryogenic Electron Microscopy. *Microscopy and Microanalysis* 26 (3):413–418. DOI: 10.1017/S1431927620001385.

Dobro, M. J., L. A. Melanson, G. J. Jensen, and A. W. McDowall (2010). Plunge Freezing for Electron Cryomicroscopy. *Methods in Enzymology*. 1st ed. Vol. 481. (C). Elsevier Inc., p. 63–82. DOI: 10.1016/S0076-6879(10)81003-1.

Dobro, M. J., C. M. Oikonomou, A. Piper, J. Cohen, K. Guo, T. Jensen, J. Tadayon, J. Donermeyer, Y. Park, B. A. Solis, A. Kjær, A. I. Jewett, A. W. McDowall, S. Chen, Y. W. Chang, J. Shi, P. Subramanian, C. V. Iancu, Z. Li, A. Briegel, E. I. Tocheva, M. Pilhofer, and G. J. Jensen (2017). Uncharacterized bacterial structures revealed by electron cryotomography. *Journal of Bacteriology* 199 (17):1–14. DOI: 10.1128/JB.00100-17.

Dubochet, J. (1995). High-pressure freezing for cryoelectron microscopy. *Trends in Cell Biology* 5 (9):366–368. DOI: 10.1016/S0962-8924(00)89071-6.

Dubochet, J., J. Lepault, R. Freeman, J. A. Berriman, and J. C. Homo (1982). Electron microscopy of frozen water and aqueous solutions. *Journal of Microscopy* 128 (3):219–237. DOI: 10.1111/j.1365-2818.1982.tb04625.x.

Dubochet, J., B. Zuber, M. Eltsov, C. Bouchet-Marquis, A. Al-Amoudi, F. Livolant, C. Bouchet-Marquis, A. Al-Amoudi, and F. Livolant (2007). How to "Read" a Vitreous Section. *Methods in Cell Biology* 79 (79):385–406. DOI: 10.1016/S0091-679X(06)79015-X.

Dunleavy, J. E., M. K. O'Bryan, P. G. Stanton, and L. O'Donnell (2019). The cytoskeleton in spermatogenesis. *Reproduction* 157 (2):R53–R72. DOI: 10.1530/REP-18-0457.

Dutcher, S. K. (2001). Motile organelles: The importance of specific tubulin isoforms. *Current Biology* 11 (11):419–422. DOI: 10.1016/S0960-9822(01)00250-0.

Eddy, E. M., K. Toshimori, and D. A. O'Brien (2003). Fibrous sheath of mammalian spermatozoa. *Microscopy Research and Technique* 61 (1):103–115. DOI: 10.1002/jemt.10320.

Edwards, R. G., B. D. Bavister, and P. C. Steptoe (1969). Early stages of fertilization in vitro of human oocytes matured in vitro. *Nature* 221 (5181):632–635. DOI: 10.1038/221632a0.

Elkhatib, R. A., M. Paci, G. Longepied, J. Saias-Magnan, B. Courbière, M. R. Guichaoua, N. Lévy, C. Metzler-Guillemain, and M. J. Mitchell (2017). Homozygous deletion of SUN5 in three men with decapitated spermatozoa. *Human Molecular Genetics* 26 (16):3167–3171. DOI: 10.1093/hmg/ddx200.

Farabella, I., D. Vasishtan, A. P. Joseph, A. P. Pandurangan, H. Sahota, and M. Topf (2015). TEMPy : a Python library for assessment of three-dimensional electron microscopy density fits. *Journal of Applied Crystallography* 48 (4):1314–1323. DOI: 10.1107/S1600576715010092.

Fawcett, D. W. (1970). A Comparative View of Sperm Ultrastructure. *Biology of Reproduction* 2 (suppl_2):90–127. DOI: 10.1095/biolreprod2.Supplement_2.90.

— (1975). The mammalian spermatozoon. *Developmental Biology* 44 (2):394–436. DOI: 10.1016/0012-1606(75)90411-X.

Fawcett, D. W. and D. M. Phillips (1969). The fine structure and development of the neck region of the mammalian spermatozoon. *The Anatomical Record* 165 (2):153–183. DOI: 10.1002/ar.1091650204.

Fawcett, D. W. and K. R. Porter (1954). A study of the fine structure of ciliated epithelia. *Journal of Morphology* 94 (2):221–281.

Firman, R. C. and L. W. Simmons (2010). Sperm midpiece length predicts sperm swimming velocity in house mice. *Biology Letters* 6 (4):513–516. DOI: 10.1098/rsbl.2009.1027.

Fisher, H. S., E. Jacobs-Palmer, J.-M. Lassance, and H. E. Hoekstra (2016). The genetic basis and fitness consequences of sperm midpiece size in deer mice. *Nature Communications* 7 (1):13652. DOI: 10.1038/ncomms13652.

Fishman, E. L., K. Jo, Q. P. H. Nguyen, D. Kong, R. Royfman, A. R. Cekic, S. Khanal, A. L. Miller, C. Simerly, G. Schatten, J. Loncarek, V. Mennella, and T. Avidor-Reiss (2018). A novel atypical sperm centriole is functional during human fertilization. *Nature Communications* 9 (1):2210. DOI: 10.1038/s41467-018-04678-8.

Fléchon, J.-E. (2016). The acrosome of eutherian mammals. *Cell and Tissue Research* 363 (1):147–157. DOI: 10.1007/s00441-015-2238-0.

Franke, W. W., U. Scheer, G. Krohne, and E. D. Jarasch (1981). The nuclear envelope and the architecture of the nuclear periphery. *Journal of Cell Biology* 91 (3):39s–50s. DOI: 10.1083/jcb.91.3.39s.

Frazier, Z., M. Xu, and F. Alber (2017). TomoMiner and TomoMinerCloud: A Software Platform for Large-Scale Subtomogram Structural Analysis. *Structure* 25 (6):951–961.e2. DOI: 10.1016/j.str.2017.04.016.

Friedrich, B. M., I. H. Riedel-Kruse, J. Howard, and F. Jülicher (2010). High-precision tracking of sperm swimming fine structure provides strong test of resistive force theory. *Journal of Experimental Biology* 213 (8):1226–1234. DOI: 10.1242/jeb.039800.

Friend, D. S. and J. E. Heuser (1981). Orderly particle arrays on the mitochondrial outer membrane in rapidly-frozen sperm. *The Anatomical Record* 199 (2):159–175. DOI: 10.1002/ar.1091990202.

Fu, G., L. Zhao, E. Dymek, Y. Hou, K. Song, N. Phan, Z. Shang, E. F. Smith, G. B. Witman, and D. Nicastro (2019). Structural organization of the C1a-e-c supercomplex within the ciliary central apparatus. *Journal of Cell Biology* 218 (12):4236–4251. DOI: 10.1083/jcb.201906006.

Fujihara, Y., Y. Lu, T. Noda, A. Oji, T. Larasati, K. Kojima-Kita, Z. Yu, R. M. Matzuk, M. M. Matzuk, and M. Ikawa (2020). Spermatozoa lacking Fertilization Influencing Membrane Protein (FIMP) fail to fuse with oocytes in mice. *Proceedings of the National Academy of Sciences of the United States of America* 117 (17):9393–9400. DOI: 10.1073/pnas.1917060117.

Fukuda, Y., A. Abe, T. Tamura, T. Kishimoto, A. Sogabe, S. Akanuma, S. I. Yokobori, A. Yamagishi, K. Imada, and K. Inagaki (2016). Epistasis effects of multiple ancestral-consensus amino acid substitutions on the thermal stability of glycerol kinase from Cellulomonas sp. NT3060. *Journal of Bioscience and Bioengineering* 121 (5):497–502. DOI: 10.1016/j.jbiosc.2015.09.011.

Fukuda, Y., F. Beck, J. M. Plitzko, and W. Baumeister (2017). In situ structural studies of tripeptidyl peptidase II (TPPII) reveal spatial association with proteasomes. *Proceedings of the National Academy of Sciences of the United States of America* 114 (17):4412–4417. DOI: 10.1073/pnas.1701367114.

Fukuda, Y., U. Laugks, V. Lučić, W. Baumeister, and R. Danev (2015). Electron cryotomography of vitrified cells with a Volta phase plate. *Journal of Structural Biology* 190 (2):143–154. DOI: 10.1016/j.jsb.2015.03.004.

Gadadhar, S., G. Alvarez Viar, J. N. Hansen, A. Gong, A. Kostarev, C. Ialy-Radio, S. Leboucher, M. Whitfield, A. Ziyyat, A. Touré, L. Alvarez, G. Pigino, and C. Janke (2021). Tubulin glycylation controls axonemal dynein activity, flagellar beat, and male fertility. *Science* 371 (6525):eabd4914. DOI: 10.1126/science.abd4914.

Gadêlha, H. and E. A. Gaffney (2019). Flagellar ultrastructure suppresses buckling instabilities and enables mammalian sperm navigation in high-viscosity media. *Journal of the Royal Society Interface* 16 (152):DOI: 10.1098/rsif.2018.0668.

Gadêlha, H., P. Hernández-Herrera, F. Montoya, A. Darszon, and G. Corkidi (2020). Human sperm uses asymmetric and anisotropic flagellar controls to regulate swimming symmetry and cell steering. *Science Advances* 6 (31):eaba5168. DOI: 10.1126/sciadv.aba5168.

Gadella, B. M. (2008). Sperm membrane physiology and relevance for fertilization. *Animal Reproduction Science* 107 (3-4):229–236. DOI: 10.1016/j.anireprosci.2008.05.006.

Gaffney, E., H. Gadêlha, D. Smith, J. Blake, and J. Kirkman-Brown (2011). Mammalian Sperm Motility: Observation and Theory. *Annual Review of Fluid Mechanics* 43 (1):501–528. DOI: 10.1146/annurev-fluid-121108-145442.

Gage, M. J. G. (2012). Complex sperm evolution. *Proceedings of the National Academy of Sciences of the United States of America* 109 (12):4341–4342. DOI: 10.1073/pnas.1201827109.

Gervasi, M. G., X. Xu, B. Carbajal-Gonzalez, M. G. Buffone, P. E. Visconti, and D. Krapf (2018). The actin cytoskeleton of the mouse sperm flagellum is organized in a helical structure. *Journal of Cell Science* 131 (11):jcs215897. DOI: 10.1242/jcs.215897.

Gervasi, M. G. and P. E. Visconti (2016). Chang's meaning of capacitation: A molecular perspective. *Molecular Reproduction and Development* 83 (10):860–874. DOI: 10.1002/mrd.22663.

Glaeser, R. M. (2019). How Good Can Single-Particle Cryo-EM Become? What Remains Before It Approaches Its Physical Limits? *Annual Review of Biophysics* 48 (1):45–61. DOI: 10.1146/annurev-biophys-070317-032828.

Glancy, B., L. M. Hartnell, D. Malide, Z. X. Yu, C. A. Combs, P. S. Connelly, S. Subramaniam, and R. S. Balaban (2015). Mitochondrial reticulum for cellular energy distribution in muscle. *Nature* 523 (7562):617–620. DOI: 10.1038/nature14614.

Goddard, T. D., C. C. Huang, E. C. Meng, E. F. Pettersen, G. S. Couch, J. H. Morris, and T. E. Ferrin (2018). UCSF ChimeraX: Meeting modern challenges in visualization and analysis. *Protein Science* 27 (1):14–25. DOI: 10.1002/pro.3235.

Gonçalves, R. P., N. Buzhynskyy, V. Prima, J. N. Sturgis, and S. Scheuring (2007). Supramolecular Assembly of VDAC in Native Mitochondrial Outer Membranes. *Journal of Molecular Biology* 369 (2):413–418. DOI: 10.1016/j.jmb.2007.03.063.

Goodsell, D. S., A. J. Olson, and S. Forli (2020). Art and Science of the Cellular Mesoscale. *Trends in Biochemical Sciences* 45 (6):472–483. DOI: 10.1016/j.tibs.2020.02.010.

Gorelick, S., G. Buckley, G. Gervinskas, T. K. Johnson, A. Handley, M. P. Caggiano, J. C. Whisstock, R. Pocock, and A. de Marco (2019). PIE-scope, integrated cryo-correlative light and FIB/SEM microscopy. *eLife* 8:1–15. DOI: 10.7554/eLife.45919.

Goto, M., D. A. O'Brien, and E. M. Eddy (2010). Speriolin is a novel human and mouse sperm centrosome protein. *Human Reproduction* 25 (8):1884–1894. DOI: 10.1093/humrep/deq138.

Grange, M., D. Vasishtan, and K. Grünewald (2017). Cellular electron cryo tomography and in situ sub-volume averaging reveal the context of microtubule-based processes. *Journal of Structural Biology* 197 (2):181–190. DOI: 10.1016/j.jsb.2016.06.024.

Greenan, G. A., B. Keszthelyi, R. D. Vale, and D. A. Agard (2018). Insights into centriole geometry revealed by cryotomography of doublet and triplet centrioles. *eLife* 7:1–18. DOI: 10.7554/elife.36851.

Greenan, G. A., R. D. Vale, and D. A. Agard (2020). Electron cryotomography of intact motile cilia defines the basal body to axoneme transition. *Journal of Cell Biology* 219 (1):1–14. DOI: 10.1083/jcb.201907060.

Greenawalt, J. W., C. S. Rossi, and A. L. Lehninger (1964). Effect of Active Accumulation of Calcium and Phosphate Ions on the Structure of Rat Liver Mitochondria. *Journal of Cell Biology* 23:21–38. DOI: 10.1083/jcb.23.1.21.

Grünewald, K., P. Desai, D. C. Winkler, J. B. Heymann, D. M. Belnap, W. Baumeister, and A. C. Steven (2003). Three-Dimensional Structure of Herpes Simplex Virus from Cryo-Electron Tomography. *Science* 302 (5649):1396–1398. DOI: 10.1126/science.1090284.

Guichard, P., V. Hachet, N. Majubu, A. Neves, D. Demurtas, N. Olieric, I. Fluckiger, A. Yamada, K. Kihara, Y. Nishida, S. Moriya, M. O. Steinmetz, Y. Hongoh, and P. Gönczy (2013). Native architecture of the centriole proximal region reveals features underlying its 9-fold radial symmetry. *Current Biology* 23 (17):1620–1628. DOI: 10.1016/j.cub.2013.06.061.

Gumbs, R., C. L. Gray, M. Böhm, M. Hoffmann, R. Grenyer, W. Jetz, S. Meiri, U. Roll, N. R. Owen, and J. Rosindell (2020). Global priorities for conservation of reptilian phylogenetic diversity in the face of human impacts. *Nature Communications* 11 (1):1–13. DOI: 10.1038/s41467-020-16410-6.

Gundersen, G. G. and H. J. Worman (2013). Nuclear positioning. *Cell* 152 (6):1376–1389. DOI: 10.1016/j.cell.2013.02.031.

Guo, X. W. and C. A. Mannella (1993). Conformational change in the mitochondrial channel, VDAC, detected by electron cryo-microscopy. *Biophysical Journal* 64 (2):545–549. DOI: 10.1016/S0006-3495(93)81399-7.

Guyonnet, B., N. Egge, and G. A. Cornwall (2014). Functional Amyloids in the Mouse Sperm Acrosome. *Molecular and Cellular Biology* 34 (14):2624–2634. DOI: 10.1128/mcb.00073-14.

Haidl, G., A. Becker, and R. Henkel (1991). Poor development of outer dense fibres as a major cause of tail abnormalities in the spermatozoa of asthenoteratozoospermic men. *Human Reproduction* 6 (10):1431–1438. DOI: 10.1093/oxfordjournals.humrep.a137283.

Haldar, S., E. Mekhedov, C. D. McCormick, P. S. Blank, and J. Zimmerberg (2019). Lipid-dependence of target membrane stability during influenza viral fusion. *Journal of Cell Science* 132 (4):jcs218321. DOI: 10.1242/jcs.218321.

Haraguchi, C. M., T. Mabuchi, S. Hirata, T. Shoda, T. Tokumoto, K. Hoshi, and S. Yokota (2007). Possible function of caudal nuclear pocket: Degradation of nucleoproteins by ubiquitin-proteasome system in rat spermatids and human sperm. *Journal of Histochemistry and Cytochemistry* 55 (6):585–595. DOI: 10.1369/jhc.6A7136.2007.

Harrison, R. A. P. and B. M. Gadella (2005). Bicarbonate-induced membrane processing in sperm capacitation. *Theriogenology* 63 (2):342–351. DOI: 10.1016/j.theriogenology.2004.09.016.

He, C., R. Keren, M. Whittaker, I. F. Farag, J. Doudna, J. H. Cate, and J. F. Banfield (2020). Huge and variable diversity of episymbiotic CPR bacteria and DPANN archaea in groundwater ecosystems. *bioRxiv*:DOI: 10.1101/2020.05.14.094862.

Healy, J. and G. Jamieson (1994). The ultrastructure of spermatogenesis and epididymal spermatozoa of the tuatara Sphenodon punctatus (Sphenodontida, Amniota). *Philosophical Transactions of the Royal Society of London. Series B: Biological Sciences* 344 (1308):187–199. DOI: 10.1098/rstb.1994.0060.

Hemmerling, A., E. Christopher, and B. Y. Holt (2020). Towards a roadmap to advance non-hormonal contraceptive multipurpose prevention technologies: Strategic insights from key stakeholders. *Biology of Reproduction* 103 (2):289–298. DOI: 10.1093/biolre/ioaa092.

Hess, R. A., R. J. Thurston, and D. H. Gist (1991). Ultrastructure of the turtle spermatozoon. *The Anatomical Record* 229 (4):473–481. DOI: 10.1002/ar.1092290406.

Heumann, J. M., A. Hoenger, and D. N. Mastronarde (2011). Clustering and variance maps for cryo-electron tomography using wedge-masked differences. *Journal of Structural Biology* 175 (3):288–299. DOI: 10.1016/j.jsb.2011.05.011.

Heuser, T., M. Raytchev, J. Krell, M. E. Porter, and D. Nicastro (2009). The dynein regulatory complex is the nexin link and a major regulatory node in cilia and flagella. *Journal of Cell Biology* 187 (6):921–933. DOI: 10.1083/jcb.200908067.

Hidalgo, D. M., A. Romarowski, M. G. Gervasi, F. Navarrete, M. Balbach, A. M. Salicioni, L. R. Levin, J. Buck, and P. E. Visconti (2020). Capacitation increases glucose consumption in murine sperm. *Molecular Reproduction and Development* 87 (10):1037–1047. DOI: 10.1002/mrd.23421.

Hino, T., Y. Muro, M. Tamura-Nakano, M. Okabe, H. Tateno, and R. Yanagimachi (2016). The Behavior and Acrosomal Status of Mouse Spermatozoa In Vitro, and Within the Oviduct During Fertilization after Natural Mating. *Biology of Reproduction* 95 (3):50–50. DOI: 10.1095/biolreprod.116.140400.

Hinsch, K. D., V. De Pinto, V. A. Aires, X. Schneider, A. Messina, and E. Hinsch (2004). Voltage-dependent Anion-selective Channels VDAC2 and VDAC3 Are Abundant Proteins in Bovine

Outer Dense Fibers, a Cytoskeletal Component of the Sperm Flagellum. *Journal of Biological Chemistry* 279 (15):15281–15288. DOI: 10.1074/jbc.M313433200.

Hirose, M., A. Honda, H. Fulka, M. Tamura-Nakano, S. Matoba, T. Tomishima, K. Mochida, A. Hasegawa, K. Nagashima, K. Inoue, M. Ohtsuka, T. Baba, R. Yanagimachi, and A. Ogura (2020). Acrosin is essential for sperm penetration through the zona pellucida in hamsters. *Proceedings of the National Academy of Sciences of the United States of America* 117 (5):2513–2518. DOI: 10.1073/pnas.1917595117.

Ho, C. M., X. Li, M. Lai, T. C. Terwilliger, J. R. Beck, J. Wohlschlegel, D. E. Goldberg, A. W. Fitzpatrick, and Z. H. Zhou (2020). Bottom-up structural proteomics: cryoEM of protein complexes enriched from the cellular milieu. *Nature Methods* 17 (1):79–85. DOI: 10.1038/s41592-019-0637-y.

Ho, H. C. C. (2010). Redistribution of nuclear pores during formation of the redundant nuclear envelope in mouse spermatids. *Journal of Anatomy* 216 (4):525–532. DOI: 10.1111/j.1469-7580.2009.01204.x.

Ho, H. C. C. and S. S. Suarez (2003). Characterization of the intracellular calcium store at the base of the sperm flagellum that regulates hyperactivated motility. *Biology of Reproduction* 68 (5):1590–1596. DOI: 10.1095/biolreprod.102.011320.

Ho, H.-C. C. and S. Wey (2007). Three dimensional rendering of the mitochondrial sheath morphogenesis during mouse spermiogenesis. *Microscopy Research and Technique* 70 (8):719–723. DOI: 10.1002/jemt.20457.

Holt, W. V., A. R. Pickard, J. C. Rodger, and D. E. Wildt (2003). Reproductive science and integrated conservation. *Australian Mammalogy* 25 (2):219–220. DOI: 10.1071/am03219_br.

Hoogenboom, B. W., K. Suda, A. Engel, and D. Fotiadis (2007). The Supramolecular Assemblies of Voltage-dependent Anion Channels in the Native Membrane. *Journal of Molecular Biology* 370 (2):246–255. DOI: 10.1016/j.jmb.2007.04.073.

Hörning, M., A. Schertel, R. Schneider, M. L. Lemloh, M. R. Schweikert, and I. M. Weiss (2020). Mineralized scale patterns on the cell periphery of the chrysophyte Mallomonas determined by comparative 3D Cryo-FIB SEM data processing. *Journal of Structural Biology* 209 (1):107403. DOI: 10.1016/j.jsb.2019.10.005.

Huang, X., L. Sun, S. Ji, T. Zhao, W. Zhang, J. Xu, J. Zhang, Y. Wang, X. Wang, C. Franzini-Armstrong, M. Zheng, and H. Cheng (2013). Kissing and nanotunneling mediate intermitochondrial communication in the heart. *Proceedings of the National Academy of Sciences of the United States of America* 110 (8):2846–2851. DOI: 10.1073/pnas.1300741110.

Hud, N., M. Allen, K. Downing, J. Lee, and R. Balhorn (1993). Identification of the Elemental Packing Unit of DNA in Mammalian Sperm Cells by Atomic Force Microscopy. *Biochemical and Biophysical Research Communications* 193 (3):1347–1354. DOI: 10.1006/bbrc.1993.1773.

Hunyadi, V., D. Chrétien, and I. M. Jánosi (2005). Mechanical stress induced mechanism of microtubule catastrophes. *Journal of Molecular Biology* 348 (4):927–938. DOI: 10.1016/j.jmb.2005.03.019.

Hutcheon, K., E. A. McLaughlin, S. J. Stanger, I. R. Bernstein, M. D. Dun, A. L. Eamens, and B. Nixon (2017). Analysis of the small non-protein-coding RNA profile of mouse spermatozoa reveals specific enrichment of piRNAs within mature spermatozoa. *RNA Biology* 14 (12):1776–1790. DOI: 10.1080/15476286.2017.1356569.

Ichikawa, M. and K. H. Bui (2018). Microtubule Inner Proteins: A Meshwork of Luminal Proteins Stabilizing the Doublet Microtubule. *BioEssays* 40 (3):1–7. DOI: 10.1002/bies.201700209.

Ichikawa, M., A. A. Z. Khalifa, S. Kubo, D. Dai, K. Basu, M. A. F. Maghrebi, J. Vargas, and K. H. Bui (2019). Tubulin lattice in cilia is in a stressed form regulated by microtubule inner proteins. *Proceedings of the National Academy of Sciences of the United States of America* 116 (40):19930–19938. DOI: 10.1073/pnas.1911119116.

Ichikawa, M., D. Liu, P. L. Kastritis, K. Basu, T. C. Hsu, S. Yang, and K. H. Bui (2017). Subnanometre-resolution structure of the doublet microtubule reveals new classes of microtubuleassociated proteins. *Nature Communications* 8:DOI: 10.1038/ncomms15035.

Imai, H., N. Hakkaku, R. Iwamoto, J. Suzuki, T. Suzuki, Y. Tajima, K. Konishi, S. Minami, S. Ichinose, K. Ishizaka, S. Shioda, S. Arata, M. Nishimuřa, S. Naito, and Y. Nakagawa (2009). Depletion of selenoprotein GPx4 in spermatocytes causes male infertility in mice. *Journal of Biological Chemistry* 284 (47):32522–32532. DOI: 10.1074/jbc.M109.016139.

Imhof, S., J. Zhang, H. Wang, K. H. Bui, H. Nguyen, I. Atanasov, W. H. Hui, S. K. Yang, Z. H. Zhou, and K. L. Hill (2019). Cryo electron tomography with Volta phase plate reveals novel structural foundations of the 96-nm axonemal repeat in the pathogen Trypanosoma brucei. *eLife* 8:1–30. DOI: 10.7554/elife.52058.

Inoue, N., M. Ikawa, A. Isotani, and M. Okabe (2005). The immunoglobulin superfamily protein Izumo is required for sperm to fuse with eggs. *Nature* 434 (7030):234–238. DOI: 10.1038/nature03362.

Inoue, N., Y. Satouh, M. Ikawa, M. Okabe, and R. Yanagimachi (2011). Acrosome-reacted mouse spermatozoa recovered from the perivitelline space can fertilize other eggs. *Proceedings of the National Academy of Sciences of the United States of America* 108 (50):20008–20011. DOI: 10.1073/pnas.1116965108.

Ishikawa, T. (2017). Axoneme structure from motile cilia. *Cold Spring Harbor Perspectives in Biology* 9 (1):a028076. DOI: 10.1101/cshperspect.a028076.

Isotani, A., T. Matsumura, M. Ogawa, T. Tanaka, K. Yamagata, M. Ikawa, and M. Okabe (2017). A delayed sperm penetration of cumulus layers by disruption of acrosin gene in rats. *Biology of Reproduction* 97 (1):61–68. DOI: 10.1093/biolre/iox066.

Ito, C., H. Akutsu, R. Yao, K. Yoshida, K. Yamatoya, T. Mutoh, T. Makino, K. Aoyama, H. Ishikawa, K. Kunimoto, S. Tsukita, T. Noda, M. Kikkawa, and K. Toshimori (2019). Odf2 haploinsufficiency causes a new type of decapitated and decaudated spermatozoa, Odf2-DDS, in mice. *Scientific Reports* 9 (1):1–13. DOI: 10.1038/s41598-019-50516-2.

Jacob, W. A., A. Bakker, R. C. Hertsens, and W. Biermans (1994). Mitochondrial matrix granules: their behavior during changing metabolic situations and their relationship to contact sites between inner and outer mitochondrial membranes. *Microscopy Research and Technique* 27 (4):307–318. DOI: 10.1002/jemt.1070270406.

Jamieson, B. G., D. M. Scheltinga, and A. D. Tucker (1997). The ultrastructure of spermatozoa of the Australian freshwater crocodile, Crocodylus johnstoni Krefft, 1873 (Crocodylidae, Reptilia). *Journal of Submicroscopic Cytology and Pathology* 29 (2):265–274.

Janke, C. and M. M. Magiera (2020). The tubulin code and its role in controlling microtubule properties and functions. *Nature Reviews Molecular Cell Biology* 21 (6):307–326. DOI: 10.1038/s41580-020-0214-3.

Jeulin, C., L. M. Lewin, C. Chevrier, and D. Schoevaert-Brossault (1996). Changes in Flagellar Movement of Rat Spermatozoa Along the Length of the Epididymis: Manual and Computer-Aided Image Analysis. *Cell Motility and the Cytoskeleton* 35 (2):147–161. DOI: 10.1002/(SICI)1097-0169(1996)35:2<147::AID-CM7>3.0.CO;2-7.

Jin, M., E. Fujiwara, Y. Kakiuchi, M. Okabe, Y. Satouh, S. A. Baba, K. Chiba, and N. Hirohashi (2011). Most fertilizing mouse spermatozoa begin their acrosome reaction before contact with the zona pellucida during in vitro fertilization. *Proceedings of the National*

Academy of Sciences of the United States of America 108 (12):4892–6. DOI: 10.1073/pnas.1018202108.

Johnson, G. D., C. Lalancette, A. K. Linnemann, G. Boissonneault, and S. A. Krawetz (2010). The sperm nucleus: chromatin, RNA, and the nuclear matrix. *Reproduction* 141 (1):21–36. DOI: 10.1530/REP-10-0322.

Kamp, G., G. Büsselmann, and J. Lauterwein (1996). Spermatozoa: Models for studying regulatory aspects of energy metabolism. *Experientia* 52 (5):487–494. DOI: 10.1007/BF01919321.

Kang, J. S., J. H. Tian, P. Y. Pan, P. Zald, C. Li, C. Deng, and Z. H. Sheng (2008). Docking of Axonal Mitochondria by Syntaphilin Controls Their Mobility and Affects Short-Term Facilitation. *Cell* 132 (1):137–148. DOI: 10.1016/j.cell.2007.11.024.

Kellenberger, E. and J. Kistler (1979). The Physics of Specimen Preparation. *Unconventional Electron Microscopy for Molecular Structure Determination*. Wiesbaden: Vieweg+Teubner Verlag, p. 49–79. DOI: 10.1007/978-3-322-86362-1_3.

Kemphues, K. J., T. C. Kaufman, R. A. Raff, and E. C. Raff (1982). The testis-specific β-tubulin subunit in drosophila melanogaster has multiple functions in spermatogenesis. *Cell* 31 (3):655–670. DOI: 10.1016/0092-8674(82)90321-X.

Khalifa, A., M. Ichikawa, D. Dai, S. Kubo, C. Black, K. Peri, T. S. McAlear, S. Veyron, S. K. Yang, J. Vargas, S. Bechstedt, J.-F. Trempe, and K. H. Bui (2020). The inner junction complex of the cilia is an interaction hub that involves tubulin post-translational modifications. *eLife* 9 (e52760):1–25. DOI: 10.1101/774695.

Khan, S. and J. M. Scholey (2018). Assembly, Functions and Evolution of Archaella, Flagella and Cilia. *Current Biology* 28 (6):R278–R292. DOI: 10.1016/j.cub.2018.01.085.

Kim, D. E., D. Chivian, and D. Baker (2004). Protein structure prediction and analysis using the Robetta server. *Nucleic Acids Research* 32 (Web Server):W526–W531. DOI: 10.1093/nar/gkh468.

Kim, K.-S., J. A. Foster, and G. L. Gerton (2005). Differential Release of Guinea Pig Sperm Acrosomal Components During Exocytosis. *Biology of Reproduction* 64 (1):148–156. DOI: 10.1095/biolreprod64.1.148.

Kim, K.-S., J. A. Foster, K. W. Kvasnicka, and G. L. Gerton (2011). Transitional states of acrosomal exocytosis and proteolytic processing of the acrosomal matrix in guinea pig sperm. *Molecular Reproduction and Development* 78 (12):930–941. DOI: 10.1002/mrd.21387.

Kim, K.-S. and G. L. Gerton (2003). Differential release of soluble and matrix components: evidence for intermediate states of secretion during spontaneous acrosomal exocytosis in mouse sperm. *Developmental Biology* 264 (1):141–152. DOI: 10.1016/J.YDBIO.2003.08.006.

Kirby, T. J. and J. Lammerding (2018). Emerging views of the nucleus as a cellular mechanosensor. *Nature Cell Biology* 20 (4):373–381. DOI: 10.1038/s41556-018-0038-y.

Konieczny, P., P. Fuchs, S. Reipert, W. S. Kunz, A. Zeöld, I. Fischer, D. Paulin, R. Schröder, and G. Wiche (2008). Myofiber integrity depends on desmin network targeting to Z-disks and costameres via distinct plectin isoforms. *Journal of Cell Biology* 181 (4):667–681. DOI: 10.1083/jcb.200711058.

Konno, A., K. Shiba, C. Cai, and K. Inaba (2015). Branchial cilia and sperm flagella recruit distinct axonemal components. *PLoS ONE* 10 (5):1–20. DOI: 10.1371/journal.pone.0126005.

Kremer, A., S. Lippens, S. Bartunkova, B. Asselbergh, C. Blanpain, M. Fendrych, A. Goossens, M. Holt, S. Janssens, M. Krols, J. C. Larsimont, C. Mc Guire, M. K. Nowack, X. Saelens,

A. Schertel, B. Schepens, M. Slezak, V. Timmerman, C. Theunis, R. Van Brempt, Y. Visser, and C. J. Guérin (2015). Developing 3D SEM in a broad biological context. *Journal of Microscopy* 259 (2):80–96. DOI: 10.1111/jmi.12211.

Kremer, J. R., D. N. Mastronarde, and J. R. McIntosh (1996). Computer Visualization of Three-Dimensional Image Data Using IMOD. *Journal of Structural Biology* 116 (1):71–6. DOI: 10.1006/jsbi.1996.0013.

Krisfalusi, M., K. Miki, P. L. Magyar, and D. A. O'Brien (2006). Multiple Glycolytic Enzymes Are Tightly Bound to the Fibrous Sheath of Mouse Spermatozoa1. *Biology of Reproduction* 75 (2):270–278. DOI: 10.1095/biolreprod.105.049684.

Kudryashev, M., S. Lepper, R. Stanway, S. Bohn, W. Baumeister, M. Cyrklaff, and F. Frischknecht (2010). Positioning of large organelles by a membrane- associated cytoskeleton in Plasmodium sporozoites. *Cellular Microbiology* 12 (3):362–371. DOI: 10.1111/j.1462-5822.2009.01399.x.

Kurachi, M., M. Hoshi, and H. Tashiro (1995). Buckling of a single microtubule by optical trapping forces: Direct measurement of microtubule rigidity. *Cell Motility and the Cytoskeleton* 30 (3):221–228. DOI: 10.1002/cm.970300306.

Kwon, W. S., Y. J. Park, E. S. A. Mohamed, and M. G. Pang (2013). Voltage-dependent anion channels are a key factor of male fertility. *Fertility and Sterility* 99 (2):354–361. DOI: 10.1016/j.fertnstert.2012.09.021.

La Spina, F. A., L. C. Puga Molina, A. Romarowski, A. M. Vitale, T. L. Falzone, D. Krapf, N. Hirohashi, and M. G. Buffone (2016). Mouse sperm begin to undergo acrosomal exocytosis in the upper isthmus of the oviduct. *Developmental Biology* 411 (2):172–182. DOI: 10.1016/j.ydbio.2016.02.006.

Lamas-Toranzo, I., J. G. Hamze, E. Bianchi, B. Fernández-Fuertes, S. Pérez-Cerezales, R. Laguna-Barraza, R. Fernández-González, P. Lonergan, A. Gutiérrez-Adán, G. J. Wright, M. Jiménez-Movilla, and P. Bermejo-álvarez (2020). TMEM95 is a sperm membrane protein essential for mammalian fertilization. *eLife* 9:1–18. DOI: 10.7554/eLife.53913.

Lavorato, M., V. R. Iyer, W. Dewight, R. R. Cupo, V. Debattisti, L. Gomez, S. De La Fuente, Y. T. Zhao, H. H. Valdivia, G. Hajnóczky, and C. Franzini-Armstrong (2017). Increased mitochondrial nanotunneling activity, induced by calcium imbalance, affects intermitochondrial matrix exchanges. *Proceedings of the National Academy of Sciences of the United States of America* 114 (5):E849–E858. DOI: 10.1073/pnas.1617788113.

Le Guennec, M., N. Klena, D. Gambarotto, M. H. Laporte, A.-m. Tassin, H. van den Hoek, P. S. Erdmann, M. Schaffer, L. Kovacik, S. Borgers, K. N. Goldie, H. Stahlberg, M. Bornens, J. Azimzadeh, B. D. Engel, V. Hamel, and P. Guichard (2020). A helical inner scaffold provides a structural basis for centriole cohesion. *Science Advances* 6 (7):eaaz4137. DOI: 10.1126/sciadv.aaz4137.

Lechtreck, K. F., P. Delmotte, M. L. Robinson, M. J. Sanderson, and G. B. Witman (2008). Mutations in Hydin impair ciliary motility in mice. *Journal of Cell Biology* 180 (3):633–643. DOI: 10.1083/jcb.200710162.

Lepault, J. and J. Dubochet (1986). Electron Microscopy of Frozen Hydrated Specimens: Preparation and Characteristics. *Methods in Enzymology* 127:719–730. DOI: 10.1016/0889-1605(86)90041-8.

Lesich, K. A., T. G. de Pinho, L. Dang, and C. B. Lindemann (2014). Ultrastructural evidence that motility changes caused by variations in ATP, Mg2+, and ADP correlate to conformational changes in reactivated bull sperm axonemes. *Cytoskeleton* 71 (11):649–661. DOI: 10.1002/cm.21199.

Li, S., J. J. Fernandez, W. F. Marshall, and D. A. Agard (2012). Three-dimensional structure of basal body triplet revealed by electron cryo-tomography. *EMBO Journal* 31 (3):552–562. DOI: 10.1038/emboj.2011.460.

Lin, J. and D. Nicastro (2018). Asymmetric distribution and spatial switching of dynein activity generates ciliary motility. *Science* 360 (6387):1–12. DOI: 10.1126/science.aar1968.

Lin, J., K. Okada, M. Raytchev, M. C. Smith, and D. Nicastro (2014a). Structural mechanism of the dynein power stroke. *Nature Cell Biology* 16 (5):479–485. DOI: 10.1038/ncb2939.

Lin, J., W. Yin, M. C. Smith, K. Song, M. W. Leigh, M. A. Zariwala, M. R. Knowles, L. E. Ostrowski, and D. Nicastro (2014b). Cryo-electron tomography reveals ciliary defects underlying human RSPH1 primary ciliary dyskinesia. *Nature Communications* 5 (1):5727. DOI: 10.1038/ncomms6727.

Lindemann, C. B. (1996). Functional significance of the outer dense fibers of mammalian sperm examined by computer simulations with the geometric clutch model. *Cell Motility and the Cytoskeleton* 34 (4):258–270. DOI: 10.1002/(SICI)1097-0169(1996)34:4<258::AID-CM1>3.0.CO;2-4.

Lindemann, C. B. and K. A. Lesich (2016). Functional anatomy of the mammalian sperm flagellum. *Cytoskeleton* 73 (11):652–669. DOI: 10.1002/cm.21338.

Lindemann, C. B., L. J. Macauley, and K. A. Lesich (2005). The counterbend phenomenon in dynein-disabled rat sperm flagella and what it reveals about the interdoublet elasticity. *Biophysical Journal* 89 (2):1165–1174. DOI: 10.1529/biophysj.105.060681.

Liu, F., P. Lössl, B. M. Rabbitts, R. S. Balaban, and A. J. Heck (2018). The interactome of intact mitochondria by cross-linking mass spectrometry provides evidence for coexisting respiratory supercomplexes. *Molecular and Cellular Proteomics* 17 (2):216–232. DOI: 10.1074/mcp.RA117.000470.

Loncarek, J. and M. Bettencourt-Dias (2018). Building the right centriole for each cell type. *Journal of Cell Biology* 217 (3):823–835. DOI: 10.1083/jcb.201704093.

Lučić, V., F. Förster, and W. Baumeister (2005). Structural Studies by Electron Tomography: From Cells to Molecules. *Annual Review of Biochemistry* 74 (1):833–865. DOI: 10.1146/annurev.biochem.73.011303.074112.

Luef, B., K. R. Frischkorn, K. C. Wrighton, H. Y. N. Holman, G. Birarda, B. C. Thomas, A. Singh, K. H. Williams, C. E. Siegerist, S. G. Tringe, K. H. Downing, L. R. Comolli, and J. F. Banfield (2015). Diverse uncultivated ultra-small bacterial cells in groundwater. *Nature Communications* 6:DOI: 10.1038/ncomms7372.

Lüpold, S. and S. Pitnick (2018). Sperm form and function: what do we know about the role of sexual selection? *Reproduction* 155 (5):R229–R243. DOI: 10.1530/rep-17-0536.

Luxton, G. W., E. R. Gomes, E. S. Folker, E. Vintinner, and G. G. Gundersen (2010). Linear arrays of nuclear envelope proteins harness retrograde actin flow for nuclear movement. *Science* 329 (5994):956–959. DOI: 10.1126/science.1189072.

Ma, M., M. Stoyanova, G. Rademacher, S. K. Dutcher, A. Brown, and R. Zhang (2019). Structure of the Decorated Ciliary Doublet Microtubule. *Cell* 179 (4):909–922.e12. DOI: 10.1016/j.cell.2019.09.030.

Mahamid, J., S. Pfeffer, M. Schaffer, E. Villa, R. Danev, L. K. Cuellar, F. Förster, A. A. Hyman, J. M. Plitzko, and W. Baumeister (2016). Visualizing the molecular sociology at the HeLa cell nuclear periphery. *Science* 351 (6276):969–972. DOI: 10.1126/science.aad8857.

Malyala, S., Y. Zhang, J. O. Strubbe, and J. N. Bazil (2019). Calcium phosphate precipitation inhibits mitochondrial energy metabolism. *PLoS Computational Biology* 15 (1):1–19. DOI: 10.1371/journal.pcbi.1006719.

Manandhar, G., H. Schatten, and P. Sutovsky (2005). Centrosome Reduction During Gametogenesis and Its Significance. *Biology of Reproduction* 72 (1):2–13. DOI: 10.1095/biolreprod.104.031245.

Manandhar, G., C. Simerly, and G. Schatten (2000). Highly degenerated distal centrioles in rhesus and human spermatozoa. *Human Reproduction* 15 (2):256–263. DOI: 10.1093/humrep/15.2.256.

Manandhar, G., P. Sutovsky, H. C. Joshi, T. Stearns, and G. Schatten (1998). Centrosome reduction during mouse spermiogenesis. *Developmental Biology* 203 (2):424–434. DOI: 10.1006/dbio.1998.8947.

Mannella, C. A. (1982). Structure of the outer mitochondrial membrane: Ordered arrays of porelike subunits in outer-membrane fractions from Neurospora crassa mitochondria. *Journal of Cell Biology* 94 (3):680–687. DOI: 10.1083/jcb.94.3.680.

— (1998). Conformational changes in the mitochondrial channel protein, VDAC, and their functional implications. *Journal of Structural Biology* 121 (2):207–218. DOI: 10.1006/jsbi.1997.3954.

Marin, S., K. Chiang, S. Bassilian, W. N. P. Lee, L. G. Boros, J. M. Fernández-Novell, J. J. Centelles, A. Medrano, J. E. Rodriguez-Gil, and M. Cascante (2003). Metabolic strategy of boar spermatozoa revealed by a metabolomic characterization. *FEBS Letters* 554 (3):342–346. DOI: 10.1016/S0014-5793(03)01185-2.

Marko, M., C. Hsieh, R. Schalek, J. Frank, and C. Mannella (2007). Focused-ion-beam thinning of frozen-hydrated biological specimens for cryo-electron microscopy. *Nature Methods* 4 (3):215–217. DOI: 10.1038/nmeth1014.

Mastronarde, D. N. (2005). Automated electron microscope tomography using robust prediction of specimen movements. *Journal of Structural Biology* 152 (1):36–51. DOI: 10.1016/j.jsb.2005.07.007.

Mayorga, L. S., C. N. Tomes, and S. A. Belmonte (2007). Acrosomal exocytosis, a special type of regulated secretion. *IUBMB Life* 59 (4-5):286–292. DOI: 10.1080/15216540701222872.

Mi, Y., Z. Shi, and J. Li (2015). Spata19 is critical for sperm mitochondrial function and male fertility. *Molecular Reproduction and Development* 82 (11):907–913. DOI: 10.1002/mrd.22536.

Miki, K., W. Qu, E. H. Goulding, W. D. Willis, D. O. Bunch, L. F. Strader, S. D. Perreault, E. M. Eddy, and D. A. O'Brien (2004). Glyceraldehyde 3-phosphate dehydrogenase-S, a sperm-specific glycolytic enzyme, is required for sperm motility and male fertility. *Proceedings of the National Academy of Sciences of the United States of America* 101 (47):16501–16506. DOI: 10.1073/pnas.0407708101.

Miller, D., M. Brinkworth, and D. Iles (2010). Paternal DNA packaging in spermatozoa: More than the sum of its parts? DNA, histones, protamines and epigenetics. *Reproduction* 139 (2):287–301. DOI: 10.1530/REP-09-0281.

Milner, D. J., M. Mavroidis, N. Weisleder, and Y. Capetanaki (2000). Desmin cytoskeleton linked to muscle mitochondrial distribution and respiratory function. *Journal of Cell Biology* 150 (6):1283–1297. DOI: 10.1083/jcb.150.6.1283.

Mitchell, D. R. (2017). Evolution of cilia. *Cold Spring Harbor Perspectives in Biology* 9 (1):DOI: 10.1101/cshperspect.a028290.

Miyata, H., Y. Satouh, D. Mashiko, M. Muto, K. Nozawa, K. Shiba, Y. Fujihara, A. Isotani, K. Inaba, and M. Ikawa (2015). Sperm calcineurin inhibition prevents mouse fertility with implications for male contraceptive. *Science* 350 (6259):442–445. DOI: 10.1126/science.aad0836.

Moor, H. (1987). Theory and Practice of High Pressure Freezing. *Cryotechniques in Biological Electron Microscopy*. Berlin, Heidelberg: Springer Berlin Heidelberg, p. 175–191. DOI: 10.1007/978-3-642-72815-0_8.

Moore, A. S. and E. L. Holzbaur (2018). Mitochondrial-cytoskeletal interactions: dynamic associations that facilitate network function and remodeling. *Current Opinion in Physiology* 3:94–100. DOI: 10.1016/j.cophys.2018.03.003.

Mortimer, D. (1994). *Practical Laboratory Andrology*. New York: Oxford University Press.

— (2018). The functional anatomy of the human spermatozoon: relating ultrastructure and function. *Molecular Human Reproduction* 24 (12):1–26. DOI: 10.1093/molehr/gay040.

Moser, F., V. Prazák, V. Mordhorst, D. M. Andrade, L. A. Baker, C. Hagen, K. Grünewald, and R. Kaufmann (2019). Cryo-SOFI enabling low-dose super-resolution correlative light and electron cryo-microscopy. *Proceedings of the National Academy of Sciences of the United States of America* 116 (11):4804–4809. DOI: 10.1073/pnas.1810690116.

Mühleip, A. W., C. E. Dewar, A. Schnaufer, W. Kühlbrandt, and K. M. Davies (2017). In situ structure of trypanosomal ATP synthase dimer reveals a unique arrangement of catalytic subunits. *Proceedings of the National Academy of Sciences of the United States of America* 114 (5):992–997. DOI: 10.1073/pnas.1612386114.

Mukai, C. and M. Okuno (2004). Glycolysis Plays a Major Role for Adenosine Triphosphate Supplementation in Mouse Sperm Flagellar Movement. *Biology of Reproduction* 71 (2):540–547. DOI: 10.1095/biolreprod.103.026054.

Muro, Y., H. Hasuwa, A. Isotani, H. Miyata, K. Yamagata, M. Ikawa, R. Yanagimachi, and M. Okabe (2016). Behavior of Mouse Spermatozoa in the Female Reproductive Tract from Soon after Mating to the Beginning of Fertilization1. *Biology of Reproduction* 94 (4):1–7. DOI: 10.1095/biolreprod.115.135368.

Nachtigall, R. D. (2006). International disparities in access to infertility services. *Fertility and Sterility* 85 (4):871–875. DOI: 10.1016/j.fertnstert.2005.08.066.

Nagae, T., R. Yanagimachi, P. N. Srivastava, and H. Yanagimachi (1986). Acrosome reaction in human spermatozoa. *Fertility and Sterility* 45 (5):701–707. DOI: 10.1016/S0015-0282(16)49344-1.

Nagayama, K., S. Yamazaki, Y. Yahiro, and T. Matsumoto (2014). Estimation of the mechanical connection between apical stress fibers and the nucleus in vascular smooth muscle cells cultured on a substrate. *Journal of Biomechanics* 47 (6):1422–1429. DOI: 10.1016/j.jbiomech.2014.01.042.

Neal, C. V., A. L. Hall-McNair, J. Kirkman-Brown, D. J. Smith, and M. T. Gallagher (2020). Doing more with less: The flagellar end piece enhances the propulsive effectiveness of human spermatozoa. *Physical Review Fluids* 5 (7):073101. DOI: 10.1103/PhysRevFluids.5.073101. arXiv: 1910.01470.

Nicastro, D., X. Fu, T. Heuser, A. Tso, M. E. Porter, and R. W. Linck (2011). Cryo-electron tomography reveals conserved features of doublet microtubules in flagella. *Proceedings of the National Academy of Sciences of the United States of America* 108 (42):E845–E853. DOI: 10.1073/pnas.1106178108.

Nicastro, D., C. Schwartz, J. Pierson, R. Gaudette, M. E. Porter, and J. R. McIntosh (2006). The molecular architecture of axonemes revealed by cryoelectron tomography. *Science* 313 (5789):944–948. DOI: 10.1126/science.1128618.

Nielsen, M. G., F. R. Turner, J. A. Hutchens, and E. C. Raff (2001). Axoneme-specific β-tubulin specialization: A conserved C-terminal motif specifies the central pair. *Current Biology* 11 (7):529–533. DOI: 10.1016/S0960-9822(01)00150-6.

Nixon, B., S. L. Cafe, A. L. Eamens, G. N. De Iuliis, E. G. Bromfield, J. H. Martin, D. A. Skerrett-Byrne, and M. D. Dun (2020). Molecular insights into the divergence and diversity of post-testicular maturation strategies. *Molecular and Cellular Endocrinology* 517:110955. DOI: 10.1016/j.mce.2020.110955.

Noda, T., Y. Lu, Y. Fujihara, S. Oura, T. Koyano, S. Kobayashi, M. M. Matzuk, and M. Ikawa (2020). Sperm proteins SOF1, TMEM95, and SPACA6 are required for sperm-oocyte fusion in mice. *Proceedings of the National Academy of Sciences of the United States of America* 117 (21):DOI: 10.1073/pnas.1922650117.

Nogales, E., M. Whittaker, R. A. Milligan, and K. H. Downing (1999). High-resolution model of the microtubule. *Cell* 96 (1):79–88. DOI: 10.1016/S0092-8674(00)80961-7.

Nolan, J. P. and R. H. Hammerstedt (1997). Regulation of membrane stability and the acrosome reaction in mammalian sperm. *The FASEB Journal* 11 (8):670–682. DOI: 10.1096/fasebj.11.8.9240968.

Norman, C., E. Goldberg, I. Porterfield, and C. Johnson (1960). Prolonged Survival of Human Sperm in chemically defined Media at Room Temperatures. *Nature* 188 (4752):760–760. DOI: 10.1038/188760a0.

Novikoff, A. (1945). The concept of integrative levels and biology. *Science* 101 (2618):209–215. DOI: 10.1126/science.101.2618.209.

O'Reilly, F. J., L. Xue, A. Graziadei, L. Sinn, S. Lenz, D. Tegunov, C. Blötz, N. Singh, W. J. Hagen, P. Cramer, J. Stülke, J. Mahamid, and J. Rappsilber (2020). In-cell architecture of an actively transcribing-translating expressome. *Science* 369 (6503):554–557. DOI: 10.1126/science.abb3758.

Oda, T., H. Yanagisawa, R. Kamiya, and M. Kikkawa (2014). A molecular ruler determines the repeat length in eukaryotic cilia and flagella. *Science* 346 (6211):857–860. DOI: 10.1126/science.1260214.

Odet, F., S. Gabel, R. E. London, E. Goldberg, and E. M. Eddy (2013). Glycolysis and Mitochondrial Respiration in Mouse LDHC-Null Sperm. *Biology of Reproduction* 88 (4):1–7. DOI: 10.1095/biolreprod.113.108530.

Olson, G. E. and R. W. Linck (1977). Observations of the structural components of flagellar axonemes and central pair microtubules from rat sperm. *Journal of Ultrasructure Research* 61 (1):21–43. DOI: 10.1016/S0022-5320(77)90004-1.

Olson, G. E. and V. Winfrey (1994). Structure of Acrosomal Matrix Domains of Rabbit Sperm. *Journal of Structural Biology* 112:41–48.

Olson, G. E. and V. P. Winfrey (1986). Identification of a cytoskeletal network adherent to the mitochondria of mammalian spermatozoa. *Journal of Ultrastructure Research and Molecular Structure Research* 94 (2):131–139. DOI: 10.1016/0889-1605(86)90059-5.

— (1990). Mitochondria-cytoskeleton interactions in the sperm midpiece. *Journal of Structural Biology* 103 (1):13–22. DOI: 10.1016/1047-8477(90)90081-M.

— (1992). Structural organization of surface domains of sperm mitochondria. *Molecular Reproduction and Development* 33 (1):89–98. DOI: 10.1002/mrd.1080330113.

Ombelet, W. (2011). Global access to infertility care in developing countries: A case of human rights, equity and social justice. *Facts, Views & Vision in ObGyn* 3 (4):257–266.

Otani, H., O. Tanaka, K. .-. Kasai, and T. Yoshioka (1988). Development of mitochondrial helical sheath in the middle piece of the mouse spermatid tail: Regular dispositions and synchronized changes. *The Anatomical Record* 222 (1):26–33. DOI: 10.1002/ar.1092220106.

Ounjai, P., K. D. Kim, P. V. Lishko, and K. H. Downing (2012). Three-Dimensional Structure of the Bovine Sperm Connecting Piece Revealed by Electron Cryotomography. *Biology of Reproduction* 87 (3):73. DOI: 10.1095/biolreprod.112.101980.

Owa, M., T. Uchihashi, H. aki Yanagisawa, T. Yamano, H. Iguchi, H. Fukuzawa, K. ichi Wakabayashi, T. Ando, and M. Kikkawa (2019). Inner lumen proteins stabilize doublet microtubules in cilia and flagella. *Nature Communications* 10 (1):1143. DOI: 10.1038/s41467-019-09051-x.

Palade, G. E. (1953). An electron microscope study of the mitochondrial structure. *Journal of Histochemistry & Cytochemistry* 1 (4):188–211. DOI: 10.1177/1.4.188.

— (1955a). A small particulate component of the cytoplasm. *The Journal of Biophysical and Biochemical Cytology* 1 (1):59–68. DOI: 10.1083/jcb.1.1.59.

— (1955b). Studies on the endoplasmic reticulum. *The Journal of Biophysical and Biochemical Cytology* 1 (6):567–582. DOI: 10.1083/jcb.1.6.567.

Pampaloni, F., G. Lattanzi, A. Jonáš, T. Surrey, E. Frey, and E. L. Florin (2006). Thermal fluctuations of grafted microtubules provide evidence of a length-dependent persistence length. *Proceedings of the National Academy of Sciences of the United States of America* 103 (27):10248–10253. DOI: 10.1073/pnas.0603931103.

Pereira, C. D., J. B. Serrano, F. Martins, O. A. da Cruz e Silva, and S. Rebelo (2019). Nuclear envelope dynamics during mammalian spermatogenesis: new insights on male fertility. *Biological Reviews* 94 (4):1195–1219. DOI: 10.1111/brv.12498.

Perkins, G. A. and M. H. Ellisman (2011). Mitochondrial configurations in peripheral nerve suggest differential ATP production. *Journal of Structural Biology* 173 (1):117–127. DOI: 10.1016/j.jsb.2010.06.017.

Petersen, C., L. Füzesi, and S. Hoyer-Fender (1999). Outer dense fibre proteins from human sperm tail: Molecular cloning and expression analyses of two cDNA transcripts encoding proteins of ˜70 kDa. *Molecular Human Reproduction* 5 (7):627–635. DOI: 10.1093/molehr/5.7.627.

Pettersen, E. F., T. D. Goddard, C. C. Huang, G. S. Couch, D. M. Greenblatt, E. C. Meng, and T. E. Ferrin (2004). UCSF Chimera - A visualization system for exploratory research and analysis. *Journal of Computational Chemistry* 25 (13):1605–1612. DOI: 10.1002/jcc.20084.

Phillips, D. M. (1972). Comparative analysis of mammalian sperm motility. *Journal of Cell Biology* 53 (2):561–573. DOI: 10.1083/jcb.53.2.561.

Picard, M., M. J. McManus, G. Csordás, P. Várnai, G. W. Dorn, D. Williams, G. Hajnóczky, and D. C. Wallace (2015). Trans-mitochondrial coordination of cristae at regulated membrane junctions. *Nature Communications* 6 (1):6259. DOI: 10.1038/ncomms7259.

Pigino, G., K. H. Bui, A. Maheshwari, P. Lupetti, D. Diener, and T. Ishikawa (2011). Cryoelectron tomography of radial spokes in cilia and flagella. *Journal of Cell Biology* 195 (4):673–687. DOI: 10.1083/jcb.201106125.

Pigino, G., A. Maheshwari, K. H. Bui, C. Shingyoji, S. Kamimura, and T. Ishikawa (2012). Comparative structural analysis of eukaryotic flagella and cilia from Chlamydomonas, Tetrahymena, and sea urchins. *Journal of Structural Biology* 178 (2):199–206. DOI: 10.1016/j.jsb.2012.02.012.

Pilhofer, M., M. S. Ladinsky, A. W. McDowall, and G. J. Jensen (2010). Bacterial TEM. New insights from cryo-microscopy. *Methods in Cell Biology*. Vol. 96. (C). Elsevier Inc., p. 21–45. DOI: 10.1016/S0091-679X(10)96002-0.

Pitnick, S., D. J. Hosken, and T. R. Birkhead (2009). Sperm morphological diversity. *Sperm Biology*. Elsevier Ltd, p. 69–149. DOI: 10.1016/B978-0-12-372568-4.00003-3.

Pleuger, C., M. S. Lehti, J. E. Dunleavy, D. Fietz, and M. K. O'Bryan (2020). Haploid male germ cells—the Grand Central Station of protein transport. *Human Reproduction Update* 26 (4):474–500. DOI: 10.1093/humupd/dmaa004.

Porter, K. R., A. Claude, and E. F. Fullam (1945). A study of tissue culture cells by electron microscopy: Methods and preliminary observations. *Journal of Experimental Medicine* 81 (3):233–246. DOI: 10.1084/jem.81.3.233.

Puga Molina, L. C., G. M. Luque, P. A. Balestrini, C. I. Marín-Briggiler, A. Romarowski, and M. G. Buffone (2018). Molecular Basis of Human Sperm Capacitation. *Frontiers in Cell and Developmental Biology* 6:72. DOI: 10.3389/fcell.2018.00072.

Qian, M.-X., Y. Pang, C. H. Liu, K. Haratake, B.-Y. Du, D.-Y. Ji, G.-F. Wang, Q.-Q. Zhu, W. Song, Y. Yu, X.-X. Zhang, H.-T. Huang, S. Miao, L.-B. Chen, Z.-H. Zhang, Y.-N. Liang, S. Liu, H. Cha, D. Yang, Y. Zhai, T. Komatsu, F. Tsuruta, H. Li, C. Cao, W. Li, G.-H. Li, Y. Cheng, T. Chiba, L. Wang, A. L. Goldberg, Y. Shen, and X.-B. Qiu (2013). Acetylation-Mediated Proteasomal Degradation of Core Histones during DNA Repair and Spermatogenesis. *Cell* 153 (5):1012–1024. DOI: 10.1016/j.cell.2013.04.032.

Quillin, M. L. and B. W. Matthews (2000). Accurate calculation of the density of proteins. *Acta Crystallographica Section D Biological Crystallography* 56 (7):791–794. DOI: 10.1107/S090744490000679X.

Raff, E. C., H. D. Hoyle, E. M. Popodi, and F. R. Turner (2008). Axoneme β-Tubulin Sequence Determines Attachment of Outer Dynein Arms. *Current Biology* 18 (12):911–914. DOI: 10.1016/j.cub.2008.05.031.

Rast, A., M. Schaffer, S. Albert, W. Wan, S. Pfeffer, F. Beck, J. M. Plitzko, J. Nickelsen, and B. D. Engel (2019). Biogenic regions of cyanobacterial thylakoids form contact sites with the plasma membrane. *Nature Plants* 5 (4):436–446. DOI: 10.1038/s41477-019-0399-7.

Rathke, C., W. M. Baarends, S. Awe, and R. Renkawitz-Pohl (2014). Chromatin dynamics during spermiogenesis. *Biochimica et Biophysica Acta - Gene Regulatory Mechanisms* 1839 (3):155–168. DOI: 10.1016/j.bbagrm.2013.08.004.

Rathore, S. S., Y. Liu, H. Yu, C. Wan, M. S. Lee, Q. Yin, M. H. Stowell, and J. Shen (2019). Intracellular Vesicle Fusion Requires a Membrane-Destabilizing Peptide Located at the Juxtamembrane Region of the v-SNARE. *Cell Reports* 29 (13):4583–4592.e3. DOI: 10.1016/j.celrep.2019.11.107.

Riedel-Kruse, I. H. and A. Hilfinger (2007). How molecular motors shape the flagellar beat. *HFSP Journal* 1 (3):192–208. DOI: 10.2976/1.2773861.

Rigort, A., F. J. Bäuerlein, E. Villa, M. Eibauer, T. Laugks, W. Baumeister, and J. M. M. Plitzko (2012). Focused ion beam micromachining of eukaryotic cells for cryoelectron tomography. *Proceedings of the National Academy of Sciences of the United States of America* 109 (12):4449–4454. DOI: 10.1073/pnas.1201333109.

Roll-Mecak, A. (2020). The Tubulin Code in Microtubule Dynamics and Information Encoding. *Developmental Cell* 54 (1):7–20. DOI: 10.1016/j.devcel.2020.06.008.

Ross, L. and B. B. Normark (2015). Evolutionary problems in centrosome and centriole biology. *Journal of Evolutionary Biology* 28 (5):995–1004. DOI: 10.1111/jeb.12620.

Russell, L., R. Peterson, and M. Freund (1979). Direct evidence for formation of hybrid vesicles by fusion of plasma and outer acrosomal membranes during the acrosome reaction in boar spermatozoa. *Journal of Experimental Zoology* 208 (1):41–55. DOI: 10.1002/jez.1402080106.

Saggiorato, G., L. Alvarez, J. F. Jikeli, U. B. Kaupp, G. Gompper, and J. Elgeti (2017). Human sperm steer with second harmonics of the flagellar beat. *Nature Communications* 8 (1):DOI: 10.1038/s41467-017-01462-y.

San Agustin, J. T., G. J. Pazour, and G. B. Witman (2015). Intraflagellar transport is essential for mammalian spermiogenesis but is absent in mature sperm. *Molecular Biology of the Cell* 26 (24):ed. by W. Marshall, 4358–4372. DOI: 10.1091/mbc.E15-08-0578.

Sathananthan, A. H., S. S. Ratnam, S. C. Ng, J. J. Tarín, L. Gianaroli, and A. Trounson (1996). The sperm centriole: Its inheritance, replication and perpetuation in early human embryos. *Human Reproduction* 11 (2):345–356. DOI: 10.1093/HUMREP/11.2.345.

Satouh, Y., N. Inoue, M. Ikawa, and M. Okabe (2012). Visualization of the moment of mouse sperm–egg fusion and dynamic localization of IZUMO1. *Journal of Cell Science* 125 (21):4985–4990. DOI: 10.1242/jcs.100867.

Schaffer, M., J. Mahamid, B. D. Engel, T. Laugks, W. Baumeister, and J. M. Plitzko (2017). Optimized cryo-focused ion beam sample preparation aimed at in situ structural studies of membrane proteins. *Journal of Structural Biology* 197 (2):73–82. DOI: 10.1016/j.jsb.2016.07.010.

Schaffer, M., S. Pfeffer, J. Mahamid, S. Kleindiek, T. Laugks, S. Albert, B. D. Engel, A. Rummel, A. J. Smith, W. Baumeister, and J. M. Plitzko (2019). A cryo-FIB lift-out technique enables molecular-resolution cryo-ET within native Caenorhabditis elegans tissue. *Nature Methods* 16 (8):757–762. DOI: 10.1038/s41592-019-0497-5.

Schatten, G. (1994). The Centrosome and Its Mode of Inheritance: The Reduction of the Centrosome during Gametogenesis and Its Restoration during Fertilization. *Developmental Biology* 165 (2):299–335. DOI: 10.1006/dbio.1994.1256.

Schatten, H. (2011). Low voltage high-resolution SEM (LVHRSEM) for biological structural and molecular analysis. *Micron* 42 (2):175–185. DOI: 10.1016/j.micron.2010.08.008.

Scheffer, L. K. et al. (2020). A Connectome and Analysis of the Adult Drosophila Central Brain. *bioRxiv*:2020.04.07.030213. DOI: 10.1101/2020.04.07.030213.

Schertel, A., N. Snaidero, H. M. Han, T. Ruhwedel, M. Laue, M. Grabenbauer, and W. Möbius (2013). Cryo FIB-SEM: Volume imaging of cellular ultrastructure in native frozen specimens. *Journal of Structural Biology* 184 (2):355–360. DOI: 10.1016/j.jsb.2013.09.024.

Schneider, M., H. Forster, A. Boersma, A. Seiler, H. Wehnes, F. Sinowatz, C. Neumüller, M. J. Deutsch, A. Walch, M. H. Angelis, W. Wurst, F. Ursini, A. Roveri, M. Maleszewski, M. Maiorino, and M. Conrad (2009). Mitochondrial glutathione peroxidase 4 disruption causes male infertility. *The FASEB Journal* 23 (9):3233–3242. DOI: 10.1096/fj.09-132795.

Schnick, C., S. D. Polley, Q. L. Fivelman, L. C. Ranford-Cartwright, S. R. Wilkinson, J. A. Brannigan, A. J. Wilkinson, and D. A. Baker (2009). Structure and non-essential function of glycerol kinase in Plasmodium falciparum blood stages. *Molecular Microbiology* 71 (2):533–545. DOI: 10.1111/j.1365-2958.2008.06544.x.

Serres, C., D. Escalier, and G. David (1984). Ultrastructural morphometry of the human sperm flagellum with a stereological analysis of the lengths of the dense fibres. *Biology of the Cell* 49 (2):153–161. DOI: 10.1111/j.1768-322X.1984.tb00233.x.

Serres, C., D. Feneux, and P. Jouannet (1986). Abnormal distribution of the periaxonemal structures in a human sperm flagellar dyskinesia. *Cell Motility and the Cytoskeleton* 6 (1):68–76. DOI: 10.1002/cm.970060109.

Sha, Y. W., X. Wang, X. Xu, L. Ding, W. S. Liu, P. Li, Z. Y. Su, J. Chen, L. B. Mei, L. K. Zheng, H. L. Wang, S. B. Kong, M. You, and J. F. Wu (2019). Biallelic mutations in PMFBP1 cause acephalic spermatozoa. *Clinical Genetics* 95 (2):277–286. DOI: 10.1111/cge.13461.

Shang, Y., J. Yan, W. Tang, C. Liu, S. Xiao, Y. Guo, L. Yuan, L. Chen, H. Jiang, X. Guo, J. Qiao, and W. Li (2018). Mechanistic insights into acephalic spermatozoa syndrome–associated

mutations in the human SUN5 gene. *Journal of Biological Chemistry* 293 (7):2395–2407. DOI: 10.1074/jbc.RA117.000861.

Shang, Y., F. Zhu, L. Wang, Y.-C. Ouyang, M.-Z. Dong, C. Liu, H. Zhao, X. Cui, D. Ma, Z. Zhang, X. Yang, Y. Guo, F. Liu, L. Yuan, F. Gao, X. Guo, Q.-Y. Sun, Y. Cao, and W. Li (2017). Essential role for SUN5 in anchoring sperm head to the tail. *eLife* 6:DOI: 10.7554/elife.28199.

Shimada, K., H. Kato, H. Miyata, and M. Ikawa (2019). Glycerol kinase 2 is essential for proper arrangement of crescent-like mitochondria to form the mitochondrial sheath during mouse spermatogenesis. *Journal of Reproduction and Development* 65 (2):155–162.

Smith, D. J., E. A. Gaffney, H. Gadelha, N. Kapur, and J. C. Kirkman-Brown (2009). Bend propagation in the flagella of migrating human sperm, and Its modulation by viscosity. *Cell Motility and the Cytoskeleton* 66 (4):220–236. DOI: 10.1002/cm.20345.

Smith, F. D., J. L. Esseltine, P. J. Nygren, D. Veesler, D. P. Byrne, M. Vonderach, I. Strashnov, C. E. Eyers, P. A. Eyers, L. K. Langeberg, and J. D. Scott (2017). Local protein kinase A action proceeds through intact holoenzymes. *Science* 356 (6344):1288–1293. DOI: 10.1126/science.aaj1669.

Smith, F. D., S. L. Reichow, J. L. Esseltine, D. Shi, L. K. Langeberg, J. D. Scott, and T. Gonen (2013). Intrinsic disorder within an AKAP-protein kinase A complex guides local substrate phosphorylation. *eLife* 2013 (2):1–19. DOI: 10.7554/eLife.01319.001.

So, C., K. B. Seres, A. M. Steyer, E. Mönnich, D. Clift, A. Pejkovska, W. Möbius, and M. Schuh (2019). A liquid-like spindle domain promotes acentrosomal spindle assembly in mammalian oocytes. *Science* 364 (6447):eaat9557. DOI: 10.1126/science.aat9557.

Song, K., Z. Shang, X. Fu, X. Lou, N. Grigorieff, and D. Nicastro (2020). In situ structure determination at nanometer resolution using TYGRESS. *Nature Methods* 17 (2):201–208. DOI: 10.1038/s41592-019-0651-0.

Sosa, B. A., U. Kutay, and T. U. Schwartz (2013). Structural insights into LINC complexes. *Current Opinion in Structural Biology* 23 (2):285–291. DOI: 10.1016/j.sbi.2013.03.005.

Sosa, B. A., A. Rothballer, U. Kutay, and T. U. Schwartz (2012). LINC complexes form by binding of three KASH peptides to domain interfaces of trimeric SUN proteins. *Cell* 149 (5):1035–1047. DOI: 10.1016/j.cell.2012.03.046.

Sosa, C. M., M. A. Pavarotti, M. N. Zanetti, F. C. M. Zoppino, G. A. Blas, and L. S. Mayorga (2015). Kinetics of human sperm acrosomal exocytosis. *Molecular Human Reproduction* 21 (3):244–254. DOI: 10.1093/molehr/gau110.

Starr, D. A. and H. N. Fridolfsson (2010). Interactions Between Nuclei and the Cytoskeleton Are Mediated by SUN-KASH Nuclear-Envelope Bridges. *Annual Review of Cell and Developmental Biology* 26 (1):421–444. DOI: 10.1146/annurev-cellbio-100109-104037.

Steeghs, K., F. Oerlemans, and B. Wieringa (1995). Mice deficient in ubiquitous mitochondrial creatine kinase are viable and fertile. *Biochimica et Biophysica Acta - Bioenergetics* 1230 (3):130–138. DOI: 10.1016/0005-2728(95)00044-J.

Steen, K., D. Chen, F. Wang, R. Majumdar, S. Chen, S. Kumar, D. B. Lombard, R. Weigert, A. G. Zieman, C. A. Parent, and P. A. Coulombe (2020). A role for keratins in supporting mitochondrial organization and function in skin keratinocytes. *Molecular Biology of the Cell* 31 (11):1103–1111. DOI: 10.1091/mbc.E19-10-0565.

Steib, E., M. H. Laporte, D. Gambarotto, N. Olieric, C. Zheng, S. Borgers, V. Olieric, M. Le Guennec, F. Koll, A.-M. Tassin, M. O. Steinmetz, P. Guichard, and V. Hamel (2020). WDR90 is a centriolar microtubule wall protein important for centriole architecture integrity. *eLife* 9:1–28. DOI: 10.7554/eLife.57205.

Steptoe, P. and R. Edwards (1978). Birth after the reimplantation of a human embryo. *The Lancet* 312 (8085):366. DOI: 10.1016/S0140-6736(78)92957-4.

Stival, C., C. Ritagliati, X. Xu, M. G. Gervasi, G. M. Luque, C. B. Graf, J. L. De La Vega-Beltrn, N. Torres, A. Darszon, D. Krapf, M. G. Buffone, P. E. Visconti, and D. Krapf (2018). Disruption of protein kinase A localization induces acrosomal exocytosis in capacitated mouse sperm. *Journal of Biological Chemistry* 293 (24):9435–9447. DOI: 10.1074/jbc.RA118.002286.

Stock, C. E. and L. R. Fraser (1987). The acrosome reaction in human sperm from men of proven fertility. *Human Reproduction* 2 (2):109–119. DOI: 10.1093/oxfordjournals.humrep.a136494.

Strubbe-Rivera, J. O., J. R. Schrad, E. V. Pavlov, J. F. Conway, K. N. Parent, and J. N. Bazil (2020). The Mitochondrial Permeability Transition Phenomenon Elucidated by Cryo-EM Reveals the Genuine Impact of Calcium Overload on Mitochondrial Structure and Function. *bioRxiv*:1–20. DOI: 10.1101/2020.03.13.991349.

Suarez, S. S. (2008). Control of hyperactivation in sperm. *Human Reproduction Update* 14 (6):647–657. DOI: 10.1093/humupd/dmn029.

Sully, E. A., A. Biddlecom, J. E. Darroch, T. Riley, N. Lince-Deroche, L. Firestein, R. Murro, and L. S. Ashford (2020). *Adding It Up: Investing in Sexual and Reproductive Health 2019*. New York: Guttmacher Institute. DOI: 10.1363/2020.31593.

Sunagawa, S., S. G. Acinas, P. Bork, C. Bowler, S. G. Acinas, M. Babin, P. Bork, E. Boss, C. Bowler, G. Cochrane, C. de Vargas, M. Follows, G. Gorsky, N. Grimsley, L. Guidi, P. Hingamp, D. Iudicone, O. Jaillon, S. Kandels, L. Karp-Boss, E. Karsenti, M. Lescot, F. Not, H. Ogata, S. Pesant, N. Poulton, J. Raes, C. Sardet, M. Sieracki, S. Speich, L. Stemmann, M. B. Sullivan, S. Sunagawa, P. Wincker, D. Eveillard, G. Gorsky, L. Guidi, D. Iudicone, E. Karsenti, F. Lombard, H. Ogata, S. Pesant, M. B. Sullivan, P. Wincker, and C. de Vargas (2020). Tara Oceans: towards global ocean ecosystems biology. *Nature Reviews Microbiology* 18 (8):428–445. DOI: 10.1038/s41579-020-0364-5.

Sutton, G., D. Sun, X. Fu, A. Kotecha, C. W. Hecksel, D. K. Clare, P. Zhang, D. I. Stuart, and M. Boyce (2020). Assembly intermediates of orthoreovirus captured in the cell. *Nature Communications* 11 (1):1–7. DOI: 10.1038/s41467-020-18243-9.

Takao, D. and S. Kamimura (2008). FRAP analysis of molecular diffusion inside sea-urchin spermatozoa. *Journal of Experimental Biology* 211 (22):3594–3600. DOI: 10.1242/jeb.021923.

Talbot, P. and R. S. Chacon (1982). Ultrastructural observations on binding and membrane fusion between human sperm and zona pellucida-free hamster oocytes. *Fertility and Sterility* 37 (2):240–248. DOI: 10.1016/S0015-0282(16)46047-4.

Taute, K. M., F. Pampaloni, E. Frey, and E. L. Florin (2008). Microtubule dynamics depart from the wormlike chain model. *Physical Review Letters* 100 (2):1–4. DOI: 10.1103/PhysRevLett.100.028102. arXiv: 0708.1928.

Tegunov, D. and P. Cramer (2019). Real-time cryo-electron microscopy data preprocessing with Warp. *Nature Methods* 16 (11):1146–1152. DOI: 10.1038/s41592-019-0580-y.

Tegunov, D., L. Xue, C. Dienemann, P. Cramer, and J. Mahamid (2020). Multi-particle cryo-EM refinement with M visualizes ribosome-antibiotic complex at 3.7-Å inside cells. *bioRxiv*:DOI: 10.1101/2020.06.05.136341.

Thirumalai, A. and S. T. Page (2020). Male Hormonal Contraception. *Annual Review of Medicine* 71:17–31. DOI: 10.1146/annurev-med-042418-010947.

Titze, B. and C. Genoud (2016). Volume scanning electron microscopy for imaging biological ultrastructure. *Biology of the Cell* 108 (11):307–323. DOI: 10.1111/boc.201600024.

Tivol, W. F., A. Briegel, and G. J. Jensen (2008). An Improved Cryogen for Plunge Freezing. *Microscopy and Microanalysis* 14 (5):375–379. DOI: 10.1017/S1431927608080781.

Tombes, R. M. and B. M. Shapiro (1987). Enzyme Termini of a Phosphocreatine Shuttle. *Journal of Biological Chemistry* 262 (33):16011–16019.

Tourmente, M., P. Villar-Moya, E. Rial, and E. R. Roldan (2015). Differences in ATP generation via glycolysis and oxidative phosphorylation and relationships with sperm motility in mouse species. *Journal of Biological Chemistry* 290 (33):20613–20626. DOI: 10.1074/jbc.M115.664813.

Travis, A. J. and G. S. Kopf (2002). The role of cholesterol efflux in regulating the fertilization potential of mammalian spermatozoa. *Journal of Clinical Investigation* 110 (6):731–736. DOI: 10.1172/JCI16392.

Tsai, P.-S. S., N. Garcia-Gil, T. van Haeften, and B. M. Gadella (2010). How pig sperm prepares to fertilize: stable acrosome docking to the plasma membrane. *PLoS ONE* 5 (6):DOI: 10.1371/journal.pone.0011204.

Tsuiki, A., H. Hoshiai, K. Takahashi, M. Suzuki, K. Hoshi, and A. Tsuiki (1986). Sperm-Egg Interactions Observed by Scanning Electron Microscopy. *Archives of Andrology* 16 (1):35–47. DOI: 10.3109/01485018608986921.

Ueno, H., T. Ishikawa, K. H. Bui, K. Gonda, T. Ishikawa, and T. Yamaguchi (2012). Mouse respiratory cilia with the asymmetric axonemal structure on sparsely distributed ciliary cells can generate overall directional flow. *Nanomedicine: Nanotechnology, Biology, and Medicine* 8 (7):1081–1087. DOI: 10.1016/j.nano.2012.01.004.

Ungricht, R. and U. Kutay (2017). Mechanisms and functions of nuclear envelope remodelling. *Nature Reviews Molecular Cell Biology* 18 (4):229–245. DOI: 10.1038/nrm.2016.153.

Van Leeuwenhoek, A. (1677). Observationes D. Anthonii Lewenhoeck, de natis'e semine genitali animalculis. *Philosophical Transactions of the Royal Society of London* 12 (142):1040–1046. DOI: 10.1098/rstl.1677.0068.

VanBuren, V., D. J. Odde, and L. Cassimeris (2002). Estimates of lateral and longitudinal bond energies within the microtubule lattice. *Proceedings of the National Academy of Sciences of the United States of America* 99 (9):6035–6040. DOI: 10.1073/pnas.092504999.

Vernon, G. G. and D. M. Woolley (2004). Basal sliding and the mechanics of oscillation in a mammalian sperm flagellum. *Biophysical Journal* 87 (6):3934–3944. DOI: 10.1529/biophysj.104.042648.

Viana, M. P., A. I. Brown, I. A. Mueller, C. Goul, E. F. Koslover, and S. M. Rafelski (2020). Mitochondrial Fission and Fusion Dynamics Generate Efficient, Robust, and Evenly Distributed Network Topologies in Budding Yeast Cells. *Cell Systems* 10 (3):287–297.e5. DOI: 10.1016/j.cels.2020.02.002.

Vickaryous, M. K. and B. K. Hall (2006). Human cell type diversity, evolution, development, and classification with special reference to cells derived from the neural crest. *Biological Reviews of the Cambridge Philosophical Society* 81 (3):425–455. DOI: 10.1017/S1464793106007068.

Villa, E., M. Schaffer, J. M. Plitzko, and W. Baumeister (2013). Opening windows into the cell: focused-ion-beam milling for cryo-electron tomography. *Current Opinion in Structural Biology* 23 (5):771–777. DOI: 10.1016/j.sbi.2013.08.006.

Vincent, A. E., K. White, T. Davey, J. Philips, R. T. Ogden, C. Lawess, C. Warren, M. G. Hall, Y. S. Ng, G. Falkous, T. Holden, D. Deehan, R. W. Taylor, D. M. Turnbull, and M. Picard (2019). Quantitative 3D Mapping of the Human Skeletal Muscle Mitochondrial Network. *Cell Reports* 26 (4):996–1009.e4. DOI: 10.1016/j.celrep.2019.01.010.

Vincent, A. E., D. M. Turnbull, V. Eisner, G. Hajnóczky, and M. Picard (2017). Mitochondrial Nanotunnels. *Trends in Cell Biology* 27 (11):787–799. DOI: 10.1016/j.tcb.2017.08.009.

Von Kügelgen, A., H. Tang, G. G. Hardy, D. Kureisaite-Ciziene, Y. V. Brun, P. J. Stansfeld, C. V. Robinson, and T. A. Bharat (2020). In Situ Structure of an Intact Lipopolysaccharide-Bound Bacterial Surface Layer. *Cell* 180 (2):348–358.e15. DOI: 10.1016/j.cell.2019.12.006.

Wallmeier, J., K. G. Nielsen, C. E. Kuehni, J. S. Lucas, M. W. Leigh, M. A. Zariwala, and H. Omran (2020). Motile ciliopathies. *Nature Reviews Disease Primers* 6 (1):77. DOI: 10.1038/s41572-020-0209-6.

Wan, K. Y. (2018). Coordination of eukaryotic cilia and flagella. *Essays in Biochemistry* 62 (6):829–838. DOI: 10.1042/EBC20180029.

Wan, W. and J. Briggs (2016). Cryo-Electron Tomography and Subtomogram Averaging. *Methods in Enzymology*. 1st ed. Vol. 579. Elsevier Inc., p. 329–367. DOI: 10.1016/bs.mie.2016.04.014.

Watanabe, R., R. Buschauer, J. Böhning, M. Audagnotto, K. Lasker, T.-w. Lu, D. Boassa, S. Taylor, and E. Villa (2020). The In Situ Structure of Parkinson's Disease-Linked LRRK2. *Cell*:1–11. DOI: 10.1016/j.cell.2020.08.004.

Webster, M., K. L. Wikin, and O. Cohen-Fix (2009). Sizing up the nucleus: Nuclear shape, size and nuclear-envelope assembly. *Journal of Cell Science* 122 (10):1477–1486. DOI: 10.1242/jcs.037333.

Wildt, D. E., P. Comizzoli, B. Pukazhenthi, and N. Songsasen (2010). Lessons from biodiversity - The value of nontraditional species to advance reproductive science, conservation, and human health. *Molecular Reproduction and Development* 77 (5):397–409. DOI: 10.1002/mrd.21137.

Winey, M., J. B. Meehl, E. T. O'Toole, and T. H. Giddings (2014). Conventional transmission electron microscopy. *Molecular Biology of the Cell* 25 (3):319–323. DOI: 10.1091/mbc.E12-12-0863.

Woese, C. R. (2004). A New Biology for a New Century. *Microbiology and Molecular Biology Reviews* 68 (2):173–186. DOI: 10.1128/MMBR.68.2.173-186.2004.

Wolf, S., Y. Mutsafi, T. Dadosh, T. Ilani, Z. Lansky, B. Horowitz, S. Rubin, M. Elbaum, and D. Fass (2017). 3D visualization of mitochondrial solid-phase calcium stores in whole cells. *eLife* 6:DOI: 10.7554/eLife.29929.

Wolff, G., R. W. A. L. Limpens, J. C. Zevenhoven-Dobbe, U. Laugks, S. Zheng, A. W. M. de Jong, R. I. Koning, D. A. Agard, K. Grünewald, A. J. Koster, E. J. Snijder, and M. Bárcena (2020). A molecular pore spans the double membrane of the coronavirus replication organelle. *Science* 3629 (6509):eabd3629. DOI: 10.1126/science.abd3629.

Wolff, G., R. W. Limpens, S. Zheng, E. J. Snijder, D. A. Agard, A. J. Koster, and M. Bárcena (2019). Mind the gap: Micro-expansion joints drastically decrease the bending of FIB-milled cryo-lamellae. *Journal of Structural Biology* 208 (3):107389. DOI: 10.1016/j.jsb.2019.09.006.

Woolley, D. M. and R. A. Beatty (1967). Inheritance of Midpiece Length in Mouse Spermatozoa. *Nature* 215 (5096):94–95. DOI: 10.1038/215094a0.

Woolley, D. M. and G. G. Vernon (2001). A study of helical and planar waves on sea urchin sperm flagella, with a theory of how they are generated. *Journal of Experimental Biology* 204 (7):1333–1345.

Woolley, D. M., D. A. Carter, and G. N. Tilly (2008). Compliance in the neck structures of the guinea pig spermatozoon, as indicated by rapid freezing and electron microscopy. *Journal of Anatomy* 213 (3):336–341. DOI: 10.1111/j.1469-7580.2008.00919.x.

Woolley, D. M. and D. W. Fawcett (1973). The degeneration and disappearance of the centrioles during the development of the rat spermatozoon. *The Anatomical Record* 177 (2):289–301. DOI: 10.1002/ar.1091770209.

Wu, G. H., P. G. Mitchell, J. G. Galaz-Montoya, C. W. Hecksel, E. M. Sontag, V. Gangadharan, J. Marshman, D. Mankus, M. E. Bisher, A. K. Lytton-Jean, J. Frydman, K. Czymmek, and W. Chiu (2020). Multi-scale 3D Cryo-Correlative Microscopy for Vitrified Cells. *Structure*:1–7. DOI: 10.1016/j.str.2020.07.017.

Wu, M. and G. C. Lander (2020). Present and emerging methodologies in cryo-EM single particle analysis. *Biophysical Journal* 0 (0):1–9. DOI: 10.1016/j.bpj.2020.08.027.

Xu, C. S., K. J. Hayworth, Z. Lu, P. Grob, A. M. Hassan, J. G. García-Cerdán, K. K. Niyogi, E. Nogales, R. J. Weinberg, and H. F. Hess (2017). Enhanced FIB-SEM systems for large-volume 3D imaging. *eLife* 6:1–36. DOI: 10.7554/eLife.25916.

Xu, C. S., S. Pang, K. J. Hayworth, and H. F. Hess (2019). Enabling FIB-SEM Systems for Large Volume Connectomics and Cell Biology. *bioRxiv* C:852863. DOI: 10.1101/852863.

Xu, K., L. Yang, L. Zhang, and H. Qi (2020). Lack of AKAP3 disrupts integrity of the subcellular structure and proteome of mouse sperm and causes male sterility. *Development* 147 (2):dev181057. DOI: 10.1242/dev.181057.

Yamaguchi, H., T. Oda, M. Kikkawa, and H. Takeda (2018). Systematic studies of all PIH proteins in zebrafish reveal their distinct roles in axonemal dynein assembly. *eLife* 7:1–25. DOI: 10.7554/elife.36979.

Yanagimachi, R. and Y. D. Noda (1970). Electron microscope studies of sperm incorporation into the golden hamster egg. *American Journal of Anatomy* 128 (4):429–461. DOI: 10.1002/aja.1001280404.

Yanagimachi, R. (1981). Mechanisms of Fertilization in Mammals. *Fertilization and Embryonic Development In Vitro*. Ed. by L. Mastroianni and J. Biggers. Boston, MA: Springer, p. 81–182. DOI: 10.1007/978-1-4684-4016-4_6.

Yanagimachi, R. and M. C. Chang (1963). Fertilization of Hamster Eggs in vitro. *Nature* 200 (4903):281–282. DOI: 10.1038/200281b0.

Yeung, C. H., G. C. Majumder, C. Rolf, H. M. Behre, and T. G. Cooper (1996). The role of phosphocreatine kinase in the motility of human spermatozoa supported by different metabolic substrates. *Molecular Human Reproduction* 2 (8):591–596. DOI: 10.1093/molehr/2.8.591.

Yuan, S., C. J. Stratton, J. Bao, H. Zheng, B. P. Bhetwal, R. Yanagimachi, and W. Yan (2015). SPATA6 is required for normal assembly of the sperm connecting piece and tight head-tail conjunction. *Proceedings of the National Academy of Sciences of the United States of America* 112 (5):E430–E439. DOI: 10.1073/pnas.1424648112.

Yudin, A. I., W. Gottlieb, and S. Meizel (1988). Ultrastructural studies of the early events of the human sperm acrosome reaction as initiated by human follicular fluid. *Gamete Research* 20 (1):11–24. DOI: 10.1002/mrd.1120200103.

Zabeo, D., J. T. Croft, and J. L. Höög (2019). Axonemal doublet microtubules can split into two complete singlets in human sperm flagellum tips. *FEBS Letters* 593 (9):892–902. DOI: 10.1002/1873-3468.13379.

Zabeo, D., J. M. Heumann, C. L. Schwartz, A. Suzuki-Shinjo, G. Morgan, P. O. Widlund, and J. L. Höög (2018). A lumenal interrupted helix in human sperm tail microtubules. *Scientific Reports* 8 (1):2727. DOI: 10.1038/s41598-018-21165-8.

Zanetti, N. and L. S. Mayorga (2009). Acrosomal Swelling and Membrane Docking Are Required for Hybrid Vesicle Formation During the Human Sperm Acrosome Reaction. *Biology of Reproduction* 81 (2):396–405. DOI: 10.1095/biolreprod.109.076166.

Zeng, G. L. (2012). A filtered backprojection algorithm with characteristics of the iterative landweber algorithm. *Medical Physics* 39 (2):603–607. DOI: 10.1118/1.3673956.

Zeng, X., M. R. Leung, T. Zeev-Ben-Mordehai, and M. Xu (2018). A convolutional autoencoder approach for mining features in cellular electron cryo-tomograms and weakly supervised coarse segmentation. *Journal of Structural Biology* 202 (2):150–160. DOI: 10.1016/J.JSB.2017.12.015.

Zhang, J., D. Zhang, L. Sun, G. Ji, X. Huang, T. Niu, and F. Sun (2019). VHUT-cryo-FIB, a method to fabricate frozen-hydrated lamella of tissue specimen for in situ cryo-electron tomography. *bioRxiv*:727149. DOI: 10.1101/727149.

Zhang, Y., Y. Ou, M. Cheng, H. Shojaei Saadi, J. C. Thundathil, and F. A. van der Hoorn (2012). KLC3 is involved in sperm tail midpiece formation and sperm function. *Developmental Biology* 366 (2):101–110. DOI: 10.1016/j.ydbio.2012.04.026.

Zhao, W., Z. Li, P. Ping, G. Wang, X. Yuan, and F. Sun (2018). Outer dense fibers stabilize the axoneme to maintain sperm motility. *Journal of Cellular and Molecular Medicine* 22 (3):1755–1768. DOI: 10.1111/jcmm.13457.

Zheng, S. Q., E. Palovcak, J. P. Armache, K. A. Verba, Y. Cheng, and D. A. Agard (2017). MotionCor2: Anisotropic correction of beam-induced motion for improved cryo-electron microscopy. *Nature Methods* 14 (4):331–332. DOI: 10.1038/nmeth.4193. arXiv: 15334406.

Zhu, F., C. Liu, F. Wang, X. Yang, J. Zhang, H. Wu, Z. Zhang, X. He, Z. Zhang, P. Zhou, Z. Wei, Y. Shang, L. Wang, R. Zhang, Y. C. Ouyang, Q. Y. Sun, Y. Cao, and W. Li (2018). Mutations in PMFBP1 Cause Acephalic Spermatozoa Syndrome. *American Journal of Human Genetics* 103 (2):188–199. DOI: 10.1016/j.ajhg.2018.06.010.

Zhu, Y., D. Sun, A. Schertel, J. Ning, X. Fu, P. P. Gwo, A. M. Watson, and P. Zhang (2020). Serial cryoFIB/SEM reveals profound cytoarchitectural disruptions caused by a pathogenic mutation in Leigh syndrome patient cells. *bioRxiv*:1–19. DOI: 10.1101/2020.05.28.121111.